Precipitation and plasticity couplings in a 7xxx aluminium alloy: application to thermomechanical treatments for distortion correction of aerospace component

Guillaume Fribourg

To cite this version:

Guillaume Fribourg. Precipitation and plasticity couplings in a 7xxx aluminium alloy: application to thermomechanical treatments for distortion correction of aerospace component. Mechanics [physics.med-ph]. Institut National Polytechnique de Grenoble - INPG, 2009. English. NNT : . tel-00502536

HAL Id: tel-00502536
https://theses.hal.science/tel-00502536

Submitted on 15 Jul 2010

HAL is a multi-disciplinary open access archive for the deposit and dissemination of scientific research documents, whether they are published or not. The documents may come from teaching and research institutions in France or abroad, or from public or private research centers.

L'archive ouverte pluridisciplinaire **HAL**, est destinée au dépôt et à la diffusion de documents scientifiques de niveau recherche, publiés ou non, émanant des établissements d'enseignement et de recherche français ou étrangers, des laboratoires publics ou privés.

INSTITUT POLYTECHNIQUE DE GRENOBLE

N° attribué par la bibliothèque
|__|__|__|__|__|__|__|__|__|__|

THESE

pour obtenir le grade de

DOCTEUR DE L'Institut Polytechnique de Grenoble

Spécialité : *Matériaux, Mécanique, Génie Civil, Electrochimie*

préparée au laboratoire *Sciences et Ingénierie des Matériaux et Procédés*
dans le cadre de ***l'Ecole Doctorale*** *Ingénierie – Matériaux, Mécanique, Environnement, Energétique, Procédés, Production*

présentée et soutenue publiquement

par

Guillaume FRIBOURG

le 20 mai 2009

Titre :

Couplages entre précipitation et plasticité dans un alliage d'aluminium 7xxx : application à des traitements thermomécaniques de réduction des distorsions dans des composants aéronautiques

Directeurs de thèse :

Alexis DESCHAMPS et Yves BRECHET

Jury :

M. David EMBURY,	Président
M^{me}. Anne-Françoise GOURGUES-LORENZON,	Rapporteur
M. Jeremy ROBINSON,	Rapporteur
M. Alexis DESCHAMPS,	Directeur de thèse
M. Yves BRECHET,	Directeur de thèse
Mme. Ulrike HECKENBERGER,	Examinateur

Precipitation and plasticity couplings in a 7xxx aluminium alloy: application to thermomechanical treatments for distortion correction of aerospace components

Couplages entre précipitation et plasticité dans un alliage d'aluminium 7xxx : application à des traitements thermomécaniques de réduction des distorsions dans des composants aéronautiques

Final version

Version définitive

10/01/2010

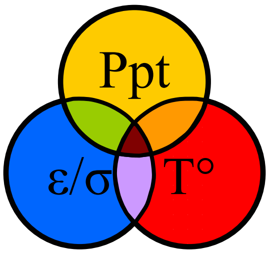

Chapter 0. Thesis presentation

Summary

After a short summary of the thesis, this chapter then presents the different chapters.
While the rest of the thesis is written in Shakespeare's language, part C of this chapter is written in French. The objective is to summarize in a more complete way the main results of the thesis.

Rien ne vaut la recherche lorsqu'on veut trouver quelque chose.

J.R.R. Tolkien

Ce à quoi Anatole France répondit :

On a beau chercher, on ne trouve jamais que soi-même.

Et Platon de surenchérir :

La finalité de la Vie, c'est l'admiration du Beau.

And so what ?

Me dis-je, en entendant ces discussions…

A. Thesis presentation

A.1. Abstract

7xxx aluminium alloys are high strength alloys mainly used for aerospace applications due to their high specific mechanical properties. Manufacturing these age-hardenable alloys involves complex thermomechanical treatments that develop the precipitation microstructure responsible for the mechanical properties. Undesirable long-range internal stresses are also produced during these treatments, and may induce severe distortions in the final products.

Different thermomechanical processes: shot peening, laser forming and age-forming (respectively a purely mechanical, a purely thermal and a thermomechanical treatment) are used to reduce internal stresses and/or part distortion in aerospace aluminium 7xxx machined components. However, they modify the material's microstructure and consequently the mechanical properties.

We have examined the couplings between these thermomechanical treatments, the microstructure and the mechanical properties, throughout experimental characterization and physically based modelling. The effect of precipitation on the strain hardening properties is investigated, to establish a physically-based strain hardening model able to be used in a shot peening finite element model. Then, the effect of laser forming on the precipitation state and on the material strength is examined. The last part is dedicated to the study of the effect of age forming – a process combining simultaneous plastic deformation and heat treatment - on precipitation.

A.2. Résumé

Les alliages d'aluminium de la série 7xxx sont des alliages à durcissement structural, principalement utilisés dans des applications aéronautiques en raison de leurs propriétés mécaniques spécifiques élevées. Le composant principal de leur résistance mécanique est leur microstructure de précipitation, obtenue par le biais de traitements thermomécaniques complexes. Ceux-ci induisent cependant des contraintes internes à longue distance, susceptibles de générer des distorsions sévères dans les pièces aéronautiques.

Certains traitements thermomécaniques comme le grenaillage (*shot peening*), le formage laser (*laser forming*) et le formage revenu (*age-forming*), des procédés respectivement purement mécanique, purement thermique et thermomécanique, permettent de réduire les distorsions de pièces usinées. Ils modifient cependant la microstructure, et, par conséquent, les propriétés mécaniques.

La présente étude, portant sur les couplages entre ces traitements thermomécaniques, la microstructure et les propriétés mécaniques d'un alliage 7xxx, comprend un travail de caractérisation expérimentale et de modélisation à base physique. L'effet de la précipitation sur l'écrouissage du matériau est ainsi examiné, et un modèle d'écrouissage destiné à être implémenté dans un modèle éléments finis de simulation du grenaillage est proposé. L'étude du formage laser aboutit quant à elle à un modèle prédictif de l'état de précipitation et des propriétés mécaniques locales induits par ce procédé. La dernière partie est consacrée à l'étude de l'effet du formage revenu – procédé combinant déformation plastique et traitement thermique simultanés – sur la précipitation.

A.3. Contents

Chapter 0: Thesis presentation

Chapter I: General introduction 1

Chapter V: Microstructural evolution during thermomechanical treatments 151

Chapter VI: Conclusion and perspectives 195

A.4. Acknowledgements

This work is carried out in the COMPACT project which is a collaboration between Airbus UK (Project Co-ordinator), Rio Tinto Alcan, Limerick University, University of Bristol, Enabling Process Technologies, University of Hannover, EADS Germany, University of Patras, Alenia Aeronautica, Ultra RS, Institut Polytechnique de Grenoble and the University of Sheffield. The project is jointly funded by the European Union Framework 6 initiative and the project partners.

Thank you to the different persons who contributed actively to this work:

- Pr. Alexis Deschamps and Pr. Yves Bréchet for having allowing me to perform this PhD, for having driving me and for fruitful discussions,
- Dr. Françoise Bley for her kind and active commitment in the SAXS experiments,
- Jean-Louis Chemin for the incommensurable work he furnished for the development of the TSAXS device,
- The staff of beamline BM02-D2AM at ESRF for technical help during the SAXS experiments,
- Dr. Michel Perez from INSA de Lyon (Lyon, France) for his patient collaboration for the modelling of precipitation kinetics,
- Dr. Aude Simar from UCL (Louvain-la-Neuve, Belgium) for her enthusiastic and friendly collaboration in the strain hardening modelling,
- Dr. Thorsten Marlaud and Dr. Nicolas Meyer, for their technical support in the everyday work.

Thank you also to my PhD committee:

- Pr. J. David Embury, from Mc Master University (Ontario, Canada), who made me the honour to be the chairman of my jury,
- Pr. Anne-Françoise Gourgues-Lorenzon from l'Ecole des Mines de Paris – Paritech (Paris, France), who accepted to be reviewer of this PhD committee,
- Dr. Jeremy Robinson, from University of Limerick (Limerick, Ireland), who kindly came from Limerick to participate to this PhD jury as reviewer,
- Ulrike Heckenberger, from EADS Research Centre (Ottobrunn, Germany), who followed my PhD from the beginning of this project, and accepted to come to this PhD defence.

B. Short break

Après cet exercice formel…

Imaginez un pauvre Normand débarqué de sa fraîche et rayonnante région dans un pays aussi hostile que le cœur des Alpes, où les gens portent à longueur de journée des chaussures de randonnée et des sacs à dos, occupent leurs soirées et week-ends à grimper, courir ou skier, et dont les principaux sujets de conversation sont la météo, le profil du prochain raid ou le dernier 7a qu'ils ont passé ! J'oubliais aussi que ces mêmes gens parlent également d'énergie d'activation, de dislocations ou de dopage électronique ; encore des termes de sportifs, me disais-je à l'époque... Imaginez le choc culturel !

Et pourtant je m'y suis habitué ; j'ai appris, et j'y ai pris plaisir… à cette thèse comme à la vie Grenobloise ! Je tiens ici à remercier plus personnellement celles et ceux qui ont contribué, par leur soutien quotidien ou ponctuel, à m'aider à franchir ces épreuves.

Je tiens à remercier une nouvelle fois Alexis Deschamps et Yves Bréchet. Vous m'avez permis de travailler dans un contexte scientifique rigoureux et dynamique et m'avez fait confiance… J'ai également apprécié les moments moins académiques que nous avons pu partager. Je me souviens en particulier d'un chocolat chaud au Train Bleu en Gare de Lyon avec Yves, 4 ans plus tôt ; chocolat chaud après lequel je me suis décidé à venir à Grenoble effectuer mon stage de fin d'études, et, par la suite, ma thèse. Je me rappelle également de cette fameuse dégustation de fromage que nous avions organisée ensemble, où la suprématie gustative du Camembert a fait fondre (de jalousie) le St Nectaire. Je garde également d'excellents souvenirs de ces (mouvementés) déplacements à Naples et Athènes, en particulier de la visite de l'Acropole, par une belle fin d'après-midi d'été. Mes souvenirs avec Alexis sont liés aux barbecues lacustres et alpins que nous avons pu organiser, aux rives des lacs d'Aiguebelette et du Monteynard, et à ton enthousiaste volonté de faire découvrir tes passions aux doctorants du labo, moi compris : randonnée, ski, canyoning… Je garde également des souvenirs impérissables de cette fameuse expédition, où Alexis au pilotage et Yves en « éveilleur » avaient réussit à emmener un minibus plein à craquer de jeunes chercheurs à la conférence Euromat à Nüremberg.

Merci également à l'équipe du projet Compact. Merci en particulier à Wei-Ming Sim, Georges Mylonas, Georges Labeas, Ulricke Heckenberger et Jeremy Robinson. Travailler avec vous fut un plaisir.

Merci encore à Aude Simar et Michel Perez. Ils se sont tous les deux impliqués dans mon projet naturellement et activement. Merci en particulier à Aude pour son sympathique accueil en Belgique.

Je tiens à saluer les jeunes chercheurs du laboratoire, avec lesquels j'ai partagé ces discussions et manips, parfois durant de longues nuits à l'ESRF… mais également ces sympathiques soirées, tournois de foot et autres barbecues, au cours des 1, 2, 3 voire presque 4 années que nous avons passées ensemble : Jean-Louis Collet, Oussama Youssfi, Bechir Chehab, Sinh Vu Hoang, Benjamin Decreus, Mohammad El Jawad, Sylvain Ringeval, Gwenaël Texier, Benoit Malard, Jean-Joël Raharijaona, Aurélie Thomazic, Céline Dorgans, Coraline Crozet, Emre Yalamac, Mickaël Beaudhuin, Manuel Houmard, Jennifer Ragani, ainsi que la team GPM2. Merci aux moins jeunes chercheurs du groupe PM également, pour leur aide et leur support technique : Patricia Donnadieu, Mireille Maret, Bruno Gilles, Marc De Boissieu, Frédéric Livet, Jean-Paul Simon, Marc Verdier, ainsi que les intermédiairement jeunes chercheurs Fréderic de Geuser et Guillaume Parry. Un grand merci en particulier à Jean-Louis Chemin et Beatrice Doisneau pour leur gentillesse et leur investissement dans mon projet, et surtout à Françoise Bley, pour le temps qu'elle a consacré à ma formation sur les manips SAXS, et son soutien sans faille lors des longues soirées à l'ESRF. Merci également à Jean-Marc Chaix et Michel Pons, directeurs du laboratoire SIMaP, et à Jacqueline Cuoq pour son aide et sa disponibilité, ainsi que son enthousiaste participation à la vie du laboratoire.

Merci également à mes collègues et amis du laboratoire : Nicolas Meyer, Sylvain Charmond, Ian Zuazo, Laurent Lazszyck, Malika Perrier, Valérie Bounhoure et Gregory Largillier. Merci également à John Dunlop, qui fut probablement le premier doctorant que j'y ai rencontré, qui m'a accueilli et montré la voie. J'allais oublier ;) mes deux collègues de bureau préférés : Thorsten Marlaud et Fabiola Liscio, qui ont passé 3 années à me supporter… dans le sens anglais comme dans le sens français ! Que de bons moments passés ensemble !

Merci, finalement, à mes parents, qui m'ont soutenu pendant ces années passées à Grenoble… mais qui m'ont également supporté pendant les 26 années qui ont précédé cette soutenance ! Merci de m'avoir poussé dans cette voie. J'ai également une pensée pour mes grands-parents. Je tiens à terminer ce délicat exercice par Stéphanie, qui était présente au quotidien et m'a soutenu dans les moments parfois difficiles que j'ai pu avoir, au cours de ces 3 années de thèse. Merci !

C. Résumé détaillé

C.1. Introduction

Après ce bref résumé et le plan de ce manuscrit, la dernière partie de ce chapitre a pour objectif de résumer en français et d'une manière plus détaillée ce manuscrit, écrit par la suite dans la langue de Shakespeare.

C.1.a. Contexte

Cette thèse a été réalisée dans le cadre du projet COMPACT, un projet Européen piloté par Airbus. Il vise à étudier l'effet des différentes étapes du cycle de fabrication de pièces aéronautiques en aluminium 7xxx sur les contraintes internes et sur les distorsions géométriques résultantes, dans le but de réduire celles-ci.

Le matériau étudié est l'alliage d'aluminium 7449, un alliage à hautes performances mécaniques, notamment utilisé sous forme de tôles de fortes épaisseurs pour fabriquer certaines nervures d'ailes des avions gros porteurs A380. La résistance mécanique de ce type d'alliage est principalement liée à sa microstructure de précipitation, obtenue par le biais de traitements thermomécaniques complexes. Ceux-ci, et notamment la trempe, induisent cependant des contraintes internes à longue distance, qui évoluent et se redistribuent au cours du cycle de fabrication, et peuvent conduire à des distorsions géométriques sévères sur les pièces finies

Si le projet COMPACT s'intéresse à cette problématique sur l'ensemble du cycle de fabrication, depuis la conception jusqu'aux procédés de post-usinage, en passant par le traitement thermique et l'usinage, la partie du projet qui nous concerne s'intéresse en particulier aux traitements de post-usinage permettant de réduire les distorsions. Trois procédés thermomécaniques sont ainsi étudiés : le grenaillage (*shot peening*), le formage laser (*laser forming*) et le formage revenu (*age-forming*), des procédés respectivement mécaniques, thermiques et thermomécaniques.

L'objectif est d'une part de mieux comprendre l'effet de ces traitements sur les contraintes internes et les distorsions, mais également d'évaluer leur l'influence sur la microstructure et les propriétés mécaniques finales, celles-ci évoluant sous l'effet de ces procédés thermomécaniques.

C.1.b. Objectifs de la thèse

La présente étude s'intéresse tout particulièrement à la compréhension des couplages entre ces traitements thermomécaniques, la microstructure et les propriétés mécaniques de l'alliage AA7449. Il s'agit d'une part de caractériser ces couplages expérimentalement, mais également de les modéliser, afin d'en proposer une approche prédictive.

Cet objectif « scientifique » est décliné, d'un point de vue plus « industriel », et dans le cadre d'un projet COMPACT, sur les trois procédés de réduction des contraintes internes et des distorsions.

Concernant le grenaillage, l'objectif est de proposer un modèle analytique de loi de comportement du matériau, prenant en compte sa microstructure. Ce modèle doit être applicable à des états métallurgiques différents, et être utilisé dans un modèle éléments finis du grenaillage. Cette contrainte impose notamment de prendre en compte l'effet de la vitesse de déformation, mais également de dissocier l'écrouissage cinématique de l'écrouissage isotrope dans le modèle.

L'objectif concernant le formage laser est de développer un modèle analytique décrivant l'évolution de la microstructure au cours du traitement laser, mais également de prédire l'influence de ce traitement sur les caractéristiques mécaniques.

L'étude du dernier procédé, le formage revenu, doit conduire à proposer un modèle décrivant l'évolution de la microstructure de précipitation sous l'effet d'un traitement thermomécanique, c'est-à-dire combinant contrainte et traitement thermique simultanés. Deux cas sont distingués. On cherche d'une part à être représentatif du formage revenu industriel, auquel cas on s'intéresse à l'influence de l'état métallurgique et de la déformation sur microstructure. On cherche d'autre part à être représentatif d'un traitement local de correction des distorsions sur pièce finie, auquel cas le matériau initial est à l'état T7651, et c'est la température et la contrainte qui varient.

C.1.c. Démarche

Pour remplir ces objectifs, la démarche générale est la suivante.

Il s'agit dans un premier temps de qualifier les interactions physiques mises en jeu dans ces procédés (aspects thermiques et mécaniques) et de les quantifier (températures, durées, vitesses, contraintes…). Dans le cadre de cette thèse, les réponses à ces questions proviennent en partie d'une étude de la littérature, mais également de simulations éléments finis réalisées par l'Université de Patras. Ceci concerne en particulier l'étude des profils thermiques générés par le formage laser.

Il s'agit ensuite d'évaluer l'évolution de la microstructure sous l'effet de ces sollicitations. La démarche a généralement consisté à caractériser ces effets sur des pièces traitées, puis à réaliser des essais "modèles" dans un but d'analyse et de compréhension des mécanismes, pour finalement aboutir à des modèles décrivant l'évolution de la microstructure. Pour le formage revenu, ceci a notamment nécessité un important travail de développement instrumental, permettant de suivre in situ l'évolution de la précipitation sous l'effet combiné d'une contrainte et d'un traitement thermique (TSAXS).

Le dernier point consiste à relier la microstructure aux propriétés mécaniques. Ceci a nécessité un travail expérimental important, consistant à générer divers états métallurgiques, à caractériser leur microstructure et leurs propriétés mécaniques, pour finalement proposer des modèles de comportement mécanique intégrant la microstructure (notamment la précipitation) de manière explicite.

C.1.d. Collaborations

Cette étude a été menée en collaboration avec un certain nombre d'universités et de partenaires industriels, notamment au travers du projet COMPACT.

Le pilotage industriel était ainsi réalisé par Airbus Filton (Royaume-Uni) et EADS Corporate Research Centre (Allemagne), qui a également réalisé les essais de formage laser.

Rio Tinto Alcan (France) a fourni le matériau initial, sous forme de tôles en AA7449 à l'état T7651.

L'Université de Patras (Grèce), en charge dans le projet COMPACT de la modélisation par éléments finis des traitements post-usinage, a calculé les profils thermiques induits par le formage laser.

L'Université Catholique de Louvain (UCL, Belgique) a contribué à la modélisation de l'écrouissage.

La modélisation de la précipitation a été réalisée en collaboration avec l'Institut National des Sciences Appliquées de Lyon (INSA de Lyon, France).

C.2. Résumé des chapitres

Le plan de ce manuscrit n'est pas directement issu de la démarche explicitée précédemment (voir C.1.c). Ce découpage conceptuel transparait cependant au fil des chapitres. Il a ainsi été décidé de consacrer un chapitre à chacun des 3 procédés (chapitres III, IV, V), et d'analyser, pour chacun d'entre eux, son influence sur la microstructure et les propriétés mécaniques. La composition et les principaux résultats de ces chapitres sont résumés dans les paragraphes qui suivent.

C.2.a. Chapitre I – Introduction générale

La première partie du chapitre I présente le contexte général de cette étude : les alliages d'aluminium pour applications aéronautiques, les problématiques liées au traitement thermique et le projet COMPACT. Il présente également les objectifs de ce travail et introduit les différents chapitres.

La seconde partie de ce chapitre est consacrée à une revue de la littérature générale consacrée à ces sujets, dans le but de fournir une matière première pour l'analyse des résultats expérimentaux, dans les chapitres qui suivent. Sont notamment abordés : la microstructure -en particulier la précipitation- et les traitements thermiques des alliages d'aluminium 7xxx, ainsi que les mécanismes de plasticité, et, plus généralement, les relations entre microstructure et propriétés mécaniques.

Dans les alliages d'aluminium à durcissement structural, les propriétés mécaniques sont principalement dépendantes de l'état de précipitation. Le comportement macroscopique est ainsi lié aux interactions dislocation-dislocation et précipité-dislocation, et en particulier aux mécanismes de plasticité décrits dans les figures suivantes (contournement et cisaillement des précipités).

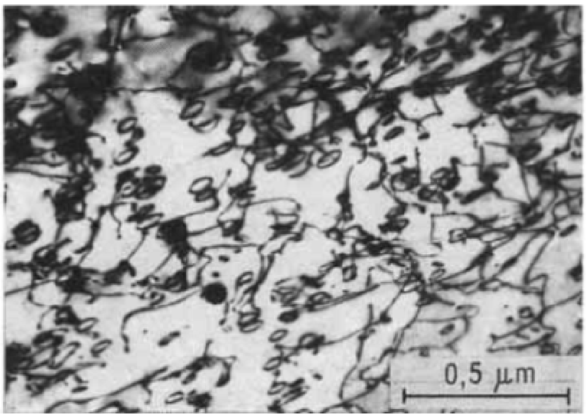

Fig. 0.1. Boucles d'Orowan autour de précipités non cisaillables

Cliché MET - Précipités δ' Al_3Li. Voir Fig. I.29

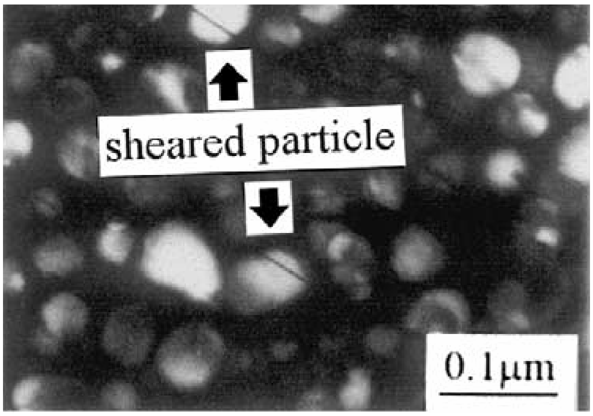

Fig. 0.2. Précipités cisaillés

Cliché MET de précipités δ' Al_3Li Voir Fig. I.30

C.2.b. Chapitre II – Matériau et méthodes expérimentales

Le second chapitre présente plus précisément le matériau étudié, ainsi que les principales techniques expérimentales utilisées dans ce travail. Les techniques de caractérisations microstructurales et mécaniques standards (MO, MEB, MET, traction, dureté,…) sont brièvement présentées.

Une attention particulière est donnée à une technique moins classique, le SAXS, permettant de caractériser la microstructure de précipitation, notamment de la quantifier, en obtenant la taille moyenne ou la distribution de taille des précipités et leur fraction volumique. Cette technique a été utilisée *ex situ* sur des échantillons *post mortem* de traction, ou pour réaliser des cartographies de précipitation sur des échantillons traités au laser, ou *in situ* sur un micro-four permettant de suivre l'évolution de la précipitation au cours d'un traitement thermique. Cette technique a été utilisée en utilisant une anode tournante de laboratoire comme source de Rayons X, mais également à l'ESRF (European Synchrotron Research Facility).

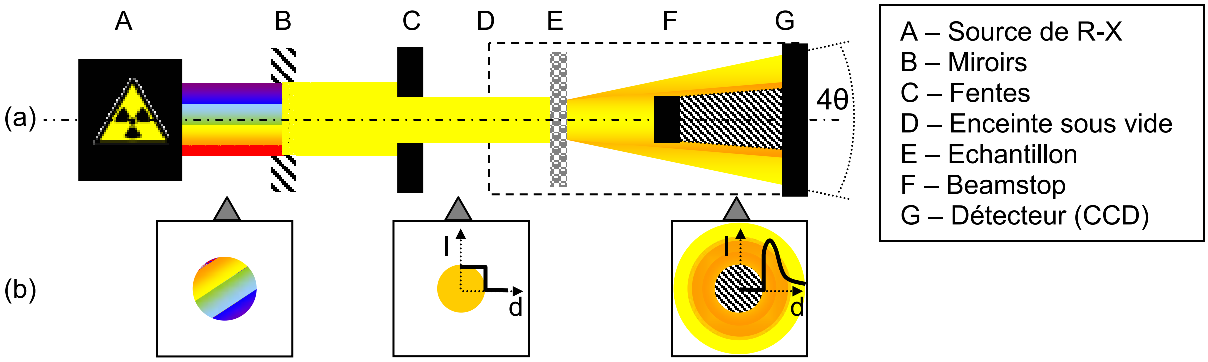

Fig. 0.3. Montage SAXS

(Voir Figure II.19)

Le fonctionnement de la micro machine de traction chauffante TSAXS est également explicité dans ce chapitre. Celle-ci, montée dans une enceinte de SAXS, permet de réaliser des traitements thermomécaniques sur des micro-éprouvettes de traction tout en mesurant *in situ* l'évolution de la précipitation. Cette machine et la technique de préparation des échantillons ont été développées intégralement dans le cadre de cette thèse. Un asservissement permet de réaliser des essais de fluage, relaxation, traction, dans une gamme de température allant de l'ambiante à 400°C. Elle permet notamment de reproduire des traitements de formage-revenu ou de correction des distorsions.

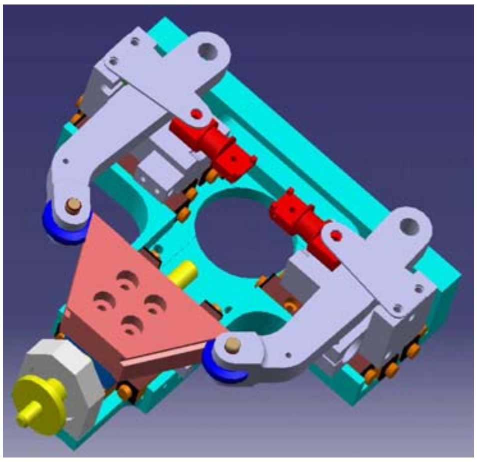

Fig. 0.4. Modèle Catia de la machine TSAXS

Voir Fig. II.24

Fig. 0.5. TSAXS dans l'enceinte sous vide et module de contrôle TSAXS

Voir Fig. II.25

C.2.c. Chapitre III – Modèle d'écrouissage

Dans le chapitre **III**, qui s'inscrit dans le cadre de l'étude du grenaillage, nous nous intéressons à l'effet de la précipitation sur l'écrouissage, pour finalement aboutir à un modèle d'écrouissage devant être intégré par l'Université de Patras à un code élément fini simulant le grenaillage. Ce modèle doit donc être représentatif de ce procédé et être applicable à une grande variété d'états métallurgiques.

Pour cela, des traitements thermiques appropriés ont permis de générer un grand nombre d'états métallurgiques : des états trempé, maturés à l'ambiante, légèrement sous-revenus jusqu'à des états très largement sur-revenus, d'une durée de traitement thermique supérieure à 2000h.

Ces microstructures ont ensuite été caractérisées par MET et SAXS, *ex situ ou in situ*, puis testées au travers d'essais de dureté, traction et Bauschinger. Ces derniers, qui consistent à effectuer un cycle de traction suivi d'une compression, permettent notamment de différencier la part d'écrouissage cinématique de l'écrouissage isotrope, et d'intégrer ainsi ces deux comportements au modèle.

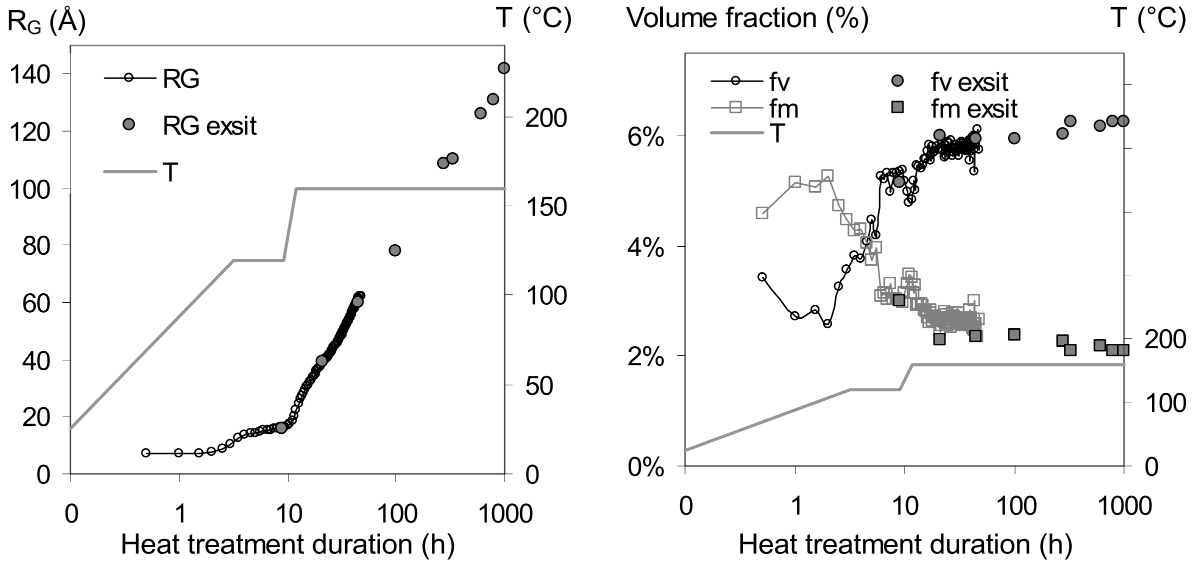

Fig. 0.6. Cinétique de précipitation au cours du revenu

(a) Evolution du rayon de Guinier des précipités (RG). (b Evolution de la fraction volumique précipitée (fv) et de la fraction de soluté dans la matrice (fm). Température (trait gris continu). Les mesures ex situ (“exsit”), généralement obtenues pour des traitements longs, sont comparées aux mesures in situ. Voir Fig. III.14.

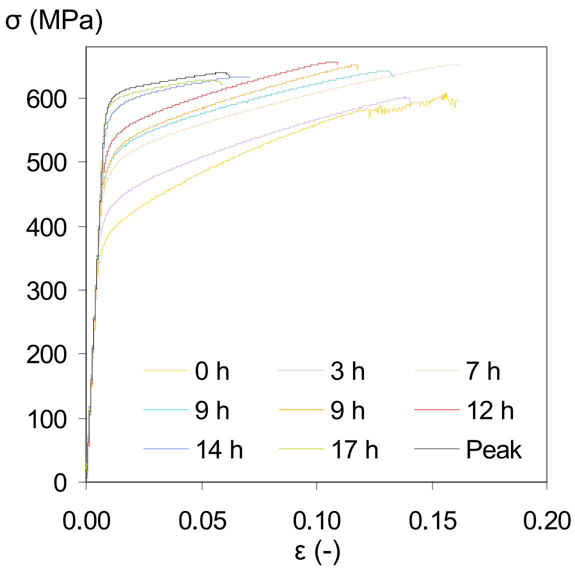

Fig. 0.7. Influence de la durée de revenu sur la courbe de traction (états sous-revenus)

Voir Fig. III.23

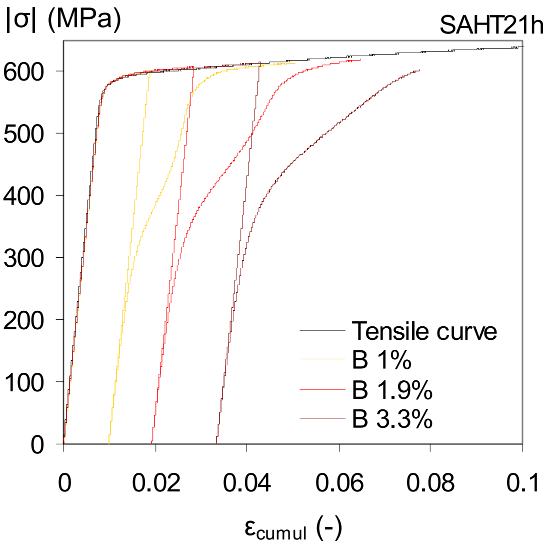

Fig. 0.8. Courbe de traction et courbes Bauschinger à différents niveaux de pré-déformation sur état pic de durcissement

Voir Fig. III.28

Dans le but de proposer un modèle adapté au grenaillage, l'effet de la vitesse de déformation est également étudié, par le biais d'essais spécifiques : des essais de traction à haute vitesse, des essais de traction avec sauts de vitesse et des essais de traction à basse température (-96°C), permettant de simuler une haute vitesse de déformation.

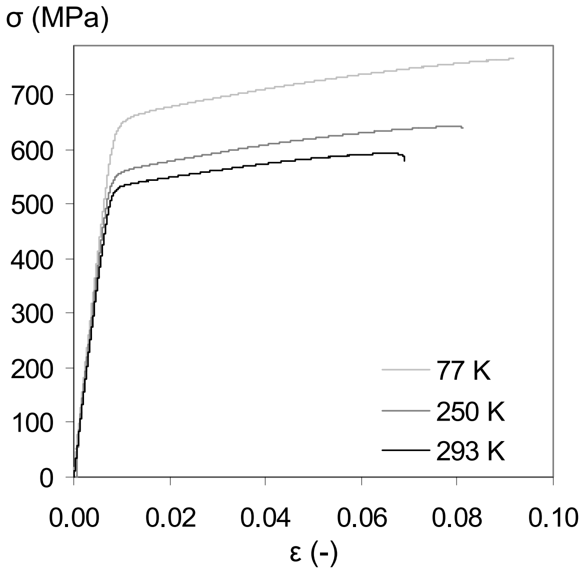

Fig. 0.9. Courbes de traction à différentes températures - Etat T7651

Voir Fig. III.34

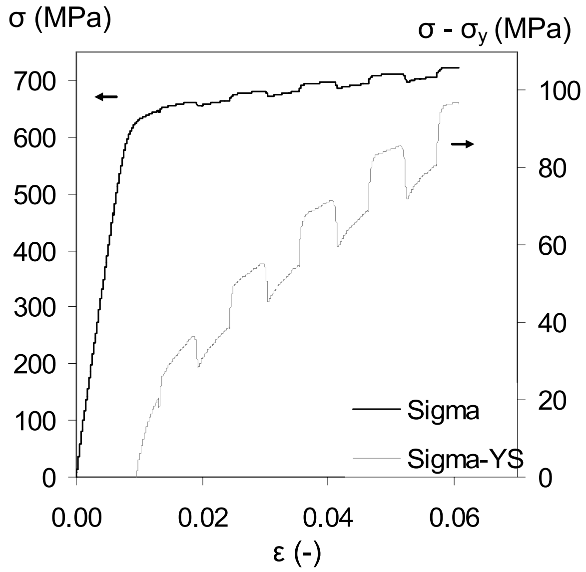

Fig. 0.10. Courbe de traction à 77K avec sauts de vitesse de 10^{-2} à $10^{-4}.s^{-1}$ - Etat T7651

Voir Fig. III.38

Un premier modèle à base physique de limite élastique est proposé, suivant sur une approche classique de transition cisaillement/contournement d'Orowan des précipités ; ce modèle, dont les paramètres sont généralement mesurés expérimentalement, ou parfois issus de la littérature, décrit parfaitement l'évolution de la limite élastique au cours du revenu (voir figure ci-dessous). Le modèle proposé est le suivant :

$$\sigma_y = \sigma_0 + \sigma_{ss} + \sigma_P = \sigma_0 + K_{ss} \times C_{ss}^{2/3} + \begin{cases} K_{ua} \times M\mu\sqrt{f_v R/b} \\ \sigma_{0oa} + K_{oa} \times M\mu b\sqrt{f_v}/R \end{cases} \qquad (0.1.)$$

σ_0, σ_{ss} et σ_P sont les contributions respectives des joints de grains et du réseau, du soluté et des précipités à la limite élastique.

Le premier cas correspond au comportement sous-revenu, où le cisaillement des précipités est privilégié. Le second cas est caractéristique du comportement sur-revenu, où le mécanisme de franchissement des précipités est le contournement d'Orowan.

C_{ss}, R et f_v sont les valeurs mesurées expérimentalement par SAXS et correspondent respectivement aux fractions de soluté, taille des précipités et fractions volumiques. K_{ss} a été calculé à partir d'essais de traction sur état brut de trempe.

σ_0, M, μ, b sont issus de la littérature.

Seuls σ_{0oa} K_{oa} et K_{ua} ont été ajustés, dans des gammes correspondant aux valeurs de la littérature.

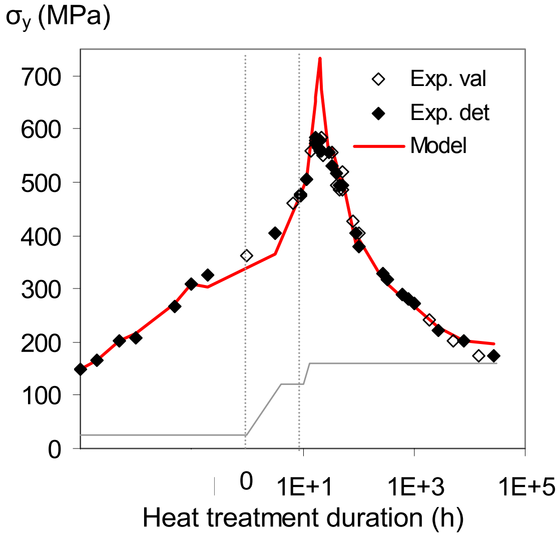

Fig. 0.11. Limite élastique – Modèle comparé aux résultats expérimentaux

Voir Fig. III.47

Le modèle d'écrouissage proposé, dérivé du modèle de Kocks, Mecking et Estrin [Kocks 1976, Mecking 1981, Estrin 1984], prend explicitement en compte la microstructure, et notamment la précipitation. Il est basé sur un comportement plastique décrit comme une compétition entre stockage des dislocations d'une part, et restauration dynamique d'autre part, l'enjeu étant de décrire les mécanismes en eux-mêmes et leurs cinétiques respectives (voir III.B.2).

Le modèle proposé incorpore également les modifications proposées par Simar [Simar 2006]. Ce modèle intègre le fait que les distances d'annihilation entre dislocations dépendent de la précipitation d'une part, mais également que plus la taille des précipités est importante, plus ceux-ci sont capables de stocker de boucles d'Orowan. La combinaison du stockage classique des dislocations mobiles sur les dislocations de forêt et du stockage sur les précipités correspond au terme d'écrouissage isotrope.

Le terme d'écrouissage cinématique est quant à lui dérivé du modèle de Proudhon [Proudhon 2008], qui suppose une saturation du nombre de boucles autour des précipités, pour une taille de précipités donnée. Nous avons généralisé ce modèle en rendant compte de la capacité de stockage plus importante des précipités les plus gros, en utilisant la même approche que pour le modèle de Simar. Le nombre de paramètres du modèle cinématique est ainsi minime, puisque ceux-ci sont en grande partie identiques à ceux du terme d'écrouissage isotrope.

Les modèles de Kocks, Mecking, Estrin, de Simar et de Proudhon sont ainsi généralisés dans un modèle où les termes de durcissement de joints de grains et de solution solide et l'écrouissage cinématique se combinent linéairement, rendant ainsi compte de la réversibilité de l'écrouissage cinématique, auxquels s'ajoutent une loi d'addition quadratique des termes de durcissement lié aux précipités et l'écrouissage isotrope. Cette combinaison permet de reproduire de manière tout à fait satisfaisante l'écrouissage observé expérimentalement sur les courbes d'écrouissage des états sur-revenus, avec un nombre mimine de paramètres ajustables.

$$\sigma = \sigma_0 + \sigma_{ss} + \sigma_{kin} + \left(\sigma_P{}^2 + \sigma_{iso}{}^2\right)^{\frac{1}{2}} \qquad (0.2.)$$

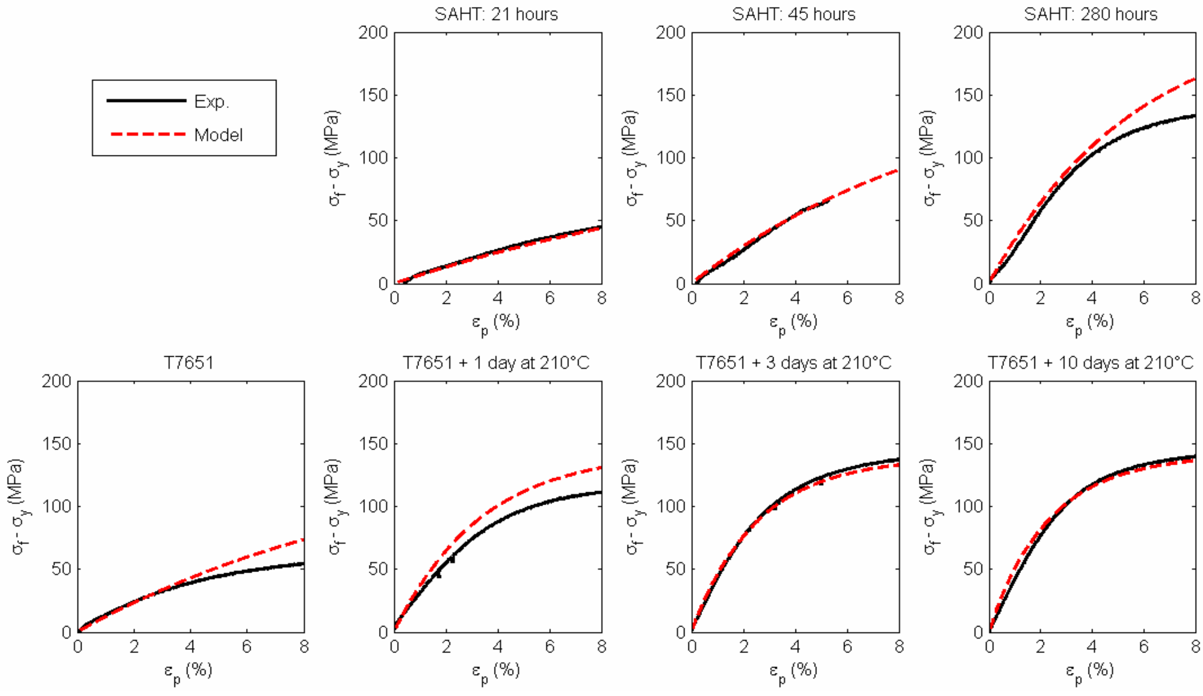

Fig. 0.12. Comportement plastique de différents états sur-revenus – comparaison modèle/résultats expérimentaux

Voir Fig. III.52

C.2.d. Chapitre IV – Evolution de la précipitation au cours du formage laser

Ce quatrième chapitre est consacré à l'étude de l'influence du formage laser sur des échantillons à l'état initial T7651. Ce traitement peut être considéré comme un traitement anisotherme local, au même titre que certains procédés de soudage.

Si ce traitement a pour effet de relaxer les contraintes, il conduit également à modifier localement la précipitation, comme le montrent les cartographies de dureté et de précipitation obtenues sur les échantillons traités. Avec les paramètres du procédé choisis, la zone affectée thermiquement est typiquement de 1mm de profondeur et de 5 mm de large, soit la largeur du faisceau laser.

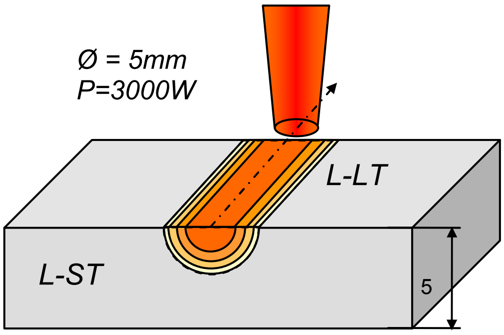

Fig. 0.13. Schéma de principe du traitement de formage laser

Voir Fig. IV.8

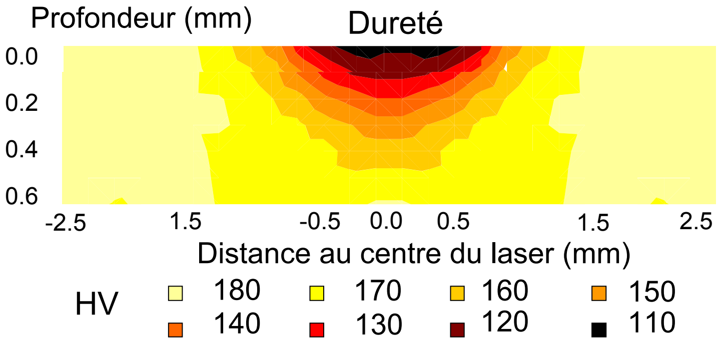

Fig. 0.14. Cartographie de dureté après traitement laser

Voir Fig. IV.12

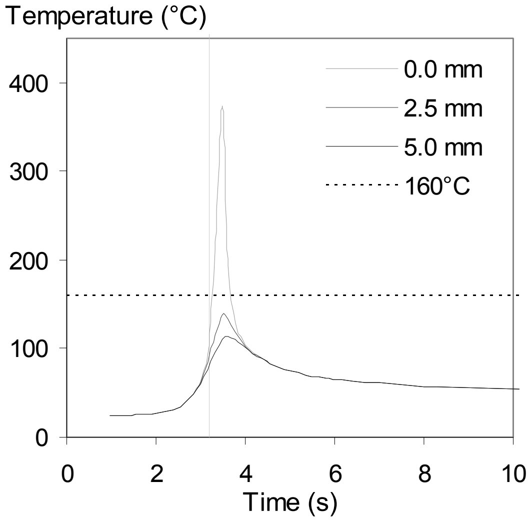

Fig. 0.15. Profil thermique induit par le formage laser, calculé à différentes profondeurs

Voir Fig. IV.21

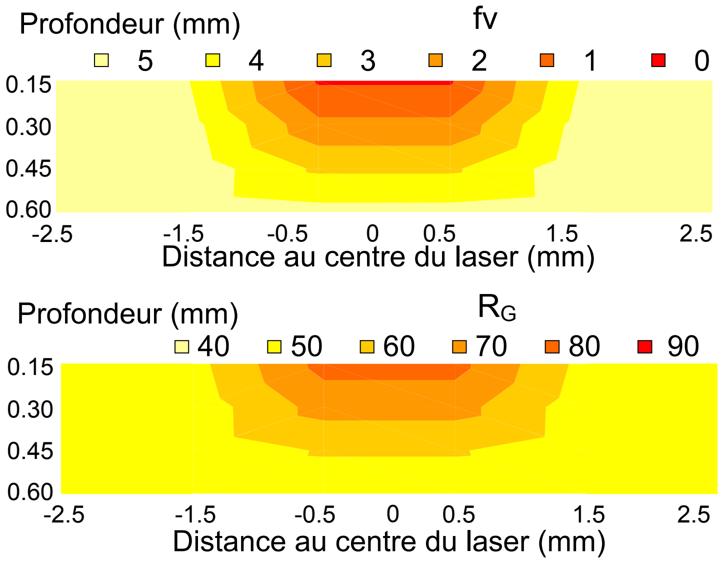

Fig. 0.16. Cartographie de précipitation après traitement laser mesurée par SAXS

Fraction volumique et rayon de Guinier des précipités. Voir Fig. IV.16

Ces effets constatés expérimentalement, l'objectif a été de modéliser ces résultats. La première étape a consisté à calculer les profils thermiques générés par ce traitement. Ces calculs ont été réalisés par l'Université de Patras, suivant une méthodologie explicitée dans la référence suivante : [Labeas 2008].

Ce profil a permis de borner la gamme de température subie par les échantillons : typiquement un profil anisotherme constitué d'un pic de température de 200°C à 400°C de moins d'une seconde sur la zone située au centre du faisceau laser, suivi d'un refroidissement logarithmique, et d'un nouveau pic se produisant à chaque nouvelle passe, d'une température moyenne de plus en plus élevée (voir figure 0.15).

Le modèle utilisé est dérivé du modèle de précipitation par classe proposé par Perez et Acevedo [Perez 2007, Acevedo 2007]. Ce modèle prend en compte la germination, la croissance et la coalescence des précipités, et suit ainsi l'évolution de la distribution de taille et de la densité des précipités (et, par calcul, de la fraction volumique), sous l'effet de traitements thermiques. Le système est simplifié. Les seuls éléments considérés sont ainsi l'aluminium, le zinc et le magnésium (où la teneur en zinc effective est égale à la somme des teneurs nominales en zinc et en cuivre). Une autre simplification a consisté à ne considérer qu'une seule famille de précipités, de composition stœchiométrique $MgZn_2$.

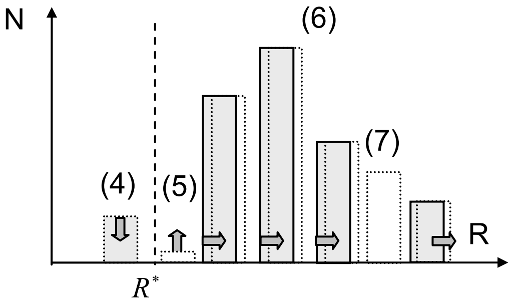

Fig. 0.17. Principe du modèle de précipitation par classe (type Lagrangien)

(4) Disparition d'une classe de taille inférieure au rayon critique. (5) Création d'une nouvelle classe. (6) Evolution de rayon des classes. (7) Insertion d'une nouvelle classe pour minimiser la distance interclasse. Voir Fig. IV.5.

L'étape suivante a consisté à réaliser des mesures SAXS *in situ* de cinétique de précipitation sous l'effet de traitements isothermes et anisothermes (réversions), afin de calibrer ce modèle. Un exemple du résultat de cette calibration est montré dans la figure qui suit.

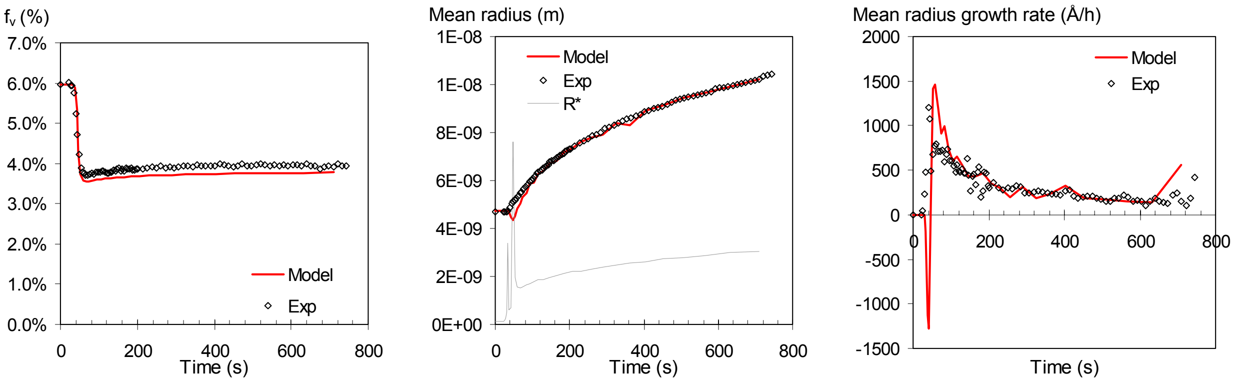

Fig. 0.18. Cinétique de précipitation sous l'effet d'un traitement isotherme à 240°C

Comparaison entre résultats mesurés par SAXS et modèle : fraction volumique, rayon moyen, vitesse de croissance des précipités. Voir Fig. IV.29.

Le profil thermique calculé (voir Fig. 0.15) est ensuite réinjecté dans le modèle de précipitation, afin de modéliser la fraction volumique et la taille moyenne des précipités à l'issue du traitement laser. Les calculs sont en bon accord avec les résultats expérimentaux, notamment en ce qui concerne la fraction volumique. La corrélation est moins bonne en ce qui concerne la taille moyenne des précipités. L'hypothèse est que les précipités les plus fins n'ont pas pu être captés du fait de conditions expérimentales adaptées aux précipités les plus grossiers d'une part, et d'autre part que les conditions de nucléation n'ont pas été optimisées dans le modèle.

La dernière étape a consisté à réinjecter les résultats de ces calculs dans le modèle de limite élastique présenté dans le chapitre III, permettant ainsi de relier ces résultats à la dureté, à travers un modèle empirique reliant la dureté à la limite élastique.

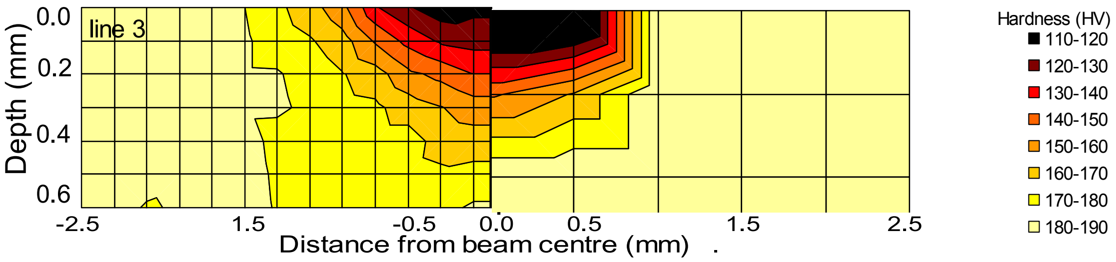

Fig. 0.19. Superposition des cartographies de dureté mesurées et modélisées

A gauche: dureté mesurée. A droite: dureté calculée. Voir Fig. IV.38

Une chaîne de modélisation complète a donc été proposée, comprenant 3 calculs en série : un calcul par élément fini du profil thermique induit par le laser, suivi d'une modélisation de évolution de la précipitation sous ce profil, puis finalement une modélisation reliant la précipitation aux propriétés mécaniques. Cette approche permet de relier les paramètres du formage laser aux caractéristiques mécaniques finales du matériau, avec un très bon accord avec les résultats expérimentaux.

C.2.e. Chapitre V - Evolution de la microstructure au cours de traitements thermomécaniques

Ce cinquième chapitre est consacré à l'étude de l'influence de traitements thermomécaniques sur la précipitation, au moyen de la machine TSAXS d'une part, mais également par la modélisation. Ces traitements thermomécaniques, représentatifs de traitements industriels, sont de deux types.

i. Correction des distorsions géométriques sur pièce à l'état T7651

Le premier est un traitement local de correction des distorsions sur pièce finie ou semi-finie, utilisant des éléments chauffants et en appliquant une contrainte de flexion sur la pièce. Ce procédé est simulé sur la machine TSAXS en effectuant des traitements à contrainte imposées, à différentes températures, sur un état initial T7651. L'objectif, en faisant varier la température et la contrainte imposée, est ainsi de cartographier les domaines critiques temps/température/contrainte de ce procédé, permettant de corriger les distorsions géométriques en limitant la dégradation de la microstructure, et, par conséquent, des propriétés mécaniques.

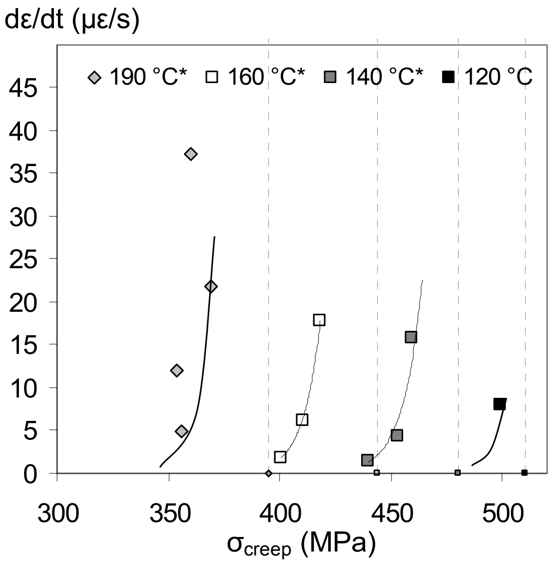

Fig. 0.20. Vitesse de fluage en fonction de la température et de la contrainte

Mesuré sur la machine TSAXS, sur état initial T7651. Voir Fig. V.19.

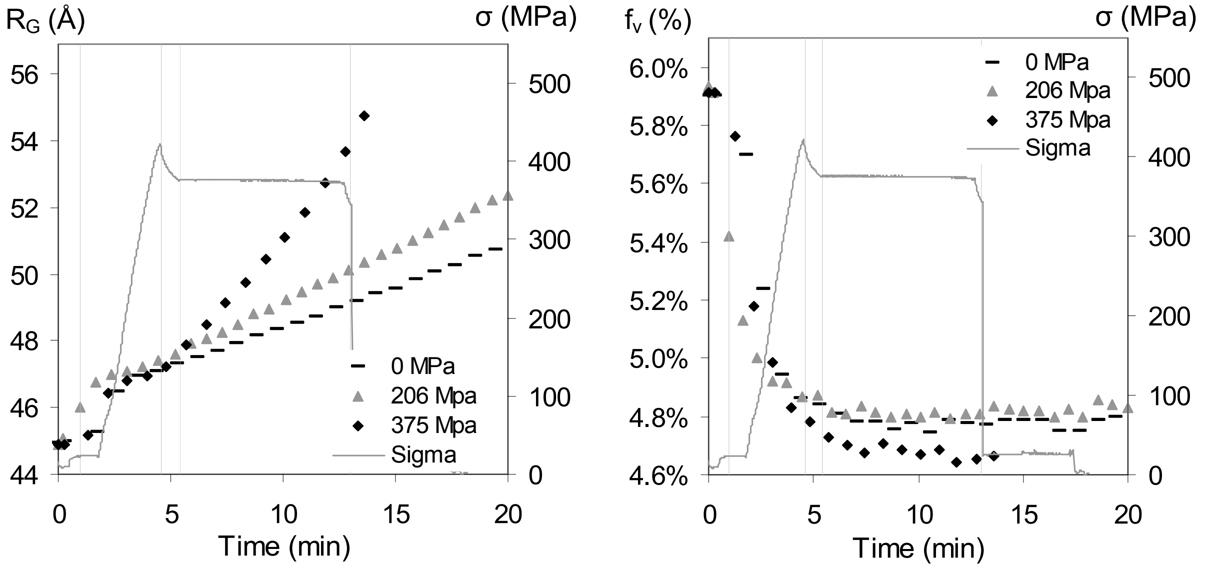

Fig. 0.21. Effet de la contrainte de fluage sur la cinétique de précipitation à 190°C

(a) Rayon de Guinier. (b) Fraction volumique précipitée. En gris : cycle de contrainte appliqué. Voir Fig. V.21.

On peut voir sur cette dernière figure que la précipitation est influencée par le niveau de contrainte, avec une dissolution d'une partie des précipités et une augmentation du rayon moyen des précipités. Il faut atteindre une contrainte importante (90% de la limite élastique) pour activer le fluage (voir Fig. 0.20) ; au-delà de cette contrainte seuil, plus la contrainte est élevée, plus la précipitation est affectée.

Ceci permet d'identifier un paramètre de sensibilité de la précipitation à la contrainte, pour chaque température. Cet outil peut être utilisé pour optimiser les traitements de correction des distorsions géométriques, les principales contraintes de ces traitements étant effectivement d'atteindre le niveau de déformation souhaité, tout en contrôlant la précipitation (et donc les caractéristiques mécaniques).

ii. Formage-revenu sur différents états métallurgiques

Le second consiste à réaliser une opération de formage revenu sur un état métallurgique sous-revenu, ce qui permet ainsi de réduire le niveau de contraintes internes dans les pièces [Starink 2006]. Ce traitement est simulé sur la machine TSAXS par un cycle thermomécanique à vitesse de déformation imposée, à la température de revenu habituelle du matériau, et ce sur différents état métallurgiques initiaux. L'objectif est de caractériser la cinétique de précipitation dans ces différentes conditions.

La figure qui suit montre l'évolution de la précipitation d'un état légèrement sous-revenu au cours d'un essai de traction à 160°C comparée à une référence, testée dans les mêmes conditions mais sans déformation. Deux résultats principaux ressortent de cette expérience. Le premier est que la vitesse de croissance des précipités augmente dès lors que la déformation plastique commence, jusqu'à un pic, correspondant à la fin de la déformation plastique. Le second résultat est que la vitesse de croissance des précipités décroit progressivement lors du traitement de relaxation qui suit, jusqu'à saturer à une valeur qui reste supérieure à la vitesse de croissance de référence, sans déformation.

Sur la base de cette analyse, on peut identifier deux mécanismes : une précipitation liée à des phénomènes dynamiques d'une part (croissance des précipités qui s'accélère avec la déformation), et statiques d'autre part (taux de croissance des précipités élevé, alors que la déformation est stoppée).

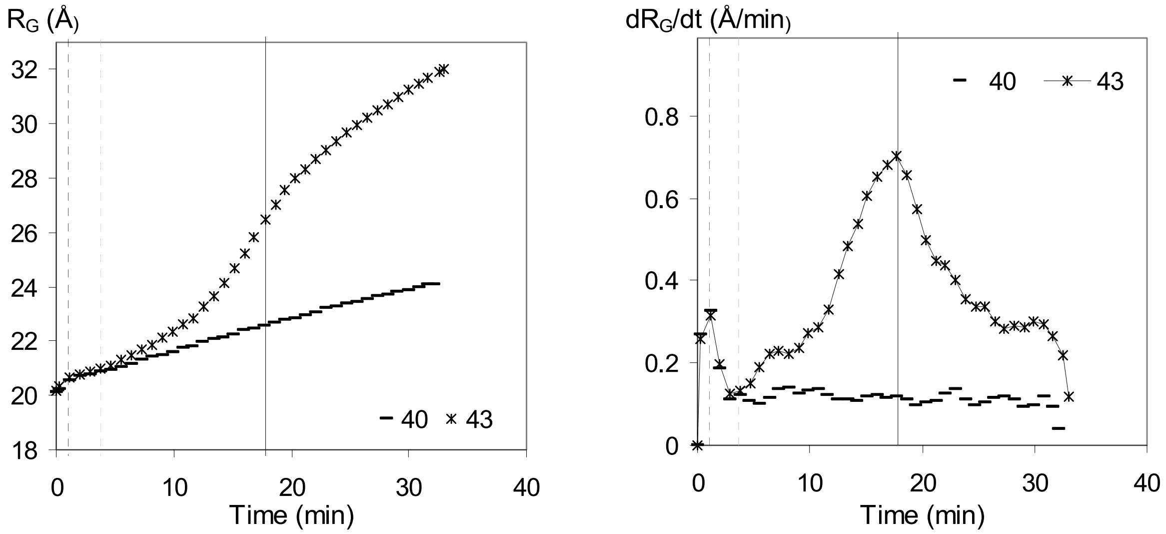

Fig. 0.22. Evolution de la précipitation au cours d'un essai de traction à 160°C

(a) Rayon de Guinier. (b) Vitesse de croissance des précipités. L'échantillon #40 n'a subi que le traitement thermique. L'échantillon #43 a subi le traitement thermique suivant : montée en température (jusqu'au trait vertical pointillé noir), chargement élastique (jusqu'au trait pointillé gris) puis plastique (fin au trait vertical plein), puis relaxation. Voir Fig. V.31.

Cette expérience a été répétée sur différents état métallurgiques (#2, #3, #4, #5), ce qui permet ainsi de mesurer, pour chacune des conditions, l'influence du niveau de déformation sur la vitesse de croissance des précipités, au pic et à saturation.

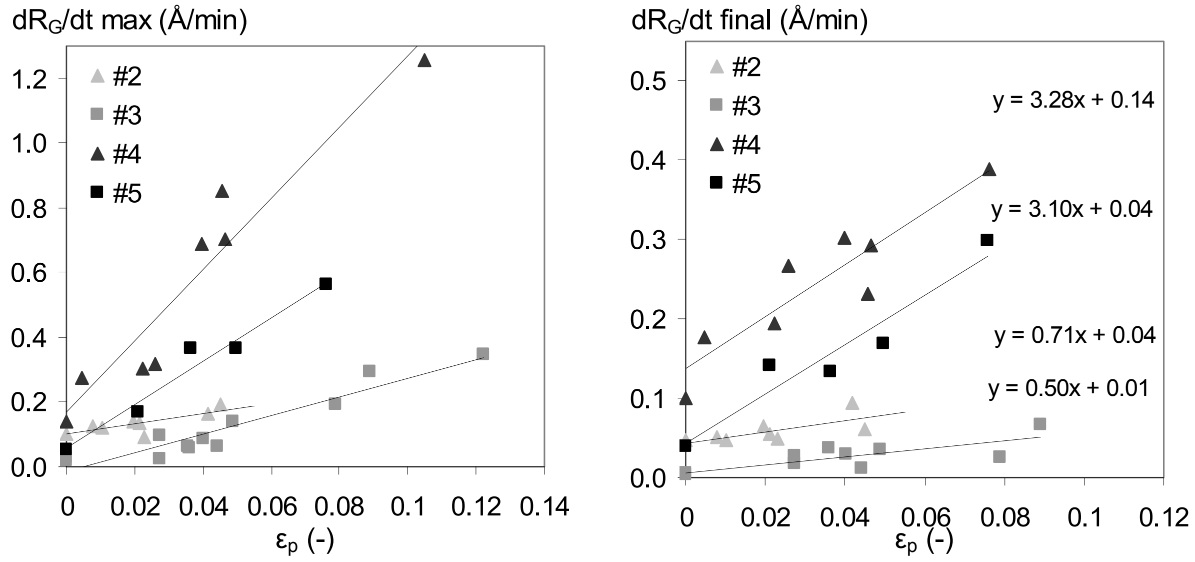

Fig. 0.23. Influence de la déformation sur la vitesse de croissance des précipités, pour différents états métallurgiques

Vitesse de croissance des précipités au pic (a) et finale (b) en fonction de la déformation plastique. Les groupes #2 and #3 ont été déformés à 120°C; #4 et #5 à 160°C. Voir Fig. V.42.

Ces constatations faites, il s'agit maintenant de modéliser l'influence de la déformation sur la précipitation. Le modèle de précipitation utilisé est dérivé du modèle de précipitation présenté au chapitre IV. L'approche proposée consiste à ajouter deux termes au coefficient de diffusion des éléments, défini initialement comme une loi d'Arrhenius. Le premier terme, qui dépend de la déformation totale appliquée, rend ainsi compte de l'effet statique mis en évidence expérimentalement. Le second, qui permet d'intégrer l'effet dynamique, est proportionnel à la vitesse de déformation. Ces

2 coefficients ont été calibrés sur une expérience « modèle », avant d'être validés sur des expériences effectuées dans d'autres conditions de déformation.

$$(0.3.)\quad D^* = D(T,\varepsilon,\dot{\varepsilon}) = D_0\, exp\left(\frac{-Q}{RT}\right)(1 + D_1\varepsilon + D_2\dot{\varepsilon})$$

Le résultat d'une de ces modélisations est présenté dans la figure qui suit. On peut voir que ce modèle physique très simple a permis de rendre compte de manière tout à fait satisfaisante des cinétiques de précipitation observées expérimentalement, avec un nombre de paramètres ajustables minimum.

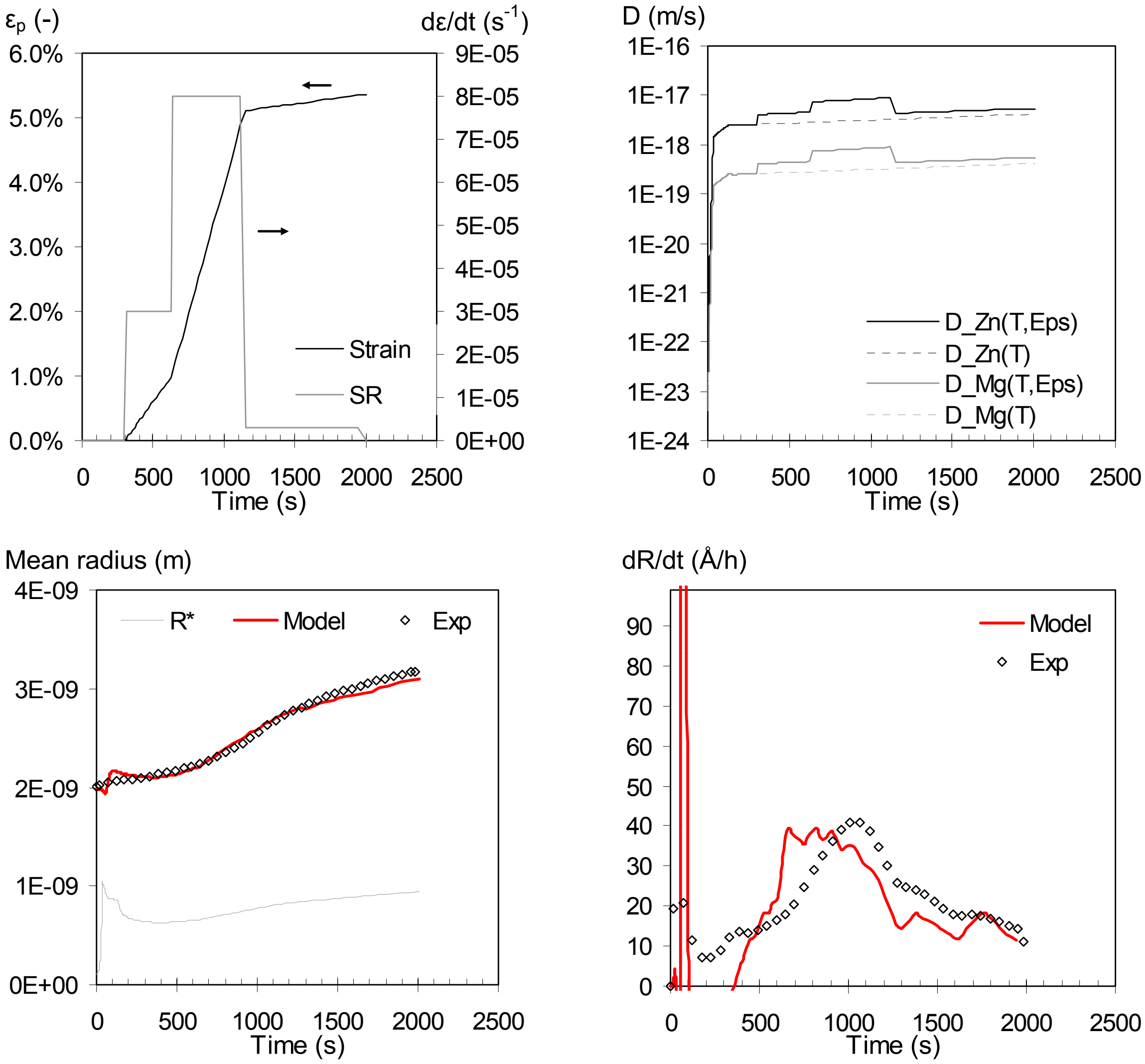

Fig. 0.24. Modélisation de la cinétique de précipitation de l'échantillon #43

(a) Traitement thermomécanique. (b) Effet du traitement thermomécaniques sur les coefficients de diffusion effectifs. (c) Evolution du rayon de Guinier des précipités (d) Vitesse de croissance des précipités. Voir Fig. V.46.

C.3. Conclusion

C.3.a. Modèle d'écrouissage pour le grenaillage

L'influence de la microstructure de précipitation sur l'écrouissage a été mise en évidence expérimentalement. En partant de ces observations, un modèle à base physique a été proposé, permettant de décrire le comportement plastique de matériaux à durcissement structural. Ce modèle unifie le modèle de Simar [Simar 2006] pour l'écrouissage isotrope, et le modèle de Proudhon [Proudhon 2008] pour l'écrouissage cinématique. Il modifie l'approche initiale de Kocks, Mecking et Estrin et prend en compte deux variables internes: les dislocations de forêt et les boucles d'Orowan. Ce modèle décrit ainsi les courbes de traction expérimentales de manière tout à fait satisfaisante, pour une large gamme d'états métallurgiques. Cette étude propose également une nouvelle analyse des essais Bauschinger, et une nouvelle approche des essais de sauts de vitesse.

Le modèle proposé peut être implémenté dans un code éléments finis dans le but de modéliser de traitements mécaniques complexes, faisant intervenir la vitesse de déformation ou des changements de chemin de déformation, comme c'est le cas pour le grenaillage.

C.3.b. Effet du formage laser sur la précipitation et les propriétés mécaniques

Les relations entre le traitement laser, leur effet sur la microstructure et les propriétés mécaniques du matériau ont été établies, à travers des caractérisations expérimentales (cartographies de précipitation par SAXS et dureté) et par modélisation.

L'effet du traitement laser est ainsi de dissoudre partiellement les précipités durcissant en zone sub-surfacique, ce qui génère localement un abattement important des caractéristiques mécaniques statiques. Il s'avère toutefois qu'un traitement de maturation à température ambiante, facilement réalisable en conditions industrielles, permet d'en restaurer la majeure partie.

Le modèle de précipitation par classe proposé permet de simuler l'effet de traitements thermiques complexes, qu'il s'agisse de traitement isothermes ou anisothermes. Le développement de ce modèle a nécessité de nombreuses étapes, intégrant ainsi 3 modélisations en série, elles-mêmes calibrées par des expérimentations complexes. Cette démarche complexe et exigeante a permis de modéliser les résultats expérimentaux avec un très bon accord, permettant ainsi de remplir les objectifs initiaux.

C.3.c. Effets de traitement thermomécaniques sur la précipitation

La micro machine de traction chauffante pour mesures SAXS in situ (TSAXS) développée au cours de cette thèse est un outil particulièrement puissant pour simuler des traitements thermomécaniques variés et complexes, tout en mesurant quantitativement leur effet sur la précipitation.

Déformer (ou imposer une contrainte) le matériau au cours d'un traitement thermique, comme c'est le cas dans les traitements de formage revenu, conduit à modifier la cinétique de précipitation. S'il reste difficile de quantifier leur part respective, il est cependant possible de mettre en évidence des effets statiques et des effets dynamiques, liés respectivement à la présence et à la mobilité des dislocations. Un modèle de précipitation sous l'effet de traitement thermomécanique a été proposé, basé sur le modèle de classe utilisé précédemment, et incluant un coefficient de diffusion dépendant de la déformation cumulée et de la vitesse de déformation/ instantanée. Ce modèle, très simple, décrit très bien la cinétique mesurée expérimentalement.

C.3.d. Bilan

Cette étude était basée sur 3 ingrédients principaux. Du développement instrumental d'une part, notamment la machine TSAXS et une machine de traction inverse pour essais de traction à très basse température. De la caractérisation expérimentale d'autre part, à travers des essais mécaniques et des caractérisations microstructurales (notamment le SAXS, sous rayonnement synchrotron), dans le but d'alimenter les modèles. Enfin, pour chacune des grandes parties de cette étude, des modèles à base physique ont été proposés, utilisant un minimum de paramètres ajustables, et d'une simplicité adaptée aux différents besoins. Cette dernière partie permet ainsi d'avoir une approche prédictive de ces problèmes d'une part, mais également d'apporter une dimension plus universelle à ces analyses.

A travers cette étude, répondant à des besoins industriels, nous nous sommes intéressés plus généralement à l'étude des couplages entre la précipitation et la plasticité. Le chapitre sur le grenaillage s'intéresse en particulier au couplage microstructure/mécanique. Le chapitre sur le formage laser s'est axé sur une étude des interactions thermique/microstructure. Le chapitre sur le formage laser sur les couplages microstructure/mécanique/thermique.

Ces distinctions, qui permettent de simplifier considérablement l'approche, sont cependant surtout conceptuelles, puisque chacun de ces traitements est en réalité un traitement thermomécanique au sens propre du terme, combinant effectivement un aspect thermique et un aspect mécanique. Une nouvelle approche consisterait à reconsidérer ces différents cas en prenant en compte la combinaison de ces deux effets : la thermique et la mécanique.

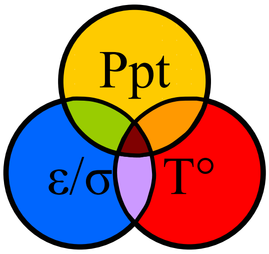

Chapter I. General introduction

Summary

This chapter first presents the general context of the study: aluminium alloys for the aerospace industry, the issues related to their processing and the objectives of the COMPACT project, in which this work is embedded. It then presents the specific objectives of this work and introduces the different chapters.

The second part of this chapter is dedicated to a review of the main ingredients required for the further work: microstructure and precipitation in 7xxx alloys are investigated, as well as the plasticity mechanisms and relationships between microstructure and mechanical properties.

Outline

I.A. COMPACT project and thesis objectives

I.A.1. Aluminium alloys for aerospace applications

I.A.1.a. Aerospace and materials

The main material constraints in the aerospace industry are weight (which will directly affect the fuel consumption and the environmental impact), safety and maintenance costs (through lifetime safety, since a commercial aircraft is used between 30 and 40 years). General requirements for aircraft structural materials are therefore high specific properties and a good material stability: low corrosion susceptibility, mechanical properties stability, high damage tolerance and extended fatigue performance.

Despite the growing competition with polymer matrix carbon fibre reinforced composite materials (mainly present in the next generation of long range aircrafts: B787 and A350), aluminium is still the predominant material used in commercial aircrafts. For instance aluminium alloys represent 66% of the structural materials used in A380, the rest being mostly composite materials (16%) and titanium alloys and steels (10%) [Williams 2003].

I.A.1.b. Aluminium for aerospace applications

The high specific properties of some aluminium alloys, called “high strength” aluminium alloys make them perfectly suitable to be used in aircrafts. Fig. I-1 shows the location of aluminium alloys in a commercial aircraft, showing that aluminium is mainly present in the fuselage (frames, panels, spars) and the wings (spars, skins, stringers). Those parts are defined in Fig. I-2.

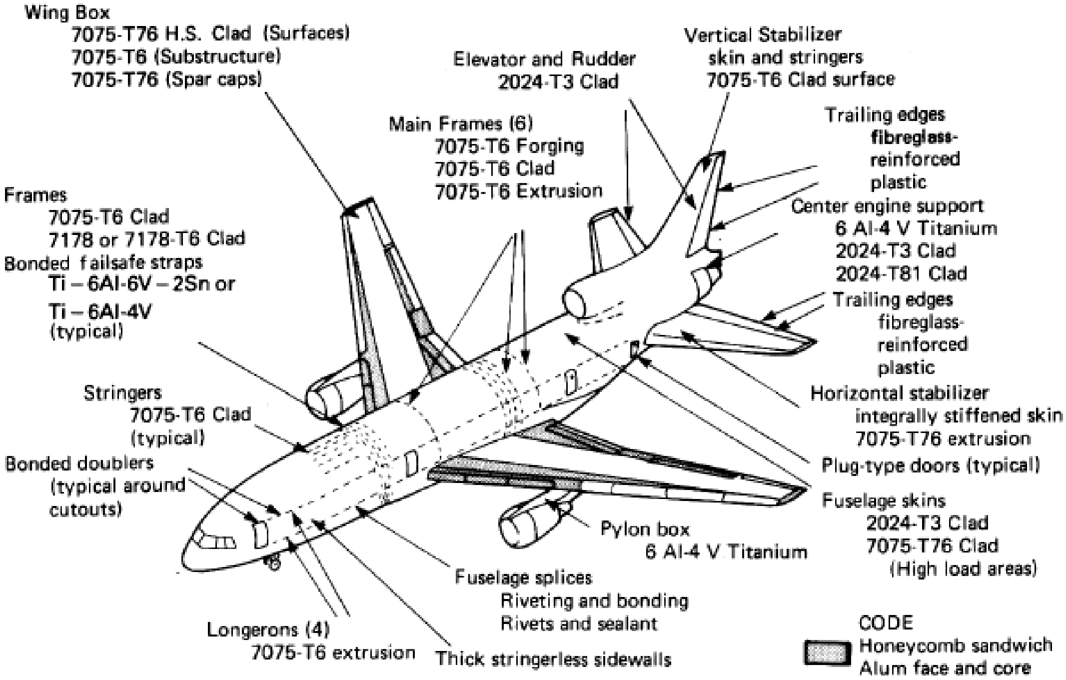

Fig. I-1. Aluminium alloys in a commercial airplane

[Charles 1984]

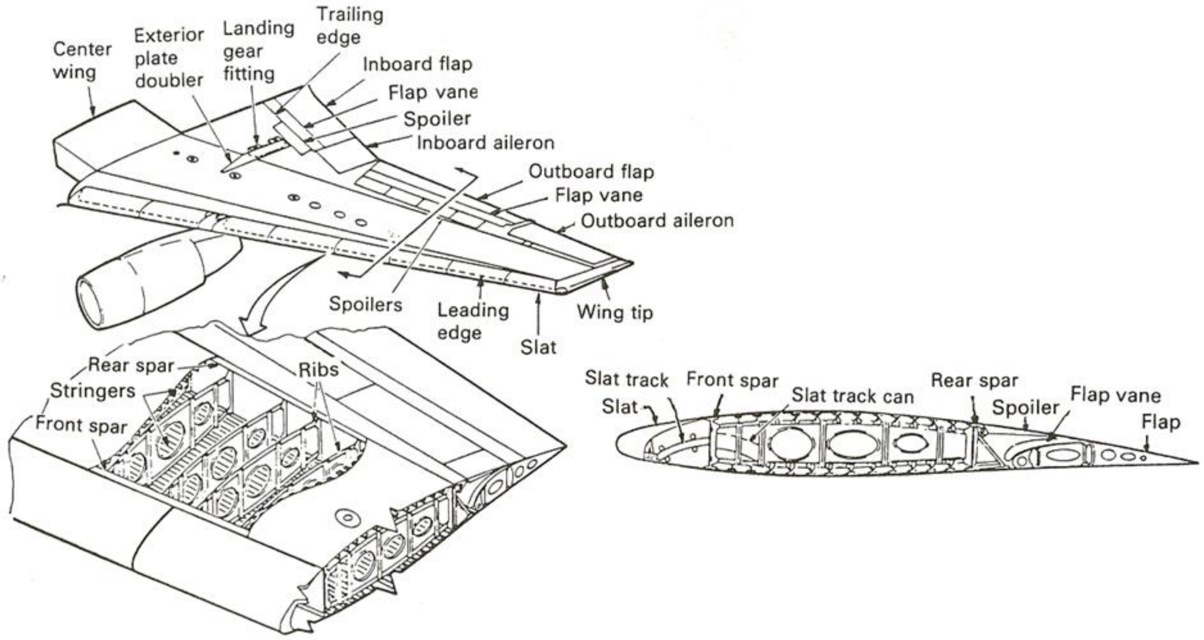

Fig. I-2. Commercial aircraft wing structure

Each component is subjected to different solicitations (mechanical, physical) and requires specific material properties (specifications). The main aluminium alloys that are used in commercial aircrafts are age-hardened 2xxx (Al-Cu) and 7xxx (Al-Zn-Mg-(Cu)) series alloys (see Fig. I-1). This is also illustrated in Fig. I-3. For instance fuselage panels require good formability and good damage tolerance, which is achieved by using a 2xxx alloy T3 tempered. The upper wings have to resist to compression stresses, which can be optimized by using 7xxx family, often in a T7X temper. Despite their higher mechanical properties, 7xxx alloys cannot be safely used in components subjected to tension, as it is the case for the lower wings. Due to their relatively poor toughness (see Fig. I-3) they are replaced by 2xxx series alloys.

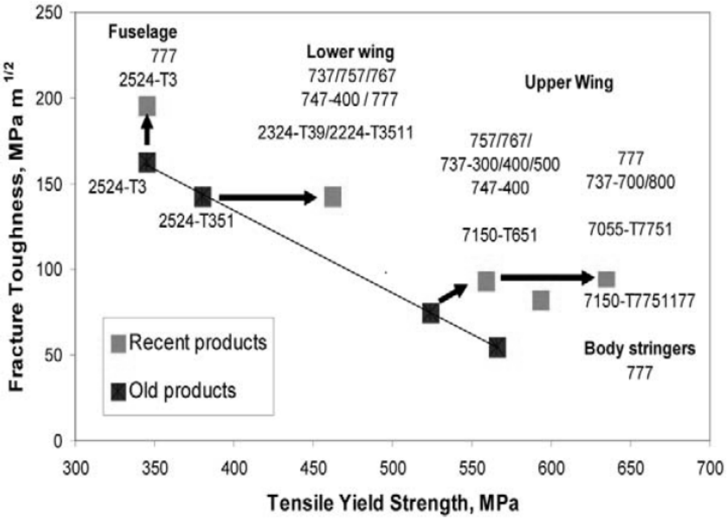

Fig. I-3. Improvements in strength-toughness combinations of some newer aluminium alloys

Previous and more recent alloys are presented, as a function of the location in the plane and for different aircrafts of the Boeing family [Williams 2003]

The alloy chosen for this study is aluminium alloy 7449, present at different locations in A380 aircrafts: in the upper wing skins (T7951 temper), ribs (T7651 temper) and upper wing stringers (extruded T79511 temper).

I.A.2. Internal stresses: origin and consequences on part distortion

I.A.2.a. Manufacturing process of aluminium aerospace components

High strength aerospace aluminium alloy plates are subjected to complex thermomechanical processing, including casting, homogenizing, rolling and age-hardening heat treatment. The temper of the delivered material is defined by this final stage, which mainly controls the material properties. This heat treatment includes a solution heat treatment (~470°C for AA7xxx), a fast cooling stage (water quench) and the ageing heat treatment itself (typically 15 to 30 hours between 120°C and 180°C).

As represented in Fig. I-4, the plate in the final temper is then sent to the customer where it is machined, eventually "finished"[1] and finally assembled, which requires very accurate components geometries.

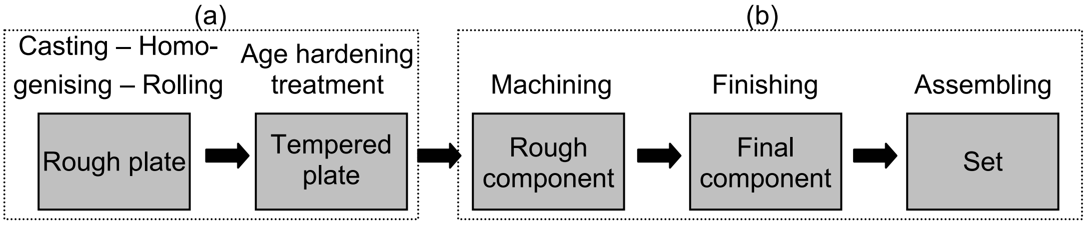

Fig. I-4. Simplified view of the manufacturing process of aerospace aluminium components

It includes the material processing (a) and the manufacturing process (b)

I.A.2.b. Origin and consequences of part distortion

Although carefully machined, some components do not have the required shape at the end of the process: in some cases the final part is distorted, as can be seen on Fig. I-5. This distortion leads to increase in re-work, scrap material, concessions and expensive downstream correction processes. It is estimated that part distortion incurred a €5.7M overspend on the development of the first wing for A380 alone [COMPACT 2005].

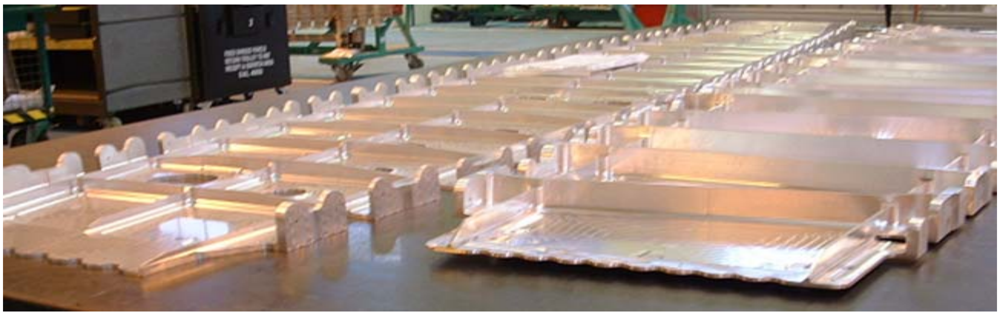

Fig. I-5. Distorted rib after machining

Correct flat component (left) vs. distorted component (right). Courtesy of Airbus.

It is now understood that part distortion (PD) is a function of residual stress (RS), caused by complex relationships between material processing, component design and manufacturing [Brinksmeier 2007].

Quenching is probably the main operation affecting the RS level. Indeed these alloys require a rapid quenching operation to achieve through thickness mechanical and corrosion resistance properties required for aerospace parts. This involves a high cooling rate gradient between the skin (rapidly cooled) and the core (more slowly cooled) of the plate, leading to large RS levels. These are compressive stresses in the surface and balanced tensile stresses in the core (about ±200 MPa) [Dolan 2004].

---

[1] "Finishing" is concerned by secondary processes; this can include surface treatment, dimensional correction…

To reduce the RS magnitude remaining after quenching, forgings are cold compressed (Txx52 treatment), while rolled plate products are stretched (Txx51). These stress-relieving techniques, industrially applied since the 1950s, decrease the RS magnitudes up to ±30 MPa [Tanner 2003].

These remaining RS can be further relieved to some extent during aging, the kinetics of stress relief being accelerated at higher temperatures. However a complete removal of RS is not achieved.

The machining operation, by removing the material (up to 90% in the ribs, for instance), tends to redistribute the internal stresses and leads to PD [Koc 2006], mainly due to the load of the cutting. The local heating generated by the cutting of AA7xxx seems to be not sufficient to affect the RS [Denkena 2008].

Moreover stress-relief may also happen at room temperature during storage stages and lead to PD.

I.A.2.c. How to cope with part distortion

Controlling (or dealing with) the RS distribution throughout the process, in order to control the component final geometry is one of the challenges the aircraft manufacturers have to face. This is even more the case as the planes are becoming larger (A380), requiring larger and thicker components. In order to reduce PD, three fundamental streams of activity may be investigated: material processing, manufacturing and design.

I.A.3. The COMPACT project: improving residual stress and part distortion management

I.A.3.a. Project objectives

The COMPACT project ("a Concurrent approach to Manufacturing induced Part distortion for Aerospace ComponenTs") is a sixth framework European STREP project (Specific Targeted Research Project) launched in October 2005. Led by the aircraft manufacturer Airbus U.K., the objective of this research project is to understand how residual stress evolves through the industrial process, and how to reduce the part distortions. It involves 12 industrial and academic European partners: Airbus U.K. (ind.[2]), Alcan CRV (ind.), University of Limerick, University of Bristol, Enabling Process Technology (ind.), University of Hannover, EADS Corporate Research Centre (ind.), Patras University, Alenia Aeronautica (ind.), Ultra RS (ind.), Grenoble INP and University of Sheffield.

The project is divided into 9 different workpackages (WP), each of them having a specific objective. 2 of them are support workpackages: WP1 (Project coordination, exploitation plan and dissemination) and WP6 (Knowledge Integration). The 7 other workpackages are research targeted: WP2a (Materials – Effect of material processing parameters on RS), WP2b (Materials – RS determination methods), WP3a (Manufacturing - Machining), WP3b (Manufacturing – Bending), WP3c (Manufacturing - Post-machining processes), WP4 (Through process Finite Element modelling) and WP5 (Effect of design on part distortion).

I.A.3.b. Workpackage 3c

WP3c investigates different solutions to correct PD after the machining operations, to allow assembling of formerly distorted components. Three strategies are evaluated, which may be used to redistribute or relieve RS in the final components.

---

[2] "ind." stands for "industrial partner"

The first one is a mechanical process, shot peening or shot peening forming (SPF), which consists in launching particles with a high pressure on the material surface [Wang 2006a]. The second one is a thermal treatment: laser beam forming (LBF), which consists in a local heating of the material with a laser beam [Dearden 2006, Labeas 2008]. The last one is a thermomechanical process: age forming [Zhu 2001a, Lin 2006], which involves both temperature and strain/stress.

Nevertheless those treatments are often empirically defined and neither the way they affect RS and PD, nor the effect on the material microstructure and its final properties are known. This requires on the one hand modelling of the post-machining treatment itself, to allow the optimization of the process to reach the planned final shape. On the other hand, this also requires ensuring that the material properties after these treatments are in agreement with the specifications.

The objective of this workpackage is to provide a quantitative study of the effect of different post-machining correction processes on the RS and PD and on the material microstructure and properties.

I.A.4. Thesis objectives

I.A.4.a. Thesis scope

This PhD work has been carried out in the framework of the workpackage 3c of the COMPACT project. It is the result of a collaboration with EADS Corporate Research Centre in Germany, Patras University in Greece and Alcan CRV in France. Alcan has provided the initial 76 mm thick AA7449 T7651 plates. EADS has provided the laser treated material. Patras University, which is in charge of the Finite Element Modelling of the post-machining treatments, has provided temperature calculations for the laser treatment.

The objective of this PhD is to provide quantitative information about how the different past-machining correction processes affects the material microstructure and final properties.

In the present context, the word “microstructure” will often be understood as the precipitate microstructure. Indeed, the other microstructural parameters (grain size, texture…) will be kept constant, whereas the precipitation state, which is the main parameter affecting the properties in age-hardenable alloys, will vary. This precipitation state is defined by a number of parameters: precipitate volume fraction, solute solution, precipitate size distribution, precipitate type and morphology…

Applying a thermomechanical (either a purely thermal or a thermomechanical) treatment to an age-hardenable material will affect its precipitation state, and as a consequence the material properties: the mechanical properties (yield strength, strain hardening, ductility, toughness, fatigue…) will be modified [Dumont 2003], but also the corrosion performance for instance [Tanner 2003].

I.A.4.b. Objectives within COMPACT

For workpackage 3c2 (shot peening) we have to provide an analytical model for the materials constitutive law, as a function of the microstructure. It will be used by Patras University for their further FEM modelling of the shot peening process. This strain hardening model should include kinematic and isotropic effects, as well as a strain rate dependency, and be applicable to different microstructures.

Our work in workpackage 3c4 (laser forming) is to develop an analytical model for the microstructure and the mechanical properties evolution during laser beam treatment. This model should be able to describe the precipitation evolution during laser treatment and how the mechanical properties are affected.

Concerning workpackage 3c3 (thermomechanical process), we need to provide an analytical model describing the evolution of the precipitation as a function of thermomechanical processes for partially heat treated materials, and an analytical model for the creep rate as a function of the temperature and creep stress for the finally heat treated T7651 material.

I.A.4.c. Underlying scientific objectives

Our scientific objective is to progress in the understanding of the coupling between thermomechanical treatments, microstructure evolution and properties, on a more fundamental point of view.

The first objective is therefore to evaluate how the precipitation state is affected by thermomechanical treatments. The second objective is to relate the mechanical properties to the precipitation state. Achieving those two objectives implies both experimental and modelling work. In particular quantitative modelling will help to validate the relevance of the proposed micromechanisms, and to predict (to some extent) the final properties.

I.A.4.d. Outline

After this general introduction, a general literature review of the microstructural features of 7xxx series aluminium alloys is presented, followed by a section presenting the basis of the hardening mechanisms and the relationships between precipitation and hardening. This literature review will be used as a basis for the further analysis and understanding of the experimental results.

The second chapter presents the studied AA7449 material, as well as the main experimental techniques that have been used in this work. The standard microstructural and mechanical investigation techniques are briefly presented. A special attention is given to a less standard technique (Small-Angle X-Ray Scattering) and to the tensile and heating device that has been developed during this work for the study of precipitation during thermomechanical treatments.

In the third chapter, the effect of precipitation on strain hardening is investigated and a strain hardening model is proposed. This model will be used by University of Patras in a finite element shot peening model. In order to model shot peening for different tempers, a microstructure-dependent strain hardening model is necessary. Therefore a wide range of initial tempers has been generated by varying the duration of the aging heat treatment. The resulting microstructure has been measured and the strain hardening behaviour evaluated throughout tensile and Bauschinger tests. A microstructure-dependent strain hardening model is proposed, accounting for both isotropic and kinematic hardening.

The fourth chapter is dedicated to the study of laser beam formed parts. The effect of the laser forming treatment on the material is analysed as a non-isothermal heat treatment. It affects the precipitation state and the mechanical properties, as evidenced experimentally. Then, a complete modelling approach is proposed, to model the influence of the process parameters on the precipitation microstructure and the mechanical properties.

The fifth chapter investigates the effect of the coupling of a thermal and a mechanical treatment on precipitation. This study is mainly based on experimental characterization, performed with a specific device developed during this work (see second paragraph of this section). This device allows correlating quantitatively the effect of the thermomechanical process parameters (strain rate, strain, temperature, initial state) to the material's response (precipitation state, stress). The effect of temperature and stress on creep rate and precipitation kinetics for the T7651 temper is studied. The effect of age-forming or stretch-forming treatments on precipitation kinetics for other under-aged tempers has been measured and modelled, by using as a basis the precipitation model developed for chapter IV.

I.B. Literature review: 7xxx alloys microstructure

I.B.1. Material processing

I.B.1.a. Complete thermomechanical treatment

The complete processing route of 7xxx aluminium plate is represented in Fig. I-6. The corresponding thermomechanical treatment is shown in Fig. I-7.

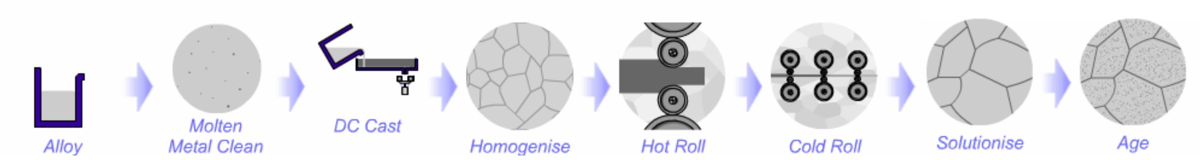

Fig. I-6. Schematics of the processing steps for AA7xxx

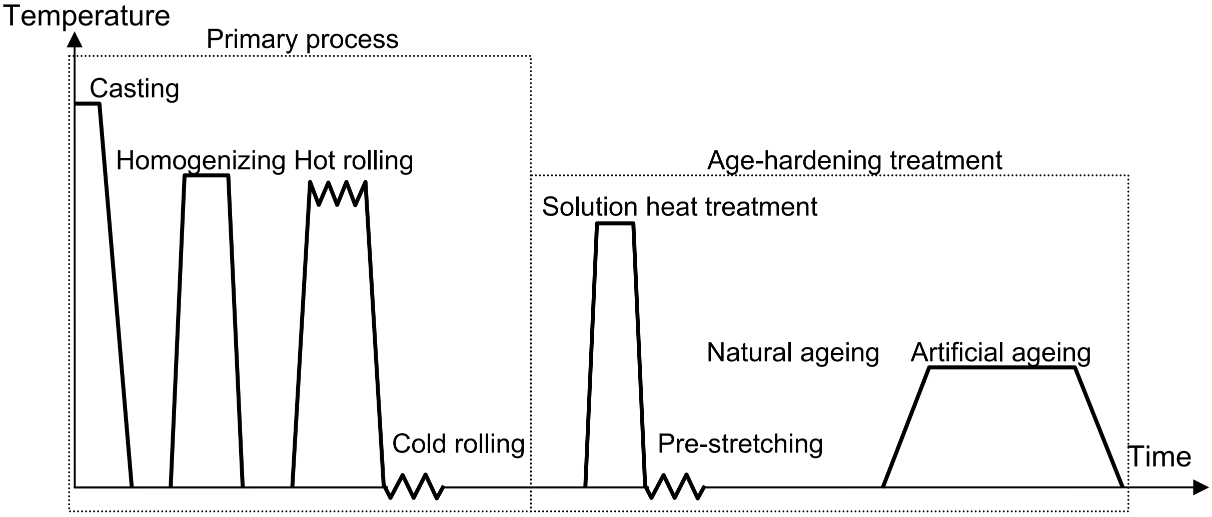

Fig. I-7. Thermomechanical treatment for AA7xxx

It can be divided into 2 main stages. The first stage is the material elaboration, in which the alloy is molten, cast, homogenised, hot rolled and cold rolled (see Fig. I-6). This step controls the material composition and the material grain structure. The second stage, the age-hardening treatment, concerns the design of the precipitation state and is mainly responsible for the mechanical properties of the material. The different stages will be detailed in paragraph I.B.1.b.

The resulting grain microstructure is shown in Fig. I-8. Rolling generates grain anisotropy in the plate: it elongates the grains in the rolling direction (L). What is expected is to obtain a small grain size, in order to maximize the mechanical properties (see I.C.3.e.ii). The grain microstructure is in fact composed of small sub-grains (disorientation less than 10%), but also of a small proportion of larger grains, which have recrystallised during the hot rolling treatment.

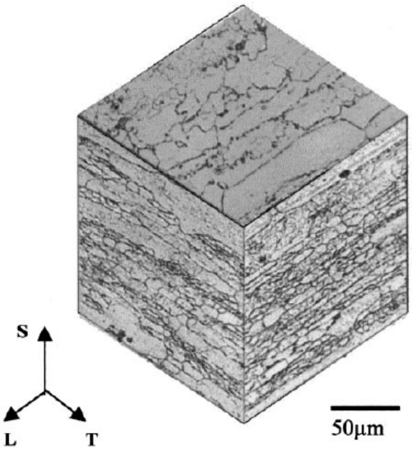

Fig. I-8. Grain microstructure of AA7449 W51

[Kamp 2002] Optical micrograph. L: rolling direction.

I.B.1.b. Age-hardening treatment

The main objective of this treatment is to design the precipitate features (size distribution, volume fraction, spatial distribution), in order to reach the required specifications: mechanical properties (mainly strength and toughness) and corrosion properties. It will be achieved through 5 main steps: solution heat treatment, quenching, pre-stretching, natural and artificial ageing.

i. Solution heat treatment

The solution heat treatment consists in heating the material at 450-500°C during a few hours.

After the previous processing steps, coarse particles have precipitated, resulting in a poor mechanical performance of the material. Heating the material above the solvus temperature dissolves these coarse precipitates and leads to a homogeneous alloying elements (Mg, Zn, Cu) distribution in the matrix. The upper limit of the solution heat treatment is the solidus temperature: incipient melting would occur if this temperature were overcome, which is very detrimental to the mechanical properties.

During this high temperature heat treatment, the density of vacancies in the matrix is increased. Those vacancies, ensuring the mobility of the solute elements, will later help the nucleation of the precipitates.

The grain structure is not affected by this treatment because the dispersoïds which pin the grain boundaries are stable at this temperature (see I.B.3.c.).

ii. Quenching

This consists in cooling the material rapidly by immersing it in into cold water (immersion quench) or aspersing it with water (aspersion quench).

The aluminium matrix that was able to dissolve the alloying elements at 470°C is supersaturated at room temperature: it will tend to reject a large amount of alloying elements, which will then form the new precipitates. The role of the quench is to freeze the solid solution, that is to say prevent atom diffusion. The quench velocity (or cooling rate) is the main factor that controls the quality of the quench. It mainly affects the vacancy density (see I.B.3.b.i) and the heterogeneous precipitation (see I.B.3.b.ii), as well as the internal stress level [Robinson 2006].The consequences can be observed on the age-hardening response [Lim 2004, Deschamps 1998a], the corrosion properties (stress corrosion and exfoliation corrosion) [Henon 2006] or the toughness properties [Dumont 2004, Morgeneyer 2006].

iii. Natural ageing

This consists in storing the material at room temperature during a few days (usually between 3 and 5). The supersaturated solid solution tends to reject solute atoms, that diffuse and form metastable clusters called GP zones (see I.B.3.a.ii).

The advantage of performing this room temperature heat treatment is that the critical radius for nucleation is small, which favours homogeneous nucleation. One obtains a high density of homogeneously distributed small clusters in the bulk that optimize the later nucleation of precipitates.

iv. Artificial ageing

This heat treatment is carried in a temperature range usually included between 120°C and 200°C and usually lasts between half a day and two days. The most standard treatments are single-step heat treatments or 2-steps heat treatments. More recently complex 3-steps heat treatments appeared: RRA (retrogression and re-ageing treatments), in order to decrease the material susceptibility to exfoliation corrosion and stress corrosion cracking [Cina 1992, Tanaka 2006], or interrupted ageing treatments [Gao 2007], which allow increasing the mechanical properties, as compared to the T6 temper.

During this heat treatment, new phases precipitate, either by phase transformation of the former GP zones or by heterogeneous nucleation on defects (see I.B.3.b.ii). The temperature and duration of the heat treatment control the precipitate size distribution, density and volume fraction, as well as the nature of the phases (η', η) and their composition. Temperature and time play a role in the diffusion process and therefore determine the precipitation kinetics. It also determines the thermodynamics of the system: it controls the phase stability, the solute and the precipitate volume fraction.

The aging heat treatment affects the final properties (physical and mechanical) of the alloy. During this stage, the yield stress increases up to a maximum, called "hardness peak" after which it decreases. Before the hardness peak one speaks of "under-aged" tempers; of "over-aged" tempers after. Hardness peak in tension is named "T6" temper. A slight over-aging ("T79") corresponds to the peak in compression. Then one finds the industrial "T76", "T74" and "T73" tempers, where the mechanical vs. corrosion properties are more balanced: lower corrosion susceptibility (stress corrosion cracking and exfoliation corrosion) and higher toughness but lower mechanical strength [Tanner 2003]. As an example, the T76 temper loses 6 to 8% yield stress as compared to T6 and the T73 10 to 15% [Develay 1986].

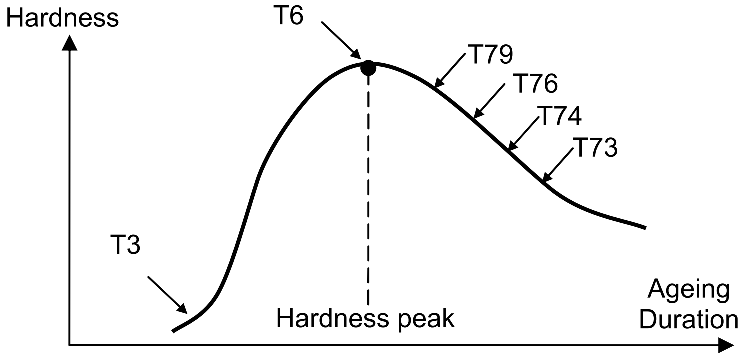

Fig. I-9. Schematic hardness evolution during aging treatment and temper position

v. Pre-stretching

This purely mechanical process takes place right after quench. It consists in plastically deforming the as-quenched plate up to 2-3% deformation. The purpose of this is to decrease the residual stress level in the plate induced by the former quench, which leads to a severe plate distortion. This step not only affects the residual stress level [Tanner 2003], but also the precipitation kinetics, as this introduces dislocations in the material. A suffix is added to the temper name, whether the plastic deformation is applied in tension or in compression: respectively "51" and "52". For instance, the T651 temper corresponds to a pre-stretched peak-aged material.

I.B.2. Generalities about precipitation

I.B.2.a. Precipitation stages

The precipitation process is classically analysed into three successive stages: nucleation, growth and coarsening. Qualitatively, nucleation corresponds to the early stage of precipitation, during which the precipitates form from the solid solution. Quantitatively, it is characterised by an increase of the precipitate density and an increase of the precipitate volume fraction (see Fig. I.10). Then, during precipitate growth, solute atoms diffuse from the solid solution to the already present precipitate nuclei. This corresponds to an increase of the precipitate size, an increase of the volume fraction and a steady precipitate density. During the final coarsening stage, the matrix supersaturation has reached its minimum and the volume fraction is constant, almost equal to thermodynamic equilibrium. The only remaining driving force is the reduction in interface energy: this leads to a decrease of the precipitate density, as well as a growing precipitate average size. The smaller precipitates dissolve and the solute atoms diffuse to the larger precipitates.

This conceptual picture does not happen exactly that way in reality, where those three stages somehow overlap, the transitions from one regime to another being very progressive.

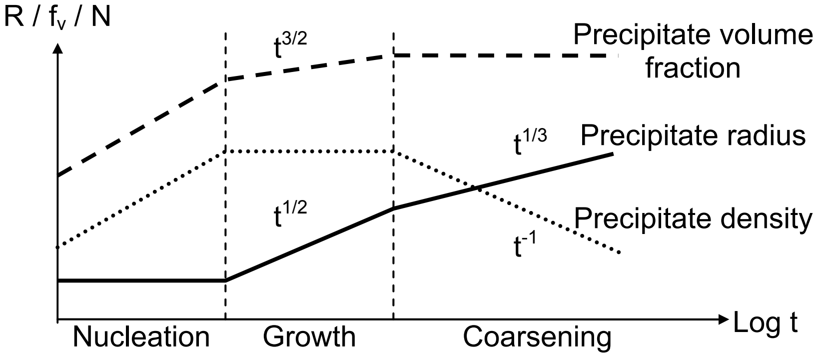

Fig. I.10. Schematic evolution of the precipitation during isothermal heat treatment

[Philibert 1998] Size (R), volume fraction (f_v) and density (N)

As indicated on this figure, precipitation kinetics changes during the various stages, especially the time dependence of the precipitate radii. This will be developed in chapter IV.

I.B.2.b. Coherency and metastable phases

Precipitation evolution refers to precipitate size evolution, but also often to phase transformations. The consequence is that the precipitate/matrix interface changes during the precipitation process, as shown in Fig. I.11.

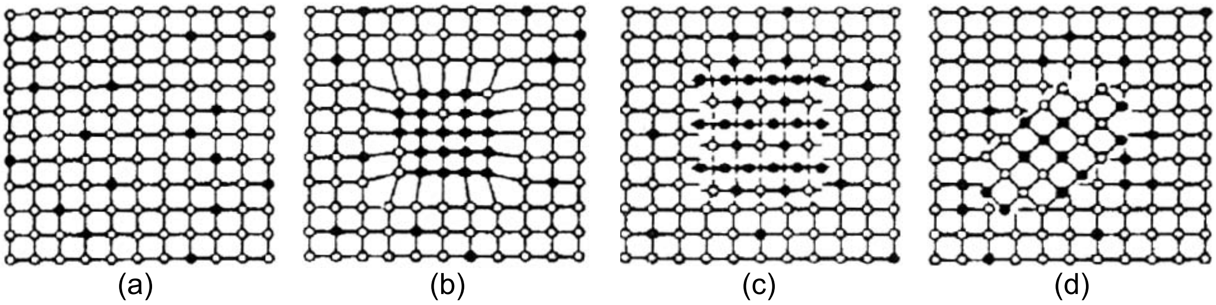

Fig. I.11. Precipitate/matrix interface evolution during heat treatment

(a) Solid solution. (b) Coherent precipitate. (c) Semi-coherent precipitate. (d) Incoherent precipitate

Right after quench, the solid solution is homogeneously distributed in the material. Then, when nuclei appear, they have the same crystallographic structure as the matrix, but different lattice parameters: the precipitate is said to be coherent. As the precipitate composition is different from the average matrix composition, the mean atomic size is different in those two areas and the lattice is strained. The increase of the precipitate size and the change in the precipitate composition leads to a change in the crystallographic structure, and the misfit between the two lattices (matrix and precipitate) increases: the precipitates become semi-coherent. When the precipitates reach a critical size, the matrix is unable to accommodate the misfit and the precipitate becomes incoherent.

The lattice is strained by the presence of precipitates, and the elastic stress field around the precipitates evolves during precipitation. The precipitate-lattice interface strongly affects the mechanical properties, as it will be explained in I.C.3.c.

I.B.3. Precipitation in 7xxx series alloys

Three main precipitate types of precipitates can be found in precipitate hardening aluminium alloys: hardening precipitates, dispersoïds and intermetallic precipitates.

The 7xxx series is composed of two groups of aluminium alloys: Al-Zn-Mg and Al-Zn-Mg-Cu alloys, but if the precipitate composition is affected by the presence of a third alloying element (copper), the precipitation mechanisms are almost identical, the copper playing a similar role as the zinc atoms.

I.B.3.a. Hardening precipitates

i. Precipitation sequence

Those precipitates are the main responsible of the mechanical performance of the material. They are composed of the main alloying elements of the alloy (Al, Zn, Mg, Cu, see and nucleate at low temperature from the decomposition of the supersaturated solid solution after the quench. Four precipitation sequences may be considered [Mondal 2005], forming either the η ($MgZn_2$), the T ($Al_2Mg_3Zn_3$), the S (Al_2CuMg) or the θ phase (Al_2Cu), depending on the alloying elements proportions and especially from the Mg/Zn ratio, as reported by Maciel et al. [Maciel 2003] (see phase diagrams below).

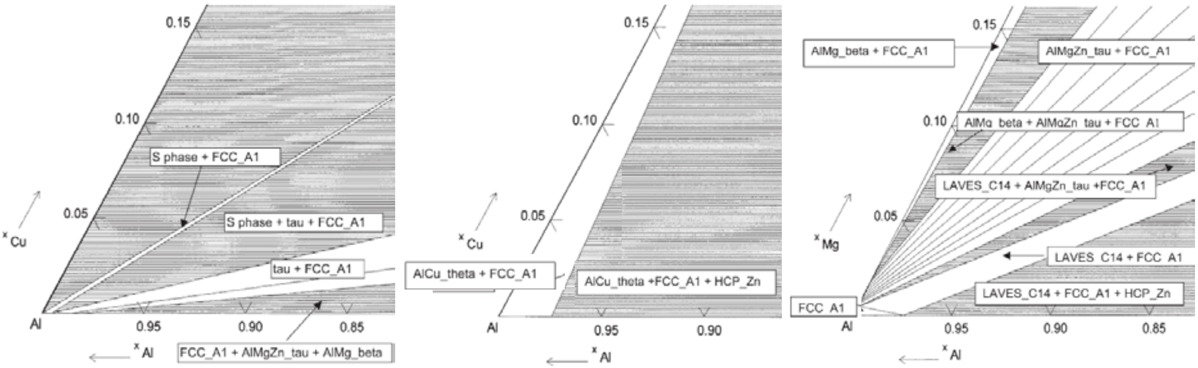

Fig. I-12. Al-Cu-Mg, Al-Cu-Zn and Al-Mg-Zn ternary phase diagrams at 400K

[Maciel 2003] The meaning of the phase labels is the following: Laves C14 (η) - Tau (T) - S (S) - FCC_Al (α) - Theta (θ)

According to Mondal & Mukhopadhyay [Mondal 2005], most of the copper remains dissolved in the η and T phases below 2.5wt%. Their XRD measurements, made on alloys whose compositions are close to the one of AA7449 (see table II.1), confirm the low fraction of the S phase and the very low fraction of the θ phase. As the copper content is even lower in AA7449 than is their alloys, one can therefore consider that those two phases are negligible in our case. The two precipitation sequences that should be considered in the low copper content 7xxx alloys are the following:

$$\text{(II.1.)}\quad s.s.s. \longrightarrow \begin{cases} GP\ zones \longrightarrow metastable\ \eta' \longrightarrow stable\ \eta & (a) \\ metastable\ T' \longrightarrow stable\ T & (b) \end{cases}$$

The second sequence is mostly present in alloys containing high magnesium fraction (>2 wt %). Furthermore the T phase does not nucleate when the ageing treatment happens at low temperature, as this phase requires a higher activation barrier to nucleate [Embury 1965]. According to Develay [Develay 1986], the second sequence happens for ageing temperatures above 190°C. One can therefore state that the sequence leading to the η phase is probably the only one relevant in our case.

Appearance, structure, shape, composition and transformation of the different hardening phases will be considered in the following paragraphs.

ii. GP zones

Guinier-Preston zones (GP) have been discovered separately by Preston and Guinier in 1938. Guinier measured by X-Ray diffraction the early-stage precipitation of Al-5%Cu and observed a few "low intensity elongated spots" in the diffraction pattern. He attributed this to "small, planar and thin clusters" [Guinier 1938b, Calvet 1938], which are now called GP zones. Those are coherent pre-precipitates that form directly from the initial supersaturated solid solution. Alekseev [Alekseev 2002] observed that GP zones appeared after 40 minutes of natural ageing in AA7050. Sha [Sha 2004] found that they nucleate homogeneously in the matrix. According to Deschamps [Deschamps 1999a], the addition of copper results in an increase of the stability of GP zones formed at room temperature (during natural ageing). DSC measurements show that they dissolve between 50 and 120°C.

As reported by Berg [Berg 2001] two types of GP zones exist in artificially aged 7xxx alloys: GPI and GPII (see Fig. I-13 and Fig. I-14). They can be distinguished with their diffraction pattern [Hansen 2002]. GPI zones are equiaxed precipitates and are formed from room temperature up to 140-150°C, independently of the quenching temperature. GPII are zinc-rich thin clusters on {111} planes, are formed from VRC (vacancy rich clusters [Werenskiold 2000]) after quenching from temperatures above 450 °C and ageing at temperatures above 70 °C. Both are coherent with the aluminium matrix and have the same atomic structure.

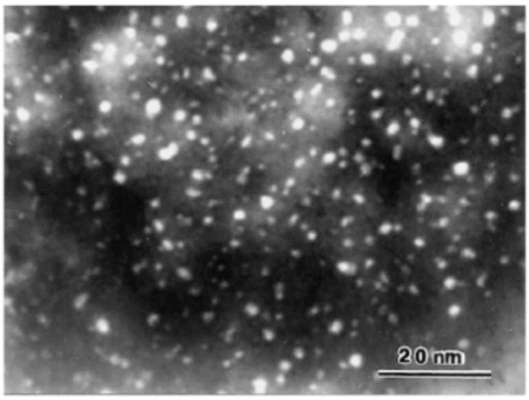

Fig. I-13. GPI zones in AA7108

[Berg 2001] Bright-field image in [001] projection

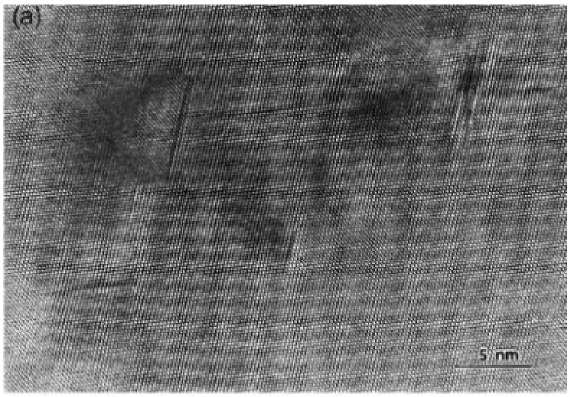

Fig. I-14. GPII zones on $(111)_{Al}$ in AA7108

[Berg 2001] HRTEM image in [110] projection

Li [Li 1999] presents GPI zones as the main type of GP zones produced at room temperature. Hansen [Hansen 2006] agrees on that point, adding that GPII zones appear only in alloys with low magnesium content (Mg/Zn ratio smaller than 0.5).

According to Chinh et al. [Chinh 2004], who did 3D-AP measurements on two Al-2.4Zn-2.1Mg (at%) alloys, with and without copper addition, the incorporation of copper introduces strain in the GP zones, which leads to ellipsoidal precipitates, contrary to copper-free alloys.

It is now generally admitted that GP zones in 7xxx alloys contain Al, Zn and Mg atoms, as well as copper, when copper is present in the alloy. Sha & Cerezo [Sha 2004] shown through 3D-AP measurements that the Zn/Mg ratio in the smaller clusters of AA7050 (which contains less Zinc than AA7449 and comparable Copper and Magnesium contents) is 0.85 and the Copper content is 12 at.%, after 90 minutes of natural ageing. They also showed that this ratio changes towards 1.2 during heat treatment, which means enrichment in Zinc content.

Some controversy exists on the role of GP zones on the further precipitation steps. Some authors [Berg 2001] suggest that GPII zones are precursors to η' precipitates. They have investigated the effect of age-hardening treatment on early-stage precipitation in AA7108, a copper-free alloy, by TEM and HRTEM. They found both GPI and GPII zones, depending on the ageing conditions (see previous paragraph), and saw some thicker GPII zones as transition precipitates towards η' precipitates. Sha & Cerezo [Sha 2004], however, assume that GPI zones transform into η' precipitates. They have recently investigated the early-stage precipitation of AA7050 by 3D-AP and TEM. They found that only blocky GPI zones (no GPII) are present at the beginning of the heat treatment (ageing at 121°C). According to them, the smaller GPI lead to the formation of elongated clusters and subsequently to η' precipitates, while the larger GPI are stable and continue to grow.

iii. Metastable η' precipitates

This phase is referred as the main hardening phase in 7xxx alloys. It appears between 120°C and 180°C and is stable up to 250°C [Poulose 1974]. Deschamps [Deschamps 1999a] reported that the addition of copper decreases the nucleation temperature of the η' phase. This phase either precipitates on former GP zones (see for instance [Sha 2004]) or nucleate directly in the matrix at higher temperature, as reported by Berg [Berg 2001]. Sha measured the transformation of GP zones into η' during artificial aging. He noted that already 6%[3] of the clusters are transformed after 30 minutes at 121°C and 60% after 240 minutes.

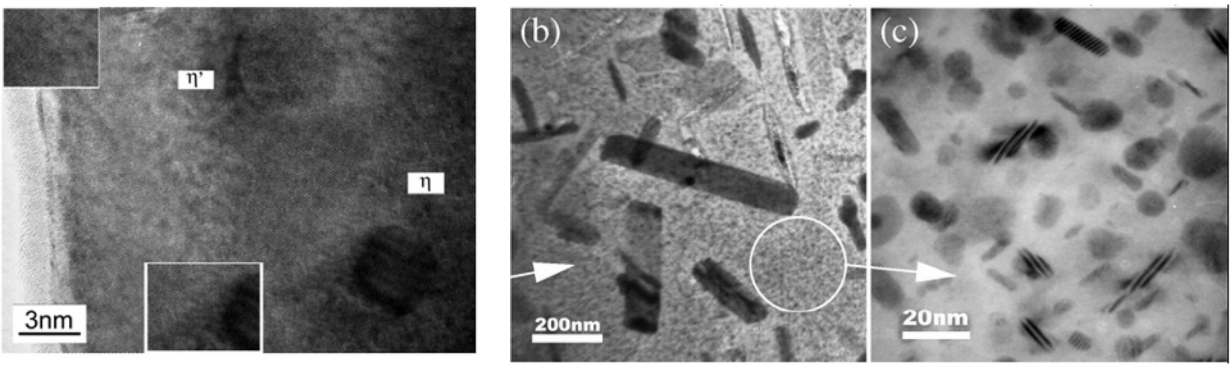

Fig. I.15. η' and η precipitates

(a) [Zhu 2006] HRTEM. (b) and (c) [Sullivan 2008] TEM image in [110] projection in the nugget zone of a Friction Stir Welded AA7449 plate. Coarse precipitates are due to coarsening during FSW and fine precipitates to re-precipitation of the dissolved volume fraction.

This semi-coherent metastable hexagonal phase can be found as platelets presenting the following orientations with the matrix [Starink 2003a]: $(0001)_\eta \;//\; (111)_\alpha$ or $(1\bar{2}10)_\eta \;//\; (110)_\alpha$ Different authors [Li 1999, Berg 2001] recently investigated the η' structure by HRTEM; they both found that its lattice parameters are a = 0.496 nm, c = 1.40 nm.

The composition of the precipitates evolves during ageing treatment. It seems now clear that they both contain Zinc and Magnesium, but also Aluminium and Copper. Dumont [Dumont 2005] suggests that their composition for AA7108 (Copper free alloy) in the T6 temper is 55% Zn, 25% Mg and 20% Al. According to Sha & Cerezo [Sha 2004], Zinc content increases in the η' platelets during heat treatment at 121°C: the Zn/Mg ratio moves from 1.09 to 1.26 between 30 and 1440 min. The solvus of those precipitates is around 250°C [Poulose 1974].

iv. Equilibrium precipitates

The equilibrium phase is a hexagonal Laves phase with the following lattice parameters: a = 0.5221 nm, c = 0.8567 nm [Berg 2001]. Equilibrium incoherent precipitates appear after over-ageing [Hansen 2002, Starink 2003a] and are stable up to 370°C [Poulose 1974, Deschamps 1999a]. The equilibrium precipitates form either at or from η' precipitates as laths or plates [Starink 2003a]. Eleven types of

---

[3] This corresponds to 15% in atomic fraction, as the size of G.P. zones and η' is different

precipitates have been reported [Deschamps 1997], labelled from η_1 to η_{11}, depending of their orientation and origin. Three main families are present in industrial ternary and quaternary 7xxx alloys: η_1, η_2 and η_4. Their respective orientation is the following: $(0001)_{\eta_1} // (110)_\alpha$, $(0001)_{\eta_2} // (1\overline{11})_\alpha$, $(0001)_{\eta_4} // (110)_\alpha$. The first family nucleate from the metastable precipitates; the second one on dislocations and the η_4 precipitates in the bulk.

If this equilibrium phase η (also called M phase) has the stœchiometric composition $MgZn_2$, it has been shown that copper and aluminium are also present in nanometer precipitates, which are classically presented as $Mg(Zn,Cu,Al)_2$ precipitates [Vratnica 2007]. Brenner [Brenner 1991] showed in 1991 that the matrix precipitates of AA7150 (relatively close to AA7449) after RRA heat treatment contains 15-25% copper and of the order of 10-15% aluminium. It is now established that the precipitate composition changes during ageing. Sigli [Sigli 2006] presents those precipitates as having the $MgZn_{2(1-z)}Cu_zAl_z$ composition. Marlaud [Marlaud 2008] recently investigated their evolution by 3D-AP (3 Dimensional Atom Probe Tomography) and anomalous Small Angle X-Ray Scattering and found that AA7449 T6 and T7 precipitates respectively have the following compositions (Table I.1):

Element	Mg	Zn	Cu	Al
T6 composition	33.3	30	9.7	27
T7 composition	33.3	45.2	10.4	11.1

Table I.1. Composition of AA7449 precipitates

[Marlaud 2008] Atomic composition measured by 3D-AP

I.B.3.b. Precipitation and age-hardening treatment

i. Role of vacancies

Vacancies, which are point defects in the material lattice, are responsible for the diffusion of the alloying elements in the bulk of the material. Supersaturated vacancies form clusters with solute atoms, which dissolve at the GP zones interface, letting the vacancies free. Those vacancies can then diffuse again in the matrix and form new clusters [Deschamps 1997].

A high vacancy density is necessary for the nucleation of a high number density of precipitates [Ber 2000] and then to enhance the diffusion rate. This will be achieved by performing the solution heat treatment at high temperature and quenching the material at a high cooling rate, as it was already reported by Seitz fifty years ago [Seitz 1950]. On the other hand those two requirements are detrimental, since they tend to induce higher residual stresses.

ii. Homogeneous vs. heterogeneous precipitation

Heterogeneous precipitation corresponds to precipitation occurring on discontinuity of the crystal lattice: grain boundaries, dispersoïds or dislocations. Heterogeneous precipitation is favoured as compared to homogeneous nucleation both thermodynamically and kinetically: on the one hand the interfacial energy is lower and the nucleation threshold is decreased; on the other hand diffusion is enhanced by these defects.

iii. Precipitation on dislocations

Quenching the material may lead to the form of prismatic dislocation loops, called vacancy loops [Dubost 1991], on which heterogeneous precipitation may occur [Wang 2007]. Pre-stretching (see I.B.1.b.v) consists in deforming plastically the plate, which also introduces dislocations in the material. This is another source of heterogeneous nucleation. More generally, the presence of dislocations both affects the thermodynamics and kinetics of precipitation. This point will be developed in chapter V.

iv. Quench-induced precipitates

Quench-induced precipitates are coarse precipitates that nucleate heterogeneously on constituent phases, dispersoïds (see Fig. I.16.a), grain and sub-grain boundaries (see Fig. I.16.b) [Deschamps 1998a]. The same author showed in another paper [Deschamps 2008] that for quench rates between 5 and 200°C/min substantial heterogeneous precipitation is observed on dispersoïds and grain boundaries, and that the ones nucleating on dispersoïds are larger than the precipitates formed on grain boundaries.

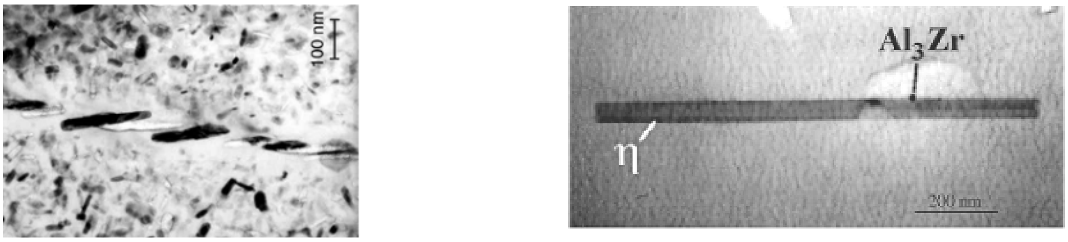

Fig. I.16. Heterogeneous precipitation

(a) [Deschamps 2001] on a grain boundary. (b) [Deschamps1998b] on a dispersoïd after air-cooling of AA7010.

Those large precipitates induce solute depleted zones which transform into precipitate-free zones and a smaller volume fraction of homogeneously nucleated precipitates after ageing (see Fig. I-17). This is very detrimental to the mechanical properties and the ageing response of the alloy is strongly affected [Deschamps 1998b]. Their presence depends on the quench sensitivity of the alloy; a high quench rate is required to avoid quench-induced precipitates.

v. Role of the two steps ageing

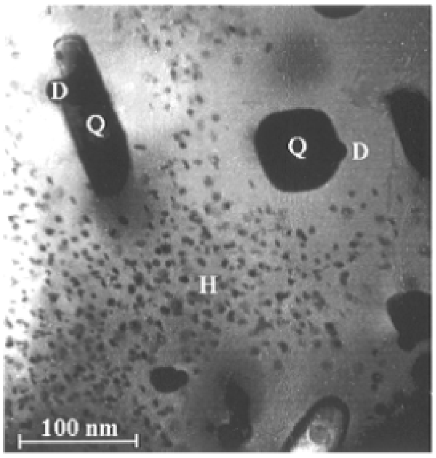

Fig. I-17. Quench-induced precipitate vs. homogeneously nucleated precipitates

[Deschamps 1998a] "D" stands for dispersoïds, "Q" for quench-induced precipitates and "H" for homogeneously nucleated precipitates

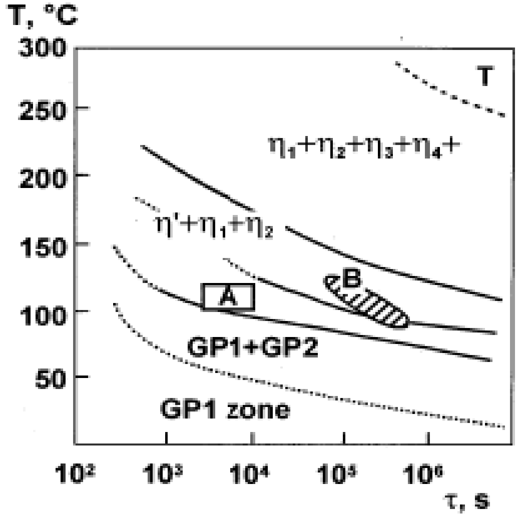

Fig. I.18. TTT diagram for ageing of Al–6.1Zn–2.4Mg–1.6Cu (wt.%) Alloy

[Ber 2000] The shaded B area corresponds to the maximum YS. The A area corresponds to first-stage ageing regimes with minimum duration, at which precipitates of GP2 and η'-phase, inherited in the case of second-stage ageing at 160–180°C, are forming.

Time-temperature equivalence allows reaching the same mechanical properties with various ageing treatments: 24h at 120°C or 16h at 140°C for instance (see Fig. I.18) [Ber 2000]. This can be optimized by performing a two-stage ageing treatment with a low temperature first stage and a higher temperature second stage, for example 3 h at 120°C and 3 h at 160°C. This two-stage heat treatment also improves the corrosion resistance [Ber 2000].

I.B.3.c. Dispersoïds

Most of the age-hardened aluminium alloys contain minute amounts of transition alloying elements such as Manganese (Mn), Chromium (Cr), Zirconium (Zr) or Scandium (Sc), which are added in order to inhibit recrystallisation during the further material processing [Clouet 2004]. These elements precipitate during homogenisation of the cast billets [Robson 2001]. Those precipitates, called dispersoïds, typically measure 10 to 100 nm.

Due to the slow diffusing rates of the constituents (Fig. I.19) and their high stability (Fig. I-21) dispersoïds do not evolve during hot forming and solution heat treatment, which prevents grain recrystallisation by a Zener pinning of the grain boundaries. This allows controlling the grain size and affects the mechanical properties, due to two effects [Dai 2007]: precipitate strengthening and grain-size strengthening (see I.C).

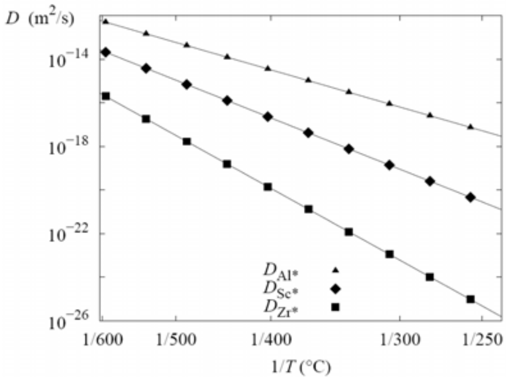

Fig. I.19. Diffusion coefficients of Al, Sc and Zr in Al

[Clouet 2004]

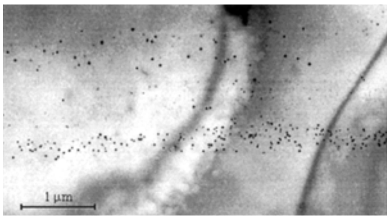

Fig. I.20. Dispersoïds bands

[Deschamps 2001]

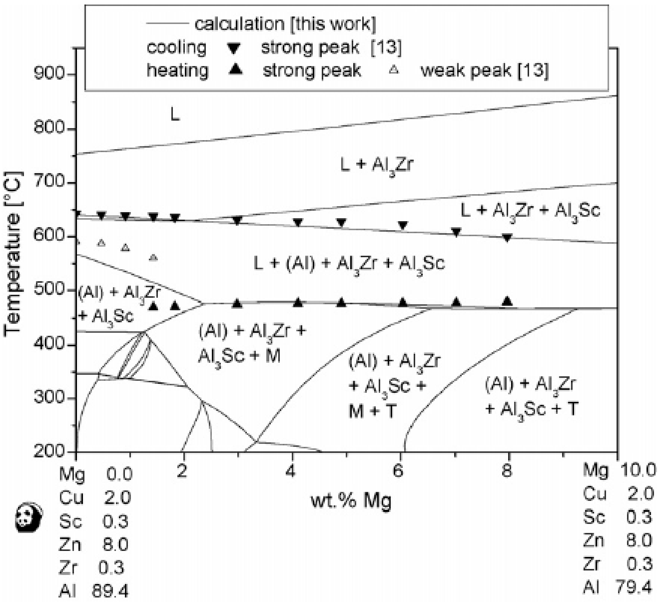

Fig. I-21. Pseudo binary Al-Zn-Mg-Cu-Sc-Zr phase diagram

[Gröbner 2007] Phase diagram presented for constant 8 wt.% Zn, 2 wt.% Cu, 0.3 wt.% Sc, and 0.3 wt.% Zr, close to AA7449 (Mg content = 2.24wt% but no Scandium; see Chapter II.)

In the 7xxx series, mainly zirconium and scandium elements are added (or sometimes chromium), which precipitate in the form of metastable coherent Al_3Zr, Al_3Sc or $Al_3(Sc,Zr)$ particles [Gröbner 2007, Dai 2007]. There is currently strong interest in adding Scandium to 7xxx aluminium alloys to improve the dispersoïds distribution and hence minimize recrystallisation [Robson 2004]. In the case of AA7449, only Al_3Zr precipitates have to be considered as there is no Sc.

The effectiveness of the dispersoïds in fulfilling this role depends on their size, spacing and distribution [Robson 2001], which are determined by the thermomechanical processing of the alloy, in particular the homogenisation step. It has been reported that dispersoïds precipitate heterogeneously. They are segregated in long thin bands extending into several grains (see Fig. I.20), due to Zr segregation to the dendrite core during solidification [Deschamps 1998a], Zr being a peritectic element. Thick AA7xxx plates often have a high fraction of recrystallised grains at the plate surface and centre compared to that at quarter thickness [Robson 2007], and through-thickness macro segregation may be one of the reasons why this happens.

I.B.3.d. Intermetallic precipitates

Coarse intermetallic particles (larger than 1 µm) are formed during the casting of the alloy, due to impurities that have not been removed during the process. Those particles are very detrimental to the mechanical properties, especially to the formability and to the toughness of the material, the particles offering a crack growth path [Starink 2005a].

In the 7xxx family, Iron (Fe) and Silicon (Si) are the main constituent of those particles, and the main intermetallic phases are Si and Fe-rich particles [Li 2001]. Vratnica [Vratnica 2007] investigated recently the effect of intermetallic particles on the fatigue crack propagation of Al-Zn-Mg-Cu alloys. He noted an average volume fraction of 0.5% and listed η, S and Mg_2Si coarse particles, as well as Fe-rich particles: $(Cu,Fe,Mn)Al_3$, Al_7Cu_2Fe, $(Cu,Fe,Mn,Cr)Al_7$ and $(Fe,Cr,Mn,Cu)_3SiAl_{12}$. He noted that the Fe-containing particles crack more often and provide sites for fatigue crack initiation.

The main ingredients concerning precipitation have been explained in this previous part. The next point will be, to set the physical metallurgy basis for the plasticity mechanisms.

I.C. Literature review: physical metallurgy and mechanical properties

The main ingredients concerning precipitation have been explained in this previous part. The next point will be, to set the physical metallurgy basis for the plasticity mechanisms.

I.C.1. Introduction

The first deformation stage is elasticity, which refers to linear and reversible deformation; the second one is plasticity, which corresponds to an (often) non-linear and irreversible deformation. On the macroscopic point of view, the yield stress corresponds to the limit between those two domains. Deforming plastically a material requires increasing the stress level above a threshold, referred as the yield stress. Various parameters define the elastic and plastic properties of a material: Young and Poisson modulus on one hand, yield strength, ultimate tensile strength and elongation at fracture on the other hand (among others). The origin of those macroscopic measurements has to be found on the micro- and nanoscopic scale: "the stress-strain curve is the macroscopic expression of the microscopic processes going on in the crystal" [Brown 1955].

I.C.2. Elasticity

The interatomic distance (see Fig. I.22), which depends on the interaction forces between the atoms, is affected by temperature and external load. Applying a tensile stress will elongate the part in the longitudinal axis. Moreover the deformation is proportional to the stress. The proportionality coefficient is the Young modulus, and the ratio between longitudinal and transverse deformation is the Poisson modulus. The effect of temperature, called thermal dilatation, will change the Young modulus, as it can be noted on Fig. I.23. The thermomechanical processing may also modify the elastic properties. In particular, an anisotropic texture will involve anisotropic mechanical properties [Augereau 2007].

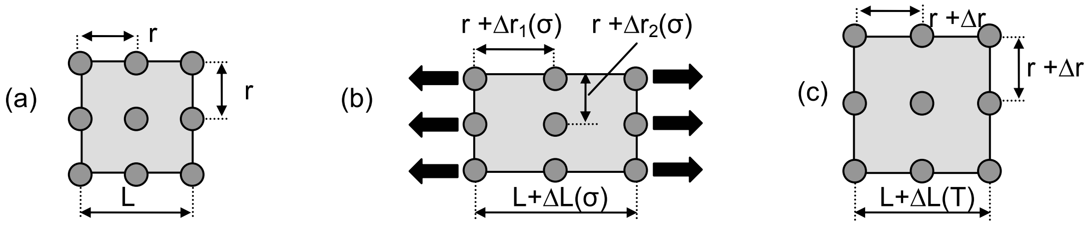

Fig. I.22. Schematic of the effect of temperature and elastic stress on inter-atomic distance

The lattice is supposed to be cubic. Case (a) is the stress-free material at 0 K; case (b) shows the effect of external loading (black arrows) (including Poisson effect) and case (c) the effect of temperature. Interatomic distance change (Δr) involves macroscopic elongation (ΔL).

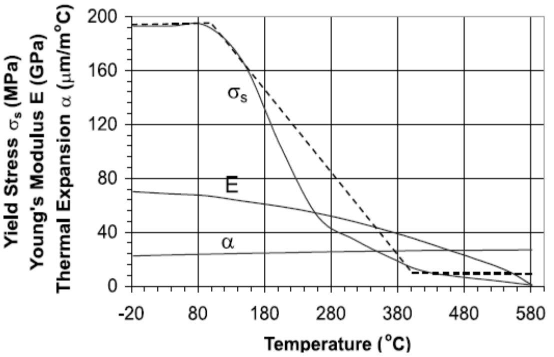

Fig. I.23. Effect of temperature on Young modulus and thermal expansion of an AA5xxx

[Zhu 2002] E is the Young modulus, α is the thermal expansion coefficient and σ_s the yield stress

I.C.3. Plasticity

I.C.3.a. Introduction

As soon as the applied stress becomes larger than the yield stress, dislocation motion and multiplication occur and the material deforms plastically. "Yield stress and work hardening can be explained by using the concept of dislocations, which are crystalline imperfections on an atomic scale" [Brown 1955]. Work hardening corresponds to an increased resistance to dislocation motion following a plastic deformation. It is caused by secondary dislocations intersecting the slip planes which multiply during plastic deformation and increase the slip resistance [Evers 2002]. Among the obstacles to dislocations motion, there are forest dislocations, solute atoms, precipitates, grain and sub-grain boundaries.

The total dislocation density directly affects the flow stress magnitude through the Taylor law. On the one hand dislocations multiply (Frank-Read mechanism, dislocation storage); on the other hand they annihilate (dynamic recovery). The competition between those two mechanisms determines the dislocation density evolution and therefore the overall strain hardening (or the contrary: softening).

I.C.3.b. Dislocations

i. Definition

Taylor in 1934 [Taylor 1934a] already introduced the concept of dislocations, in order to explain plastic deformation in metals: "The slipping is considered to occur not simultaneously over all atoms in the slip plane but over a limited region […] a dislocation, as we may call it". A dislocation is a linear defect which can be seen as a missing half plane in the lattice (see Fig. I.24). Its Burgers vector ($\vec{b}$) defines the vector necessary to "close" a perfect loop around the dislocation. When $\vec{b}$ is parallel to the dislocation line, the dislocation is "screw", "edge" when it is normal and "mixed" otherwise.

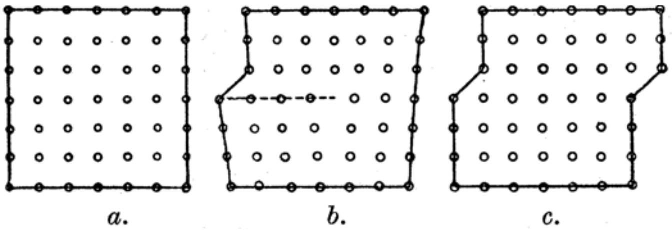

Fig. I.24. Plane slip explained by dislocation

[Taylor 1934a] (a) Perfect crystal. (b) Dislocation swepting the lattice from the left to the right. (c) The block after the unit slip or "dislocation".

ii. Dislocation sources

A first source of dislocations is the quench, which generates vacancy prismatic loops (see I.B.3.b.iii). A second source is the dislocations present at grain boundaries or precipitates for lattice accommodation (see iv). Nevertheless, if those dislocations are already present before any deformation has occurred, this does not explain strain hardening. It is therefore necessary to have multiplication mechanisms by which the few dislocations present in the annealed crystal can produce many thousands of others [Brown 1955]. This mechanism, explained by Frank and Read in 1950, is known as the "Frank-Read mill" [Friedel 1964]. The principle is the following: "a dislocation line anchored at two points inside the crystal will continuously generate closed loops of dislocation as long as the applied stress is maintained" [Forty 1954]. The stress required to activate the source is inversely proportional to the distance between the two pinning points [Benzerga 2004]. For instance a 12 MPa stress is necessary to activate a source where the pinning points are separated by 1 µm, which corresponds to the yield stress of a pure and annealed copper single-crystal [Philibert 1998].

iii. Dislocation motion

Both stress and thermal activation allow the dislocation to move, which is first limited by the matrix lattice resistance itself. Dislocation slip is energetically favoured on the denser lattice planes and in the denser atomic directions. Therefore in f.c.c. systems the main glide planes are the (111) planes and the glide direction is the <110> direction [Arsenlis 1999]. All dislocations in parallel glide planes and with parallel Burgers vector are referred to as a glide system [Ortiz 1982]. Two types of dislocation motion exist: dislocation glide and dislocation climb. At low temperature dislocation glide is favoured, while at higher temperature edge dislocations may climb (see for instance [Lagowa 2001]).

iv. Dislocation storage

A distinction can be made between mobile and forest dislocations. Forest dislocations, which are supposed to be immobile, generally tend to gather in cell walls. Mobile dislocations are generated by the Frank-Read mechanism and glide in the (111) slip planes. They may annihilate with each other (dynamic recovery) or with forest dislocations, and cause softening, or be pinned by forest dislocations or other obstacles, generating hardening.

Ashby [Ashby 1970] distinguishes statistically stored dislocations (SSD), accumulating during a uniform deformation, and geometrically necessary dislocations (GND), which are required to preserve lattice compatibility in the case of non-uniform plastic deformation, such as in the presence of lattice curvature [Gao 2003], grain boundaries [Déprés 2004] or precipitates [Fleck 2003]. Fig. I.25 shows the justification of GNDs, as proposed by Ashby, in the case of deformation in a polycrystal. The same mechanism happens in the case of precipitates.

The consequence is the presence of a dislocation density gradient in the grain: a high dislocation density near to the grain boundaries (GNDs) and less in the centre. This gradient effect is exploited in strain gradient plasticity theories [Gao 1999, Kubin 2003].

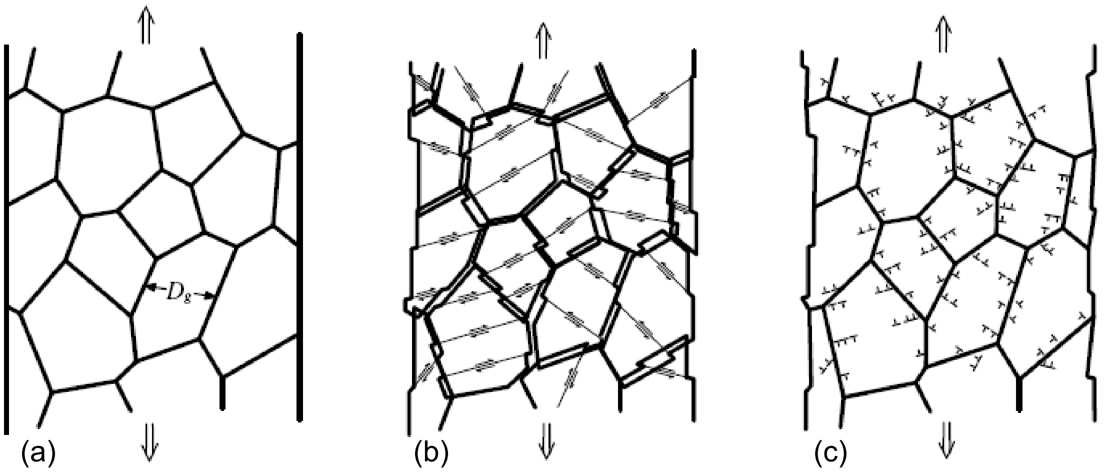

Fig. I.25. Schematic of GNDs in a polycrystal

[Déprés 2004] (a) Non-deformed polycrystal. (b) Independent deformation of the polycrystal grains. (c) Geometrical compatibility restored by the presence of GNDs.

v. Dislocation annihilation

Dislocations annihilate when the distance between two dislocations of opposite Burgers vectors is less than a critical distance. The main annihilation mechanism is dynamic recovery of screw dislocations through cross slip, but climb annihilation also happens for edge dislocations. Those two mechanisms are thermally activated mechanisms, as temperature favours the mobility of the dislocations out of their natural glide plane.

Another effect that can cause dislocation annihilation is a change in the strain path: in case of a reversible slip of dislocations on the same glide plane, changing the load direction will allow the annihilation of the stored dislocation by the moving dislocations: this reverse Orowan mechanism will cause the Bauschinger effect (see chapter III).

I.C.3.c. Strengthening: generalities

i. Obstacle to dislocation motion

Any obstacle met by a dislocation will oppose a force to the dislocation motion and therefore increase flow stress (Fig. I.26). This force varies with the obstacle type and with the distance from the mobile dislocation to the obstacle. For instance a (forest) screw dislocation generates a stress field in the form:

$$\text{(II.2.)}\quad \tau(r) = k\frac{\mu b}{2\pi r}$$

Where r is the distance to the dislocation core. The force applied on the mobile dislocation to bypass an obstacle has to overcome the lattice friction and the obstacle force itself (see Fig. I.26.b).

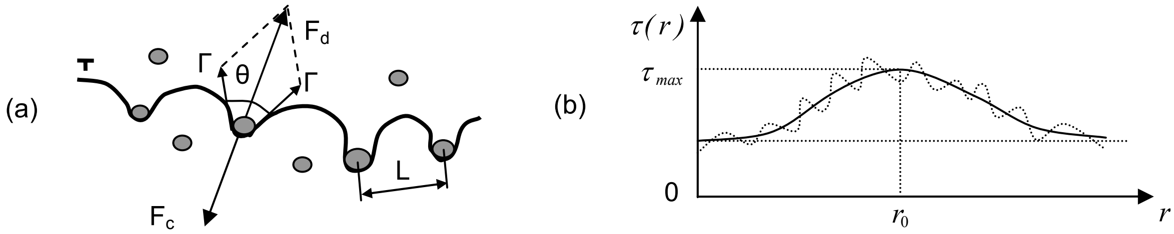

Fig. I.26. Schematic of the obstacle force

From [Embury 1989] (a) Dislocation line is represented by the symbol “T”. (b) Evolution of the obstacle stress with dislocation displacement. r_0 is the obstacle core, τ_{LF} is the lattice friction stress and τ_{max} is the stress value required to bypass the obstacle. Dashed line is the effect of short-range interaction obstacles (see I.C.3.c.ii).

On Fig. I.26.a, equilibrium between the obstacle force F_c and dislocation force F_d can be written as:

$$\text{(II.3.)}\quad F_d = F_c = 2.\Gamma.cos(\theta/2)$$

θ is the angle of the tangents to the dislocation lines at the obstacle and Γ the dislocation line tension:

$$\text{(II.4.)}\quad \Gamma = (1/2).\mu.b^2$$

Where b is the Burgers vector value and μ the shear modulus. The shear stress required to overcome an obstacle of force F_c is in the form:

$$\text{(II.5.)}\quad \Delta\tau = \frac{F_c}{b.L} = \frac{2.\Gamma.cos(\theta/2)}{b.L} = \frac{\mu.b.cos(\theta/2)}{L}$$

The determination of L, known as the Friedel length, is by no way a trivial question: L depends both on the inter-precipitates distance, their strength and the dislocation stiffness.

The higher is the critical θ_{max} value to overcome the obstacle (see Fig. I.26.b), the stronger is the obstacle. Their contribution to yield stress depends on their density and force. Among the obstacles to dislocation motion, one can list solute atoms, precipitates, grain boundaries and the matrix lattice itself.

ii. Thermal activation of obstacle bypassing

Fig. I.26 corresponds to the force required to bypass an obstacle having a long-range interactions with the dislocation. On a closer scale, some obstacles may have short-range interactions and may be bypassed by thermal activation [Rauch 1993], whose effect is presented in Fig. I.27, where:

$$\text{(II.6.)}\quad \tau = \tau_\mu + \tau_{eff}$$

In this equation, τ_μ is the athermal stress, which approximately corresponds to the stress at high temperature. After this limit, yield stress only varies with shear modulus μ. τ_{eff} is the effective stress, which is temperature- (and strain rate-) dependent. Decreasing the temperature increases τ_{eff} and therefore increase the flow stress, which is maximum at $T = 0K$. Λ is characteristic of the obstacle size, but depends on the temperature.

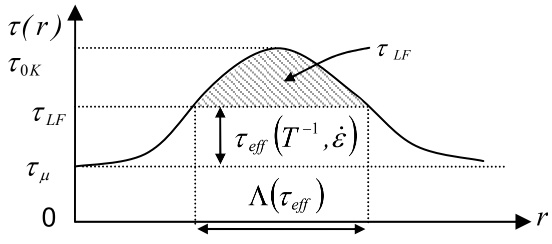

Fig. I.27. Thermal activation of obstacle bypassing

The area under the curve corresponds to the energy required to bypass the obstacle

Strain rate and temperature have an inverse effect: increasing the strain rate leaves less time to dislocations to overcome obstacles: the effective stress increases. This will be developed in chapter III.

iii. From local to macroscopic stress

The extension of the critical resolved shear stress τ to macroscopic stress σ for multiple slip systems and polycrystalline materials is obtained by using the Taylor factor M:

(II.7.) $\sigma = M.\tau$

This factor takes into account the texture and the tensile axis orientation as a function of the grain orientation. As reported by Starink [Starink 2003b], for texture free fcc metals the Taylor model (five active slip systems) predicts $M = 3.07$. Hutchinson model (3.5 active systems) calculates $M = 2.6$. This value is classically chosen between 2 and 4. After EBSD measurements on industrially rolled 7xxx alloys, Starink calculated a Taylor factor of $M \approx 2.7$ for the L direction.

iv. Contributions to strengthening

One can divide strengthening contributions into 3 groups: first the dislocations; then the structural contributions, which might be seen as deformation independent: lattice friction and Hall-Petch effect; then the chemical contributions, related to precipitation: solute atoms and precipitates.

I.C.3.d. Strengthening effects: dislocations contribution

On the overall material, the shear stress is related to the dislocation density through the Taylor hardening law [Taylor 1934a, b], where $\alpha \approx 0.3$:

(II.8.) $\tau_\rho = \alpha \mu b \sqrt{\rho}$

This relation is the basis of the Kocks and Mecking strain hardening models [Mecking 1981, Kocks 2003] and used in most of the plasticity models used nowadays (see among others [Nes 1995, Estrin 1999, Deschamps 1999b, Simar 2008].

I.C.3.e. Strengthening effects: structural contributions

i. Lattice friction

The first limit to dislocation motion is the matrix lattice itself, which generates a friction stress on the dislocation, called Peirls-Nobarro stress [Peierls 1940, Nabarro 1947]. If υ is the Poisson's ratio and $W = a/(1-\upsilon)$ the dislocation width, a and b being the lattice parameters, for an edge dislocation:

(II.9.) $$\tau_{LF} = \frac{2\mu}{1-\upsilon} exp\left(\frac{-2\pi W}{b}\right)$$

The Peirls stress is independent of the deformation [Estrin 1996] and only accounts in aluminium alloys for a very small part of the yield stress (less than 1 MPa).

ii. Grain boundaries

Grain boundaries represent strong obstacles that limit dislocation motion and generate hardening. Hall in 1951 and Petch in 1953 showed that the grain boundary contribution σ_{GB} is related to the grain size (d) throughout an empirical relation, known as the Hall-Petch relation:

(II.10.) $$\sigma_{GB} = k.d^{-n}$$

According to [Saada 2005], $k \approx 0.05\mu\sqrt{b}$ in fcc materials. Various theories [Evers 2002] try to explain this well established law but no clear experimental evidence has been able to support either of them. One of them is that larger grains are able to store more dislocations, and the generated pile-up causes stress concentration, able to activate Frank-Read sources in neighbour grains. The consequence is that the force required to extend deformation to neighbour grains is lower in larger than in smaller grains materials. In reality the grain size does not affects the "true" yield stress (σ_{Y0}) but the flow stress during deformation, as shown for instance in [Nes 2006]. In other words: $\sigma_{GB}(\varepsilon) = k(\varepsilon)/\sqrt{d}$.

As reported by Evers, the exponent n varies in the literature from 0.3 to 1, but the most common value is 0.5, which corresponds to the traditional Hall-Petch relation. According to Nes [Nes 2006], this relation is valid in the case of grains with high angle grain boundaries and the exponent changes to 1 for ultra-fine grains with low angle boundaries[4]. In our case, where the typical grain size is about 50 µm and the sub-grain size about 5 µm, the traditional Hall-Petch relation is expected. Starink [Starink 2003b] proposes a more explicit relation for strengthening due to sub-grain boundaries, predominant in 7xxx alloys (δ is the sub-grain size, $f_{Re\,X}$ the recrystallised grain fraction, $\alpha_2 \approx 2$).

(II.11.) $$\sigma_{GB} = \alpha_2 \mu b \left(1 - f_{Re\,X}\right)\delta^{-1}$$

The presence of dispersoïds prevents as much as possible grain recrystallisation (see I.B.1.a and I.B.3.c), and allows controlling the grain size. If this strengthening effect is exploited in the case of 1xxx or solution hardened (3xxx, 5xxx) alloys, this is less the case in age-hardenable alloys (2xxx, 6xxx, 7xxx), where the main contribution to hardening comes from the precipitates.

iii. Summary

Various authors gather lattice friction and grain size contribution in a single term: σ_0 , often seen as a deformation independent term. A typical value in aluminium alloys is 10 MPa (7 MPa in [Starink 2003b]; 10 MPa in [Deschamps 1999b].

I.C.3.f. Strengthening effects: chemical contributions

i. Solid solution

7xxx series alloys are mainly hardened by precipitates, contrarily to 3xxx and 5xxx alloys which are solution strengthened [Zhu 2008]. Solid solution only accounts for a few tens MPa, depending on the temper. Solute elements located either in the substitution or the insertion sites of the matrix lattice generate a stress field and contribute therefore to strengthening. Three effects can be listed: size, modulus and short range order effect [Starink 1999], both dependent of the solute concentration c .

---

[4] For very small grains, an inverse effect has been shown, σ diminishing with grain size, probably due to diffusional effects (see chapter V).

The first solution strengthening effect is called size effect and accounts for the atomic misfit with the matrix η (a is the lattice parameter). It is effective only for edge dislocations [Philibert 1998]:

$$\text{(II.12.)} \quad \sigma_{ss1} = 2^{1/3}\mu\left(\eta/10\right)^{4/3} c^{2/3}$$

$$\text{(II.13.)} \quad \eta = \frac{\Delta V}{V} = \frac{2}{a}\frac{da}{dc}$$

The second effect is the modulus effect, effective for the two dislocation types:

$$\text{(II.14.)} \quad \sigma_{ss2} = 2^{1/3}\mu\left(\frac{1}{32\pi^2}\frac{\varepsilon}{1+\varepsilon/2}\right)^{4/3} c^{2/3}$$

$$\text{(II.15.)} \quad \varepsilon = \frac{1}{\mu}\frac{d\mu}{dc}$$

A third effect, strengthening due to short-range order of dissolved atoms is given by [Starink 1999]:

$$\text{(II.16.)} \quad \sigma_{ss3} = \frac{c(1-c)}{3b^3}A$$

The addition law of those contributions i for several solute elements X would be [Philibert 1998]:

$$\text{(II.17.)} \quad \sigma_{ss} = \left(\sum_{i,X}\left(\sigma_{ssi}\big|_X^{3/2}\right)\right)^{2/3}$$

A more simple way to calculate it would be to use this formula [Deschamps 2003a, Starink 2005b], even if some authors also propose an exponent equal to 1 or $1/2$ [Zhu 2008]:

$$\text{(II.18.)} \quad \sigma_{ss} = \sum_i\left(k_i C_i^{2/3}\right)$$

Deschamps [Deschamps 2003a] proposes $k_{Mg} = 1600\,MPa$ and $k_{Zn} = 900\,MPa$ (7xxx aluminium alloys). In [Deschamps 1999b], a global average parameter is used: $\sigma_{ss} = KC^{2/3}$ with $K = 840\,MPa$.

ii. Precipitates

Precipitate hardening is the predominant contribution to hardening in high strength aluminium alloys and requires special attention. The various precipitate/matrix interfaces imply different dislocation/precipitate interactions: the precipitates are either sheared or bypassed (Orowan mechanism or cross-slip) by dislocations (see Fig. I.28 or for instance [Delmas 2003]).

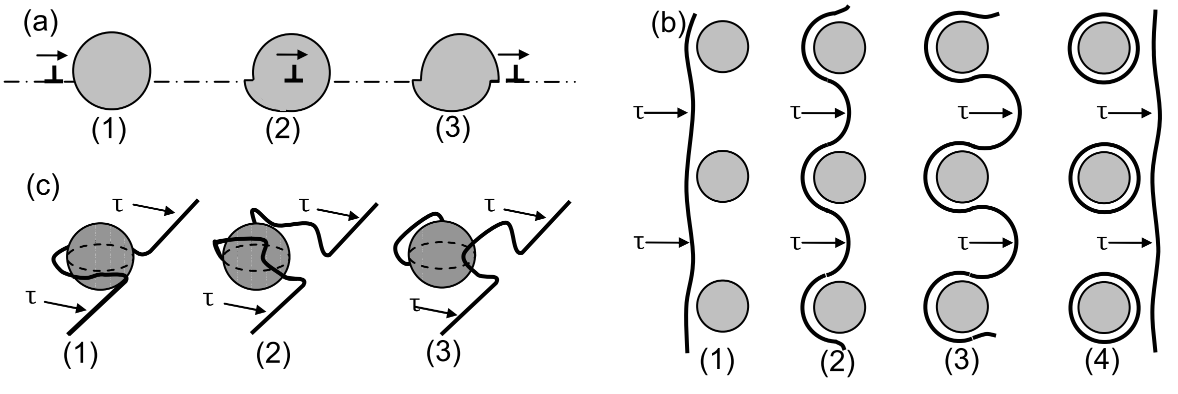

Fig. I.28. Schematic of the precipitate-dislocation possible interactions

(a) Precipitate shearing. The precipitate is stepped at the end. (b) Non-shearable precipitates bypassed by a dislocation. An Orowan loop is stored around the precipitate at the end. (c) Precipitate bypassed by cross-slip mechanism. A dislocation loop is stored in front of the precipitate.

Several strengthening mechanisms may be considered for the precipitates: chemical effect, modulus strengthening, coherency strengthening, order strengthening, dispersion strengthening and stacking fault strengthening [Deschamps 1997, Starink 1999].

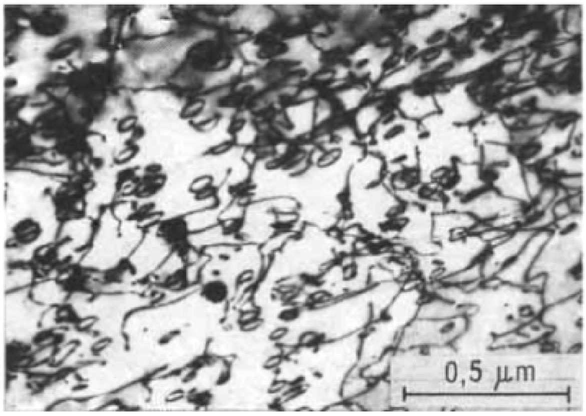

Fig. I.29. Orowan loops around non-shearable precipitates

[Dubost 1991] TEM micrograph of δ' Al_3Li precipitates

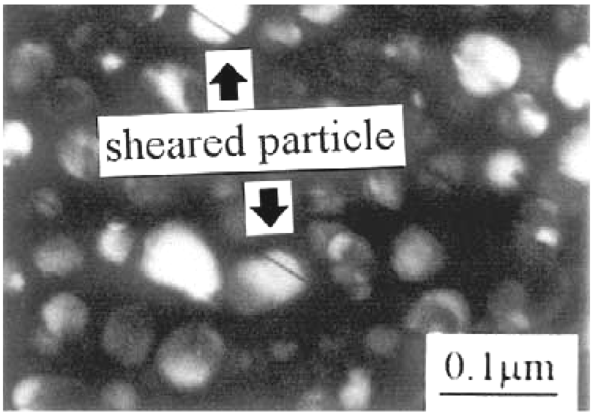

Fig. I.30. Sheared precipitates

[Zhen 2002] TEM micrograph of δ' Al_3Li precipitates

- Precipitate shearing

Coherent precipitates are sheared by the dislocations, as the lattice compatibility allows slip towards the precipitate; one speaks from shearable precipitates. The various effects listed above are often summarized in a single term [Deschamps 1997]:

$$\text{(II.19.)} \quad \tau = 0.7\alpha^{3/2}\mu\sqrt{\frac{Rf_v}{b}}$$

Starink [Starink 1999] uses a first expression for the shearable ordered precipitates, and a second one for the (non-ordered) GP zones, taking into account their modulus strengthening effect:

$$\text{(II.20.)} \quad \tau_{order} = \frac{\gamma_{apb}}{2b}\sqrt{\frac{3\pi^2\gamma_{apb}Rf_v}{32\Gamma}}$$

$$\text{(II.21.)} \quad \tau_{mod} = \frac{\Delta\mu}{4\pi\sqrt{2}}\sqrt{f_v}$$

Where γ_{apb} is the antiphase boundary energy on the glide plane, Γ the line tension and $\Delta\mu$ the difference in shear modulus between the matrix μ_{Al} and the GP zones μ_{GP}, taken as the mean value of the moduli of Magnesium and Zinc.

- Orowan strengthening

Incoherent precipitates are bypassed, either by Orowan mechanism (low temperature) of by cross-slip. Those strong obstacles are called non-shearable precipitates. In Orowan mechanism, dislocation loops are left around non-shearable precipitates (see Fig. I.28.b). The shear stress necessary to form a dislocation loop of radius r is equal to:

$$\text{(II.22.)} \quad \tau = \frac{\mu b}{2}\frac{1}{r}$$

As the critical configuration corresponds to a distance between precipitates of $L = 2r$, the shear stress necessary to form dislocation loop is equal to:

$$\text{(II.23.)} \quad \tau = \frac{\mu b}{L}$$

The interprecipitate distance L is linked to the precipitate radius R and the volume fraction f_v by:

(II.24.) $$L^2 = \frac{2\pi R^2}{3}\frac{1}{f_v}$$

Finally, shear stress becomes (other expressions in [Starink 1999, Muñoz 2008, Deschamps 1997]):

(II.25.) $$\tau_{P.Orowan} = \mu b \frac{\sqrt{\pi}}{2}\frac{\sqrt{f_v}}{R}$$

iii. Taking into account microstructural evolution during heat treatment

Solid solution concentration varies during age-hardening treatment: from full nominal concentration (maximum supersaturation) after quench to equilibrium concentration for the over-aged tempers. Simultaneously, the precipitates evolve during ageing heat treatment: for instance their size, volume fraction and coherency changes and the strengthening effect evolves, as well as the storage capability. Therefore, a quantitative study of the microstructure evolution is required, in order to model the evolution of strengthening.

Schematic evolution of yield stress during ageing has already been shown in I.B.1.b. This typical ageing curve is due to the transition in the precipitate-dislocation interactions. Depending on the precipitate size the mechanism leading to the smallest flow stress will be observed in Fig. I.31.

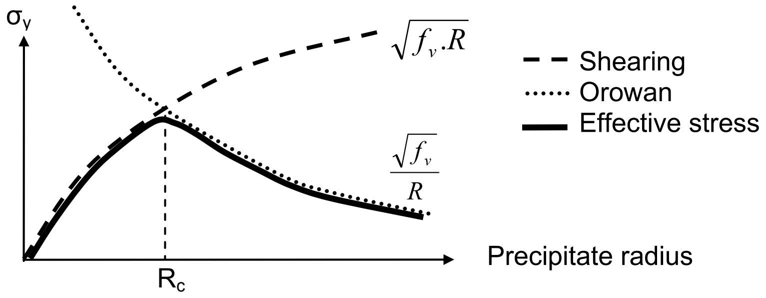

Fig. I.31. Schematic of the shearing/by-passing transition

According to the calculation presented in I.C.3.f, the shearing/Orowan transition happens for a radius R_c, which corresponds to a maximum reachable stress $\sigma_{P\,max}$ of [Deschamps 1999a]:

(II.26.) $$R_c = 0.9\frac{b}{\alpha}$$

(II.27.) $$\sigma_{P\,max} \approx 0.66\alpha\mu\sqrt{f_v}$$

I.C.3.g. Strengthening effects: addition

The addition of the contributions of the different work hardening sources listed above gives the overall work hardening of the material. The addition law depends on the interactions between the different obstacles, as proposed by Kocks, Argon and Ashby [Kocks 1975]. For instance the contributions of two obstacle types with very different densities and with different obstacle force will be added linearly:

(II.28.) $$\sigma = \sum_i \sigma_i$$

The same law is used for obstacles of the same density and same force. A quadratic law ($n = 2$) is used to add the contributions of obstacles with the same force but different densities:

(II.29.) $$\sigma = \left(\sum_i \sigma_i^{\,n}\right)^{1/n}$$

For instance Starink [Starink 2003b] proposed a yield stress model:

(II.30.) $$\sigma_y = \sigma_{GB} + M\left(\tau_{LF} + \tau_{SS} + \tau_{\rho\&P}\right)$$

Deschamps [Deschamps 1999b] used the following model (with $\sigma_0 = \sigma_{LF} + \sigma_{GB}$):

$$\text{(II.31.)} \quad \sigma = \sigma_0 + \sigma_{SS} + \sqrt{\sigma_\rho^{\ 2} + \sigma_P^{\ 2}}$$

I.C.3.h. Strain hardening

Strain hardening (or work hardening) corresponds to the flow stress increase required to deform the material plastically. This depends on the ability of the mobile dislocations to move in the material. In other words it is related to the obstacles density and force and to the dislocation density: it is microstructure dependent. A common way to represent strain hardening is to plot a θ vs. σ graph, where $\theta = \partial\sigma/\partial\varepsilon$ is the macroscopic hardening rate [Kocks 2003].

i. Single-crystal

If one considers the deformation of a single-crystal, the microscopic strain hardening curve $\theta = \partial\tau/\partial\gamma = f(\tau)$ (Fig. I.32) can be divided into 4 stages (listed from I to IV), corresponding to changes in the microscopic mechanisms (see Fig. I.34) [Kocks 2003].

The first stage or “easy glide” corresponds to slight linear hardening. The average value of the normalized hardening rate for c.f.c crystals is in the order of $\theta_I / \mu = 10^{-4}$. Deformation is usually smaller than 0.05 in aluminium alloys [Chenal 1999]. Dislocations glide easily on the slip planes: only one system is activated and simple glide happens.

The second stage corresponds to strong linear strain hardening. This hardening is temperature independent and $\theta_{II} / \mu = 2.10^{-3}$ to 5.10^{-3}. At this stage, the high number of dislocation steps has caused crystal rotation, and a second slip system is activated. Dislocation multiply, glide on their slip planes and the dislocations of the different slip systems interfere and cause forest hardening.

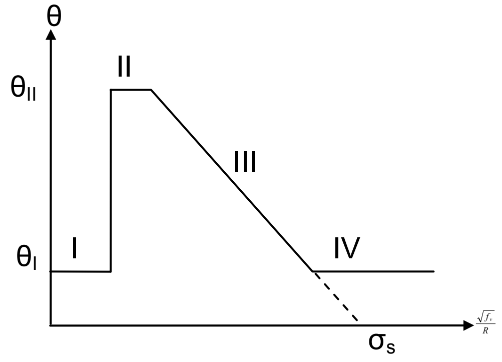

Fig. I.32. Schematic hardening curve of a single-crystal

[Philibert 1998]

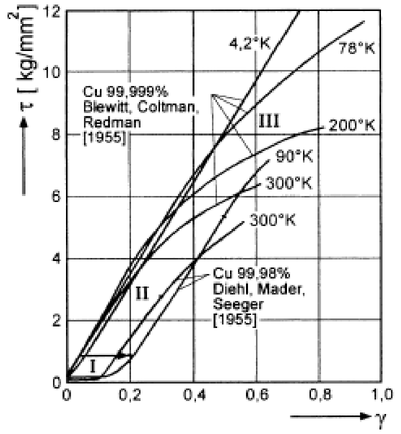

Fig. I.33. Shear stress versus shear strain curves of copper single crystals

[Kocks 2003] orientation near (100)] of 99.999% copper at various low temperatures and for a single-slip orientation

Stage III is called parabolic hardening stage. The high dislocation density causes local dislocation pile-ups therefore local high internal stress level [Zaiser 1998]. To relieve this stress, dislocation cross slip happens, which can result in mutual annihilation, called dynamic recovery. Macroscopically, this means that the strain hardening rate diminishes. This stage is very sensitive to temperature, strain rate and stacking fault energy. For instance decreasing the temperature (see Fig. I.33) will decrease the dislocation mobility and therefore decrease the recovery rate and increase the storage rate.

Stage IV corresponds to slight linear hardening, of the same order of magnitude as stage I. This very large deformation stage is not well understood, a high number of phenomena happening at this time.

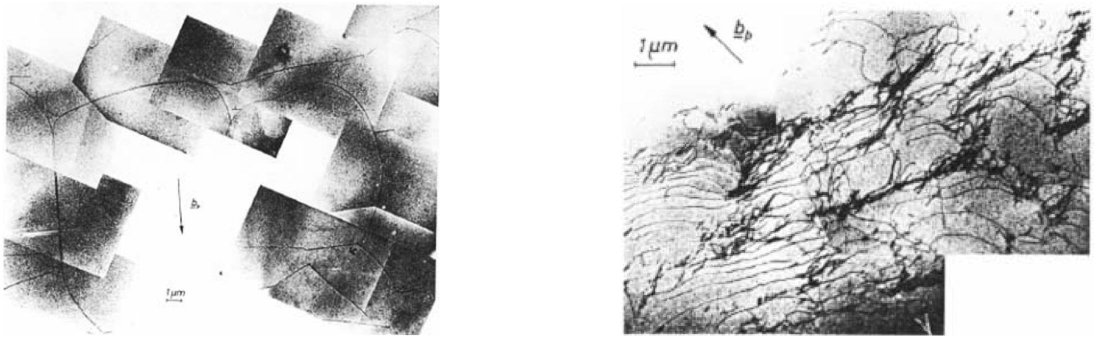

Fig. I.34. Dislocation structure observed in a copper single-crystal

[Mughrabi 1975] (111) TEM sections, T=78K. (a) Hardening stage I, shear stress=0.11MPa. (b) Stage II, 1.2MPa.

ii. Polycrystal

The requirement of grain compatible deformation (see Fig. I.25) involves the activation of different slip systems for each grain, as proposed by Taylor [Taylor 1934a]. The consequence is that forest dislocations are present at the beginning of the deformation, and stage I does not exist: stage II is the first hardening stage for polycrystals. Then, polycrystals behave similarly to single-crystals, and hardening rate is $\Theta_{II} = \partial\sigma/\partial\varepsilon \approx E/50$ [Mecking 2003].

iii. Introduction to kinematic hardening

The strain hardening related to the storage of dislocations, isotropic strain hardening, normally gives a flow stress independent of strain path. Kinematic hardening, on the other hand, is controlled by the introduction of internal stresses in the material σ_i, which are long range and polarised. These internal stresses result from incompatibilities between the deformations of different microstructural objects.

In most materials, both hardening types have to be taken into account. Therefore, developing a plasticity model taking into account a change in the strain path means considering:

$$\text{(II.32.)} \quad \sigma = f(\sigma_{iso}, \sigma_{kin})$$

Where σ_{iso} and σ_{kin} respectively refer to the isotropic and kinematic contributions to strain hardening. The different microstructural features listed in chapter I (dislocations, grain boundaries, solute atoms and precipitates), induce a number of different strengthening mechanisms, all of them contributing differently both to isotropic and kinematic hardening.

iv. Modelling strain hardening

“Dislocations and their interactions with other microstructural features, such as impurity atoms, precipitates, dispersoïds, dislocations, and grain boundaries must be incorporated into the constitutive relationships that describe plastic deformation of metallic systems […] Using the key mechanisms as input to macroscale plasticity models, it is possible to develop models capable of predicting the macroscopic response.” [Robertson 2005].

To model yield stress, the first objective is to identify the key microstructural mechanisms (see Fig. I.35). Then, one has to express them mathematically and find a combination able to describe the macroscopic mechanical behaviour of the materials. Modelling work hardening requires calculating the evolution of the dislocation density with strain: $\partial\rho/\partial\gamma$. The microstructure has to be taken into account, as it affects the storage ($\partial\rho^+$) vs. recovery ($\partial\rho^-$) competition. The general form of the dislocation density evolution is given by:

$$\text{(II.33.)} \quad \frac{\partial\rho}{\partial\gamma} = \left.\frac{\partial\rho}{\partial\gamma}\right|^{+} - \left.\frac{\partial\rho}{\partial\gamma}\right|^{-}$$

I.D. Conclusion

The precipitation and plasticity mechanisms that have been presented extensively in this chapter are the main ingredients that will be used in the next chapters for the analysis, understanding and modelling of the experimental results. They can be schematically summarized in a single figure, as proposed in Fig. I.35.

Grain “0” lists the various precipitation features: solute atoms, shearable and non-shearable precipitates, as well as heterogeneous precipitation (grain boundaries, dispersoïds, dislocations). Grains “1” and “2” describe source activation and dislocation generation. Grain “3” lists the main strain hardening mechanisms: dislocations storage, grain boundary storage, solute atoms storage, precipitate shearing and precipitate by-passing. Grain “4” shows dynamic recovery (dislocation annihilation). The integration of those various microstructural mechanisms into a strain hardening model will be done in chapter III.

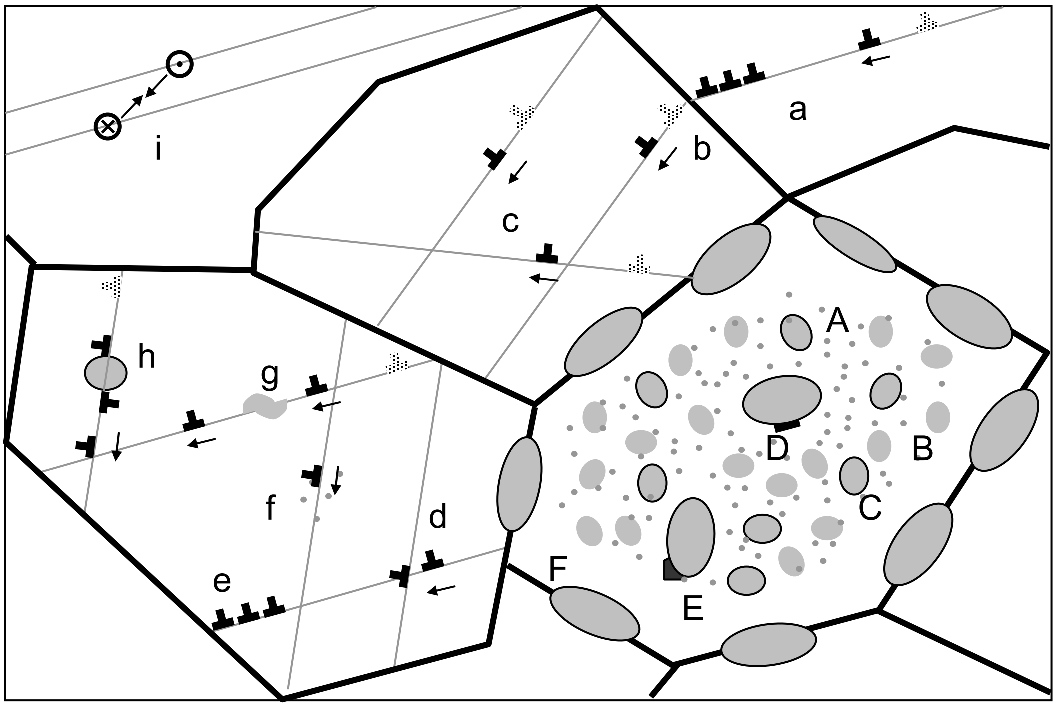

Fig. I.35. Summary: schematic of the precipitation and plasticity mechanisms

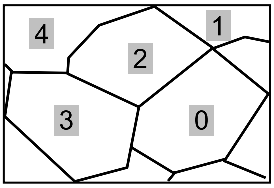

Grain #0 represents the precipitation microstructure. (A): solute atoms. (B): shearable precipitates. C: Non-shearable precipitates. Coarse precipitate on a (D) dislocation, on a (E) dispersoïd, on a (F) grain boundary.

Grains #1 to #4 show the dislocation/microstructure interactions. (a) Dislocation pile-up in grain #1 activates a source (b) in grain #2, where different slip systems are already active (c). Grain #3 shows strengthening by (d) dislocation, (e) grain boundary, (f) solute atoms, (g) shearable precipitates and (h) non-shearable precipitates. Grain #4 shows dynamic annihilation by cross-slip (i).

Chapter II. Material and experimental methods

Summary

This chapter first introduces the studied AA7449 material. It then presents the main experimental techniques used in this work, to characterise both the microstructure and the mechanical properties of the alloy.

Some of these techniques (Microhardness, tensile and Bauschinger tests for mechanical properties characterization; optical and electronic microscopy for microstructural characterisation) are widely spread and commonly used in the material science community. Some others, such as or SAXS (Small-Angle X-Ray Scattering), are less common, are require special attention.

In the scope of this PhD, experimental development has been required in order to measure more complex features. First, an inverse tensile device has been designed in order to be able to measure mechanical properties at low temperature. Secondly, a micro-tensile device for in situ SAXS measurements has been developed in order to measure precipitation kinetics during thermomechanical treatments. Both are presented in the last section of this chapter.

Outline

II.A. Material and heat treatments

AA7449 is an age-hardenable aluminium alloy, which belongs to the 7xxx aluminium alloys series, composed of all the Al-Zn-Mg-(Cu) alloys. These materials are wrought alloys, which means that they are heavily deformed during their processing. They are hardened by ageing heat treatments, which give them their final microstructure and properties.

II.A.1. Material

II.A.1.a. Material composition

This high strength alloy contains a large amount of solute elements (more than 12% in weight), which contribute to its high mechanical performance. As it is often the case in precipitation hardened alloys, smaller atoms (Mg) are associated to larger atoms (Zn, Cu) to minimize lattice distortion in the matrix, which tends to favour precipitate nucleation.

Element	Al	Zn	Mg	Cu	Zr	Fe	Ti	Si
Weight % composition	87.3	8.3	2.2	1.9	0.10	0.07	0.04	0.02
Atomic fraction (%)	92.8	3.7	2.6	0.85	0.03	0.04	0.02	0.02
Atomic mass (g/mol)	26.98	65.39	24.305	63.546	91.224	55.845	47.867	28.086
Atomic number	13	30	12	29	40	26	22	14

Table II.1. AA7449 composition and atomic number

Note: this composition is specific to the received plate.

The weight percent and atomic fraction in solute element A, respectively $[A]$ and X_A are defined as:

$$\text{(II.1.)}\quad [A] = \frac{m_A}{\sum_I m_I} = \frac{X_A M_A}{\sum_I X_I M_I}$$

$$\text{(II.2.)}\quad X_A = \frac{n_A}{\sum_I n_I} = \frac{[A]/M_A}{\sum_I ([I]/M_I)}$$

M_I, m_I and n_I are respectively the atomic mass, mass and molar number of the different species I.

II.A.1.b. T7651 heat treatment

The 76mm thick plates are solution heat treated above 470°C during a few hours. The solution treatment is followed by a fast aspersion quench and a 1.5 % to 3 % stretching operation, in order to flatten the plate and to reduce the internal stress level. Then, the plate is subjected to a natural aging treatment. The treatment leading to the final T7651 temper is a two steps over-aged heat treatment. It consists in a 6 hours plateau at 120°C followed by about 10 hours plateau at 160°C, the heating rates being respectively 15°C/h and 30°C/h.

II.A.1.c. Material properties

The main room temperature materials properties of our material are listed in Table II.2.

Those can be compared to the properties of another AA7449 material used by Kamp [Kamp 2002] (see Table II.3), where he studied the mechanical properties of various industrial AA7449 tempers. Yield stress and UTS decrease with over-aging whereas toughness increases, as expected (see chapter I). It can be noticed that these properties differ from the ones of our alloy, the composition being probably slightly different.

Property	Label	Value	Unit
Young modulus	E	72	GPa
Shear modulus	μ	27	GPa
Tensile yield stress along L (T7651)	σ_y	531	MPa
Ultimate tensile stress along L (T7651)	σ_{max}	565	MPa
Elongation at fracture (T7651)	ε_{max}	7	%
Toughness (CCT W400 B4.5) in L-T plane (T7651)	K_{app}	88	$MPa.m^{0.5}$
Density	ρ	2.86	$g.cm^{-3}$
Cell type	-	c.f.c	-
Lattice parameter	a	4.04	Å
Bürgers vector	b	2.86	Å

Table II.2. AA7449 main properties at room temperature

Specific properties of our alloy.

Heat treatment	σ_y (MPa)	σ_{max} (MPa)	K_{IC} ($MPa.m^{0.5}$)
T651	627	665	25.6
T7951	591	622	28.1
T7651	584	614	31.3

Table II.3. AA7449 mechanical properties at room temperature after various heat treatments

[Kamp 2002] Note: those properties correspond to a different base material (30 mm thick plates).

II.A.1.d. Granular microstructure

The rolling operation gives a texture to the material and elongates the grains in the L direction. Small ~5µm sub-grains are present in the material, but also recrystallised grains (see Fig. II.1), mostly present in the skins and core of the material. A small fraction of intermetallic particles can be found.

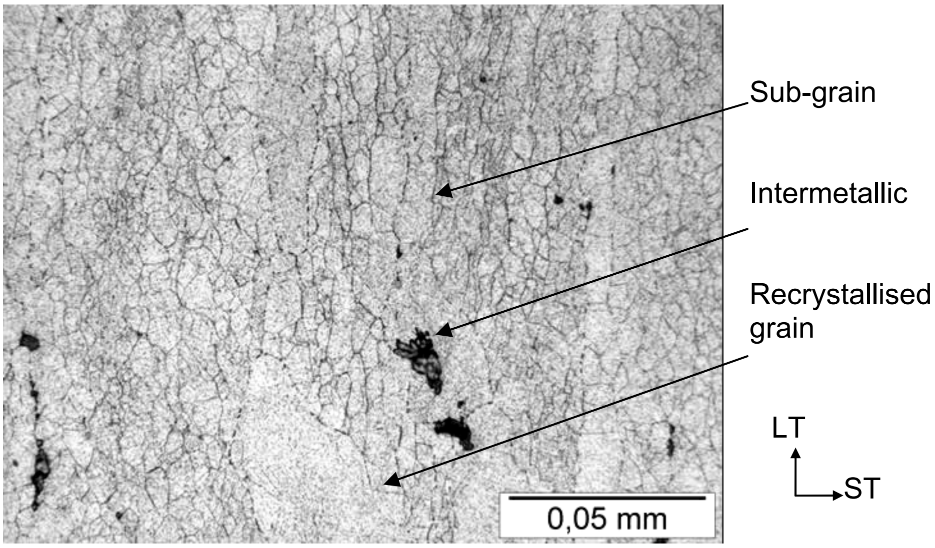

Fig. II.1. AA7449 T7651 grain microstructure

LT-ST plane. Optical micrograph after H_3PO_4 etching of our alloy.

II.A.2. Material preparation

II.A.2.a. Plate cuts

It has been decided to remove the skins and the core of the initial 76 mm thick plate, to avoid possible microstructural heterogeneities due to macro segregation effects (see II.A.1.d). Therefore every specimen[1] that has been used in the following experiments comes from one of the two resulting 25 mm thick plates shown in Fig. II.2.

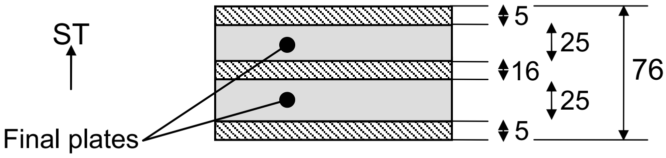

Fig. II.2. Plate cuts

II.A.2.b. Laboratory heat treatments

Some experiments have been made directly on the as-received T7651 temper material without any further heat treatment, but also a large number of experiments have required new aging heat treatments. These heat treatments (see figure II.3) resemble T7651 heat treatment, except in that they are performed on materials that has not been pre-stretched. The new heat treatment sequence will be called from now the standard aging heat treatment (SAHT).

The base material is first solution heat treated at 474°C during 6 hours. At this stage the dislocation structure is recovered and all the precipitates are dissolved. Then it is quenched into cold water and submitted to natural aging during 4 days. Finally the material is artificially aged at 120°C and 160°C: a first heating ramp (30°C/h) from room temperature to 120°C, a 6 hours plateau and a second heating ramp at 15°C/h up to 160°C.

A wide range of tempers obtained for various SAHT durations has been investigated: from under-aged materials to highly over-aged materials (the heat treatment at 160°C has been extended up to 1000 hours). In the following, the duration indicated for the different tempers represents the total duration of the artificial aging stage.

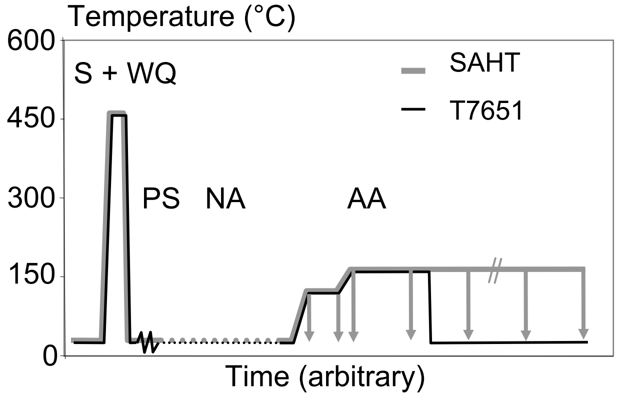

Fig. II.3. T7651 treatment vs. SAHT

Arrows indicate the interruption of the SAHT (examples)

---

[1] Except for one sample which has been used to characterise the plate anisotropy in the ST direction

II.B. Standard experimental techniques

II.B.1. Microstructural characterization

II.B.1.a. Optical microscopy

i. Objectives

An optical microscope has been used to characterize the granular microstructure (grains, sub-grains, large particles), as well as looking at the deformation structure (deformation bands).

ii. Device

The device is an optical Olympus BX60M microscope coupled with a digital Olympus camera, which can be used with different filters, polarisers and analyzers.

iii. Samples

The specimens preparation procedure was the following: the samples were mechanically polished up to grade 1200 with SiC paper, and then polished down to diamond 1µm powder.

For the grain structure observations, prior to that polishing step, the sample were heated up to 330°C during 2 hours to accelerate the coarsening of the grain boundaries precipitates. Then (after polishing) it is plunged into an orthophosphoric solution (10mL of 85% diluted H_3PO_4 in 90mL water) during a few minutes at 50°C, to reveal the grain structure. It was then observed with the optical microscope.

For the observation of the deformation structure, the samples were plastically strained after mirror polishing. The Nomarski contrast mode allowed revealing the topology.

II.B.1.b. Scanning Electron Microscopy

i. Objectives

Scanning electron microscopy has been used to characterize the fracture mode of strained specimens.

ii. Device

A LEO SEM has been used in secondary electron, deep depth-of-field mode, with a 20keV acceleration voltage.

iii. Specimens

The post-mortem study of the fractured specimens required an ultrasonic cleaning stage in methanol.

II.B.1.c. Transmission Electron Microscopy

i. Objectives

A Transmission Electron Microscope has been used in order to characterize the local precipitation state: the precipitates morphology, size, orientation and type.

ii. Device

The laboratory TEM is a 300kV JEOL 3010.

iii. Samples

The sample first has to be mechanically polished down to ~100 microns thickness. A 3mm diameter punch allows to cut off the specimen, which is then electropolished with a 15V voltage in a nitric acid solution (1/3 of diluted HNO_3, 2/3 of methanol) at -25°C with a Fischione double-jet polishing device.

II.B.2. Mechanical characterization

II.B.2.a. Microhardness

i. Objectives

Microhardness has been used to measure the local mechanical properties of the material. Indeed it gives a good approximation of the mechanical response of the material, as hardness and yield stress are approximately linearly related [Tekkaya 2000]. Nevertheless there are some differences: microhardness is local and generally isotropic while yield stress is an averaged but directional value.

Hardness has been used to evaluate the mechanical properties in a non-destructive way (case of tensile samples), or to map the local mechanical properties (case of the laser formed samples).

ii. Device

A semi-automated Buehler device with 2 kinds of indenters (Knoop and Vickers; see Fig. II.4) has been used. It allows 1D mapping measurements while controlling the distance between indents. Load has been chosen between 50 and 200g and the indent size measured with dedicated software.

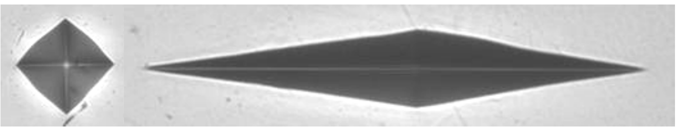

Fig. II.4. Vickers and Knoop indents

iii. Samples and measurements

The samples first have to be mirror polished, in order to obtain a flat surface. As shown by Srikant [Srikant 2006], indents generate a strain field slightly larger than 1*D in the surface and 2*D in the depth (where D is the indent diagonal). In other words: 2 indents have to be separated of a distance larger than 2.5*D in order not to interfere with each other.

II.B.2.b. Tensile tests

i. Objectives

Tensile tests have been performed to measure more accurately the mechanical properties of a wide range of material tempers: yield stress, ultimate tensile stress, elongation at fracture as well as the strain hardening behaviour.

The major part of the experiments was carried out at room temperature, in quasi-static conditions. The effect of strain rate has been investigated through dynamic, strain rate jump, and low temperature tests.

ii. Device

The schematic view a tensile machine is shown in Fig. II.5.

A mechanical Zwick tensile device with grips for flat specimens, equipped with a 20kN load cell and an axial extensometer has been used for the quasi-static tests and the low temperature tests.

For the high strain rate tests and the Bauschinger tests, we used a hydraulic MTS 810 tensile/compression device with 647 hydraulic wedge grips for 12 mm cylindrical specimens, equipped with a 100kN load cell and a 10mm gage length axial. This machine allows either “low strain rate” tests (up to 10^{-2} m.s^{-1}) or high strain rate tests (up to 4 m.s^{-1}).

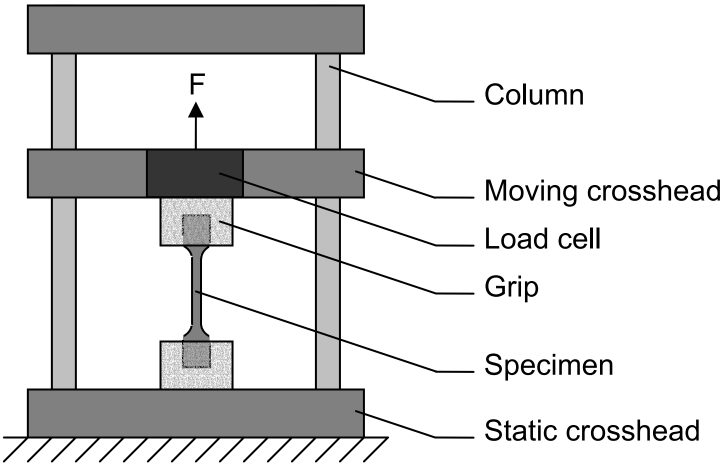

Fig. II.5. Tensile device schematic

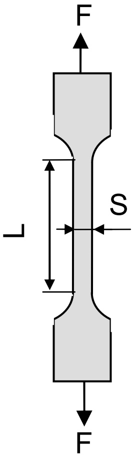

Fig. II.6. Tensile specimen schematic

iii. Specimens

Two specimens' sets have been required to do the tensile tests. Both of them are flat specimens and have the same general shape, the difference being the length of the constant section. The standard samples are presented in Fig. II.7. The samples dedicated to the plate anisotropy measurements (Fig. II.8) were limited to a total length of 76mm (ST direction length); therefore the central section was restricted to 26mm, for those samples while it was 50mm for the other specimens

A profile has been cut in the 25mm thick plates by wire spark erosion, sliced into 3mm thick specimen and finally sand blasted. Heat treatments were performed (or not, in the case of the T7651 trials) at this stage. This had no consequence on the residual stress level thanks to the small thickness of the specimens.

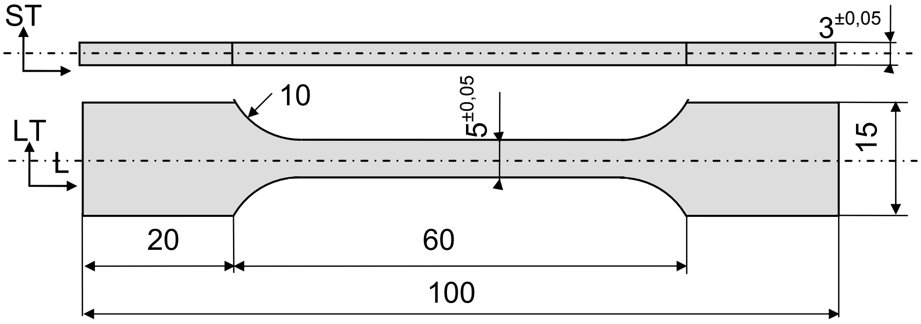

Fig. II.7. Drawing of the tensile specimen #1

Used for most of the tensile experiments - General tolerances: ±0.1 - Scale: 1

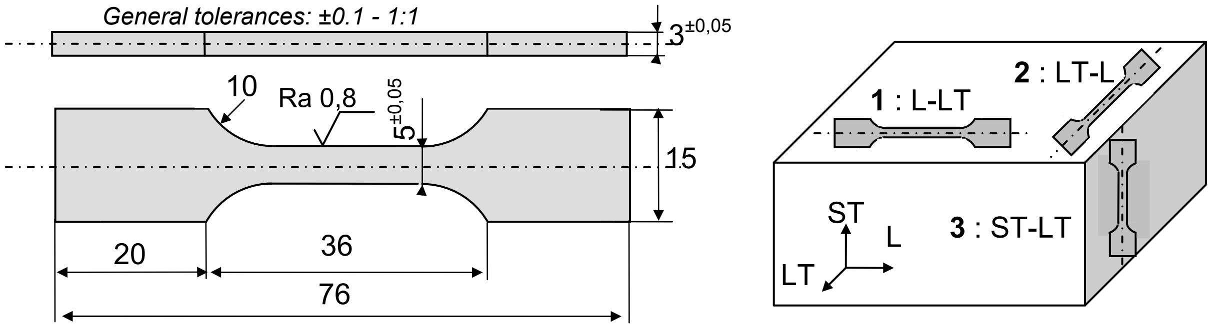

Fig. II.8. Drawing of the tensile specimen #2

(a) Specimen plan. (b) Schematics of the tensile specimens #2 cuts. Used for anisotropy characterization

iv. Data processing

The main parameters which can be extracted from a tensile test are listed in Table II.4; the corresponding experimental procedure is detailed in the following paragraphs.

Parameter	Young modulus (eng.)	Tensile yield stress (eng.)	UTS (eng.)	Elongation at fracture (eng.)	Initial hardening rate (true)	Strain hardening slope (true)
Label	E	σ_y	σ_{max}	ε_{max}	θ_0	β_0

Table II.4. Tensile test results

“Eng.” and “True” respectively corresponds to engineering and true values.

Engineering stress σ_n (MPa) and engineering strain ε_n (-) are respectively defined as:

(II.3.) $\sigma_n = F / S_0$

(II.4.) $\varepsilon_n = \Delta L / L_0$

Where F (N) is the load, S_0 (mm) is the initial specimen central section, ΔL (mm) is the specimen elongation and L_0 (mm) the initial length of the central section. On Fig. II.9 are represented the main values extracted from the engineering stress-strain curve: E is the Young modulus, σ_y the tensile yield stress (defined at 0.2% plastic offset), σ_{max} the ultimate tensile stress and ε_{max} the homogeneous maximum plastic deformation. At this point necking occurs and deformation localises.

Then true stress σ (MPa) and true strain ε (-) are calculated from the engineering values using:

(II.5.) $\sigma = \sigma_n (1 + \varepsilon_n)$

(II.6.) $\varepsilon = ln(1 + \varepsilon_n)$

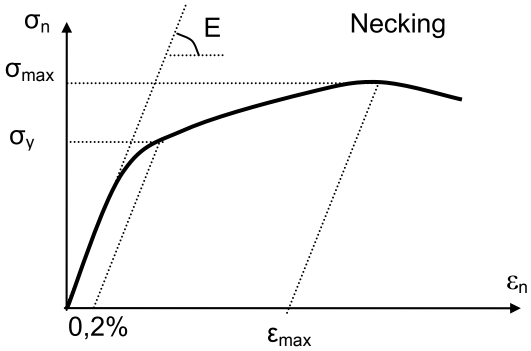

Fig. II.9. Schematic eng. tensile curve

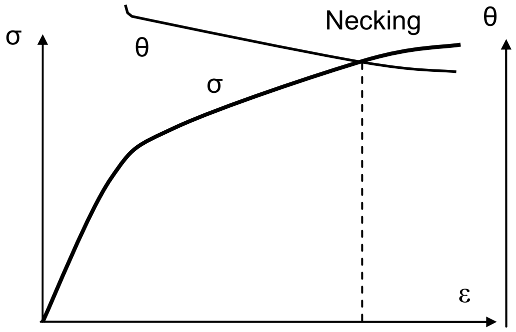

Fig. II.10. Schematic true tensile curve

Finally the strain hardening rate θ is the local slope of the true stress-strain curve:

(II.7.) $\theta = \partial\sigma / \partial\varepsilon$

If one plots the evolution of the strain hardening rate θ versus normalised flow stress $\sigma - \sigma_y$, one obtains the strain hardening curve (see Fig. II.11), from which two parameters can be extracted: the slope β_0 and the initial hardening rate θ_0. They have been obtained after the following procedure:

1. Polynomial fit (order: 4 to 8) of the true tensile curve plastic zone: $\sigma = f(\varepsilon)$
2. Derivative of the resulting fit: $\theta = \partial\sigma / \partial\varepsilon$
3. Plot of the strain hardening curve: $\theta = f(\sigma - \sigma_y)$ (see Fig. II.11.b).
4. Linear fit of the strain hardening curve: $\theta = \theta_0 - \beta_0(\sigma - \sigma_y)$

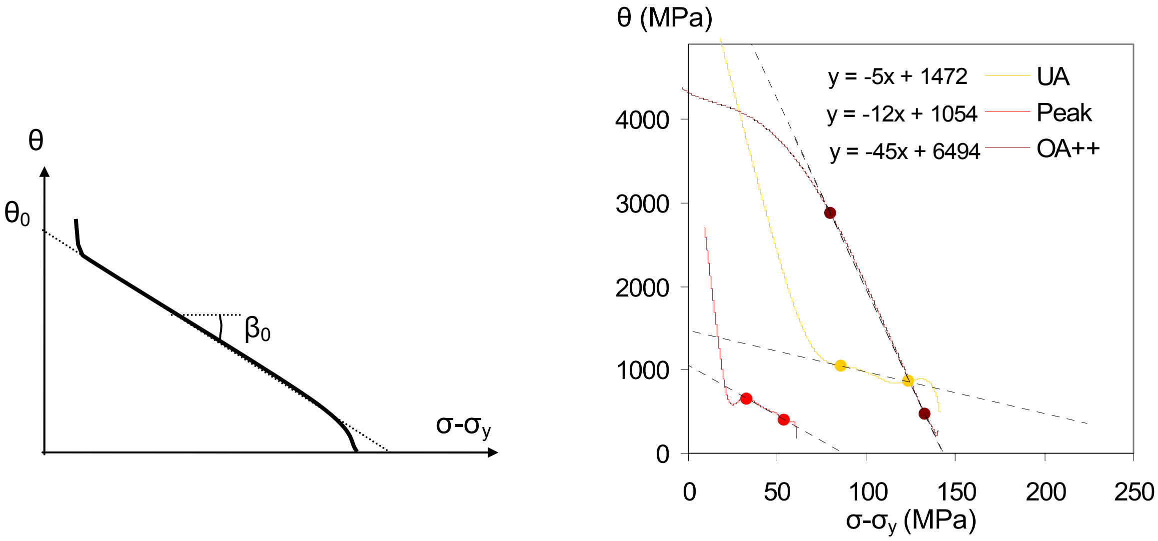

Fig. II.11. Strain hardening curves

(a) Schematic. (b) Examples for under-aged ("UA"), peak-aged ("Peak") and largely over-aged material ("OA++"). The points indicate the limits of the linear fit.

II.B.2.c. Bauschinger tests

i. Objectives

The objective of the Bauschinger tests is to evaluate the kinematic hardening contribution to the total strain hardening. These tests have been performed for a wide range of material tempers.

The test protocol is the following. The first stage (forward) consists in straining the specimen up to a certain forward plastic strain level. Once this level is reached, the specimen is unloaded up to 0 force and immediately reloaded (reverse stage), but this time in compression, as far as possible before buckling occurs. This approach has been used by Moan and Embury [Moan 1979] and more recently by Proudhon [Proudhon 2008] and Teixeira [Teixeira 2008b].

ii. Device

The device is the hydraulic MTS tensile/compression tester presented in II.B.2.b.ii.

iii. Specimens

Two sets of cylindrical specimens have been manufactured from 14mm square beams by turning, the second set being more accurate for compression tests by diminishing the length/section ratio (10mm diameter and 15 mm long in the central section).

Contrarily to the tensile specimens, heat treatments have been performed before the machining operation, to avoid distortions of the specimen during the heat treatment, and because of the necessity to have a precise geometry for Bauschinger tests.

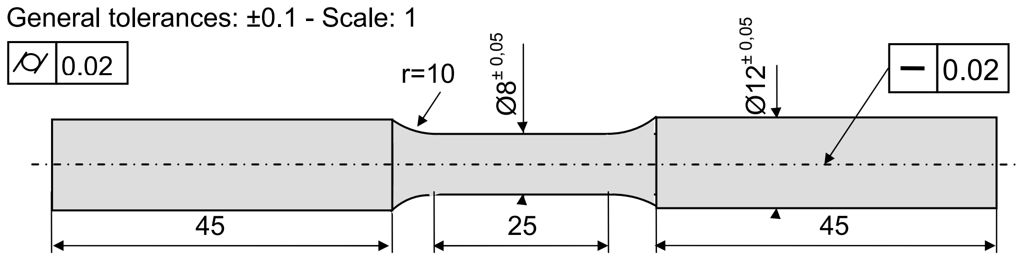

Fig. II.12. Drawing of the Bauschinger specimen #1

iv. Data processing

The rough engineering data are first converted into true data (Fig. II.13.a). Then the absolute stress versus the cumulative strain is plotted, as shown in Fig. II.13.b.

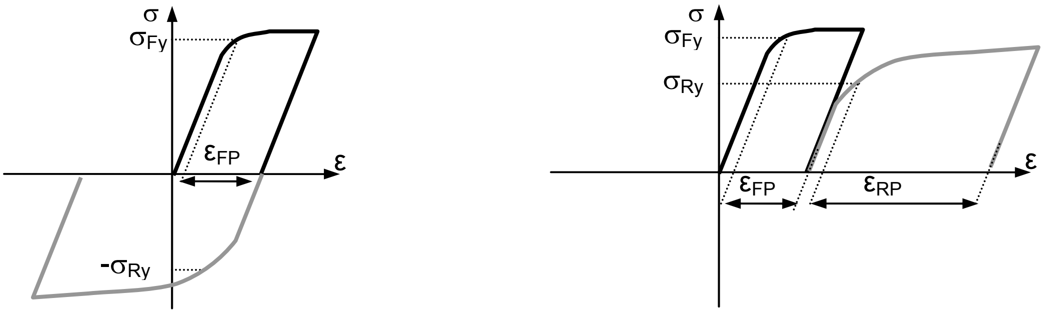

Fig. II.13. Schematic Bauschinger curve

(a) Initial (true) Bauschinger curve. (b) Absolute stress versus cumulative strain curve.

Fig. II.14 defines the main parameters that will be considered in the study of the Bauschinger effect. For each of the investigated tempers, the effect of the maximum forward plastic strain $\varepsilon_{FP-\max}$ on the reverse loading response was examined, in particular of the σ_{Ro} value, defined at a certain reverse plastic offset (ε_{Rpo}), characteristic of the Bauschinger effect. A more detailed definition of these parameters will be made in chapter III.

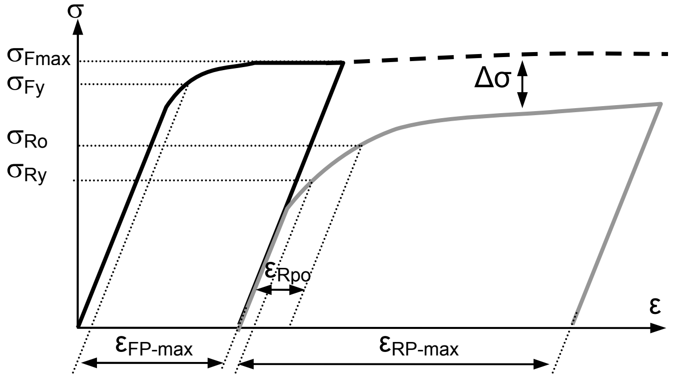

Fig. II.14. Schematic cumulative Bauschinger curve and definitions

The dashed line represents the monotonic tensile curve.

II.C. Small Angle X-Ray Scattering

II.C.1. Objectives

This technique, developed by A. Guinier in 1937 [Guinier 1938a] has been used in order to measure the precipitate volume fraction and mean size as well as the size distribution and morphology of the hardening precipitates in AA7449. More precisely, it has been used during this work to:

- measure precipitation state after different heat treatments (for instance tensile specimens),
- map precipitation state after laser forming treatments,
- measure precipitation kinetics during in situ heat treatments,
- measure precipitation kinetics during in situ thermomechanical treatments.

II.C.2. Generalities and theory

II.C.2.a. Scope

Small-Angle X-Ray Scattering (SAXS) is one of the SAS (Small-Angle Scattering) methods (with SANS: Small-Angle Neutron Scattering), used to characterize the structure of solid state materials on the nanometer scale (see Fig. II.15).

Those techniques allow studying a wide range of topics [Gerold 1978] such as phase transformations (precipitation), density and concentration fluctuations in single-phase systems and various structural defects such as voids, radiation damage, dislocations [Thomson 1999]. More recently, those techniques (especially GISAS: Grazing Incidence SAS) have been used to characterize thin films and surfaces, magnetic nanostructures and hierarchical materials [Fratzl 2003]. SAXS is also commonly used in the field of colloids and polymers [Morfin 2006].

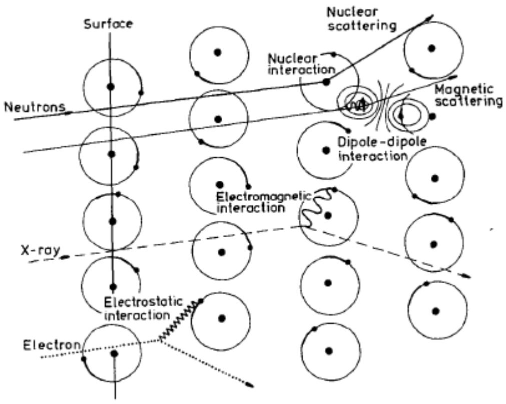

Fig. II.15. Particles interactions with atoms

[Windsor 1988]

Contrary to TEM or 3D-AP (Atom Probe Tomography) that give very local measurements, the larger analysed volume (~10^{-3} mm^3) gives a statistical measurement of the precipitation state in the material.

Fig. II.16. Sunlight diffusion in air

Courtesy of A. Deschamps. Diffusion of visible light due to ice particles at the micron scale.

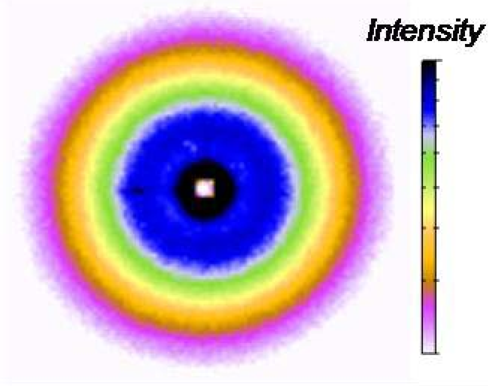

Fig. II.17. AA7449 raw diffusion image

Diffusion of X-rays due to η' / η nanoprecipitates. Each colour corresponds to an intensity level.

II.C.2.b. Principle

The small angle scattering techniques are based on the measurement of the scattering of an incident wave due to material heterogeneities. While visible light may be diffused by particles in some special whether conditions (water droplets, fog, ice particles; see Fig. II.16), neutrons are scattered by the atoms' nuclei (SANS) and X-Rays by electrons. X-Rays (wavelength between 10^{-8} and 10^{-11} m) are indeed sensitive to electron density fluctuations in a material, such as the ones existing between the matrix and the precipitates. SAXS measurements can be performed provided this contrast is large enough. Al_2Cu in AA2xxx [Gomiero 1992a] and $MgZn_2$ particles in AA7xxx [Dumont 2006, Deschamps 2003b] are easily measured but it is less suitable for Mg_2Si precipitates in AA6xxx, where the matrix/particles electronic density contrast (~Z number; see II.C.4.b.iii) is low. However it has recently been used ([Tsao 2005]).

II.C.2.c. Theory

i. Definitions

The modulus k of the wave vector $\vec{k}$ is inversely proportional to the wavelength λ :

$$\text{(II.8.)} \quad k = \frac{2\pi}{\lambda}$$

The diffraction angle 2θ is defined as the angle between the incident beam of wave vector $\vec{k}_0$ and the scattered beam of wave vector $\vec{k}_s$ (see Fig. II.18). The scattering vector $\vec{q}$ which describes the wave diffraction is the difference between the two wave vectors: $\vec{q} = \vec{k}_s - \vec{k}_0$; its magnitude is equal to:

$$\text{(II.9.)} \quad q = \frac{4\pi \sin\theta}{\lambda}$$

An equivalent interpretation can be made by using the familiar Bragg's law $\lambda = 2d \sin\theta$. If the defect phase were periodic with a single spacing d , then the scattering would occur only at the Bragg angles ($q = 2\pi / d$). The more general diffraction pattern from a non-periodic sample may be thought of as a superposition of reflections from all possible periodicities, with relative intensities dependent on the amount of each periodicity present in the sample [Windsor 1988].

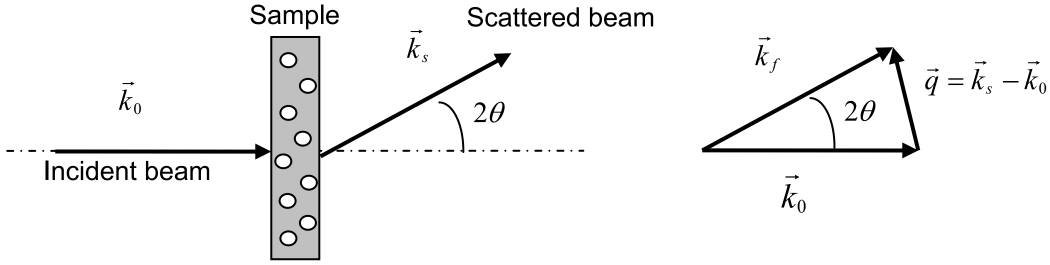

Fig. II.18. Definition of the diffusion angle and scattering vector

(a) Schematic of the beam diffusion. (b) Definition of the scattering vector

The SAS angle range is usually defined between $0 \le q \le \pi/d_a$ [Gerold 1978], where d_a is the interatomic distance in the sample. As in f.c.c. materials, the closest interatomic distance is equal to $a\sqrt{2}/4$, this would mean in our case ($a = 4.04 Å$) that $0 \le q \le 2.2 Å^{-1}$. This corresponds to a maximum diffraction angle of 15.6° for the copper K_α wavelength. The experimental reachable range itself depends on the experimental set up (sample-CCD distance, beamstop size; see Fig. II.19).

ii. Scattered intensity

The amplitude of a wave scattered in a direction (defined by q) by a single electron will be in the form:

$$\text{(II.10.)} \quad I(q) = e^{iqr}$$

Adding the contributions of all electrons (electron density: $\rho(r)$) of the investigated volume V gives the resulting amplitude:

$$F(q)=\iiint_V \rho(r)e^{iqr}dV \tag{II.11.}$$

The scattered intensity is then defined as:

$$I(q)=\left|F(q)\right|^2 \tag{II.12.}$$

As a first hypothesis, one can consider that the intensity scattered by an electron will be isotropically distributed. Furthermore, if one considers a uniform scattering length density from particles ρ_P, within a uniform matrix of scattering-length density ρ_m, this term can be simplified into [Windsor 1988]:

$$I(q)=\left(\rho_m-\rho_P\right)^2\iiint_{V_P} e^{iqr}dV \tag{II.13.}$$

This expression may be averaged over all particle orientations, the average of e^{iqr} being $sin(qr)/qr$:

$$\int_V e^{iqr}dV=\int_V \frac{sin(qr)}{qr}4\pi^2r^2dr \tag{II.14.}$$

Finally, one obtains:

$$I(q)=4\pi^2\left(\rho_m-\rho_P\right)^2\int_V \frac{sin(qr)}{qr}r^2dr \tag{II.15.}$$

II.C.3. Experiment

II.C.3.a. Set-up

i. Basic set-up

The basic set-up consists of a X-Ray generator, an optical system, a sample chamber and a detector, mounted in series (Fig. II.19.).

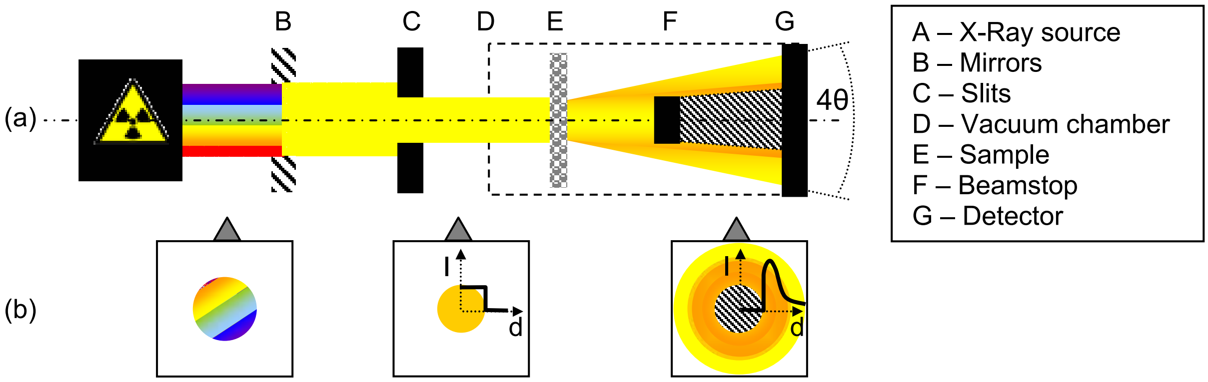

Fig. II.19. SAXS set up

(a) SAXS set up schematic; (b) Beam section schematic and intensity vs. distance from centre. In the last image, intensity is 0 close to the centre due to the beamstop (see Fig. II.17).

Once the polychromatic photon beam is generated by the X-Ray source, it is re-shaped by the optics before going through the thin sample. The material's particles scatter the beam and a detector maps out the scattered intensity as a function of the diffusion angle θ. A photomultiplicator located before and after the sample measures its absorption. The main elements are the following:

- Two X-Ray sources have been used: our laboratory rotating anode and synchrotron light.

- The optical system is composed of monochromators to select a wavelength (monochromatic beam), curved mirrors to set the beam convergence and slits to reshape the beam.
- The sample chamber is maintained under vacuum, to prevent scattering from air particles. Different sample holders have been used, depending on the experiment: either multiple samples holders for ex situ measurements or a furnace for in situ heat treatments or a micro tensile device for thermomechanical treatments (see II.D).
- The detector used is a 2-D CCD camera. A beamstop located after the sample absorbs the transmitted photon beam, which high intensity would otherwise disturb the diffused beam measurements (CCD saturation). The distance between the sample and the CCD camera determines the scattering angle range θ, limited on the one hand by the effective size of the beamstop (minimum angle), on the other hand by the camera size (maximum scattering angle).

ii. Laboratory instrument

Our laboratory X-Ray source is a rotating copper anode of power 3.2 kW. A tungsten filament generates electrons, accelerated by a 40kV voltage. The electrons impacts on the copper electrode excite target electrons which emit X-Rays of wavelength $\lambda_{CuK\alpha}$=1.541 Å (E=8.478 KeV). A rotating anode allows reaching higher fluxes (through higher powers) than fixed anodes, as the rotation leads to distribute the electron impacts on the whole anode surface, which therefore dissipates more heat. A multilayer mirror for the wavelength selection and the focus and 2 slits sets (both vertical and horizontal) complete the set up, both manually adjusted.

iii. ESRF

A synchrotron is a large electromagnetic instrument which forces electrons to rotate along a storage ring. The ring is actually made of straight segments bound with bending magnets. Light (among which X-Rays) is generated tangentially to the ring each time the electron beam is deflected by the magnets[2]. Therefore this is where the experimental lines are located, composed of an optical hutch, an experimental hutch and a control hutch. The beam is polychromatic, thin and intense (high brilliance).

Fig. II.20. ESRF in Grenoble

The *ESRF* (European Synchrotron Research Facility) opened in 1994 in Grenoble. It is the most powerful synchrotron source in Europe. Experiments have been performed on *BM02*, a French *CRG* (*CNRS*) beamline installed at the output of a bending magnet. It is dedicated to multiple wavelength (5 to 25 keV), anomalous scattering and diffraction experiments, with two interchangeable instruments: 7-circle diffractometer and Small Angle Scattering Camera. The sample environment is flexible and various user-designed sample holders can be installed for in-situ experiments [Simon 1997].

iv. Comparison: laboratory vs. ESRF experiments

The sample holders used in our lab are fully compatible with the *ESRF-BM02* environment. Therefore it can be interesting to do some experiments at *ESRF* in some cases, as the beam offers a large number of advantages: an adjustable energy level for anomalous experiments [Simon 2006, Marlaud 2008b], a high brilliance (allows for instance fast measurements: in situ reversion), a thin beam (for

---

[2] Note that at *ESRF* there is another way to generate X-rays with ondulors.

precise mappings in welds for instance [Dumont 2006]) and a larger CCD-distance which allows to reach a smaller scattering vectors and therefore larger precipitates sizes (~200 nm). On the other hand laboratory experiments are useful for long in-situ measurements.

Parameter	Laboratory rotating anode	ESRF – BM02
Settings	Manual	Automated
Wavelength	Fixed – 1.54 nm	Tuneable
Wavelength relative dispersion	~2.10^{-4} photons/s/mm²/rad²	~$1.4.10^{-4}$ photons/s/mm²/rad²
Flux (photons/s)	~10^{8}	~10^{11}
Spot size	1 x 0.8 mm	0.1 x 0.1 mm
Distance sample-CCD	~200-1000 mm	~200-2500 mm
Scattering vector	0.01 – 0.3 (Å^{-1})	0.002 – 0.5 (Å^{-1})
Typical image acquisition duration	100 s	2 s

Table II.5. Comparison: laboratory vs. ESRF experiments

II.C.3.b. Samples and holders

i. Samples

Samples are typically 10x10 mm² large, either for ex situ measurements or for in situ heat treatments. Their optimal thickness depends on the material composition and of the energy level, which determines its absorption μ. One calculates the thickness from the transmission measurements Tr:

(II.16.) $$e = -LnT_r/\mu$$

Element	Al	Mg	Zn	Zn	Fe	Si	AA7449
μ at 1.3082 Å	0.0078	0.0042	0.0253	0.2229	0.1551	0.0088	0.00964
μ at 1.5407 Å	0.0127	0.0068	0.0402	0.0449	0.2366	0.0141	0.01370
μ at 1.7712 Å	0.0190	0.0103	0.0593	0.0664	0.0420	0.0212	0.02047
Density ρ	2.699	1.738	7.133	8.96	7.874	2.33	2.861

Table II.6. AA7449 sample absorption for different wavelengths

Absorption coefficients μ in (μm^{-1})

The alloy absorption coefficient is calculated as (ρ: density, $[I]$ weight percent concentration):

(II.17.) $$\mu_{alloy} = \frac{1}{\rho_{alloy}} \sum_{I} \left([I] \frac{\mu_I}{\rho_I} \right)$$

In AA7449, for a wavelength of 1.54 Å (energy 8047eV: $\lambda E = hc$), the signal/noise ratio is satisfactory when the thickness is comprised between 70 and 150 µm. At *ESRF* it is possible to go up to 300 µm.

The samples are obtained through mechanical polishing (grades 180-1200) down to +20 µm above the desired final thickness, followed by an electropolishing at -20°C with a 15 V voltage in a solution composed of 33% nitrogen acid (68% purity) and 67% methanol.

ii. Ex situ holders

Ex situ measurements have been made for two different goals. First, to measure precipitation state after different heat treatments (on cuts from tensile samples for instance). Secondly this has been used in order to map precipitation state after laser forming treatments; a measurement point can be made every 200 µm at *ESRF*. Multiple samples holders mounted on a motorised stage (see Fig. II.21) allow automated displacement during the experiment.

iii. In situ measurements

The heat treatment is performed in situ with a resistance heating furnace surrounding the sample (see Fig. II.22), supplied with a 600W power supplier regulated with a *Eurotherm* controller. A K-thermocouple measures the temperature directly at the samples border. Controlled heating ramps or isothermal treatments can be performed from room temperature to 600°C.

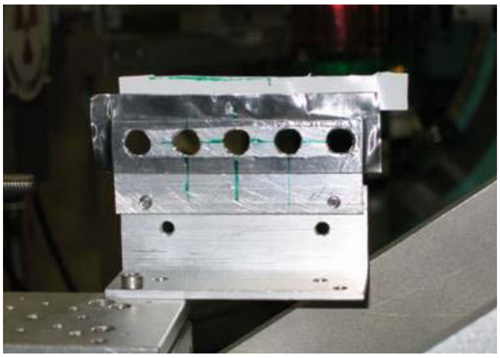

Fig. II.21. Ex situ sample holder

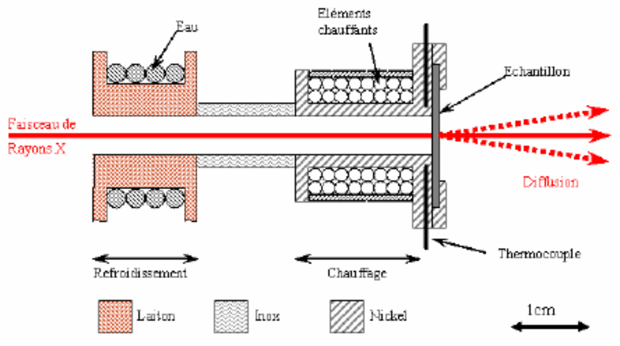

Fig. II.22. In situ SAXS furnace

"Echantillon" (right of the furnace) stands for "sample".

II.C.4. Data processing

II.C.4.a. Data correction and normalisation

i. Image correction

From the initial scattering image, the first data processing stage is the data correction and the calculation of the radial average values. The data are first corrected from the dark measurement (measurement without X-ray beam for detection of the electronic noise of reading). Then hot pixels are removed by comparison to the surrounding pixels (spatial comparison) and between two consecutive images (temporal comparison). Grid and flat (CCD camera performance) corrections are also done at this stage, as well as the background noise correction, which takes into account the residual scattering due to the incoming beam (slits, beamstop…). Once the beam centre and the masks (beamstop, errors…) have been set up by the user, a program calculates the radial mean value, and gives as output a table expressing the intensity as a function of the distance from centre.

ii. Data normalisation

The second stage is the normalisation: the data are normalised in order to be independent from the measurement conditions. The normalised intensity I_{norm} is indeed proportional to the corrected intensity I_{corr} , the proportionality term taking into account all the instrumental factors [Fratzl 2003]:

$$I_{norm}(q) = A \times I_{corr}(q) \qquad \text{(II.18.)}$$

One calculates I_{norm} as follows:

$$I_{norm}(q) = \frac{I_{corr}(q)}{K_{corr}.T_r.e.r_e^{\,2}.d\Omega} \qquad \text{(II.19.)}$$

Where K_{corr} is a correction factor coming from the measurement of a reference sample, T_r is the transmission rate of the sample, e its thickness, r_e the electron radius ($r_e = 2.82.10^{-13}\ cm$) and $d\Omega$ the solid angle for detection, calculated from the sample-CCD distance. The output file gives the absolute intensity as a function of the scattering vector.

iii. Final correction

Finally, a constant value (which is due to isotropic scattering coming from the scattering of the solid solution and from the iron fluorescence, as well as imperfections in the dark field correction of the CCD camera) is suppressed from the normalised intensity.

iv. Total intensity

As the beam is scattered along a wide range of scattering vectors, the overall diffused intensity (measured with a photomultiplicator) is the integration of equation (II.15.) over q :

$$I = \int_0^\infty I(q) \cdot dq \tag{II.20.}$$

This form can be written as the sum of three components: $I_1(q_{min})$, the scattered intensity hidden by the beamstop, $I_2(q)$ the intensity measured on the CCD camera and $I_3(q_{max})$ the intensity for $q \to \infty$:

$$I = \int_0^{q_{min}} I(q) \cdot dq + \int_{q_{min}}^{q_{max}} I(q) \cdot dq + \int_{q_{max}}^{\infty} I(q) \cdot dq = I_1(q_{min}) + I_2(q) + I_3(q_{max}) \tag{II.21.}$$

II.C.4.b. Results calculation

The experimental signal (see Fig. II.23.a) can be used either for "direct" calculation (Guinier radius, integrated intensity) or used to fit the model parameters.

i. Guinier radius

Guinier approximation tells us that for small scattering vectors values, intensity can be expressed by a relation valid for any precipitate morphology, where R_G is the particles Guinier radius.

$$I(q) = \Delta\rho^2 V^2 \, exp\left(-\frac{q^2.R_G{}^2}{3}\right) \tag{II.22.}$$

The so called Kratky plot $I(q).q^2 = f(q)$ (Fig. II.23.d) allows obtaining the Guinier radius R_G :

$$R_G = \frac{\sqrt{3}}{q(max[I.q^2])} \tag{II.23.}$$

Another way to measure the Guinier radius is to plot $Ln(I(q)) = f(q^2)$. The slope S of the Guinier plot (Fig. II.23.b) gives the Guinier radius through relation (II.24.):

$$R_G = \sqrt{-3 \times S} \tag{II.24.}$$

The Guinier radius is defined as the gyration radius of the particle [Guinier 1938a] (r_i is the distance between an atom and the mass centre of the particle):

$$R_G{}^2 = \frac{1}{N}\sum_{i=1}^{i=N} r_i{}^2 \tag{II.25.}$$

In the case of a monodisperse distribution, R_G can be related respectively to the real radius R of spherical precipitates and to the radius R and thickness a of plate-like precipitates through:

$$R_G = \sqrt{5/3}R \tag{II.26.}$$

$$R_G = \sqrt{\frac{2 + (a/R)^2}{5}}R \tag{II.27.}$$

For polydisperse precipitate distributions, R_G is generally very close to the mean radius of the precipitates [Dumont 2006].

ii. Integrated intensity

The integrated intensity Q_0 is proportional to the precipitate volume fraction. It is defined as the overall area under the $I(q)\cdot q^2$ vs. q curve (see Fig. II.23.e):

(II.28.) $$Q_0 = \int_0^\infty I(q)\cdot q^2 \cdot dq$$

Where $I(q)$ is here the scattered intensity minus the constant isotropic ("Laue") intensity. It can bee written as the sum of directly measurable ($Q_2(q)$) and non-directly measurable parameters $Q_1(q_{min})$ and $Q_3(q_{max})$, as it is represented on Fig. II.23.e

(II.29.) $$Q_0 = \int_0^{q_{min}} I(q)\cdot q^2 \cdot dq + \int_{q_{min}}^{q_{max}} I(q)\cdot q^2 \cdot dq + \int_{q_{max}}^{\infty} I(q)\cdot q^2 \cdot dq = Q_1(q_{min}) + Q_2(q) + Q_3(q_{max})$$

Indeed the intensity scattered for very small angles overlaps the transmitted signal, which is hidden by the beamstop. Therefore the first component $Q_1(q)$ is extrapolated from the $I(q)\cdot q^2 = f(q)$ curve, supposing a linear evolution of the signal between the origin and q_{min}. In other words:

(II.30.) $$Q_1(q_{min}) = I(q_{min}) \times {q_{min}}^3 / 2$$

The finite size of the CCD camera limits the measurements in the large q area, but it is possible to approximate the third component $Q_3(q)$. When the matrix and the particles are separated by a sharp interface, the scattered intensity follows an asymptotic law in the large q region, i.e. when $q >> 2\pi / R$. This law is the Porod's approximation and is written under the following form:

(II.31.) $$\lim_{q\to\infty} I(q) = A + 4\pi\Sigma(\Delta\rho)^2 q^{-4} = A + Bq^{-4}$$

Where Σ is the specific surface area of the particles (surface divided by volume, commonly expressed in m^2cm^{-3}) and $\Delta\rho = \rho_p - \rho_m$ the matrix/precipitates electronic density contrast. Multiplying (II.31.) by q^4 gives the following equation, valid for large q:

(II.32.) $$I(q)\cdot q^4 = A\cdot q^4 + B$$

The Porod plot ($I(q).q^4 = f(q^4)$, see Fig. II.23.c) results in a straight line in the large q range. Its equation gives B and A, the "*Laue*" value. This term takes into account scattering by the solid solution and incoherent scattering due to fluorescence of heavy elements (iron), as well as imperfections in the dark field correction of the CCD camera. Then for large q, Q_3 becomes:

(II.33.) $$Q_3(q_{max}) = \int_{q_{max}}^{\infty} (I(q) - Laue)\cdot q^2 \cdot dq = \int_{q_{max}}^{\infty} (B\cdot q^{-2})\cdot dq = \frac{B}{q_{max}}$$

Finally equation (II.29.) becomes:

(II.34.) $$Q_0 = \frac{I(q_{min}).{q_{min}}^3}{2} + \int_{q_{min}}^{q_{max}} I(q)\cdot q^2 \cdot dq + \frac{B}{q_{max}}$$

iii. Volume fraction

Integrated intensity can be related to volume fraction through the following equation:

(II.35.) $$Q_0 = 2\pi^2 \Delta\rho^2 f_v(1 - f_v)$$

Where the electronic density contrast $\Delta\rho$ is calculated with:

(II.36.) $$\Delta\rho = \rho_p - \rho_m = \frac{\sum_i f_i C_i^p}{V_{at}^p} - \frac{\sum_i f_i C_i^m}{V_{at}^m}$$

In this expression, C_i^p and C_i^m respectively represent the atomic concentration of element i in the precipitate and in the matrix, V_{at} is the atomic volume (supposed equal in the two medias) and f_i are the diffusion factors of element i, equal to:

(II.37.) $f_i = Z_i + f_i'$

The first term Z_i is the atomic number of the element and the energy dependant term f_i' can be found in tables (http://csrri.iit.edu/cgi-bin/). For the copper edge energy (E=9477eV):

Element	Al	Cu	Zn	Mg
Z	13	29	30	12
f_i'	0.17	-2.1	-3.55	0.1

Table II.7. Diffusion factor of the main alloying element of AA7449 at E=9477eV

To simplify the approach, the matrix and precipitate compositions are assumed to be constant during the heat treatment (contrary to what happens in reality). Instead of the standard 33% Mg and 67% Zn, the precipitate composition is the one proposed by Marlaud [Marlaud 2008] for AA7449-T6:

Element	Al	Cu	Zn	Mg
Precipitate composition (%)	17.6	7.3	41.8	33.3
Matrix composition (%)	98.9	0.3	0.6	0.3

Table II.8. AA7449-T6 precipitate and matrix composition

[Marlaud 2008]

Table II.7 and Table II.8 allow calculating the electronic density contrast using equation (II.36.). Solving equation (II.35.) finally gives the volume faction f_v as a function of Q_0 as:

(II.38.) $$f_v = 0.5\left(1+\sqrt{1-2\frac{Q_0}{\pi^2|\Delta\rho|^2}}\right)$$

iv. Modelling

For a given scattering vector q, the intensity $I(q)$ diffused by a dilute particle distribution $f(R)$ will be in the form [Morrison 1992]:

(II.39.) $$I(q)=\int_0^\infty I(q,R)\cdot f(R)\cdot dR$$

Where $I(q,R)$ represents the intensity diffused by a single particle of radius R, for a given scattering vector. For instance if one assumes that the particles are spherical, this term has the following form:

(II.40.) $$I_{sph}(q,R)=3\left[\frac{sin(qR)-qR\,cos(qR)}{(qR)^3}\right]$$

One considers a lognormal particle distribution (R is the particle radius in the case of spherical particles or an equivalent radius in the case of ellipsoids or cylinders):

(II.41.) $$f(R)=\frac{1}{\sigma\sqrt{2\pi}}\frac{1}{R}exp\left(-\frac{1}{2}\left(\frac{ln(R/\overline{R})}{\sigma}\right)^2\right)$$

As already said in II.C.4.a.iv, the overall intensity is expressed as the sum of three terms, among which the second term is the experimental measured signal:

(II.42.) $I = I_1\left(q_{min}\right) + I_2\left(q\right) + I_3\left(q_{max}\right)$

The modelling consists in fitting the $I_2(q)$ part of the experimental curve, that is to say to tune the model parameters (precipitate size distribution function and morphology) to minimize the error between the experimental and the modelled curve. An example is shown in Fig. II.23.f. However, the sensitivity of the fit is sometimes large and only good quality signals allow a good fit. In particular the CCD-Sample distance has to be chosen very carefully to measure the full scattered signal. When the full signal is not measured (which is the case for most of the experiments), the results varies between 20-30% when the range of the experimental data used for the fit is changed.

v. Summary

Fig. II.23 show an example of the various plots used for the calculation of the SAXS results. The measurement has been made on AA7449-T7651. The results are summarised in Table II.9.

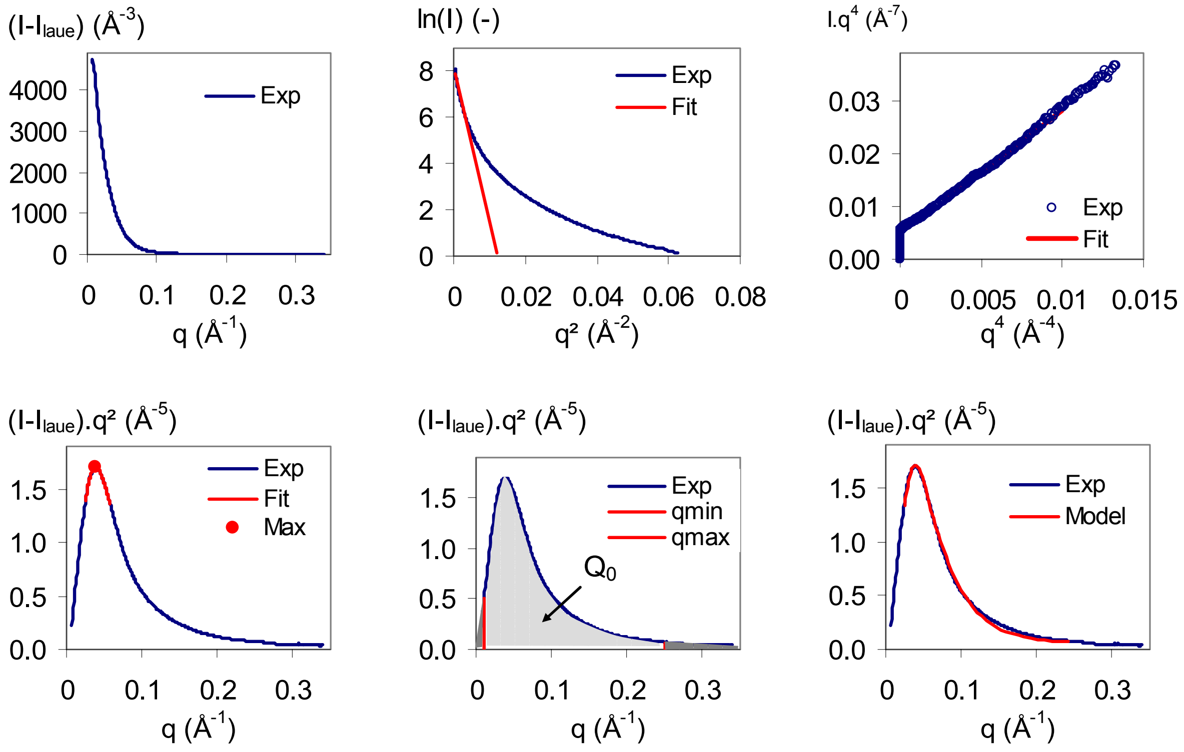

Fig. II.23. SAXS signal and various plots

(a) Initial plot. (b) Guinier plot. (c) Porod plot. (d) Kratky plot. (e) Calculation of Q_0. (f) Modelled curve.

Parameter	R_G (1)	R_G (2)	R	σ	AR	I_{Laue}	Q_0	f_v
Origin	b	d	Model	Model	Model	c	d	Eq.(II.38.)
Value	43.97 Å	44.81 Å	53.88 Å	0.233	0.353	2.386 Å^{-3}	0.154 Å^{-6}	6.10%

Table II.9. SAXS measurements results

“b”, “c” and “d”” refer in “Origin” refer to Fig. II.23. σ is the standard deviation of the lognormal distribution; the model assumes ellipsoidal particles and AR is the aspect ratio.

II.D. Experimental development

II.D.1. Micro tensile device for TMT during SAXS measurements

II.D.1.a. Objectives

Our objective is to look at the effect of thermomechanical treatments (TMTs) on precipitation kinetics, which may be affected by both temperature and deformation. Moreover, we want to model the effect of TMTs on precipitation kinetics, which means that we need a quantitative description of the precipitation evolution during TMTs, which have to be accurately controlled.

In order to achieve this, we developed a micro tensile and heating device, able to reproduce a wide range of TMTs, while measuring in situ the precipitation kinetics by SAXS. This device will be called in the following the TSAXS.

II.D.1.b. Design

i. <u>Specifications</u>

- Various TMTs have to be modelled: tensile tests, relaxation tests and creep tests.
- A large number of parameters have to be controlled during thermomechanical testing: strain rate, strain level, stress level, temperature…
- The test sequence (stress/strain/temperature vs. time) has to be controlled as well.
- Timescale of the experiments is variable: from a few minutes to a few days.
- Stress, strain and temperature vs. time have to be recorded.
- Temperature range is the one used for TMT of aluminium alloys: 20-400°C.
- Stress may reach a value of 700 MPa.
- Strain may reach 50%.
- The device will be put inside the laboratory vacuum chamber for SAXS experiments.
- The device will be displaced in the vacuum chamber (a few millimetres in X and Z).
- The device has to allow SAXS measurements; in other words, the beam should not be stopped by the device.
- The specimen geometry has to be as close as possible to standard tensile specimens; I particular deformation has to be localised in the central section. This central section should allow SAXS measurements; in other words, it should be flat, have parallel faces and be thin enough (100 to 300 µm) to transmit sufficient signal.

ii. <u>Design</u>

The main design options that have been chosen are the following: a stepped motor controls deformation; heating is ensured through resistance heating elements in the tensile grips; temperature is measured by thermocouples, strain by and inductive sensor and stress by a piezo sensor; a program controls and records those signals and the device geometry (as well as the specimen itself) is adapted to the SAXS requirements and parameter range specifications. The result of this is shown in Fig. II.24.

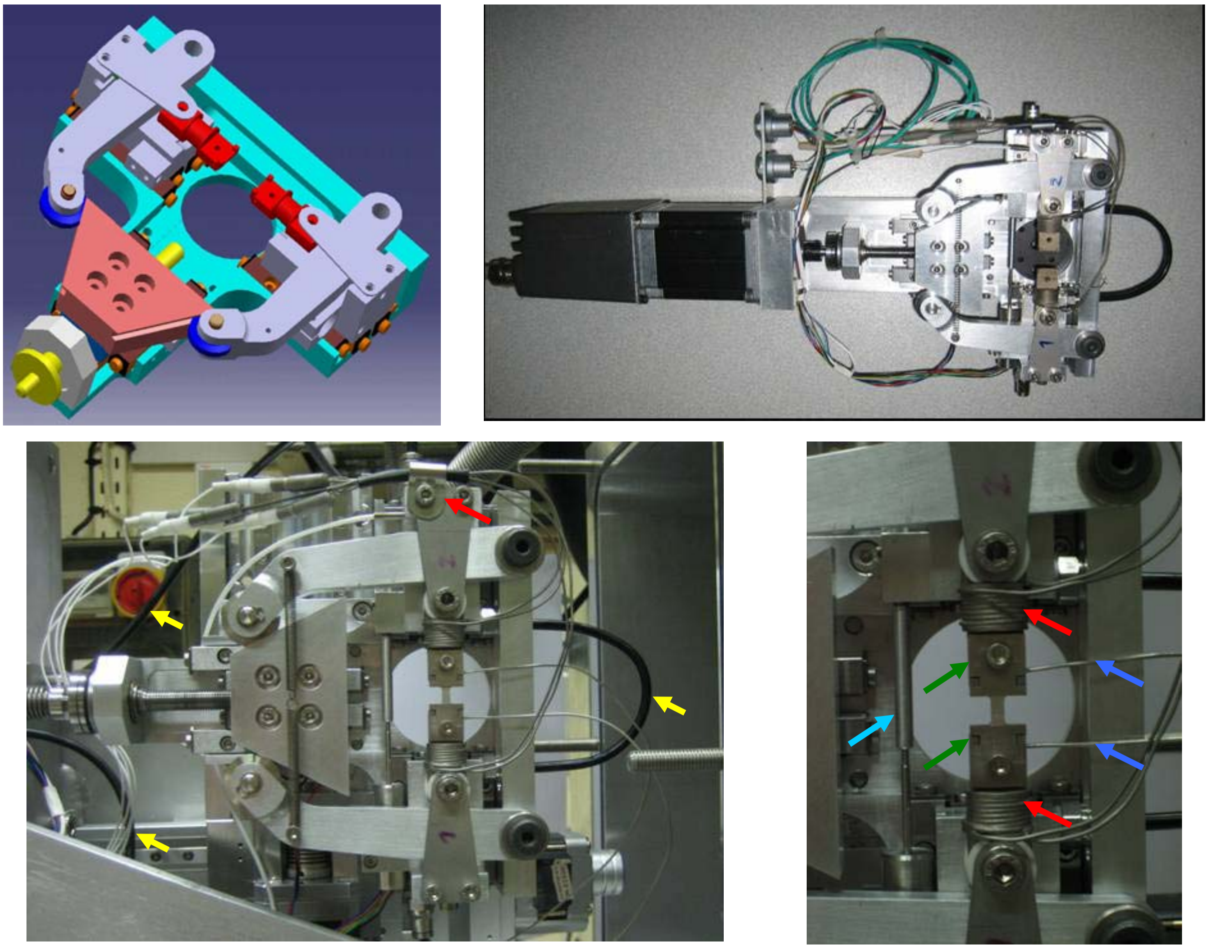

Fig. II.24. TSAXS device

(a) CATIA 3D drawing. (b) Motor and device before set-up. (c) Device in the vacuum chamber. (d) Zoom in the specimen area. The arrows in (c) show: the water circulation (yellow) and the load sensor (red), the arrows in (d): the displacement sensor (hell blue), grips (green), heating grips (red) and the temperature sensors (blue).

iii. Complete set-up and environment

The device is mounted in the laboratory vacuum chamber, on a motorised holder to set the specimen position in the beam. This chamber can be used either in the laboratory facility or at ESRF. Electronic devices (motor, load and displacement sensors) have been integrated in a control module (Fig. II.25).

Fig. II.25. TSAXS in vacuum chamber and TSAXS control module

A computer and a thermo controller/power supplier are required as well. Furthermore, a calibration device has been made to balance the power supplied to each of the heating grips. The complete set-up is presented in Fig. II.26.

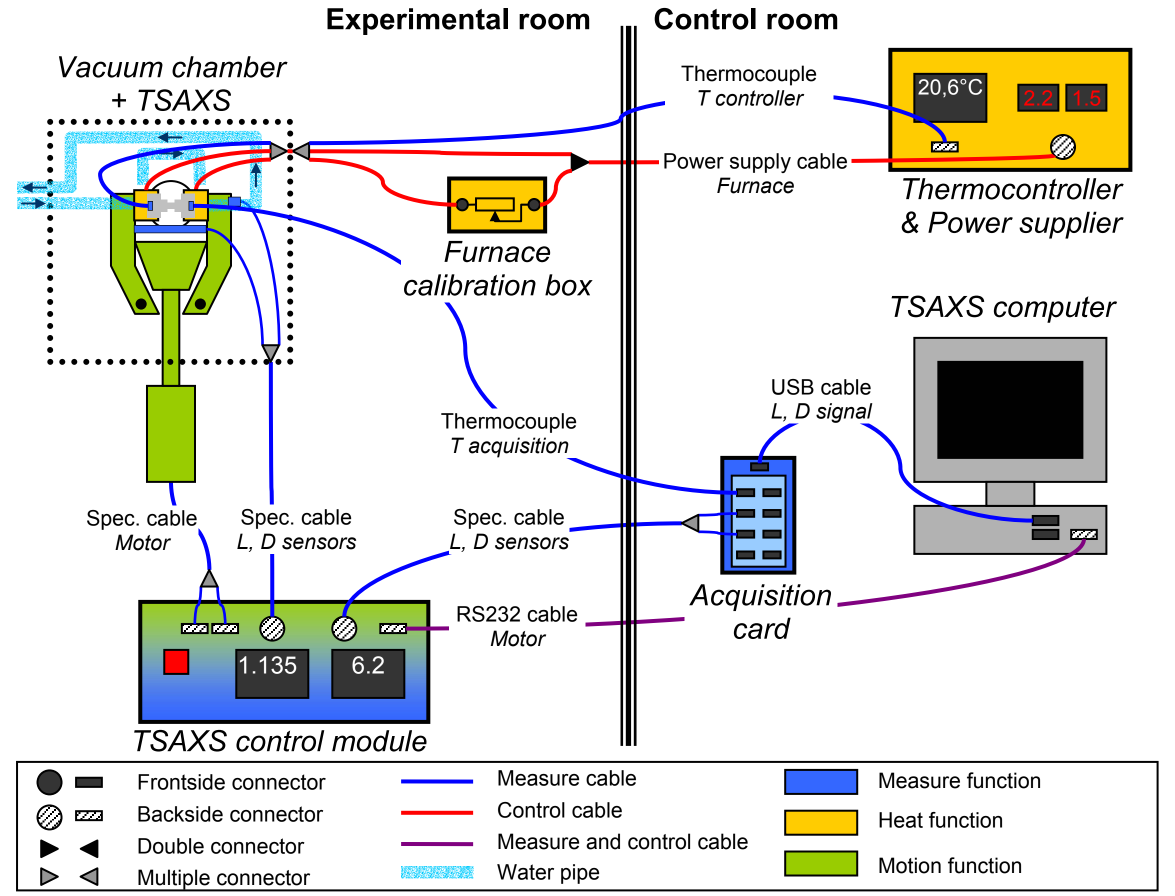

Fig. II.26. Schematic of the complete TSAXS set up

Spatial organisation of the experiment is shown; a wall separates the experimental from the control room. “Spec.” stands for “specific”, “T” for “temperature”, “D” for “displacement” and “L” for “load”. Colours distinguish the different functions.

II.D.1.c. Specimens

i. Specimens geometry

The specimen geometry (see Fig. II.27) has been chosen in order to localise strain in the central section, and to avoid as much as possible plastic deformation of other sections. The ratio between the central section and the second section is 3/5, and it can be seen on Fig. II.27.c that the deformation is localised in the central section.

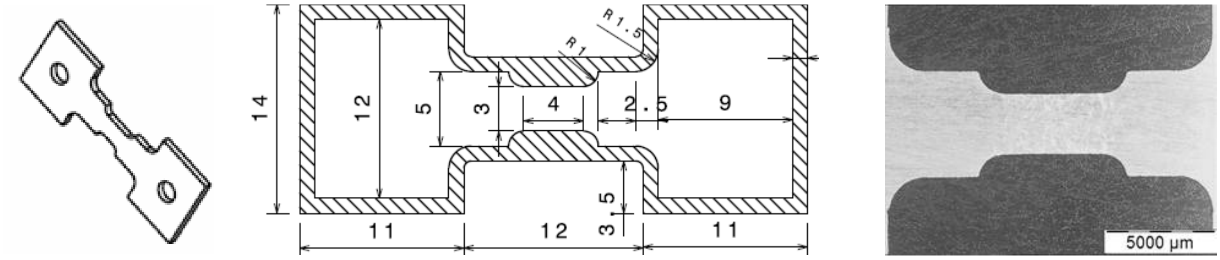

Fig. II.27. TSAXS specimen geometry

(a) 3D image of the specimen. (b) Electrode geometry; the inner measures are equal to the specimen measures + 0.3 mm. (c) A specimen after straining. The central section is the only one plastically deformed.

The specimen is held on the grips by 3 different means. On each side, two vertical stops prevent specimen motion (linear bearing); moreover, a grip blocks the slip (surface bearing). In case of slip, the screw which blocks the grip on the specimen can also play a role of punctual bearing.

ii. Specimens cutting

The specimen profile is cut by spark erosion cutting, in 5 mm thick plates taken from the original 76mm thick plates (see II.A.2.a). The electrode presented in Fig. II.28 has been designed for this operation.

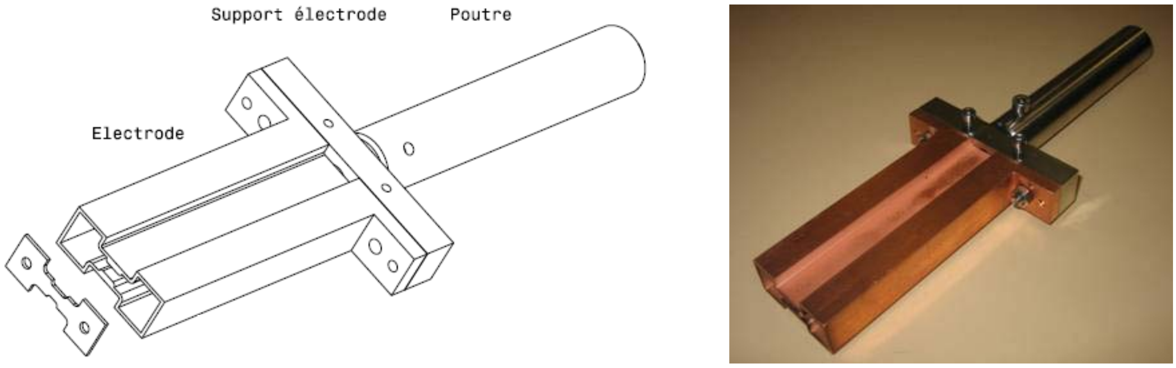

Fig. II.28. TSAXS specimen electrode

The spark erosion electrode is made of copper, mounted on a stainless steel holder.

The 5 mm thick profiles are then sliced into 500 µm specimens. Some of them remain in the T7651 state while the other are completely heat treated, in order to obtain different tempers.

iii. Specimen thinning

For the SAXS measurements, the specimen's surface has to be flat and scratch-free and it has to be between 100 and 200 µm thick for absorption requirements. Moreover, the central section has to be constant (± 1%) µm to prevent strain localisation. The high constrains for this operation has required the design of a specific polishing tool, shown in Fig. II.29.c.

Fig. II.29. TSAXS specimen polishing holder

(a) Body of the specimen polishing holder. (b) Wearpart, spark erosion cut. (c) Complete holder with body, the 2 wearparts, 2 sticks and 4 plastic screws. (d) 3 holders mounted on the polisher holder.

The holder body (Fig. II.29.a) is made of stainless steel. Two aluminium sticks (3 mm diameter) inserted in the specimen holes prevent lateral motion of the specimen, stuck on the bottom surface of the holder by a water droplet. Two AA7449 wearparts (Fig. II.29.b) increase the apparent surface of the specimen and avoid localized wear of the specimen edges. The sticks and wearparts, maintained by plastic screws, are polished together with the specimen (see Fig. II.29.c).

Specimen holder geometry has been chosen in order to fit to the polisher holder geometry provided by Buehler for standard circular specimens (see Fig. II.29.d). Three specimen holders are mounted on the holder to increase the productivity of the thinning. The thinning operation is regularly interrupted to control the specimen thickness and thickness variation, and in some cases individual thinning is performed to correct it.

At the end a typical specimen is between 100 and 200 µm ± 1 µm thick on its whole area.

II.D.1.d. Experiments

i. Programme

A *Labview* programme has been developed to measure and control the experiments. It allows strain rate or load control: tensile, relaxation and creep tests can be achieved. An automated mode allows the programming of complex mechanical sequences. Temperature is controlled by an external thermo-controller, which is not run by the programme. Time, load and strain are recorded simultaneously.

The architecture of the programme is shown in Fig. II.30. A manual mode (stage IV) has been added to the originally planned programme to authorize more complex experimental programmes and to control the end of the experiment.

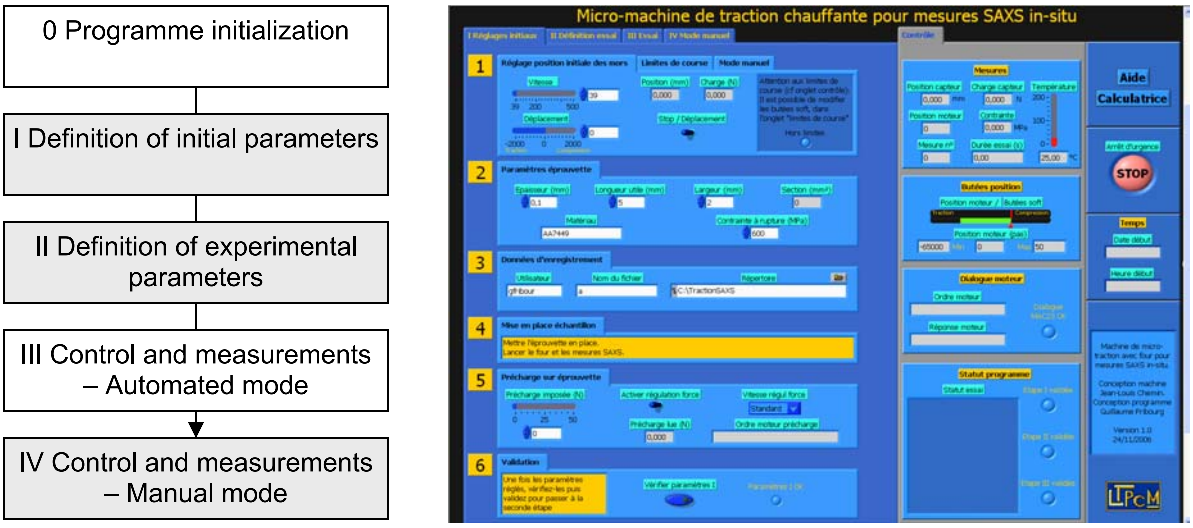

Fig. II.30. TSAXS programme

(a) Programme architecture. In white: the computer-controlled stage. In grey: the stages controlled by the user. (b) Programme user interface (Here: stage I).

ii. Results and data processing

One has to distinguish the simple SAXS from the thermomechanical measurements. The standard SAXS processing treatment described in II.C.4 is performed. However, as the thickness accounts for the integrated intensity value (see equation (II.19.)), the variation of thickness due to stress has to be accounted in the data normalization. For that purpose, the thickness is monitored in situ during the experiments with two photomultiplicators (see II.C.3.a), located before and after the specimen, which measure the specimen's absorption.

The thermomechanical data consists in load, displacement and temperature measurements. Temperature has been calibrated to have the desired temperature in the centre of the specimen. Displacement, measured as the displacement of the grips, is converted into strain throughout a correction of the device elasticity and division of the obtained value by the length of the central section of the specimen. Indeed, the observation of tensile specimens after straining has shown that the central section is the only one that is strained (see Fig. II.27.c). Load is converted into stress by dividing this value by the specimen's section.

II.D.2. Low temperature tensile device

II.D.2.a. Objectives

An inverse tensile device has been developed in the scope of this PhD. It has been used to investigate the mechanical properties at low temperature. This assembly allows a complete immersion of the specimen into a tank filled with a cooling medium. Thus, tensile tests have been performed in liquid nitrogen (77K or -196°C) and cooled ethanol (temperature controlled at -25°C).

II.D.2.b. Design

This device has been designed to be mounted on the Zwick tensile machine presented in II.B.2.b.ii. It is composed of 2 main modules, made of stainless austenitic steel: the stand (Fig. II.31.a) and the sample holder (Fig. II.31.b). The upper disc of the stand is mounted on the bottom surface of the moving crosshead (Fig. II.32.b). The sample holder is screwed on the bottom disc of the stand on one side (see Fig. II.31.c), goes through the upper disc and the moving crosshead, and is bound to the upper crosshead of the tensile machine on the other side.

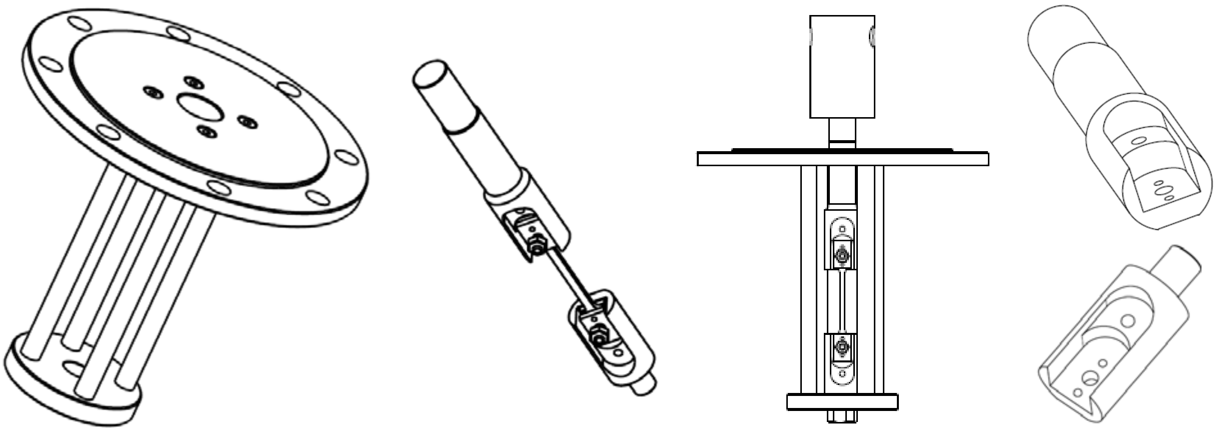

Fig. II.31. Inverse tensile device drawings

(a) Stand. (b) Sample holder and sample. (c) Complete setting. (d) Upper and bottom grips.

To perform a tensile test, the moving crosshead (see Fig. II.5) is displaced in the bottom direction. The columns of the stand are compressed and its bottom disc pulls the bottom grip of the sample holder. The specimen itself is held into the grips, whose drawings are reported in Fig. II.31.d.

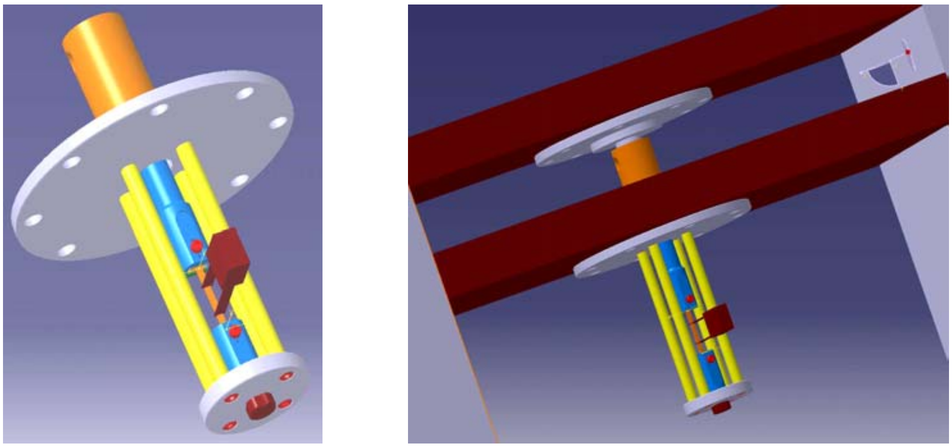

Fig. II.32. Inverse tensile device complete assembly

(a) Device alone. (b) Device mounted on a tensile machine.

II.D.2.c. Specimen and experiment

The specimen geometry is the same as the one presented in Fig. II.7, except that one hole is bored in the heads. It is maintained in each grip by the mean of a screw going through the specimen's head on the one hand (linear contacts) and squeezing the countergrip on the other hand (surface contact).

Once the specimen is mounted, the whole assembly is immersed into a tank filled with a cooling medium. 10 minutes are necessary for the temperature to stabilize, after which the tensile test begins. A dedicated low temperature extensometer measures the sample elongation during the test.

II.E. Conclusion

Both the AA7449 material and the various experimental techniques that will be used in the three experimental chapters have been presented in this chapter.

It has been necessary to explain in a detailed way the experimental set-up and data processing of some of the experimental techniques: on the one hand the less standards experimental techniques; on the other hand those developed during this PhD.

SAXS is the main technique used for microstructural characterization, either in ex situ conditions or in situ during thermal or thermomechanical treatments. Mechanical characterization will mainly consist in tensile, Bauschinger and hardness tests. Thermomechanical characterization will be exclusively performed on the home-developed TSAXS device.

Chapter III. Strain hardening constitutive laws as a function of precipitation

A tool for shot peening modelling

Summary

A physically-based model describing strain hardening of a wide range of metallurgical tempers is developed in this chapter. Based on the Kocks, Mecking and Estrin model, it takes explicitly into account the microstructure. It differentiates isotropic from kinematic hardening, and includes strain rate effects.

This model is able to be implemented in a finite element analysis for shot peening.

Outline

III.A. Introduction

III.A.1. Scientific objectives

As presented in chapter I, strain hardening (or work hardening) refers to the ability for a material to strengthen during plastic deformation. Strain hardening models (or plasticity models) describe the evolution of flow stress as a function of strain, or more generally the evolution of flow stress as a function of different parameters: strain ε , temperature T , strain rate $\dot{\varepsilon}$ and microstructure ms , which can be taken explicitly into account (physically-based models) or not (phenomenological models). The general form of constitutive equations looks as follows:

$$\text{(III.1.)} \quad \sigma = f\left(\varepsilon, \dot{\varepsilon}, T, ms \right)$$

Phenomenological models such as the Ludwick [Ludwick 1909], Hollomon [Hollomon 1945] or the Palm-Voce [Voce 1948] models do not take explicitly the microstructure into account. The consequence is that any change in the microstructure will change the parameters of the hardening law in a way which is not predictable: the validity of those models is limited to one material with a given temper, and the identification procedure for the parameters of the constitutive equation has to be done all over again when another temper is considered. On the contrary, physically-based models are able to predict the hardening law for a wide range of microstructures, provided the microstructure is known and the microscopic mechanisms are understood. To describe a full range of metallurgical tempers (precipitation evolution), it seems therefore interesting to develop a physically-based model.

Plasticity models usually decompose strain hardening into 2 parts: the calculation of the flow stress for a given microstructure and the evolution of the microstructure with strain. The Kocks, Mecking and Estrin (KME) model [Kocks 1976, Mecking 1981, Estrin 1984] is probably the most used physically-based model, because it combines simplicity and adaptability. The main idea of the KME model is to describe flow stress as a function of a physically-based parameter: the dislocation density. Indeed, as plastic deformation is controlled by dislocation motion [Taylor 1934], using dislocation density as the internal variable used to describe the microstructural state of a material is a natural choice. The second point is to relate dislocation density evolution to strain. Finally, the influence of strain rate is taken into account throughout a third equation.

However, this type of model leads to a scalar description of the stress/strain relation and is unable to describe changes in strain path, as it is the case e.g. for shot peening. A simple way to go from a scalar description to a tensorial one is to use Von Mises equivalent stress and strains. But it is not sufficient especially with severe changes in plastic path. In order to do so one has to differentiate between the work hardening which is path independent and the contribution which is polarised by the strain path which has generated it: at the very least, the scalar model has therefore to include both isotropic and kinematic hardening.

III.A.2. Shot peening

III.A.2.a. Generalities

Shot peening consists in impacting a surface with shots with an impetus sufficient to deform plastically the materials surface. The surface modifications produced by this treatment are: (a) roughening of the surface; (b) an increased near-surface, dislocation density (strain hardening); and (c) the development of a characteristic profile of residual stresses [Curtis 2005]: it introduces compressive stresses in the subsurface and balanced tensile stresses in the core [Kozaczek 1999]. It also deforms the component, which is (to some extent) elongated in the plane perpendicular to the shot direction.

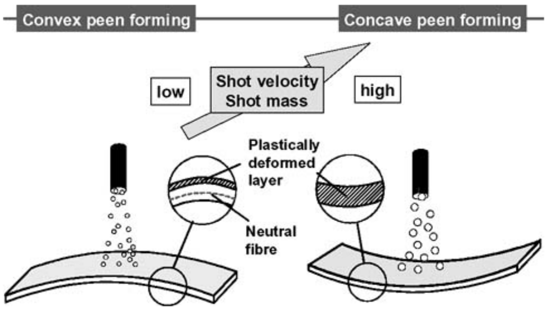

Fig. III.1. Shot peening principle

[Kopp 2002] This figure illustrates shot peen forming, and the effect of changing the shot mass

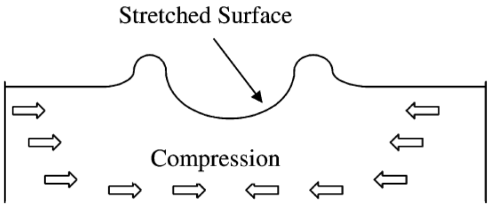

Fig. III.2. Effect of shot peening on the surface

[Meo 2003]

III.A.2.b. Aim of shot peening

This post-machining treatment is used in the aerospace industry for various applications: to improve fatigue life, to form components (in which case it is called “peen forming”) or to correct distortion.

The compressive stress state prevents crack propagation and therefore improves fatigue life and stress corrosion resistance [Ludian 2007]. It is used for instance for welded joints [Meo 2003] or for some components subjected to tension (some aircraft ribs for instance).

Shot peen forming is used to form large aerospace components like wing skin panels or fuselage panels [Kopp 2002]. This process generally has lower manufacturing costs because there is no need for dies and presses or subsequent thermal processes and it is easily reproducible. It also has better adaptability to modern aircraft designs, for example, the capability to form tapered and sculptured integral structures, single and double curved shapes and virtually any size of parts [Wang 2006a].

The same process can be used to correct part distortion after a component has been distorted by heat or machining. According to Wheelabrator group [Wheelabrator 2008], a company specialized in this process, complex structural parts, ribs and spars typically undergo this process.

III.A.2.c. Measuring the effect of shot peening

Shot peening intensity is usually quantified by means of the Almen-scale, which measures the residual arc height of a strip made of a specific material, and of a pre-defined size [Gugliano 2001], the “Almen strip”. It depends on the shot type (metallic, glass or ceramic particles [Dörr 1999]), mass, speed, distance to the surface and angle, as well as the number of impacts, which refers to the coverage rate (for instance 100% or 200%). Almen intensity alone does not provide useful information about the residual stress field induced by shot peening in components. Residual stress measurements (X-rays, hole drilling or layer removal for instance) give a more comprehensive approach and allow predicting part distortion. Those techniques are however costly and can be replaced by Finite Element Modelling.

III.A.2.d. Shot peening and residual stress

As this process implies statistical distribution of the shots, a material section will “see” more than one shot to reach coverage requirements; probably a few shots per unit area. In this FEM calculation (Fig. III.3), Guagliano [Guagliano 2001] predicts the RS field induced by multiple consecutive shot on steel.

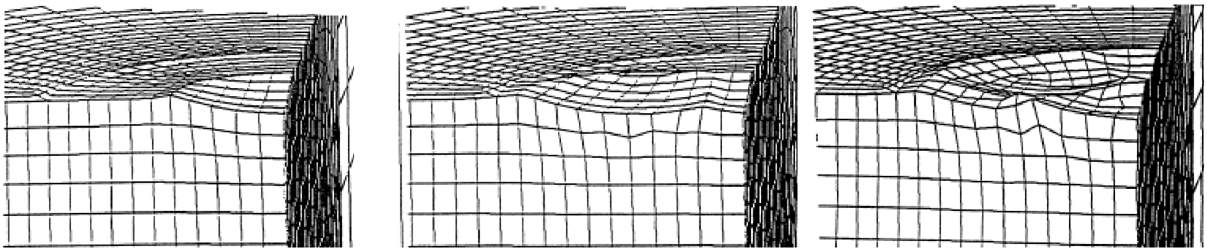

Fig. III.3. Deformation induced by shot peening after 1, 2 and 5 shots

[Guagliano 2001] FEM calculation after 5 consecutive impacts. Stress component in direction 1.

Guagliano showed that the residual stress profile evolves during the impact sequence (shot number) and changes as a function of the shot speed, even if the sensitivity is not highly affected: the larger effect is observed after the first shot. The same effect (Fig. III.4) can be observed in aluminium alloys [Kozaczek 1999, Curtis 2003, Ludian 2007]. Affected depth is classically 300 to 500 µm or sometimes up to 1 mm, depending on the Almen intensity.

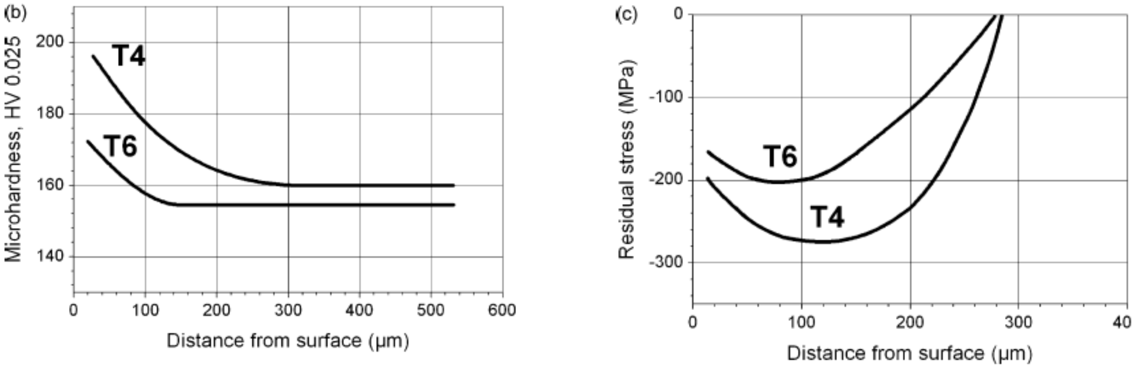

Fig. III.4. Hardness and residual stress profile induced by shot peening in AA2024

[Ludian 2007] Two tempers are plotted: T4 and T6

III.A.3. Main constraints for shot peening modelling

The shot peening model requires a constitutive law representative of the material. The chosen material is the base AA7449 in the T7651 temper, but other tempers may be considered as well.

Changing the shot peening parameters (shot size, velocity…) affects the materials response. In particular, the strain rate dependency of the material has to be accounted in the model, as the strain rate affects the mechanical properties.

To be representative of the industrial process, it also needs to model multiple consecutive shots. This generates complex strain paths, therefore this effect needs to be included in the constitutive model.

Thus the scientific objectives defined in III.A.1 for the development of a constitutive law are well adapted to the modelling of shot peening.

III.B. Literature review: strain hardening modelling

III.B.1. Generalities

III.B.1.a. Strain hardening types

i. Isotropic and kinematic strain hardening

Strain hardening is divided into two main contributions: isotropic strain hardening and kinematic strain hardening. Isotropic hardening is governed by the increase of the density of obstacles to dislocation glide during plastic deformation. This increase is mainly due to dislocation storage but can also include for instance dynamic precipitation which is the formation of new precipitates during plastic flow. Basically, the effective stress σ_{eff} necessary for a dislocation to move in the crystal is equal to the flow stress due to “intrinsic obstacles” (grain boundaries, precipitates) σ_{obst} , increased by the obstacles provided by the accumulated dislocations $\sigma_\rho(\varepsilon)$ so that dislocation motion will proceed:

(III.2.) $\sigma_{eff} = \sigma_{obst} + \sigma_\rho$

On the other hand, kinematic hardening is controlled by the introduction of internal stresses in the material σ_i , which are long range and polarised. These internal stresses result from the incompatibility between the deformations of different microstructural objects (grains, precipitates …). A simple picture is that, under an applied stress σ_{app} , dislocations are subjected to an effective stress σ_{eff} which depends on the internal stress level:

(III.3.) $\sigma_{eff} = \sigma_{app} - \sigma_i(\varepsilon)$

The difference between the two hardening types is schematically represented in Fig. III.5 for the case of biaxial loading:

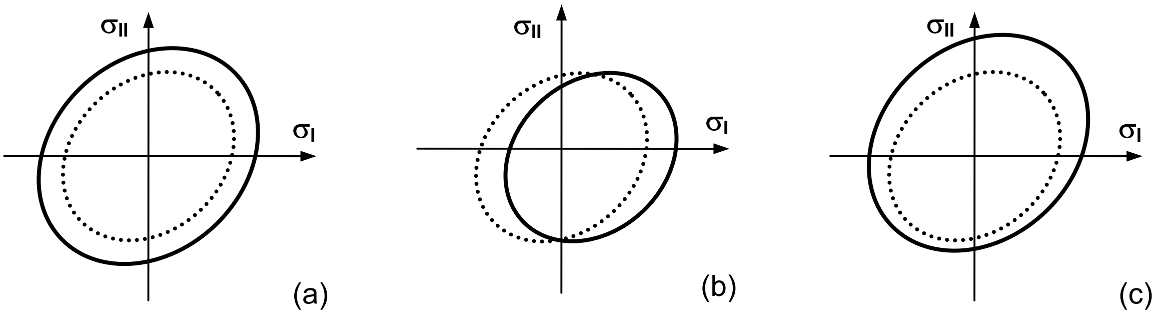

Fig. III.5. Von-Mises schematic view of the yield surface 3 different cases

(a) Pure isotropic hardening. (b) Pure kinematic hardening. (c) Combined isotropic and kinematic hardening. Dashed line represents initial yield surface; full line is the yield surface after cold working.

In case of pure isotropic hardening, whatever the load direction, the yield surface keeps the same shape, but extends. For pure kinematic hardening, loading in tension along direction I will increase the tensile flow stress at the expense of the compressive yield stress along the same direction. Case (c) is a combination of the two hardening mechanisms, which is probably the most common (see III.B.1.b)

ii. Modelling strain hardening

Developing a plasticity model taking into account a change in the strain path means considering these two phenomena:

(III.4.) $\sigma = f(\sigma_{iso}, \sigma_{kin})$

Where σ_{iso} and σ_{kin} respectively refer to the isotropic and kinematic contributions to strain hardening.

iii. Discriminating isotropic from kinematic hardening

The stress-strain characteristics directly results from the combination of equations (III.2.) and (III.3.):

$$\text{(III.5.)}\quad \sigma_{app}^{F}(\varepsilon)=\sigma_{obst}+\sigma_{\rho}(\varepsilon)+\sigma_{i}(\varepsilon)$$

If one realises a compression after a plastic deformation in tension, the isotropic contribution σ_ρ of the forward strain hardening σ_{app}^{F} will also increase the flow stress in compression σ_{app}^{R} as compared to the value of an undeformed material. In contrast, the polarised, kinematic component σ_i will decrease the value of the reverse flow stress σ_{app}^{R}. This test, called Bauschinger test, discriminates naturally between the isotropic and kinematic effect.

$$\text{(III.6.)}\quad \sigma_{app}^{R}(\varepsilon)=\sigma_{obst}+\sigma_{\rho}(\varepsilon)-\sigma_{i}(\varepsilon)$$

The difference between forward (III.5.) and reverse (III.6.) stress is proportional to internal stress:

$$\text{(III.7.)}\quad \Delta\sigma=\sigma_{app}^{F}(\varepsilon)-\sigma_{app}^{R}(\varepsilon)=2\sigma_{i}(\varepsilon)$$

III.B.1.b. Influence of microstructure on strain hardening

The different microstructural features listed in chapter I induce a number of different strengthening mechanisms, all of them contributing in a different way both to isotropic and kinematic hardening.

i. Sources of isotropic hardening

As already presented, the different obstacles contributing to dislocation storage are dislocations, grain or sub-grain boundaries, solute atoms and precipitates (shearable and non-shearable). The materials in which these different storage mechanisms have to be considered are listed in Table III.1:

Obstacle Material	Forest dislocations	Grain boundaries	Solute atoms	Precipitates
Pure single crystal	Yes	-	-	-
Pure polycrystal	Yes	Yes	-	-
Polycrystal with solute atoms	Yes	Yes	Yes	-
Polycrystal with second-phase particles	Yes	Yes	Yes	Yes

Table III.1. Micromechanical features responsible for isotropic strain hardening

ii. Sources of kinematic hardening

The same kind of approach can be made in the case of kinematic strain hardening. The back stress responsible for a Bauschinger effect in a material may be due to incompatible thermal dilatation (case of quenching for instance), grain boundaries (Incompatible deformation between grains and dislocation pile-up inside grains) or precipitates (incompatible deformation between the precipitates and the matrix). Depending on the nature of the material, these different sources of internal stress may be present or not (see Table III.2).

Obstacle Material	Incompatible thermal dilatation	Polycrystalline nature	Precipitates
Pure single crystal	Yes	-	-
Pure polycrystal	Yes	Yes	-
Polycrystal with solute atoms	Yes	Yes	-
Polycrystal with second-phase particles	Yes	Yes	Yes

Table III.2. Micromechanical features responsible for kinematic strain hardening

- Internal stresses due to thermal effects

One has to be aware of the different scales at which these mechanisms operate. The incompatible thermal dilatation is usually related to a temperature gradient at the scale of the sample, leading to a non-homogeneous plastic flow, and finally to an internal stress profile. In a polycrystal, another thermal contribution may come from non-isotropic dilatation in a different crystallographic direction. Nevertheless, this contribution is likely to be limited in aluminium alloys, which are roughly isotropic. In principle thermal stresses can be dealt with at the level of continuum mechanics.

- Internal stresses related to the plastic flow and to the polycrystalline nature

They can come either from grain-to-grain plastic incompatibilities, or from intergranular phenomena. Grain-to-grain plastic incompatibilities can be modelled using a “polycristal plasticity approach”, which basic ingredient is Elsheby’s inclusion model treated in a self-consistent manner: it will depend on texture and possibly on the non-homogeneous state of recrystallisation.

Intergranular phenomena are mainly due to the role of grain boundaries as obstacles to dislocations: dislocation pile-ups may develop, generating a back stress on dislocation sources. Then, when stress is reversed, the dislocations emitted by the source are of opposite sign and are therefore attracted by the pile-up built during the forward step: these pile-ups stresses are therefore kinematic in nature.

- Internal stresses related to polyphase microstructure

When inclusions or precipitates are present inside a grain, two cases have to be distinguished. Either they can be penetrated by dislocations and can undergo the same plastic strain as the surrounding matrix (case of shearable precipitates), or they can’t, in which case the precipitates are by-passed (case of non-shearable precipitates).

In this second case, matter continuity prescribes a matching of the total strain. Since the second phase cannot deform plastically, the “plastic mismatch” has to be counterbalanced by an elastic strain. This will generate an opposite state of internal stress in the matrix and in the precipitate, leading to an intergranular kinematic hardening.

III.B.1.c. Governing microstructural parameters in AA7449

i. Microstructure of AA7449

The complex microstructure of the AA7449 may lead this material to be affected by the various isotropic and kinematic effects listed in Table III.1 and Table III.2. Concerning isotropic hardening, all the sources listed in this table have to be considered. Concerning kinematic effects, it is probably possible to neglect long range thermal effect, if the quench rate is homogeneous in the sample (which is certainly the case, as the samples are thin). The “boundary effects” are certainly present, but the main effect reported in the literature, is the presence of non-shearable precipitates [Boger 2006].

ii. Microstructural differences between the different tempers

The objective is to describe the strain hardening behaviour of a wide range of tempers of the commercial 7449 aluminium alloy. Depending on the material temper, different microstructures have to be considered. The common point of these materials is that they all have the same grain microstructure and composition. Their difference is inherent to their precipitation state: the precipitate volume fraction, precipitate size and coherency, solute fraction in the matrix… which all have a determining role in the strain hardening behaviour of a material. The differences between all these materials are summarized in the next table:

Obstacles Material temper	Forest dislocations	Grain boundaries	Solute atoms	Shearable precipitates	Non-shearable precipitates
As-quenched	Yes	Yes	Yes	-	-
Naturally-aged	Yes	Yes	Yes	Yes	-
Under-aged	Yes	Yes	Yes	Yes	-
Peak-aged	Yes	Yes	Few	Yes	Yes
Over-aged	Yes	Yes	Few	-	Yes
Largely over-aged	Yes	Yes	Very few	-	Yes
T7651	Yes	Yes	Few	-	Yes

Table III.3. Micromechanical features responsible for work hardening for each temper

iii. Consequence on strain hardening

As said in the previous paragraph, the precipitate state affects the strain hardening behaviour, both the isotropic part (storage and dynamic recovery) and the kinematic part:

- Solute atoms affect strain hardening, in the case of dynamic precipitation, or by an indirect influence on dynamic recovery processes, which results from mutual dislocation annihilation.
- Small precipitates will be sheared by the dislocations: they will not store dislocations, neither generate long range back stresses. They may have an indirect effect by intragranular strain localisation, and may modify the dynamic recovery processes as well.
- Larger precipitates will be by-passed by dislocations, leaving Orowan loops around them. They will contribute to both isotropic and kinematic hardening. However, one has to address the question of the stability of Orowan loops around particles. Indeed, when several Orowan loops are stored around one precipitate, they can either change slip plane and propagate off-plane in the material, or exert a sufficient shear stress on the precipitate to trigger its shearing which was initially not possible, leading in this case to the annihilation of the loops.
- T7651 temper is associated with a pre-strain before precipitation, which generates dislocations, which will modify the state of precipitation for a given heat treatment, compared to the non-deformed state. This modified state of precipitation, and possibly the pre-existing dislocations at the yield point will contribute both to the yield stress and to the work hardening behaviour.

III.B.2. KME isotropic strain models

The model originally developed by Kocks and Mecking [Kocks 1976, Mecking 1981], was initially dedicated to the study of strain hardening of pure materials.

III.B.2.a. Case of pure materials

i. Flow stress dependence

The easiest way to describe strain hardening in a physically-based model is to express the evolution of the shear stress τ_f necessary to trigger plastic glide on a given slip plane as a function of the dislocation density ρ, through the Taylor equation:

$$\text{(III.8.)}\quad \tau_f = \tau_0 + \tau_\rho = \tau_0 + \alpha\mu b\sqrt{\rho}$$

Where τ_0 is the intrinsic yield stress (assuming $\rho_0 = 0$), τ_ρ the contribution of forest dislocations, $\alpha \in [0.3;0.5]$ a material dependant constant, μ the shear modulus and b the Burgers vector.

ii. Dislocation density evolution

Then the next point is to describe the evolution of the dislocation density during the straining of the material. Locally, two competing phenomena happen (see chapter I): dislocation storage (at obstacles) and dynamic recovery (dislocation annihilation). This competition can be described through the following equation, which relates the evolution of the dislocation density to the shear strain γ_p, ρ^+ and ρ^- being respectively the positive (storage) and the negative (annihilation) contributions to the total dislocation density evolution:

$$\text{(III.9.)} \quad \frac{\partial \rho}{\partial \gamma_p} = \frac{\partial \rho^+}{\partial \gamma_p} - \frac{\partial \rho^-}{\partial \gamma_p}$$

Dislocation storage is inversely proportional to the inter-obstacle distance L_0: the closer are the obstacles, the more difficult the motion and the more efficient the storage will be (i.e. the larger the stored fraction will be), k_1 being an efficiency coefficient (see appendix A.III.1 for detailed calculation):

$$\text{(III.10.)} \quad \frac{\partial \rho^+}{\partial \gamma_p} = k_1 \frac{1}{L_0}$$

Dislocation annihilation (or dynamic recovery) happens when two dislocations with opposite Burgers vector come closer than a critical distance, below which their mutual attractive force can induce for instance double cross slip, followed by annihilation. Dynamic recovery may be written as (see A.III.1):

$$\text{(III.11.)} \quad \frac{\partial \rho^-}{\partial \gamma_p} = k_2 \rho$$

Replacing (III.12.) and (III.14.) in (III.9.) gives the overall dislocation density evolution:

$$\text{(III.12.)} \quad \frac{\partial \rho}{\partial \gamma_p} = k_1 \frac{1}{L_0} - k_2 \rho$$

While dislocation storage is athermal ($\partial k_1 / \partial T = 0$), the dynamic recovery term k_2 is strain rate and temperature dependant: the higher the temperature and the lower the strain rate, the more efficient is dynamic recovery. In other words:

$$\text{(III.13.)} \quad k_2 = k_{20} \left(\dot{\gamma} \big/ \dot{\gamma}_0^* \right)^{-1/n}$$

Where the temperature dependence is included in n, inversely proportional to T [Estrin 1998].

In the case of a pure coarse-grained material, the only obstacles to the dislocation motion are the forest dislocations. The spacing between obstacles is expressed as:

$$\text{(III.14.)} \quad L_0 = \frac{1}{\sqrt{\rho}}$$

Finally, the evolution of dislocation density with shear strain becomes:

$$\text{(III.15.)} \quad \frac{\partial \rho}{\partial \gamma_p} = k_1 \sqrt{\rho} - k_2 \rho$$

iii. Strain-rate dependency

Strain rate affects the dislocation density, as shown by Orowan equation, which relates the strain rate $\dot{\gamma}$ to the mobile dislocation density ρ_m and their velocity υ:

$$\text{(III.16.)} \quad \dot{\gamma}_p = \rho_m b \upsilon$$

Dislocation velocity depends on temperature and stress level through an Arrhenius law:

(III.17.) $\upsilon = \upsilon_D b \, exp\left(-\frac{\Delta G(\tau^*)}{k_B T} \right)$

Where υ_D is the Debye frequency and ΔG the activation free enthalpy, equal to:

(III.18.) $\Delta G(\tau^*) = \Delta G_0 - V^* \tau^*$

In this equation, ΔG_0 is the activation energy, V^* the activation volume and τ^* the effective (temperature dependant) obstacle force. Combining equations (III.16.) and (III.17.) gives:

(III.19.) $\dot{\gamma}_p = \dot{\gamma}_{p0} \, exp\left(\frac{-\Delta G(\sigma^*)}{k_B T} \right)$

Where $\dot{\gamma}_{p0}$ is a reference plastic strain rate, equal to:

(III.20.) $\dot{\gamma}_{p0} = \rho_m \upsilon_D b^2$

At constant microstructure (i.e. at constant dislocation density, precipitate size etc…), $\dot{\gamma}_{p0}$ remains constant; the effect of strain rate on the stress level can be described by [Kocks 1975]:

(III.21.) $\dot{\gamma}_p = \dot{\gamma}_{p0} \, exp\left(-\frac{\tau}{\tau_\rho} \frac{\Delta G}{k_B T} \right)$

Where τ_ρ is the dislocation contribution to shear stress, as expressed by the Taylor equation (III.8.). The form is reviewed by Kocks, introducing the strain rate sensitivity factor m as the sensitivity of the strain rate to variations in applied stress:

(III.22.) $m = \frac{\partial \, ln \, \dot{\gamma}_p}{\partial \, ln(\tau/\tau_\rho)} = \frac{\partial \, ln \, \dot{\gamma}_p}{\partial \, ln(\tau_f)} = \frac{1}{k_B T}\left(-\frac{\partial \Delta G}{\partial \tau_f} \right)$

Combining equations (III.21.) and (III.22.) leads to an approximate expression linking the shear stress to the plastic strain rate:

(III.23.) $\tau = \tau_\rho \left(\frac{\dot{\gamma}_p}{\dot{\gamma}_{p0}} \right)^{1/m}$

Note: the expression of the saturation stress τ_s (stress at $\partial\tau/\partial\gamma = 0$ in the strain hardening curve; see chapter I) includes the strain rate dependency and the temperature dependency (see equation (III.13.):

(III.24.) $\tau_s = M\alpha\mu b \frac{k_1}{k_{20}} \left(\frac{\dot{\gamma}_p}{\dot{\gamma}_{p0}} \right)^{1/m - 1/n}$

iv. Strain hardening rate

The local strain hardening rate is the derivative of shear stress as a function of shear strain. When replaced by equations (III.8.) and (III.15.), this becomes:

(III.25.) $\frac{\partial \tau_f}{\partial \gamma_p} = \frac{\partial \tau_f}{\partial \rho} \frac{\partial \rho}{\partial \gamma_p} = \frac{\alpha\mu b}{2}\left(k_1 - k_2 \sqrt{\rho} \right)$

v. Summary

Generalization of the local shear stress and strain to macroscopic flow stress and strain in the case of a multiple slip systems and polycrystalline material is made using the Taylor factor M :

(III.26.) $\varepsilon = \gamma / M$

(III.27.) $\sigma = M\tau$

The expression of forest dislocation contribution becomes:

$$\sigma_\rho = M\alpha\mu b\sqrt{\rho} \tag{III.28.}$$

Dislocation density evolves as:

$$\frac{\partial\rho}{\partial\varepsilon_p} = \frac{1}{M}\left(k_1\sqrt{\rho} - k_2\rho\right) \tag{III.29.}$$

Strain rate dependency is expressed as:

$$\sigma = \sigma_\rho\left(\frac{\dot{\varepsilon}_p}{\dot{\varepsilon}_{p0}}\right)^{1/m} \tag{III.30.}$$

Strain hardening rate becomes:

$$\theta = \frac{\partial\sigma_f}{\partial\varepsilon_p} = M^2\frac{\alpha\mu b}{2}\left(k_1 - k_2\frac{\sigma_f - \sigma_y}{M\alpha\mu b}\right) \tag{III.31.}$$

This expresses the local slope of the stress/strain curve. This expression predicts a linear relationship between the strain hardening rate and the resolved stress σ_ρ:

$$\theta = \theta_0 - \beta_0\left(\sigma_f - \sigma_y\right) = \theta_0 - \beta_0\sigma_\rho \tag{III.32.}$$

Where $\theta_0 = M^2\alpha\mu bk_1/2$ and $\beta_0 = Mk_2/2$ are respectively the Y-intercept and the slope of the strain hardening curve $\theta = f\left(\sigma_f - \sigma_y\right)$. After integration of the hardening rate expression (III.32.), one obtains the following relationship, linking the flow stress to the plastic strain ε_p:

$$\sigma_f = \sigma_y + \frac{\theta_0}{\beta_0}\left(1 - exp\left(-\beta_0\varepsilon_p\right)\right) \tag{III.33.}$$

It is worth to notice that the KME model provides a physical basis for the Voce law, with a transparent meaning for θ_0 (dislocation storage) and β_0 (dislocation annihilation).

III.B.2.b. Material with precipitates

Estrin [Estrin 1996, 1998, 1999] proposed an evolution of this model to account for a more complex material, in which precipitates or grain boundaries modify the dislocation storage term. This model is known as the KME (Kocks, Mecking and Estrin) model.

i. Flow stress dependence

Some authors use a more refined model, in which two [Estrin 1998] or three [Goerdeler 2001] internal variables are considered. This is probably not useful in our case (low strain uniaxial tensile tests), as a simple one-variable model is expected to well capture the macroscopic mechanical behaviour until stage III hardening [Estrin 1998]: the flow stress evolves as in the case of a pure material.

ii. Dislocation density evolution

Derived from equation (III.10.), the storage term corresponding to Orowan loops storage around non-shearable precipitates separated by a distance L in the glide plane is equal to:

$$\left.\frac{\partial\rho^+}{\partial\gamma_p}\right|_3 = \frac{k_3}{bL} \tag{III.34.}$$

As each precipitate on the glide plane is an obstacle for the dislocation motion, the k_3 coefficient is equal to one. Adding equations (III.15.) and (III.34.)) gives the expression of the dislocation density:

(III.35.) $$\frac{\partial \rho}{\partial \gamma_p} = k_1\sqrt{\rho} + \frac{1}{bL} - k_2\rho$$

For a polycrystalline material, this becomes:

(III.36.) $$\frac{\partial \rho}{\partial \varepsilon_p} = \frac{1}{M}\left(k_1\sqrt{\rho} + \frac{1}{bL} - k_2\rho\right)$$

Where the particle spacing can be related to the precipitate mean size R and the precipitate volume fraction f_v through (see appendix A.III.2):

(III.37.) $$L = \sqrt{\frac{2\pi}{3}}\frac{R}{\sqrt{f_v}}$$

iii. Strain hardening rate

The derivative of the Voce law gives the following expression:

(III.38.) $$\theta = \frac{\partial \sigma_f}{\partial \varepsilon_p} = \theta_{01} + \frac{M^3\alpha^2\mu^2 b}{2L(\sigma_f - \sigma_y)} - \beta_0(\sigma_f - \sigma_y)$$

From now, θ_0 represents the global dislocation storage term, that is to say the Y-intercept of the strain hardening curve; θ_{01} is the forest dislocation storage term and β_0 the dynamic recovery term. If one assumes a small variation of $\sigma_f - \sigma_y$ between 0 and $\sigma_{sat} - \sigma_y$, equation (III.38.) can be approximated by its mean value:

(III.39.) $$\sigma_f - \sigma_y = \frac{\sigma_{sat} - \sigma_y}{2} = \frac{\theta_0}{2\beta_0}$$

The consequence is that the storage term θ_0 can be simplified into:

(III.40.) $$\theta_0 = \theta_{01} + \frac{M^3\alpha^2\mu^2 b}{L}\frac{\beta_0}{\theta_0}$$

Combination of equations (III.40.) and (III.37.) gives:

(III.41.) $$\theta_0{}^2 = \theta_{01}\theta_0 + \frac{M^3\alpha^2\mu^2 b}{\sqrt{\frac{2\pi}{3}}\frac{R}{\sqrt{f_v}}}\beta_0$$

Solving eq. (III.41.) gives the expression of the Y-intercept of the strain hardening curve (see (III.32.)):

(III.42.) $$\theta_0 = \frac{\theta_{01}}{2} + \sqrt{\left(\frac{\theta_{01}}{2}\right)^2 + M^3\alpha^2\mu^2 b\sqrt{\frac{3f_v}{2\pi}}\frac{1}{R}\beta_0}$$

III.B.2.c. Note on the effect of the microstructure on strain hardening

The way solid solution and temperature affect the strain hardening curves is shown in Fig. III.6. Solid solution, due to dynamic precipitation, tends to increase the storage rate and dynamic recovery rate. Temperature is known to increase the dynamic recovery rate, but does not affect the storage rate.

The contribution of the different microstructural mechanisms to the global isotropic hardening may affect both storage and recovery. It may be summarized in a single figure (see Fig. III.7), as proposed by Embury, Poole and Lloyd [Embury 2006]. For instance the high strain hardening rate in the elastic-plastic transition is attributed by the authors to the presence of non-shearable precipitates.

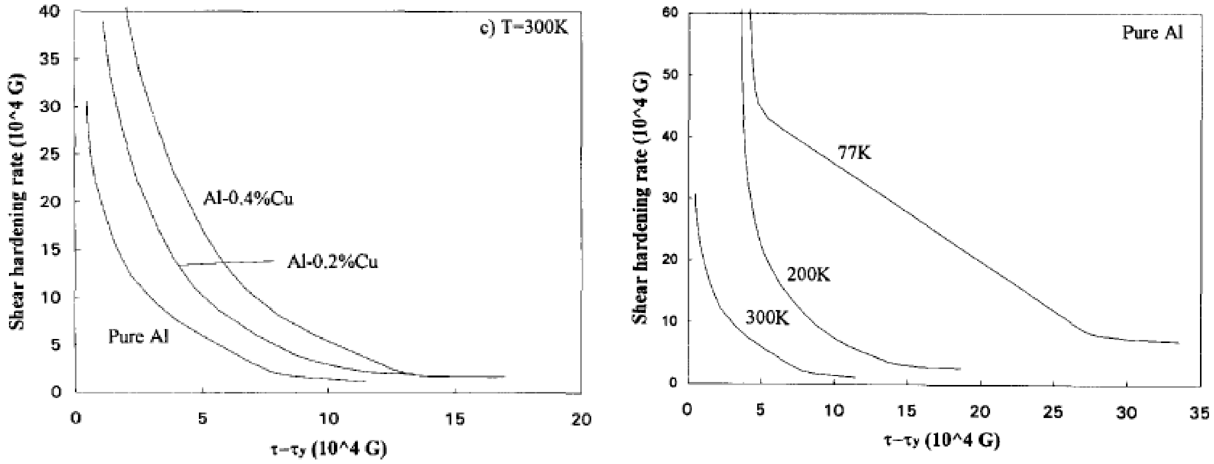

Fig. III.6. Effect of solute and temperature on the strain hardening curves of aluminium

[Deschamps 1996] (a) Effect of solute element content in Al-Cu alloys. (b) Effect of temperature in pure aluminium.

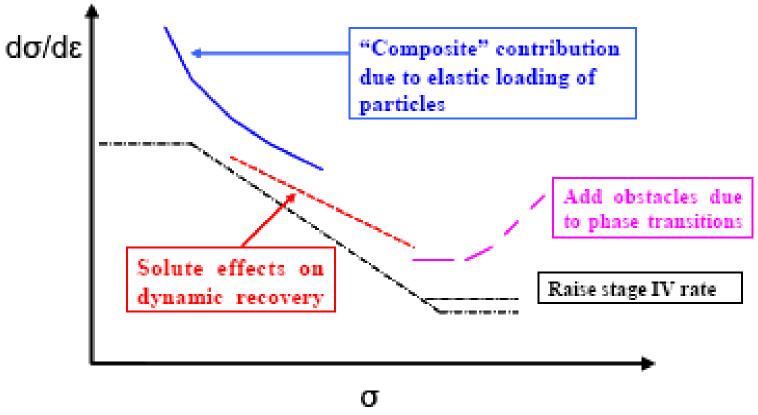

Fig. III.7. Schematic of the effect of precipitation on the overall strain hardening

[Embury 2006] The black dashed curve shows the standard strain hardening curve (dislocations). The other curves show the effect of various contributions to strain hardening: the blue curve corresponds to non-shearable precipitates; the red curve to solute atoms; the pink one to strain induced obstacle generation due to phase transitions, for example, dynamic precipitation during deformation

III.B.3. Kinematic strain hardening

III.B.3.a. Introduction

The Bauschinger effect in heat-treatable aluminium alloys strongly depends on the presence of hardening precipitates. According to Boger [Boger 2006], alloys of the 2xxx and 6xxx series that have been over-aged (semi-coherent or incoherent precipitates) show a large Bauschinger effect. The compressive yield stress is strongly affected by a forward strain and the transient period is important, also for small pre-strain values (0.4%). Materials with less aging have shorter transient periods but show some permanent softening after the reversal, which is a function of the prestrain level.

What is commonly observed during reverse loading of aluminium alloys is a reduced yield stress followed by a transient period with increasing strain-hardening and permanent softening at high strains, where the Bauschinger curve becomes parallel to the forward curve (AA6xxx for instance). This has been observed recently by Proudhon [Proudhon 2008] and Teixeira [Teixeira 2008b].

III.B.3.b. Kinematic strain hardening model

Proudhon relates the internal stress level (or Bauschinger stress) to the mean stress inside the precipitates $\overline{\sigma_P}$ and the precipitate volume fraction f_v:

(III.43.) $\sigma_B = f_v \overline{\sigma_P}$

$\overline{\sigma_P}$ can be expressed as a function of the precipitates' Young's modulus E_P and ε_p^*, the unrelaxed plastic strain, which corresponds to the strain due to Orowan loops around precipitates (see Fig. III.7):

(III.44.) $\overline{\sigma_P} = E_P \varepsilon_p^*$

The formulation of internal stress is then:

(III.45.) $\sigma_B = f_v E_P \varepsilon_p^*$

Unrelaxed plastic strain around precipitates can be approximated for spherical particles of radius r by:

(III.46.) $\varepsilon_p^* = \dfrac{bn}{2r}$

In this expression, n is the number of dislocations stored around a precipitate during the deformation process (see Fig. III.7). This strain dependant parameter has to be evaluated: in the absence of any interfacial recovery process, one would have:

(III.47.) $\dfrac{\partial n}{\partial \gamma_p} = \dfrac{2r}{b}$

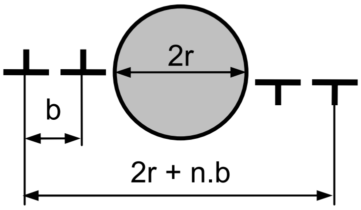

Fig. III.8. Schematic of a spherical non-shearable precipitate surrounded by Orowan loops

This purely geometric expression does not take into account any saturation of the number of loops that can be stored around a non-shearable precipitate. Indeed, the occurrence of relaxation process limits n to a maximal value n^*. A simple way to account for that is to write the Orowan loops formation rate as:

(III.48.) $\dfrac{\partial n}{\partial \gamma_p} = \dfrac{2r}{b}\left(1 - \dfrac{n}{n^*}\right)$

After generalisation to a polycrystal and integration, one obtains:

(III.49.) $n = n^*\left(1 - exp\left(-\dfrac{2rM}{bn^*}\varepsilon_p\right)\right)$

This expression takes well into account the increase of Orowan loops with strain and precipitate size, and saturation towards the n^* value. If one includes this expression into equation (III.46.), one obtains:

(III.50.) $\varepsilon_p^* = \dfrac{b}{2r} n^*\left(1 - exp\left(-\dfrac{2rM}{bn^*}\varepsilon_p\right)\right)$

The internal stress is finally equal to (see (III.45.)):

(III.51.) $\sigma_B = f_v E_P \dfrac{b}{2r} n^*\left(1 - exp\left(-\dfrac{2rM}{bn^*}\varepsilon_p\right)\right)$

This form is equivalent to the isotropic hardening law (with $A = Mf_v E$ and $B = 2rM / bn^*$):

(III.52.) $\sigma_B = \frac{A}{B}\left(1 - exp\left(-B\varepsilon_p\right)\right)$

III.B.3.c. Experimental determination

As already presented in III.B.1.a.iii, Bauschinger stress is generally expressed as:

(III.53.) $\sigma_B = 0.5\left(\sigma_F - \sigma_R\right)$

Where σ_F and σ_R are respectively forward and reverse stress values, which criteria will be discussed in the experimental results (III.C.3). From the experiments, unrelaxed plastic strain ε_p^* can be estimated using the following formulas:

(III.54.) $\varepsilon_p^* = \sigma_B / \theta_B$

Where $\theta_B = \partial\sigma_B / \partial\varepsilon_p$ is the local slope of the curve internal stress vs. forward plastic strain.

However, the difficulty remains to set accurately the criteria to evaluate these values. For this, a detailed preliminary study of the Bauschinger behaviour is required (see III.C.3.b.ii).

III.B.4. Existing approaches combining isotropic and kinematic hardening

It has been explained in chapter I that the addition law for the different contributions depends on the relative strengths and scales of the different contributions to hardening. One possibility [Deschamps 1999b] is to include the contributions of lattice friction σ_{LF} and Hall-Petch hardening σ_{GB} in a single term σ_0, which is seen as independent of the strain level and independent of the precipitation state. Then the other contributions (solid solution σ_{ss}, precipitates σ_P and dislocations σ_ρ) are added as:

(III.55.) $\sigma_f = \sigma_0 + \sigma_{SS} + \sqrt{\sigma_\rho^2 + \sigma_P^2}$

This is reasonable when the number of precipitates and dislocations per unit area are comparable. In other words, if one considers a dislocation-free material, yield stress is expressed as:

(III.56.) $\sigma_y = \sigma_0 + \sigma_{SS} + \sigma_P$

It is generally admitted that the internal stress σ_i contributes negatively to the isotropic flow stress during monotonic loading and therefore changes the effective stress σ_{eff} [Jordon 2007]:

(III.57.) $\sigma_{eff}\left(\varepsilon\right) = \sigma_f\left(\varepsilon\right) - \sigma_i\left(\varepsilon\right)$

Internal stresses are long-ranged while precipitate hardening or hardening by forest dislocations are short ranged, so that the additive treatment seems reasonable.

III.C. Results

III.C.1. Precipitation evolution during aging treatment

III.C.1.a. T7651 temper

This section presents the results of the precipitate investigation of the base material measured by SAXS and TEM. It also summarizes the procedure for obtaining them (see chapter II for more details).

i. SAXS measurements

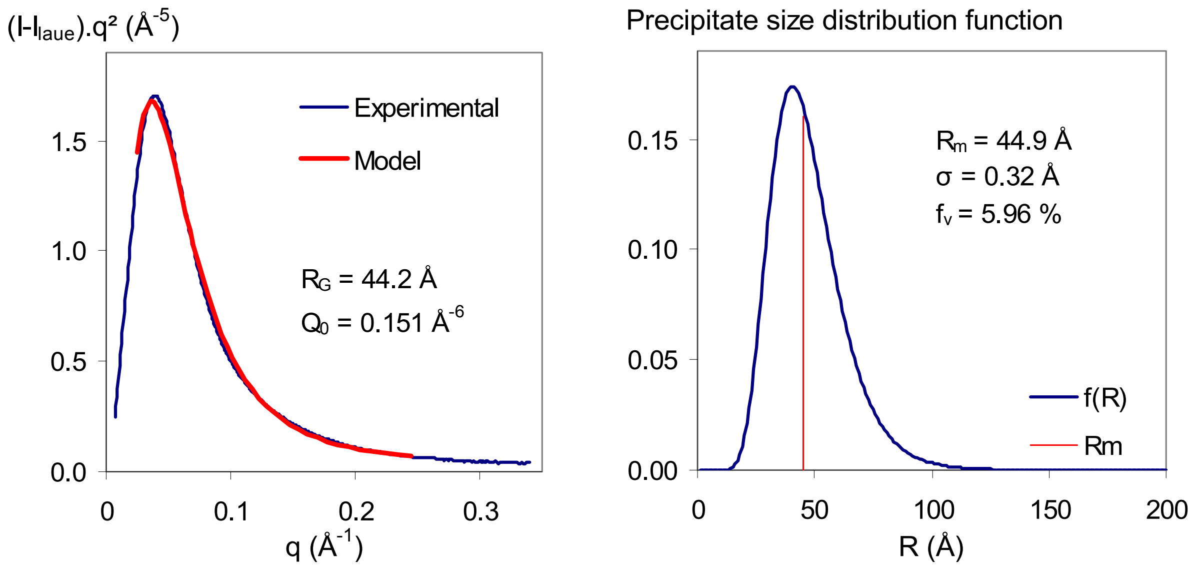

Fig. III.9. SAXS measurements on T7651

(a) Kratky plot; comparison between experimental data and model. (b) Corresponding precipitate size distribution.

Precipitate Guinier radius R_G and integrated intensity Q_0 are measured directly on Fig. III.9.a. The precipitate volume fraction is calculated from Q_0. The precipitate number density N_P is calculated as:

$$\text{(III.58.)} \quad N_P = 3f_v / 4\pi R_G^{\ 3}$$

In this equation, the Guinier radius is supposed equal to the precipitate radius and the precipitates are supposed spherical. The solute atom fraction in the matrix f_m is defined as:

$$\text{(III.59.)} \quad f_m = \left(f_{m0} - f_v\left(1 - X_{Al}^P\right)\right) / \left(1 - f_v\right)$$

Where $f_{m0} = 7.25\%$ is the initial fraction in solute elements. The term $\left(1 - X_{Al}^P\right)$ accounts that the precipitates include aluminium atoms (see chapter II); their composition is supposed constant and $X_{Al}^P = 17.6\%$. The SAXS spectrum can be modelled assuming a lognormal precipitate size distribution with ellipsoidal precipitates. Its parameters are the precipitate mean size R_m, the standard deviation of the distribution σ and the precipitate aspect ratio AR. On Fig. III.9.b, the precipitate size distribution is defined as $f(R) = f_v \times f(R)^*$ where $f(R)^*$ is the normalized distribution function: $\int f(R)^* dR = 1$.

The precipitate Guinier radius is equal to 44.2 Å and the integrated intensity to 0.151, which corresponds to a precipitate volume fraction of 5.96%. Agreement between model and experimental data is very good; it supposes a lognormal size distribution centred on Rm=44.9 Å. (see Table III.4).

ii. TEM

TEM investigations have been performed on T7651 to confirm the precipitate features measured by SAXS.

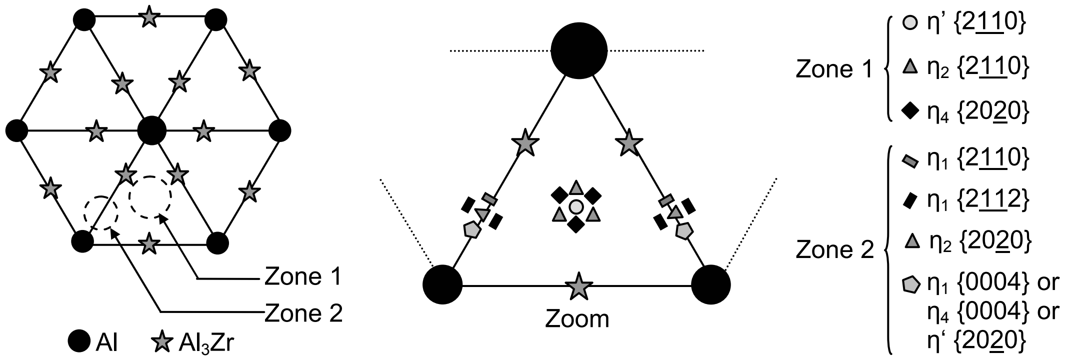

Fig. III.10. Schematic diffraction pattern in (111) projection and spot analysis

[Deschamps 1997]

Analysis of the diffraction pattern of Fig. III.11.b with the help of Fig. III.10 allows us to identify the various phases present in the T7651 microstructure. One can find Al_3Zr dispersoïds, η' and η precipitates, from which various forms exist: η_1, η_2 and η_4.

On Fig. III.11.a, the thin elongated precipitates correspond to the metastable η' precipitates; the larger precipitates are η precipitates. Their size is generally between 20 and 100 Å. They are elongated, with an aspect ratio of 0.2 to 0.7.

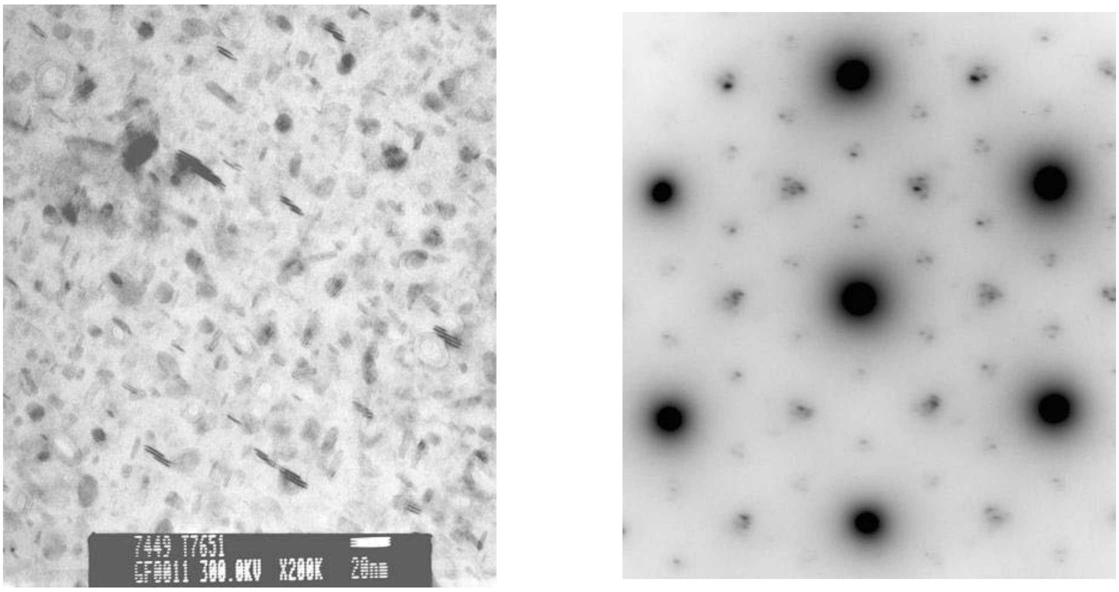

Fig. III.11. TEM results on T7651

(a) TEM image. (b) Diffraction pattern in (111) projection.

iii. Summary

Table III.4 summarises the results of this investigation. Even if a quantitative TEM study has not been made in our case, there seems to be a good agreement between SAXS and TEM. M. Dumont [Dumont 2005] already reported the very good agreement between both techniques. She found out that the precipitate Guinier radius is very close to the precipitate mean size measured by TEM. The result of the modelling is that the precipitate mean size of the lognormal distribution is equal to the precipitate Guinier radius: about 45 Å.

Parameter	Value	Origin
Guinier radius R_G	44.2 Å	SAXS (experimental)
Integrated intensity Q_0	0.151	SAXS (experimental)
Precipitate volume fraction f_v	5.96%	SAXS (experimental)
Precipitate number density N_P	2.19E+05 /µm^3	Equation (III.58.)
Solute atoms fraction f_m	2.34%	Equation (III.59.)
Distribution (III.58.)	Lognormal	SAXS (Model)
Mean radius R_m	44.9 Å	SAXS (Model)
Distribution relative standard deviation σ	0.32	SAXS (Model)
Aspect ratio AR	0.39	SAXS (Model)
Precipitate type	η' , η	TEM

Table III.4. Precipitation state in the T7651 temper

SAXS and TEM results

III.C.1.b. Precipitation evolution during natural ageing

i. Notes on the experimental procedure

Precipitation evolution has been investigated after solution heat treatment of the parent T7651 material and water quench, without pre-stretching. The specimen has been polished before the heat treatment and the measurements began 5 minutes after the quench.

As the exact composition of the GP zones is not known, the calculation of the exact precipitate volume fraction is not possible. However, an estimate of the precipitate volume fraction is made, and allows a comparative study. In reality the true value of f_v can be seen as proportional to the as-calculated value. As a consequence, the calculation of the precipitate number density is also only relative.

ii. Results

Fig. III.12.a shows the evolution of the SAXS signal (Kratky plot) during the natural aging treatment. At the very beginning of the heat treatment (less than one hour), the signal is very low. The precipitate volume fraction is close to 0, as the previous solution heat treatment has dissolved all the precipitates. Then, as shown by the growing area under the curve, the volume fraction increases drastically (see Fig. III.12.c). This is due to the nucleation of the GP zones. It can be noticed that the position of the peak intensity only varies slightly: the Guinier radius increases very slowly (see Fig. III.12.b).

After 30 to 40 hours, the precipitate number density seems to saturate, showing the end of the nucleation stage. The volume fraction still increases, as well as the Guinier radius: growth goes on.

One can calculate the average number of atoms in a spherical GP zone (GPI), using equation (III.60.):

$$\text{(III.60.)} \quad n_{at} = \frac{V(GP)}{V_{at}(Al)} = \frac{(4/3).\pi.R_G{}^3}{a^3/4}$$

The Guinier radius of the GP zones at the end of this treatment (45 hours) is around 7 Å, which corresponds to about 90 atoms. At the end of natural aging (96 hours), GP zones are about 8 to 9 Å.

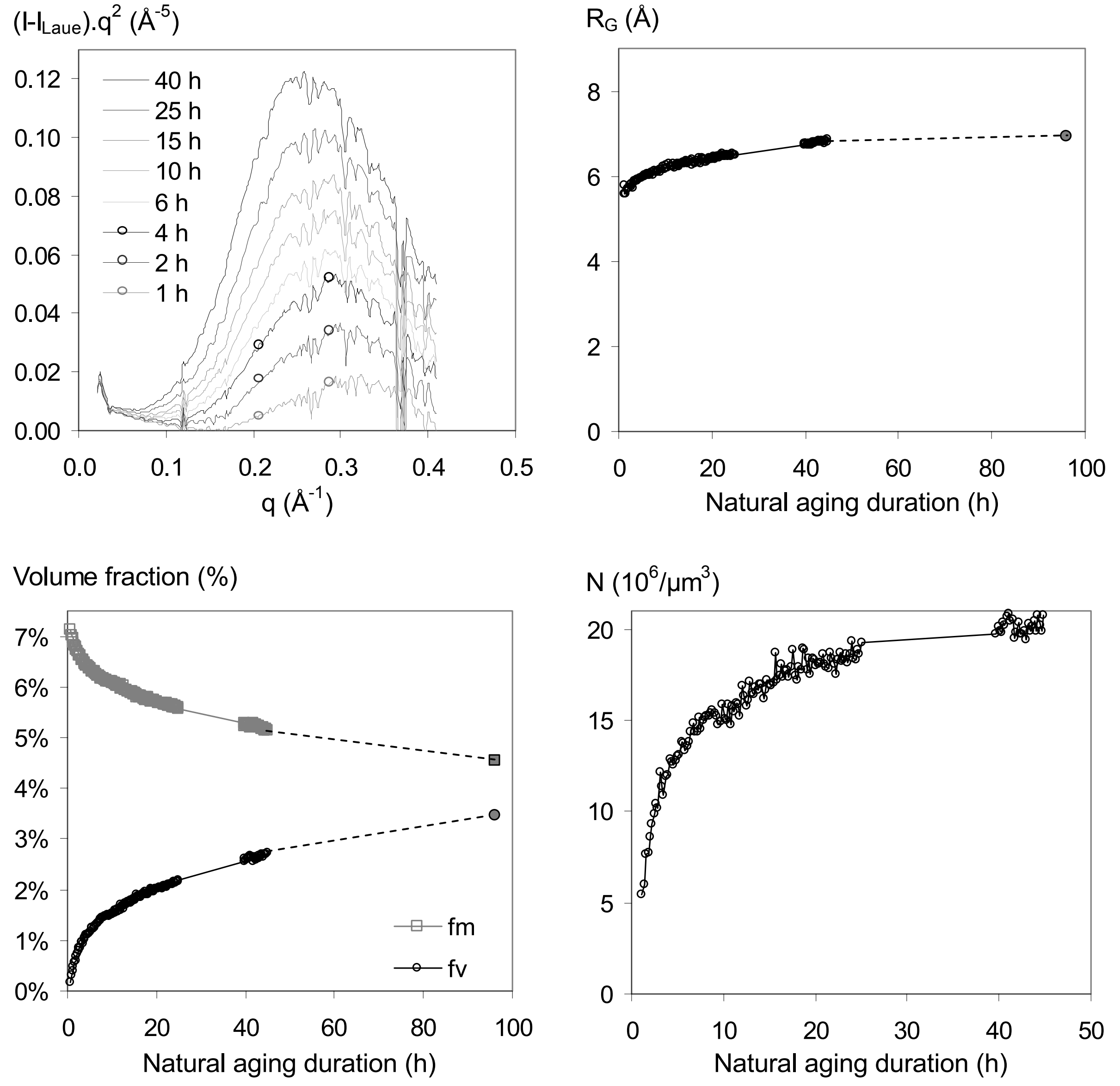

Fig. III.12. Precipitation kinetics during natural aging

In-situ SAXS measurements during natural aging. (a) SAXS signal evolution. (b) Guinier radius. (c) Precipitate volume fraction and solute atoms fraction in the matrix. (d) Precipitate number density. Each point corresponds to one measurement; the full line corresponds to an interruption; the last point to an ex situ measurement.

III.C.1.c. Precipitation evolution during artificial ageing

i. Precipitation kinetics

The effect of artificial aging on precipitation kinetics has been studied by SAXS. The results of these measurements, performed in situ during the two steps heat treatment after natural aging, are presented in Fig. III.13. It presents two main results: the evolution of the precipitate Guinier radius and the precipitate volume fraction, and two derived results: the evolution of the precipitate number density and of the cube of the Guinier radius.

The initial precipitate size corresponds to that of the GP zones, after 96 hours of natural aging: about 8 Å. It grows all along the artificial aging treatment: relatively slowly during the plateau, faster during the heating ramps. At the beginning of the first heating ramp, the volume fraction and the precipitate number density decrease, the GP zones smaller than the critical radius being dissolved.

At two thirds of the first heating ramp, the volume fraction increases again, while the precipitate density decreases very slowly. This can be attributed to the nucleation of metastable η' precipitates.

Then during the plateau at 120°C, the precipitates mainly grow, as shown by the increase of the Guinier radius and the precipitate volume fraction and the very slow decrease of the number density.

Dissolution happens as soon as the second heating ramp begins: about 15% of the precipitates are dissolved, which increases very rapidly the precipitate mean size and decreases the number density. During the second plateau, the volume fraction increases fast at the beginning, probably due to the nucleation of new η precipitates, even if growth also goes on.

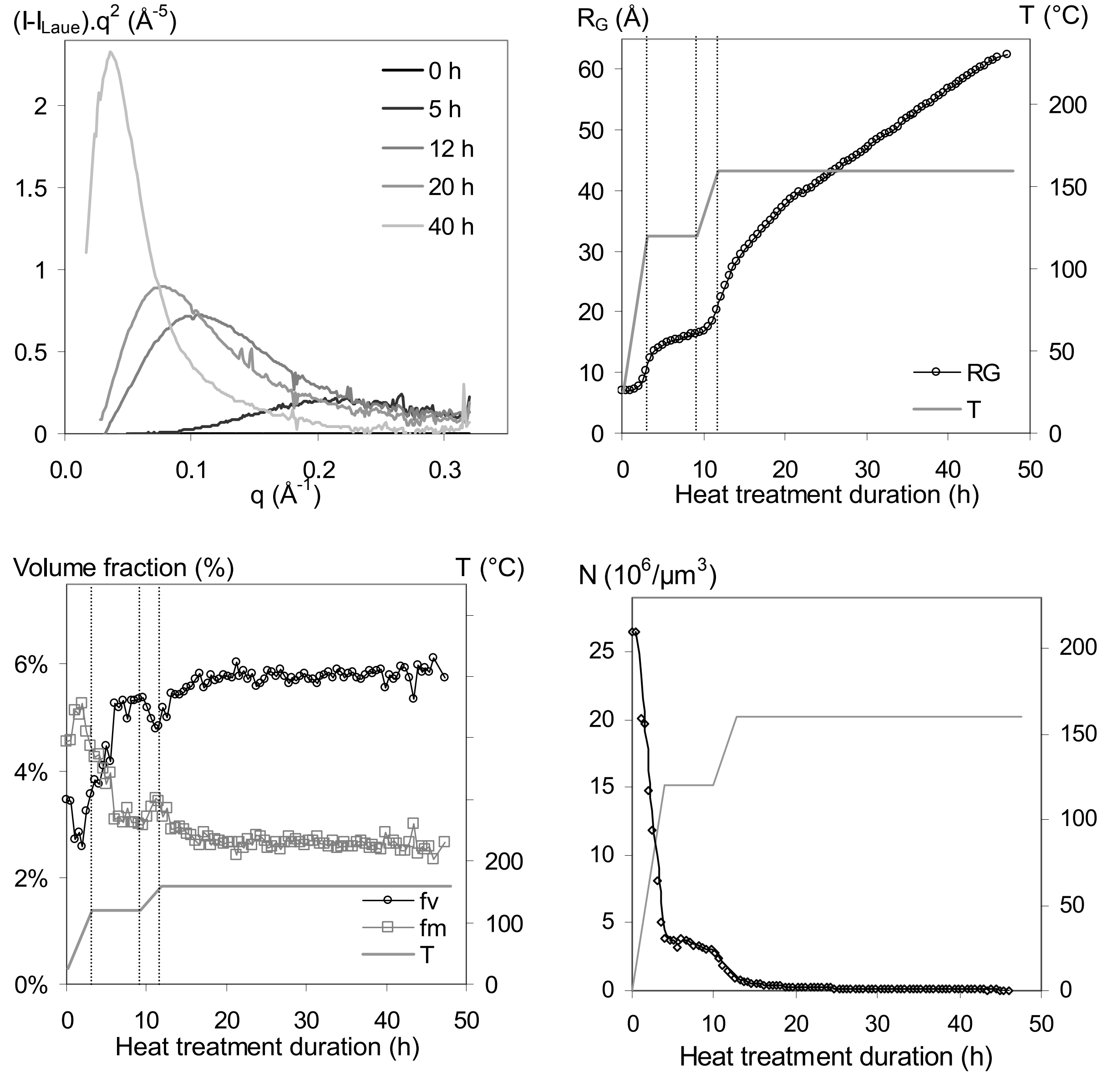

Fig. III.13. Precipitation kinetics during artificial ageing

In-situ SAXS measurements during heat treatment after 4 days natural aging. (a)SAXS signal. (b) Guinier radius. (c) Precipitate volume fraction and solute fraction. (d) Number density. Temperature in grey.

Finally coarsening take place: the precipitate number density is slightly decreasing and the volume fraction is almost constant, while the precipitate mean size goes on to increase at a (more or less) constant rate.

To confirm the evolution of the trend of Fig. III.13 after longer heat treatments, ex situ measurements (corresponding to the tensile samples that will be presented in the following) have been performed. Those results, plot on Fig. III.14, show similar trends. Precipitate volume fraction is almost stabilised at the end of the in situ treatment (45 hours), even if it seems to slightly increase. It stabilises around 6.2% after about hundred hours at 160°C.

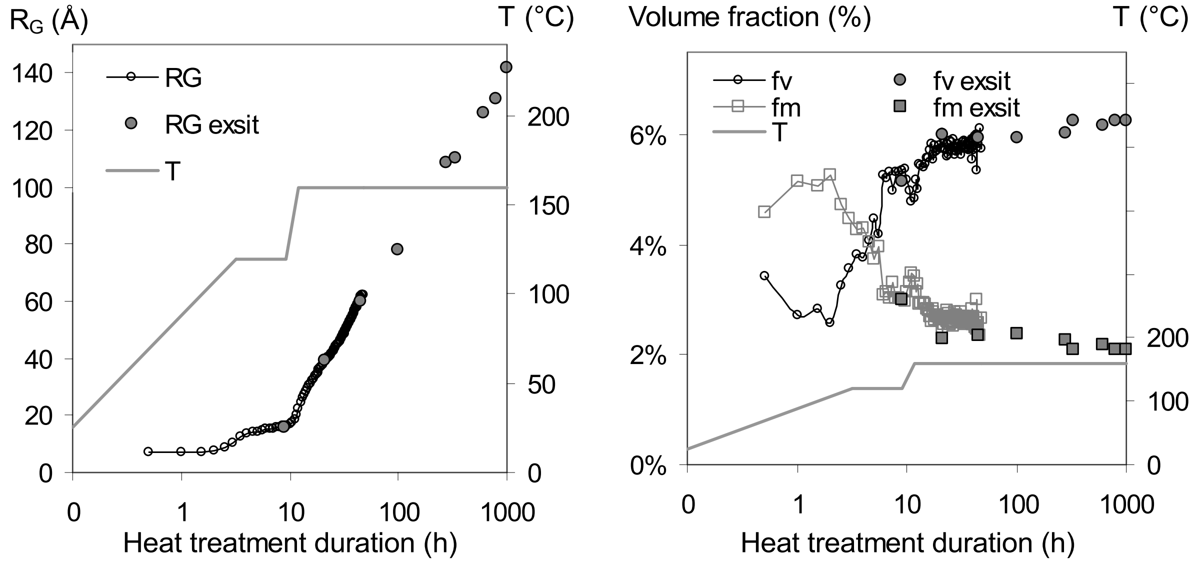

Fig. III.14. Precipitation kinetics during artificial ageing

(a) Guinier radius. (b) Precipitate volume fraction and solute fraction. Temperature in grey. Ex situ measurements ("exsit") after longer heat treatments are added to the results from Fig. III.13.

ii. Morphology and type

The standard aging heat treatment (SAHT) has been interrupted after 45 hours of heat treatment and a TEM specimen cut in the original SAXS specimen. According to the SAXS measurements, 45 hours corresponds roughly to the duration required to reach the same Guinier radius as the T7651 temper: about 45 Å. Fig. III.15 presents the corresponding TEM micrographs.

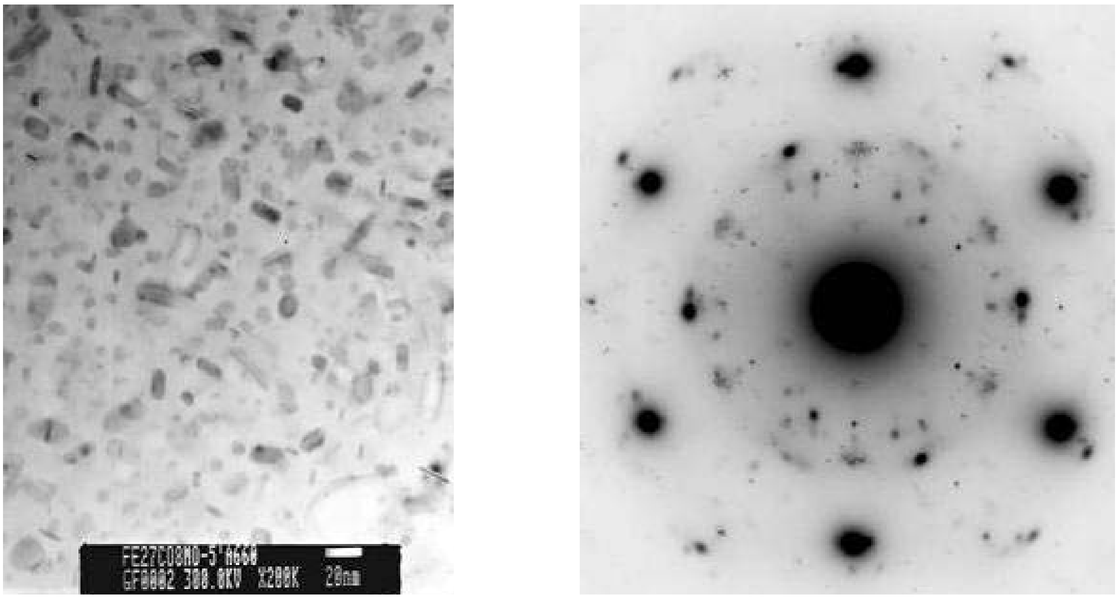

Fig. III.15. TEM results on temper SAHT 45h

(a) TEM micrograph. (b) Diffraction pattern in (111) projection.

As for the T7651 temper (see Fig. III.11), large ellipsoid and thin elongated precipitates can be observed, even if those thin precipitates are present in a very small proportion. This is confirmed by the diffraction pattern, where the spots corresponding to η' are less intense. The precipitates are in average between 3 and 10 nm long, and with an aspect ratio close to 1/3.

iii. Note on the effect of pre-stretching on precipitation

Fig. III.16.a compares the SAXS signal of the two tempers: T7651 and the equivalent (same Guinier radius, same yield stress) SAHT material, the difference between both being the pre-stretching.

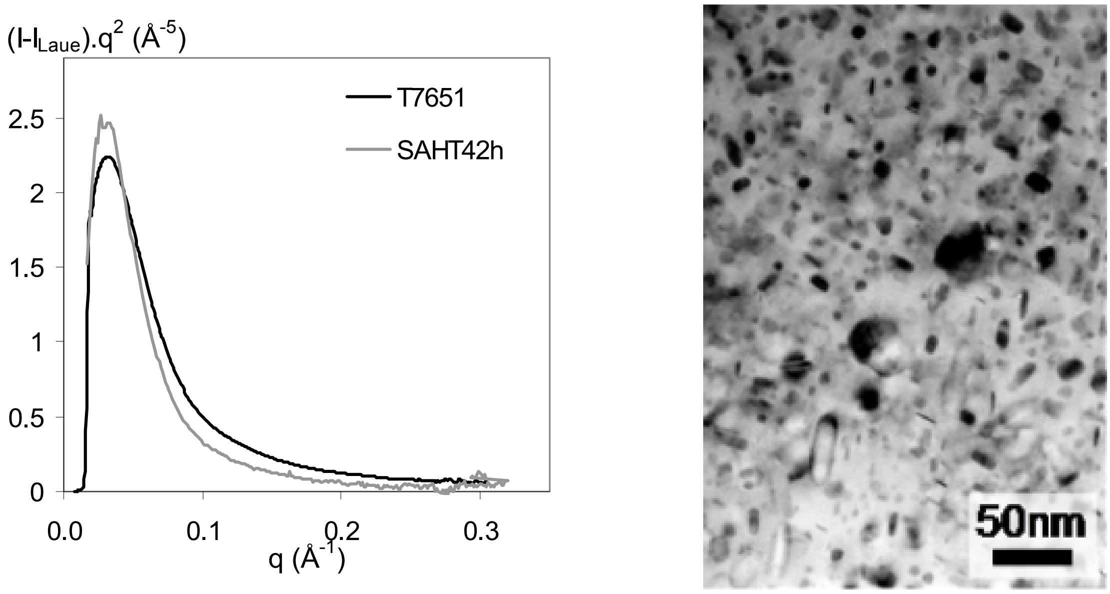

Fig. III.16. Comparison between equivalent SAHT and T7651 temper

(a) SAXS signal. (b) TEM micrograph of temper SAHT45h showing the effect heterogeneous nucleation on a dislocation.

The SAXS signal of the T7651 temper shows higher diffusion intensity at higher diffusion angles, showing the large number of small precipitates. This probably means that the precipitate size distribution is larger. If one looks at Fig. III.16.b, one can see precipitates 4 to 5 times larger than the average precipitate size; this is due to accelerated solute diffusion along dislocations (pipe diffusion; see chapter V). As the T7651 temper has been pre-stretched after the quench, dislocations have been introduced in the material, and diffusion occurred more rapidly, this is why the duration of the T7651 heat treatment is less than the equivalent non pre-stretched material. This also explains why the precipitate size distribution is wider: both homogeneous and heterogeneous precipitation (both nucleation and growth) happened for the T7651 treatment, while mostly homogenous precipitation occurred for the SAHT.

III.C.1.d. Tempers used for strain hardening modelling

From this continuous study of precipitation kinetics, specific tempers have been selected to study strain hardening in a more quantitative way. They were all subjected to tensile tests, Bauschinger tests and their precipitation state measured by SAXS, and will be used for the modelling.

Some of them have been obtained after the standard ageing heat treatment (SAHT) shown in chapter II; the other ("T7651++") have been obtained directly from the base T7651 material further aged at a higher temperature (210°C), from 0 to 10 days. Fig. III.17 shows the results of the SAXS measurements performed at ESRF on these samples.

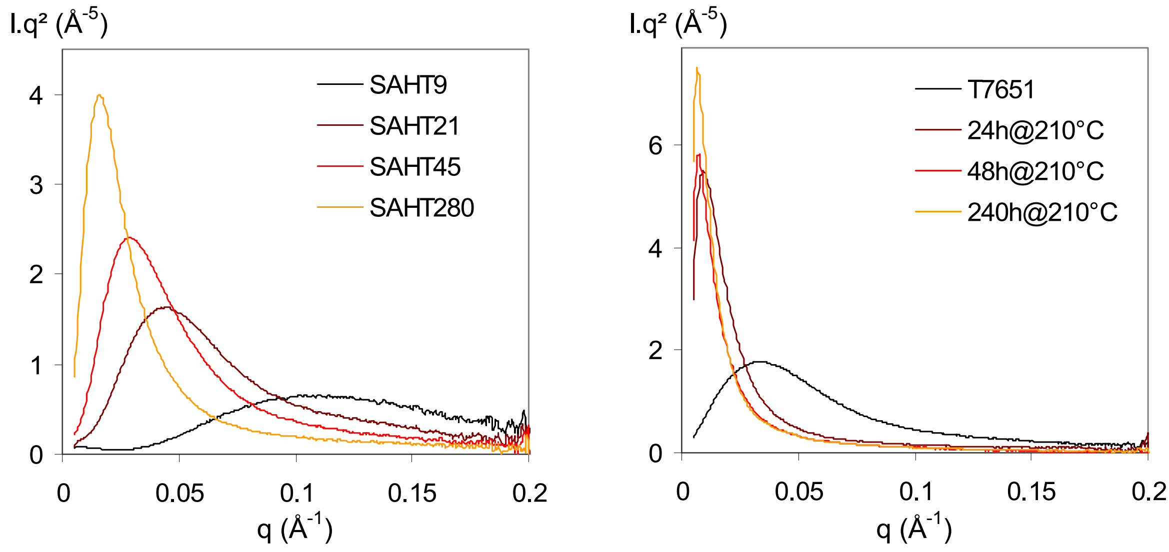

Fig. III.17. SAXS signal of the different Bauschinger specimen

(a) Tempers aged 9, 21, 45 and 280 hours along the standard aging heat treatment presented before. (b) T7651 and T7651++ tempers aged at 210°C during 24, 48 and 240 hours.

The main results (Precipitate Guinier radius and volume fraction) are summarized in Fig. III.18

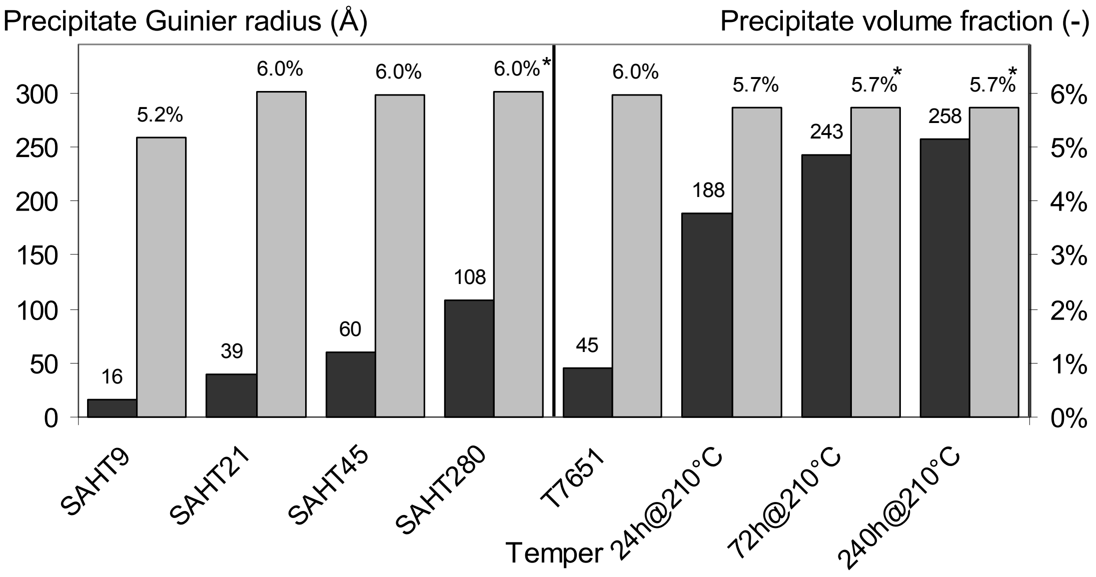

Fig. III.18. SAXS results of the various Bauschinger specimens

The stars indicate corrected values (see next paragraph).

Guinier radius grows during aging treatment: slowly during SAHT at more rapidly at 210°C. Concerning precipitate volume fraction, the behaviour is more complex.

SAHT9 is an under-aged sample, only aged at 120°C during 6 hours, which is not sufficient to reach equilibrium volume fraction. For tempers SAHT21 to SAHT280, aged at 120°C and then at 160°C, the precipitate volume fraction has reached its equilibrium value at 160°C (6%). The first T7651++ sample is the T7651 material aged at 160°C during about 10 hours, this is why its volume fraction is the same. After further ageing at 210°C it decreases to a lower value, corresponding to the equilibrium value at this temperature. For longer heat treatments it is supposed to remain constant (5.7%) even if the measured Q_0 value indicated lower values. Indeed the experimental set-up (sample-CCD distance) did not allow the measurement of the full signal (see Fig. III.17). For very large precipitates, the diffusion angle being too small (see “*” on Fig. III.18 for SAHT280, 72h@210°C and 240h@210°C).

III.C.1.e. Conclusion on precipitation

SAXS allowed a quantitative measurement of the precipitate mean size and the volume fraction, which is necessary for the strain hardening modelling. As found in the literature in 7xxx alloys, the precipitates are ellipsoidal, with an aspect ratio of ~0.4. The Guinier radius is supposed to be equal to the real precipitate mean.

III.C.2. Tensile behaviour

III.C.2.a. Evolution of hardness during aging

If one plots the evolution of Vickers hardness as a function of heat treatment duration (see Fig. III.19; temperature is shown in grey), one observes a typical bell shaped curve. In the under-aged tempers, hardness grows up to a maximum value (hardness peak), which happens at 160°C, after ~18 hours of artificial aging and decreases then for the over-aged tempers. This behaviour can be explained by the precipitate evolution, which induces a transition in the precipitates/dislocations plasticity mechanisms, as it was explained in chapter I. Peak strength happens after 17 to 20 hours of artificial aging, for $R_G \approx 3.3\,nm$.

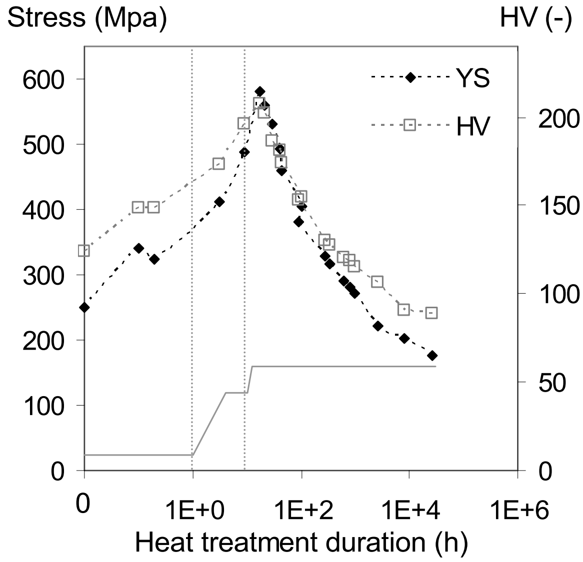

Fig. III.19. Evolution of hardness during aging

Natural and artificial aging are plot on the same figure. Temperature is shown in grey.

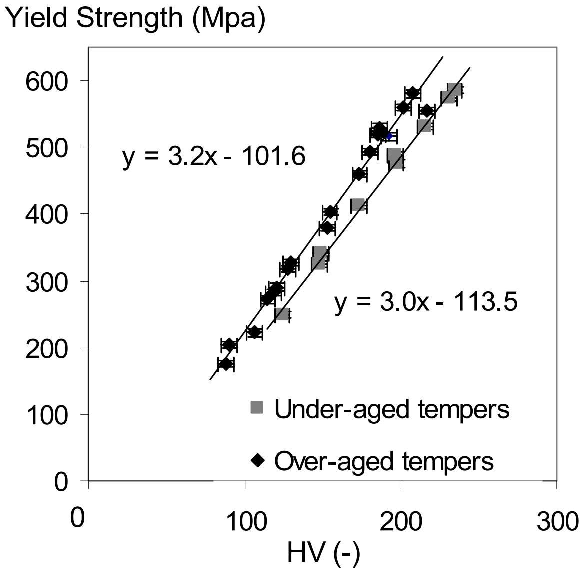

Fig. III.20. Relationship between yield stress and hardness

Yield stress follows a similar behaviour, as also shown in Fig. III.20. A slight difference can be found between under-aged and over-aged tempers. This can be explained by the fact that the strain hardening behaviour changes drastically between under-aged and over-aged materials (see Fig. III.24). As the material deforms plastically during a hardness test, not only yield stress, but also strain hardening parameters have to be taken into account to express hardness.

III.C.2.b. Tensile behaviour of naturally aged tempers

Tensile tests have been made after various durations of natural ageing: from 4 minutes to 96 hours after quench. The first temper (4-5 minutes) corresponds to the “as quenched” temper; the last one (94 hours) to the standard natural aging treatment, which will be the basis of the further artificial aging treatment. The results of those tensile tests are plot in Fig. III.21.

i. Tensile curves

The very first analysis of the stress strain curves states the following elements:

- Natural ageing duration affects strongly the stress-strain characteristics. In particular ductility generally decreases and yield stress is more than doubled during natural ageing.
- Plastic instabilities are present for all the different naturally aged tempers. The threshold (strain or stress) at which those plastic instabilities appear depends on the temper.

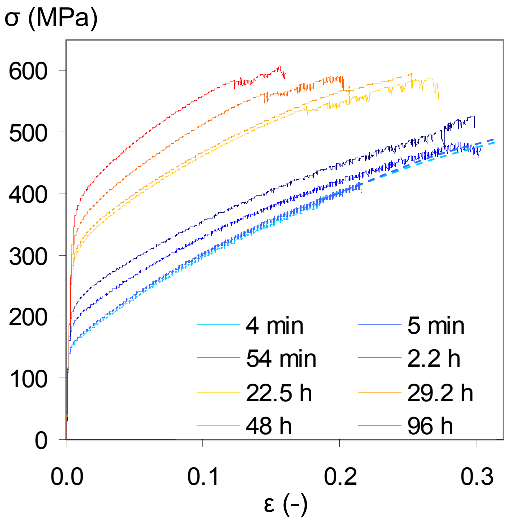

Fig. III.21. Tensile curves of naturally aged tempers

True tensile curves. Natural aging heat treatment lasts from 4 minutes to 96 hours. T=25°C. Strain rate ~10^{-3} s^{-1}.

The first point will be developed in III.C.2.d; the plastic instabilities will be briefly analysed hereafter.

The serrations on the stress-strain are characteristic of a Portevin Le Chatelier (PLC) effect [Gomiero 1992b, Bouabdallah 2006]. PLC effect belongs to the heterogeneous, permanent and propagative plastic deformation phenomena. Heterogeneous because the local and instantaneous strain rate differs from the macroscopic applied strain rate; permanent because it may be observed during the whole plastic strain; propagative because it corresponds to the propagation of PLC bands. This phenomenon is temperature and strain rate sensitive: it only appears for an intermediate temperature / strain rate domain. This dependence was treated for instance in [Bréchet 1995, Lebyodkin 1996].

Those plastic instabilities correspond to a dynamic ageing process, due to the mobility of solute atoms [Bréchet 1996]. The mean dislocation velocity can be expressed as the mean inter-obstacle distance divided by the sum between flight time and waiting time on an obstacle. If the order of magnitude of the waiting time and the atomic diffusion time along the dislocation is the same, solute atoms will diffuse along the dislocation lines; this generates an increase of the flow stress. It decreases brutally once the dislocation line escapes from the pinning. Increasing the strain rate decreases this effect, as it limits the waiting time on the obstacles.

The tensile curves show that the presence of PLC strongly depends on the solute content in the matrix, which decreases during natural ageing process, as GP zones nucleate. The higher is the solute content, the higher is the amplitude of the PLC jumps. Moreover the higher is the solute content, the sooner begin the PLC instabilities: right after yield stress for the higher solute content tempers; after a certain threshold for the longer aged materials, corresponding to a certain strain level [Bréchet 1995].

All the trends observed here are in agreement with the current knowledge of PLC instabilities and we will say no more on this somehow sideway topic.

ii. Strain hardening curves

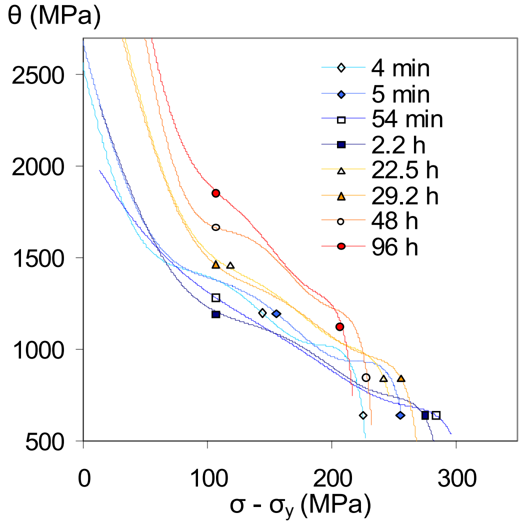

Fig. III.22. Strain hardening curves of naturally aged tempers

It can be observed that the slope corresponding to stage III hardening changes during natural aging. At the beginning it seems to translate towards higher initial hardening rates and higher saturation values. Then, a rotation of the slope towards higher dynamic recovery rates is noticeable.

If Estrin [Estrin 1996] supposes that the presence of solute atoms should only increase the value of the saturation stress, and therefore only change the slope of the strain hardening curve, other authors like Deschamps [Deschamps 1996] have shown that the addition of solute results in a translation of the strain hardening curve on the stress axis, as it is also the case in our material.

III.C.2.c. Tensile behaviour of artificially aged tempers

Fig. III.23 presents the results of the tensile tests at room temperature in quasi-static conditions on various tempers: from the naturally aged temper (already presented in the previous section) to the peak-aged temper and then to over-aged tempers, and largely over-aged tempers. Except for the last two tempers “210°C-72h” and “210°C-240h” which were aged at 210°C for a few days, all the other tempers were obtained following the standard aging heat treatment (SAHT) presented in chapter II: a two stages heat treatments at 120°C and 160°C.

i. Tensile curves

One clearly sees an increase of the yield stress up to a certain aging duration, corresponding to the peak-aged temper (black curve), followed by a continuous decrease of the yield stress along the ageing treatment. Ductility varies as well, reaching its lowest level at the hardness peak. Contrary to naturally aged tempers, where a large PLC effect was observed for all specimens, no serrations are present on the tensile curves of the artificially aged tempers. This is probably due to the fact that less solute is available as precipitation occurs. Indeed SAXS measurements (see III.C.1.c) showed that the precipitate volume fraction increases rapidly at the beginning of artificial aging, and that after 3 hours of heat treatment, the solid solution fraction in the matrix is less than ~4%.

Qualitatively, one can already observe various transitions in the stress-strain behaviour: between 0 and 3 hours, between 12 hours and peak and finally between 24 hours and 40 hours, the stress-strain curve evolves very significantly. One can probably attribute the first transition (~3 h) to the nucleation of shearable η' precipitates; the second one (~14 hours) to the appearance of non-shearable precipitates and the last one (~40 hours) to the disappearance of the shearable precipitates due to coarsening. This behaviour will be clearer if one looks at the strain hardening curves (III.C.2.c.ii).

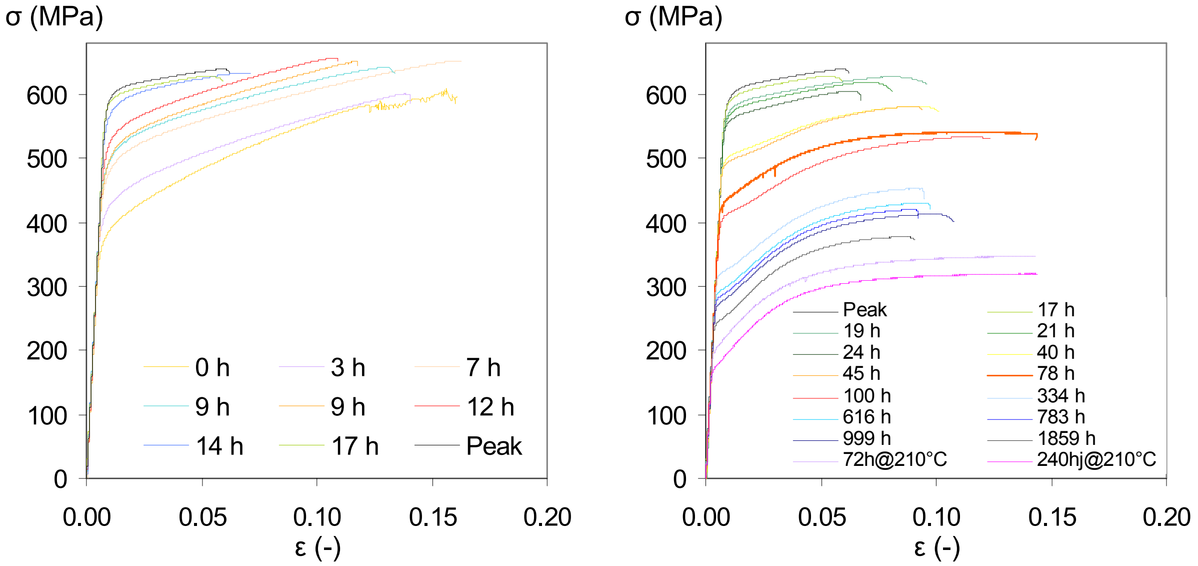

Fig. III.23. Tensile curves of artificially aged tempers

(a) Under-aged tempers: from 4 days of natural aging to peak aging. (b) Over-aged tempers: from peak aging to long over-aging. Aging treatment performed at 120°C and 160°C up to 2000 hours and at 210°C for accelerated aging for the two last samples (aging of T7651 specimen at 210°C during respectively 72 and 240 hours). Tests performed at room temperature, at a strain rate ~10^{-3} s^{-1}.

ii. Strain hardening curves

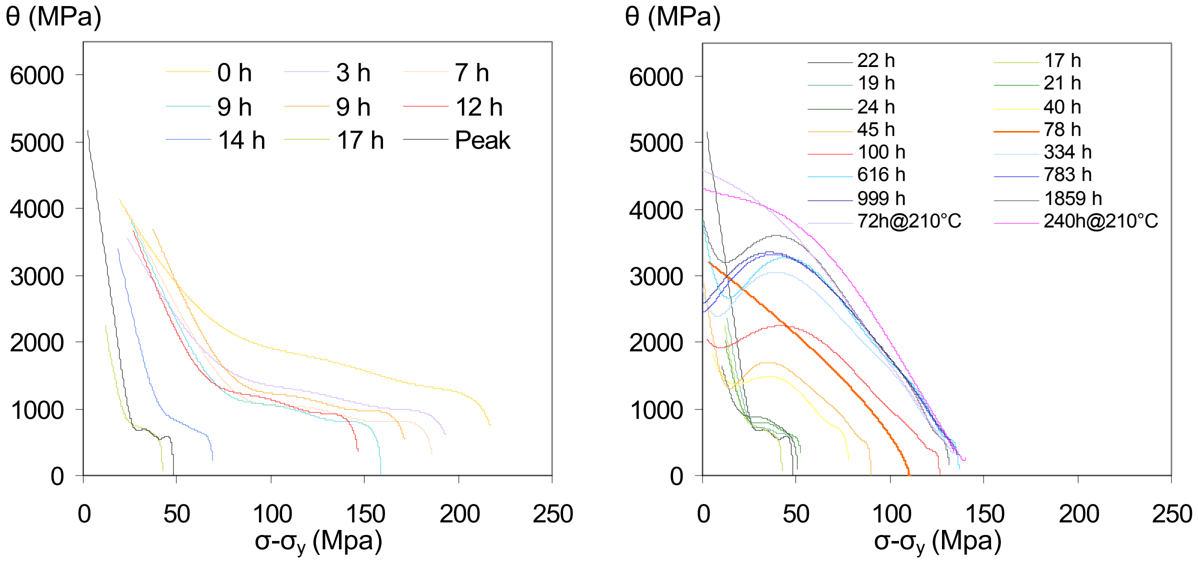

Fig. III.24. Strain hardening curves of artificially aged tempers

(a) Under-aged tempers. (b) Over-aged tempers.

The corresponding strain hardening curves presented in Fig. III.24 confirm the behaviour observed on the tensile curves:

- the initial storage rate is high in the naturally-aged temper and decreases then;
- the strain hardening slope is stronger in the near-peak area than in the under-aged tempers;
- once the near-peak area is overcome (~24 hours), both the storage rate and the initial hardening rate increase rapidly.
- it seems to saturate for the largely over-aged tempers.

A striking point is non-monotonous strain hardening rate (SHR) observed in most of the over-aged specimens. If the under-aged tempers show a traditional decreasing SHR, this is not the case for most of the over-aged tempers which exhibit a dropping SHR up to about 2% plastic deformation, followed by a reversal and finally a decreasing SHR. This may be an experimental artefact but the study of the experimental parameters[1] did not allow understanding this effect, as some contradictions appeared[2]. This behaviour has already been reported in the literature, also for over-aged materials (see [Simar 2007]). To conclude on this point, our belief (see discussion in note 2) is that this effect may be attributed to Orowan loops storage. It has been decided to let this point apart and to measure the strain hardening parameters in the steady-state part of the curve (see examples in chapter II).

III.C.2.d. Evolution of the main plasticity parameters during aging

i. Evolution of YS and UTS

Evolution of hardness during aging was presented in III.C.2.a; YS and UTS are presented in Fig. III.25 and follow a similar behaviour. A fracture study is presented in appendix A.III.5.

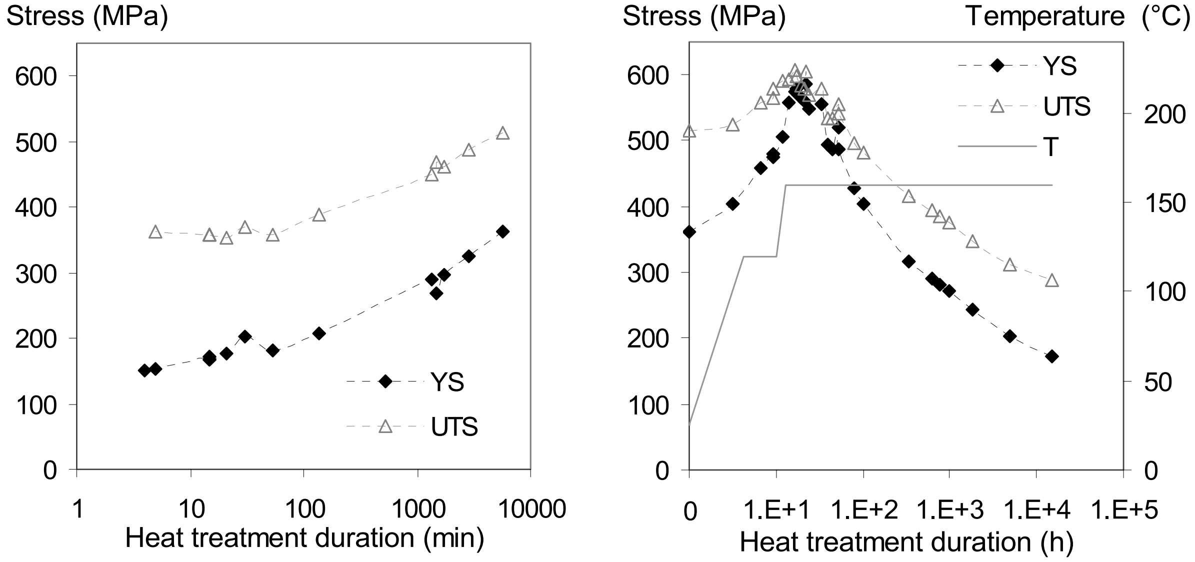

Fig. III.25. Evolution of yield stress and UTS during aging treatment

(a) Naturally aged tempers. (b) Artificially aged tempers. Note: YS and UTS are engineering values.

As presented in chapter I, in the as-quenched temper, only solute atoms are present in the aluminium matrix. The higher is the solid solution content, the higher is the yield stress. Then, GP zones nucleate at room temperature, decreasing the solute content and therefore its contribution to yield stress. On the other hand GP zones, as shearable precipitates, add a further term to hardening. Then, as the precipitates grow, they become non-shearable (near peak area). Finally, coarsening increases the inter-precipitates distance and reduces the Orowan contribution to yield stress. UTS follows a similar behaviour, but as for hardness, is heavily dependent on the strain hardening properties of the material.

---

[1] Those experiments have been performed on different specimen geometries (cylindrical, flat), on two different machines and at different moments; some of the specimen have been heat-treated before machining; some after.

[2] Our first belief was that despite the small thickness of the specimen (3 mm), internal stresses appeared during quenching, as the only over-aged specimens which do not exhibit this abnormal behaviour (“45h”, “72h@210°C” and “240h@210°C”) have been heat-treated before machining. However, some specimens heat-treated before machining also follow this behaviour.
Then, the most probable explanation would be a mechanism induced by the precipitation state, as under-aged do not show this “S” behaviour, while over-aged materials do present it. This effect is indeed highly reproducible in the over-aged tempers. It almost takes place for all the tempers and it has been observed in most of the specimen of the same temper… except for some of them. Another argument for this explanation is that a similar transient has been observed in the reverse part of the Bauschinger tests (see III.C.3). The same tempers present this S behaviour in the same testing conditions (same plastic strain offsets). On the contrary, the very over-aged tempers (72h@210°C and 240h@210°C) do not.

ii. Evolution of strain hardening parameters

One can then consider the initial strain hardening rate θ_0 and the apparent dynamic recovery rate β_0, respectively the Y-intercept and the slope of the strain hardening curves. Those parameters are calculated from Fig. III.22 and Fig. III.24 following the methodology presented in chapter II:

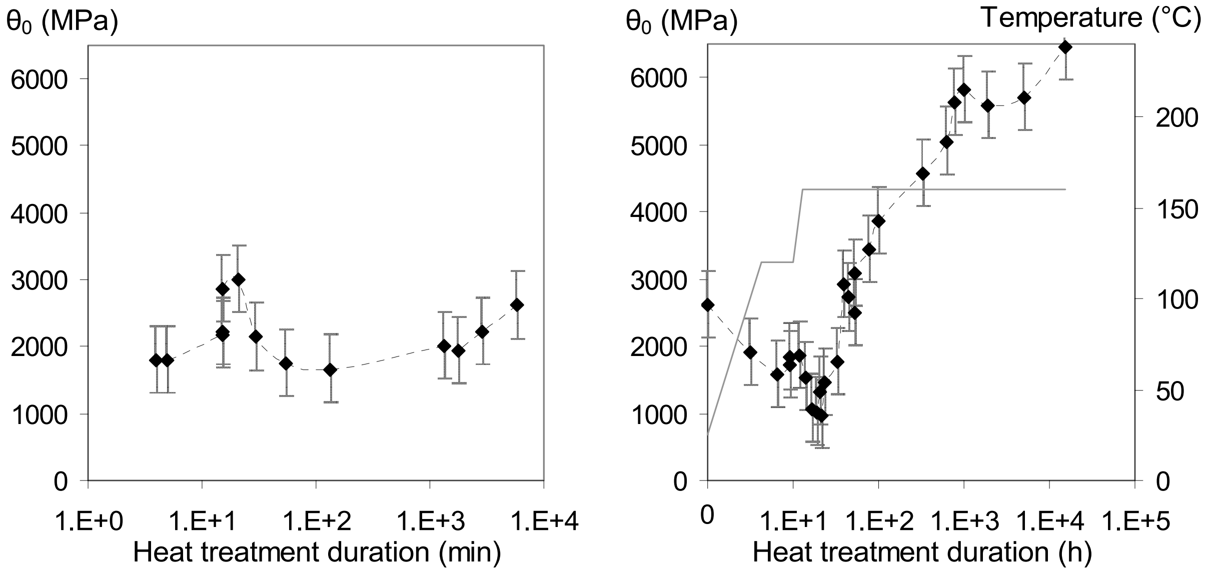

Fig. III.26. Evolution of initial strain hardening rate during aging treatment

(a) Naturally aged tempers. (b) Artificially aged tempers. Note: The last two points (equivalent 5000 and 15000h durations) have been obtained after aging at 210°C; their precipitate volume fraction is lower.

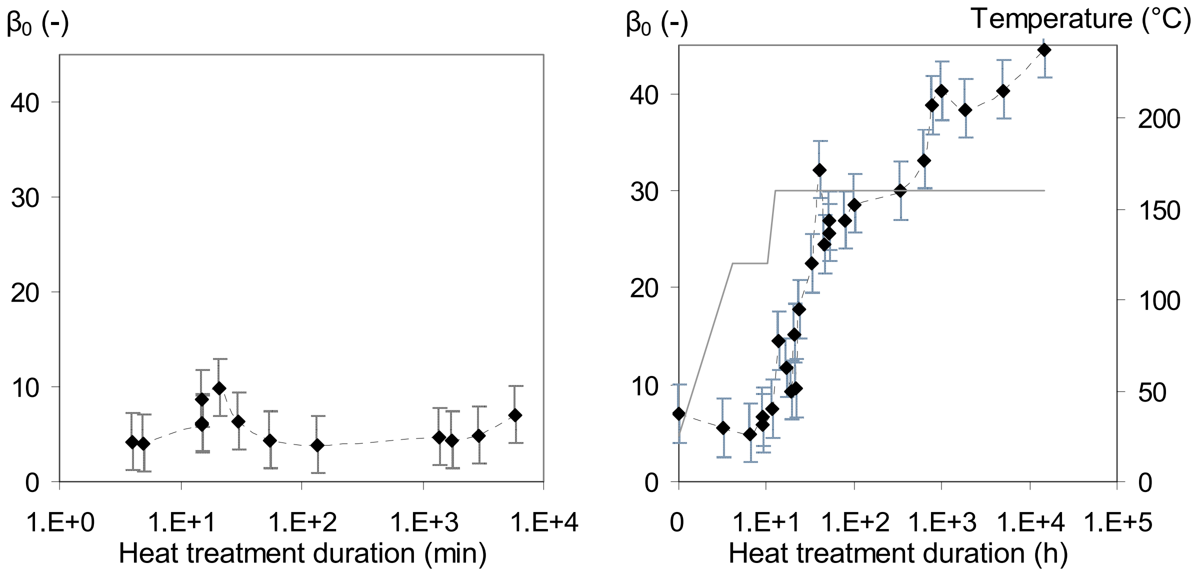

Fig. III.27. Evolution of dynamic recovery rate during aging treatment

(a) Naturally aged tempers. (b) Artificially aged tempers.

Initial strain hardening and recovery rates are almost constant (slightly growing) at the beginning of the natural aging (NA), despite a small discontinuity at the very beginning of the treatment. Both begin to grow at the very end of NA. Then they decrease more significantly as soon as artificial aging begins. Initial storage rate reaches its minimum at peak strength (~18 hours); β_0 slightly sooner: at the end of the plateau at 120°C. Then both increase during the whole treatment, even if they seem to slow down at the end of the artificial aging treatment. Contrarily to what has been observed by Simar on a 6xxx series alloy [Simar 2006], we did not observe a clear decrease of those parameters.

III.C.2.e. Conclusion on tensile behaviour

Three experimental parameters are sufficient to describe the strain hardening behaviour of the material: yield stress σ_y , the initial strain hardening rate θ_0 and the strain hardening slope β_0 . The evolution of those parameters with precipitation is understood and can be modelled, using a model derived from the KME model.

However, prior to that, the Bauschinger effect of the material has to be characterised, in order to include the kinematic contribution to the overall work hardening behaviour.

III.C.3. Bauschinger tests

III.C.3.a. Experimental results

Tension-compression Bauschinger tests were performed on the tempers presented in III.C.1.d, following the methodology proposed by Proudhon [Proudhon 2008] and presented in chapter II. Experimental results for those tempers are presented in the next section: first a comparison between tensile behaviour and Bauschinger behaviour, for various forward plastic strain values. Then the evolution of the Bauschinger stress σ_B (defined as half the difference between the tensile stress and the reverse stress value; see equation (III.61.)) with reverse plastic strain will be shown. Finally the evolution of the internal stress level $\langle\sigma\rangle$ (equal to half the difference between the stress value at maximum forward strain and the reverse stress value; see equation (III.62.)) is presented. This initial study is necessary to determine the parameters that will be used for the further modelling part.

(III.61.) $$\sigma_B\left(\varepsilon_{Rp}\right)=\frac{\sigma_{tens}\left(\varepsilon_p\right)-\left|\sigma_R\left(\varepsilon_{Rp}\right)\right|}{2}$$

(III.62.) $$\langle\sigma\left(\varepsilon_{Rp}\right)\rangle=\frac{\sigma_F\left(\varepsilon_{Fp-max}\right)-\left|\sigma_{Bau}\left(\varepsilon_{Rp}\right)\right|}{2}$$

- Bauschinger curves versus tensile curves

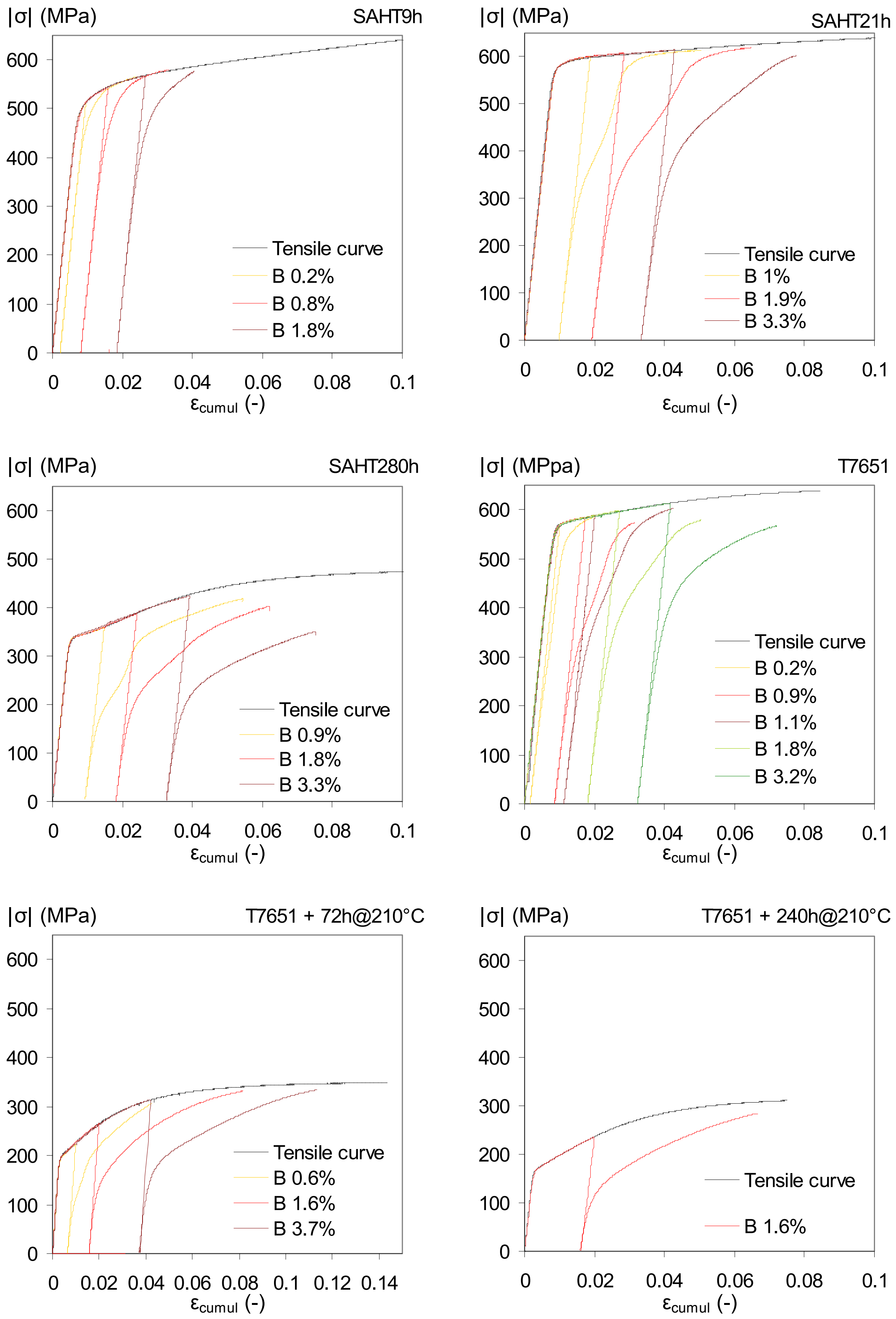

Fig. III.28. Bauschinger curves for various tempers

ε_{cumul} is the cumulative true strain. In the legends "B X%" is the (forward) plastic strain level before reversal.

- Evolution of Bauschinger stress with forward strain level

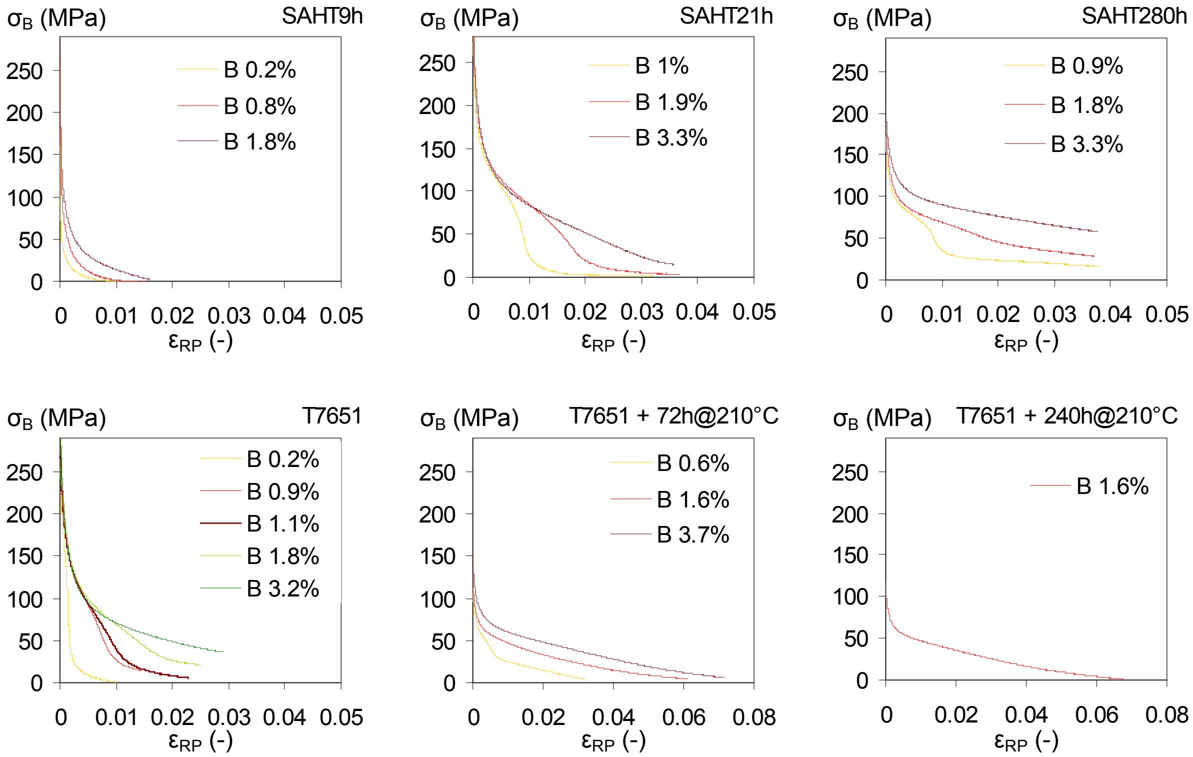

Fig. III.29. Bauschinger stress evolution during reverse loading for various tempers

ε_{RP} is the reverse plastic strain. In the legends "B X%" is the (forward) plastic strain level before reversal.

- Evolution of internal stress with forward strain level

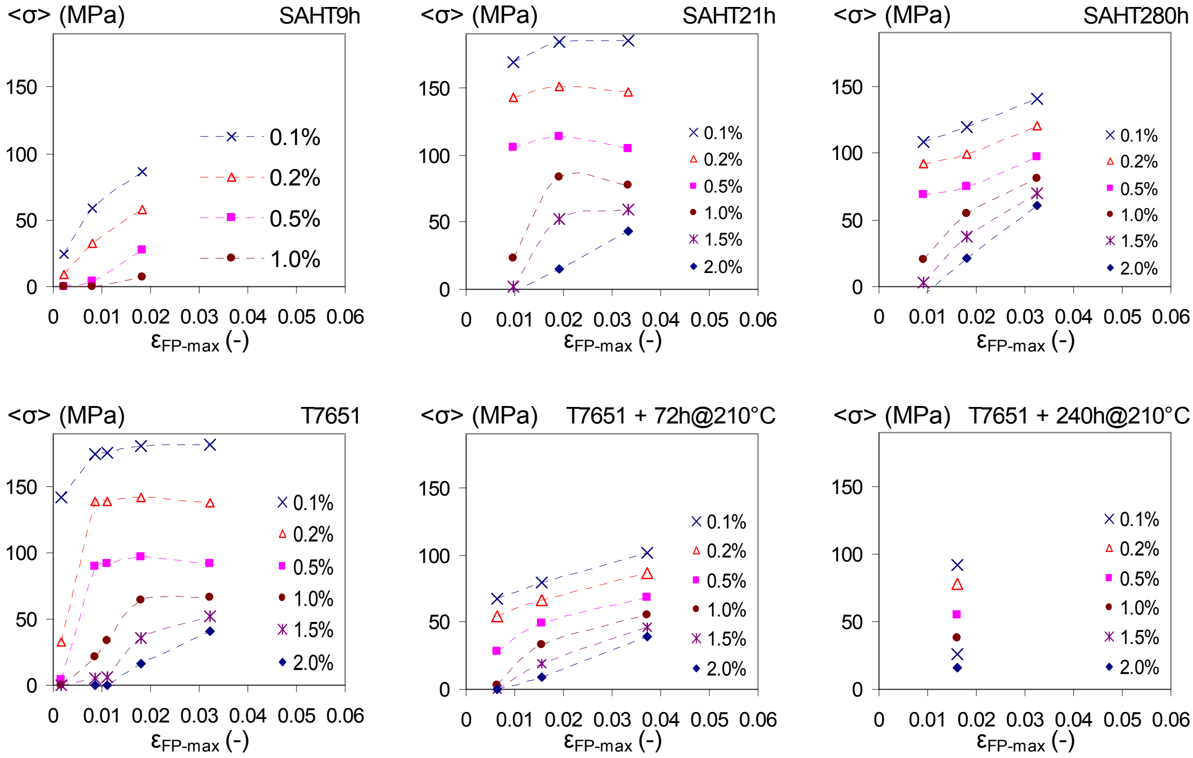

Fig. III.30. Internal stress for various tempers

$\varepsilon_{FP\text{-}max}$ is the forward plastic strain before reversal. In the legends "X%" is the plastic strain offset after reversal.

III.C.3.b. Analysis

i. General trends

Reported from Fig. III.28, the Bauschinger curves of materials SAHT9 and SAHT21 are plotted in Fig. III.31, as examples of the typical observed behaviour.

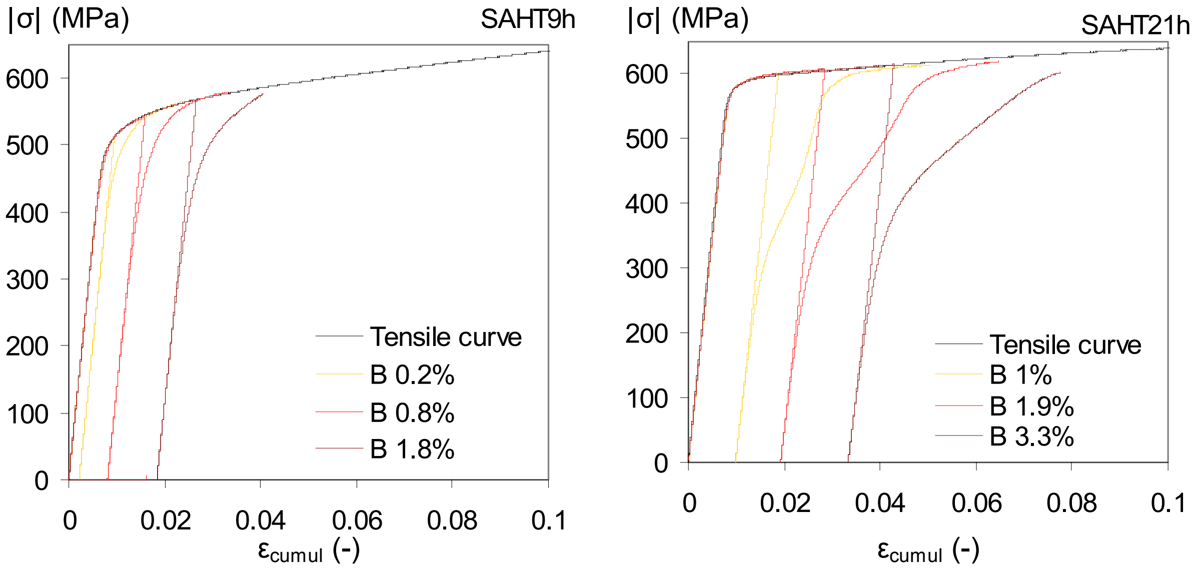

Fig. III.31. Typical Bauschinger curves

(a) Temper SAHT9h. (b) Temper SAHT21h

What one would expect, if there was no Bauschinger effect, is a reverse loading curve following exactly the tensile curve: the stress/strain curve should be independent of the strain path. This is obviously not the case here, which can be identified by a Bauschinger effect.

The first point is that the yield stress during reverse loading is not equal to the maximum flow stress reached during forward loading. Then the general behaviour is the following: a first high strain hardening rate (corresponding to the elastic-plastic transition), followed by a lower strain hardening rate, and finally a very low strain hardening rate, when approaching the tensile curve.

In Fig. III.29, the so-called Bauschinger stress ($\sigma_B = (\sigma_{tens} - \sigma_R)/2$) gives a more comprehensive representation of the Bauschinger effect. It allows identifying more clearly the elastic-plastic transition, and the reverse loading typical behaviour.

This general behaviour depends on the temper. If all the over-aged materials exhibit more or less the same behaviour, the under-aged material (SAHT9) recovers more rapidly its mechanical properties during reverse loading. This lower Bauschinger effect for underaged states was also reported in [Proudhon 2008].

This behaviour also varies with the initial forward strain level. Indeed for the less deformed (in term of forward straining) specimens, an inflexion point can be observed in the middle of the reverse part; it disappears then (here: at 3.3%). Similar observations have been found in the literature.

Various reverse strain offsets have been used in the literature to define a stress characteristic of the Bauschinger effect; classically between 0.001% [Moan 1979] and 2%. The influence of the offset value has been studied in Fig. III.30. The general behaviour is the same: an increasing internal stress level up to a certain forward strain (about 2-3%), after which $\Delta\sigma$ saturates. However, the chosen reverse offset value affects deeply the order of magnitude of the Bauschinger stress (up to 3 times more).

ii. Interpretation: tools

This material exhibits a strong Bauschinger effect, which depends on both the forward strain level and the material temper. The complex behaviour may be described using 3 parameters:

- Yield stress after reverse loading, defined as σ_{R-y} (see Fig. III.32.a). The choice of $\varepsilon_{RP} = 0.1\%$ (see Fig. III.30) represents well the micro-plastic yield stress: $\sigma_{R-y} = \sigma_{RPS-0.1\%}$
- Stress characteristic of the Bauschinger effect, σ_B (see (Fig. III.32.b. and d). $\sigma_B = \sigma_{RPS-2\%}$ has been chosen to overtake the inflexion point, generally present before 2% plastic strain (see Fig. III.29). As will be seen, this behaviour is related at least quantitatively to the reversible motion of dislocations during unloading.
- Reverse plastic strain necessary to reach the same stress as before reversal: $\varepsilon_{RP-eq} = \varepsilon_{RP}\left(\sigma_R = \sigma_{F-max}\right)$ (Fig. III.32.c.)

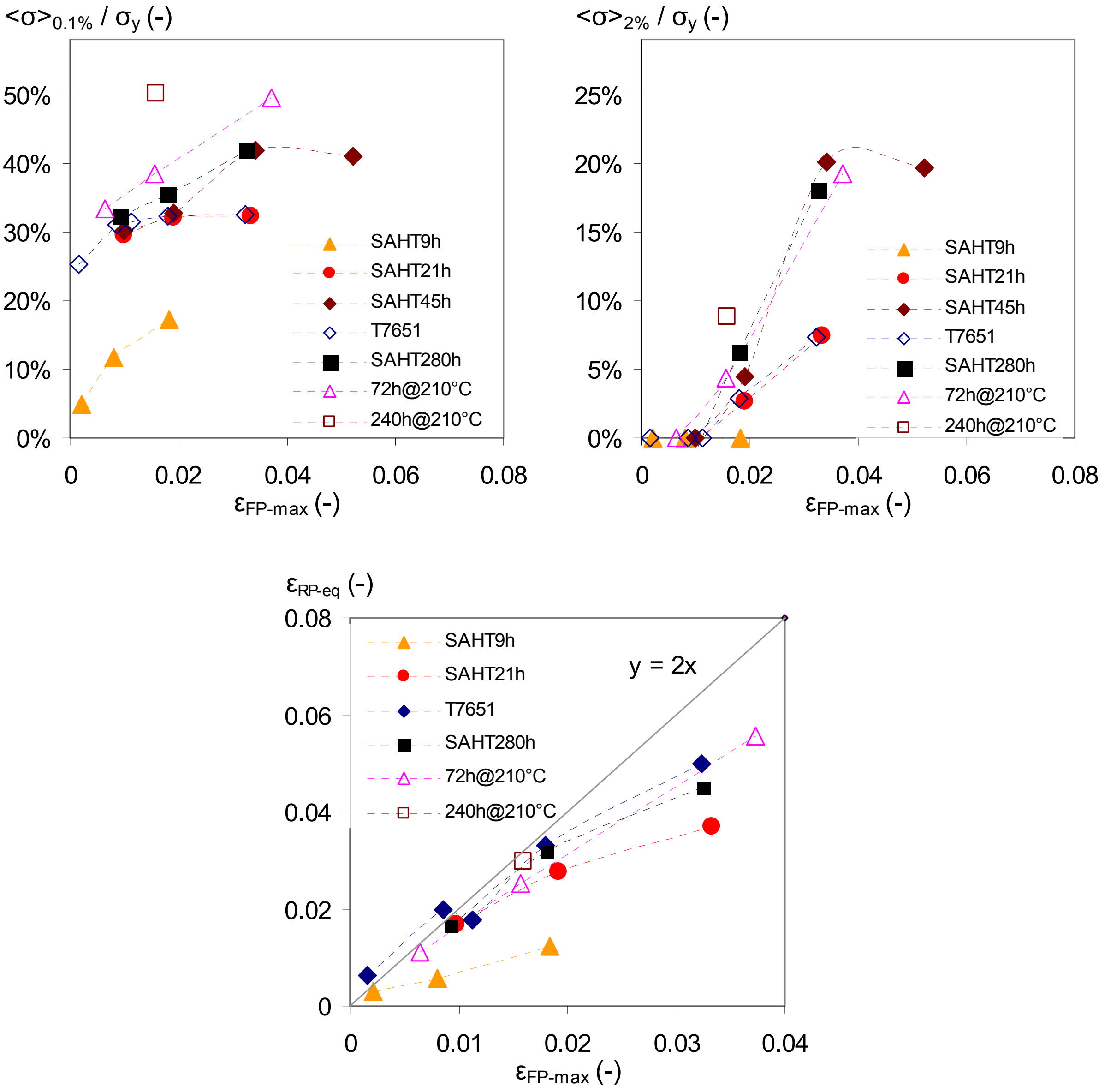

Fig. III.32. Bauschinger parameters evolution with strain of various tempers

Internal stress measured with a reverse plastic strain offset of 0.1% (a) and 2% (b) as a percentage of yield stress. (c) Reverse plastic strain necessary to reach the same stress value as before unloading.

iii. Interpretation: mechanisms

The high level of the difference between the forward and reverse yield stresses indicates that reverse loading is clearly favoured. On the other hand, this range (50-200 MPa) is too high to correspond to the back stress simply due to Orowan loops storage (expected order of magnitude, according to Proudhon's model: 10-50 MPa). An interesting hypothesis would be that dislocation glide is (partly) reversible: the mobile dislocations follow (at least partially) the same path during forward loading and reversal, but in opposite directions.

In that case, the Orowan loops stored around the non-shearable precipitates during forward straining are annealed by the mobile dislocations following the reverse path with opposite Burgers vector. This mechanism happens for instance to the dislocation labelled "2" in Fig. III.33. During the first steps of reverse loading, the non-shearable precipitates are therefore "transparent" to the mobile dislocation and do not contribute to flow stress, since the moving dislocations "swallows" the loops without really "seeing" the particles. One can call this mechanism "Orowan loop helped reverse bypass" (OHRB). If the glide was 100% reversible in a material with non-shearable precipitates, the reverse strain necessary to reach the maximum forward stress level would be $\varepsilon_{RP-eq} = 2\varepsilon_{FP-max}$. One can see on Fig. III.32.c. that this relation is verified only up to ~2% plastic strain for the over-aged materials. On the contrary, $\varepsilon_{RP-eq} \approx \varepsilon_{FP-max}$ for the under-aged SAHT9h material: it recovers its original flow stress sooner after reversal. As it contains very few non-shearable particles, there is almost no OHRB.

The reverse yield stress level is related to the forward strain level; however, it saturates after 2 or 3% of plastic deformation. The larger are the precipitates, the higher is this saturation level (when compared to the yield stress, see Fig. III.32.b). This can be explained by two reasons. On the one hand, the number of loops that can be stored around a precipitate saturates (see III.D.2.c.iii). On the other hand, the more dislocations there are in the material, the less probable is the total reversibility of the mobile dislocation path.

One can see on Fig. III.33 that dislocation "1" does not follow the same path during reverse loading. The consequence is that the Orowan loop "1L" remains around the precipitate. It will cause a permanent Bauschinger effect: the back stress generated by the Orowan loops will affect permanently the flow stress (see also [Rauch 2007]). This effect is measured at $\sigma_{RP-2\%}$. There is however no permanent softening, as shown in Fig. III.32.c. above $\varepsilon_{FP-max} = 2\%$, as $\varepsilon_{RP-eq} < 2 \times \varepsilon_{FP-max}$.

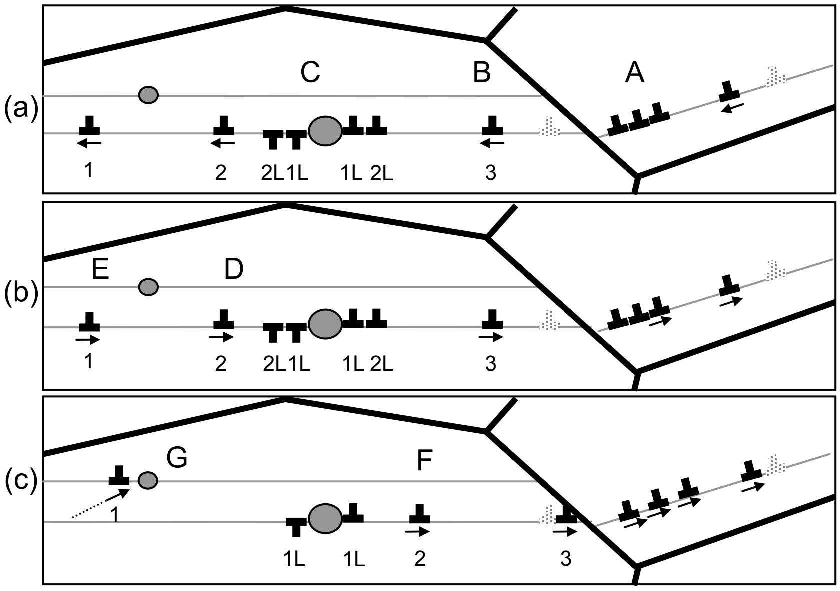

(a) Last step of forward straining.
(b) First step of reverse straining.
(c) During reverse loading.

(A): a dislocation pile-up activates a source in a neighbour grain (B), which generates dislocations. (C): Orowan loops coming from dislocations "1" and "2" stored around a non-shearable precipitate.

(D, E): the mobile dislocations move on the glide plane towards the reverse direction.

(F): dislocation "2" has followed the reverse path and annealed the Orowan loop "2L". (G): dislocation "1" followed a different path; Orowan loop "1L" remains around the precipitate.

Fig. III.33. Schematic of the Bauschinger effect in a grain

To summarize: our hypothesis is that the original relation of the Bauschinger stress is incomplete, and that the yield stress contribution evolves during the Bauschinger tests. During the forward stage, the flow stress is the sum of the yield stress, the isotropic contribution and the kinematic contribution. During the reverse stage, the (reverse) yield stress is less than its previous level because the contribution of the non-shearable precipitates is reduced. In term of equations, it would mean that:

(III.63.) $\sigma_f^{Forward} = \sigma_y + \sigma_{iso} + \sigma_{kin}$

(III.64.) $\sigma_f^{Reverse} = \chi\sigma_y + \sigma_{iso} - \sigma_{kin}$

Where $\chi \in [0;1]$ accounts for the reversibility of the strain path. Its value is a difficult question that reflects a collective behaviour of dislocations. However a simple image is that the more loops there will be around non-shearable precipitates, the smaller would be χ. Finally, the Bauschinger stress as measured on Fig. III.29 is not equal to the true kinematic strain hardening contribution σ_{kin}, but to:

(III.65.) $2\sigma_B = \Delta\sigma = \sigma_f^{Forward} - \sigma_f^{Reverse} = \sigma_y(1-\chi) + 2\sigma_{kin}$

Finally, the kinematic contribution to strain hardening during a Bauschinger test becomes:

(III.66.) $\sigma_{kin} = 0.5(\Delta\sigma - \sigma_y(1-\chi))$

Now that it has been established that kinematic hardening takes place and the mechanisms understood, the Bauschinger effect has to be included in the strain hardening model. This will be done in section III.D.2.

III.C.4. Effect of strain rate and temperature

III.C.4.a. Introduction

As already presented in chapter I, obstacle by-passing is a thermally activated mechanism. Both looking at the effect of temperature and of strain rate allows establishing the strain rate sensitivity of a material. This is true provided that precipitation is not affected by temperature, in which case strain rate and temperature may have coupled effects (see chapter V).

Decreasing the temperature increases the obstacle strength, and finally the yield stress. Then it reduces the mobility of the dislocations, which diminishes the dynamic recovery rate. Temperature and strain rate do have an inverse effect on both yield stress and strain hardening, and increasing the strain rate has exactly the same effects as decreasing the temperature. However sensitivity of flow stress to temperature is higher than its sensitivity to strain rate: stress is inversely proportional to temperature while the stress vs. strain rate relation follows a logarithmic law.

Various experiments may be performed to evaluate the strain rate sensitivity of a material: continuous tensile tests (at either various temperatures or various strain rates) or discontinuous tests (strain rate or temperature jumps). As the dislocation microstructure developed during a tensile test depends on the strain conditions (and/or strain path), both experiment groups do not show the same thing: while continuous tests inform about the evolution of the dislocation structure for a given strain rate or temperature condition, discontinuous tests inform about the material response to changing conditions, for a given dislocation structure: it tells us which obstacles may be by-passed by thermal activation.

The first objective is to establish whether the material is strain rate (or temperature) -sensitive or not. As explained previously, the best way to prove it is to perform tensile tests at various temperatures. Those tests were performed on the base T7651 material.

III.C.4.b. Tensile tests at different temperatures

The inverse tensile set-up presented in chapter II has been used to immerse the specimen in different media. Tensile tests have been performed in liquid nitrogen, cooled ethanol and at room temperature: respectively 77K, 250K and 293K. The results are reported in Fig. III.34.

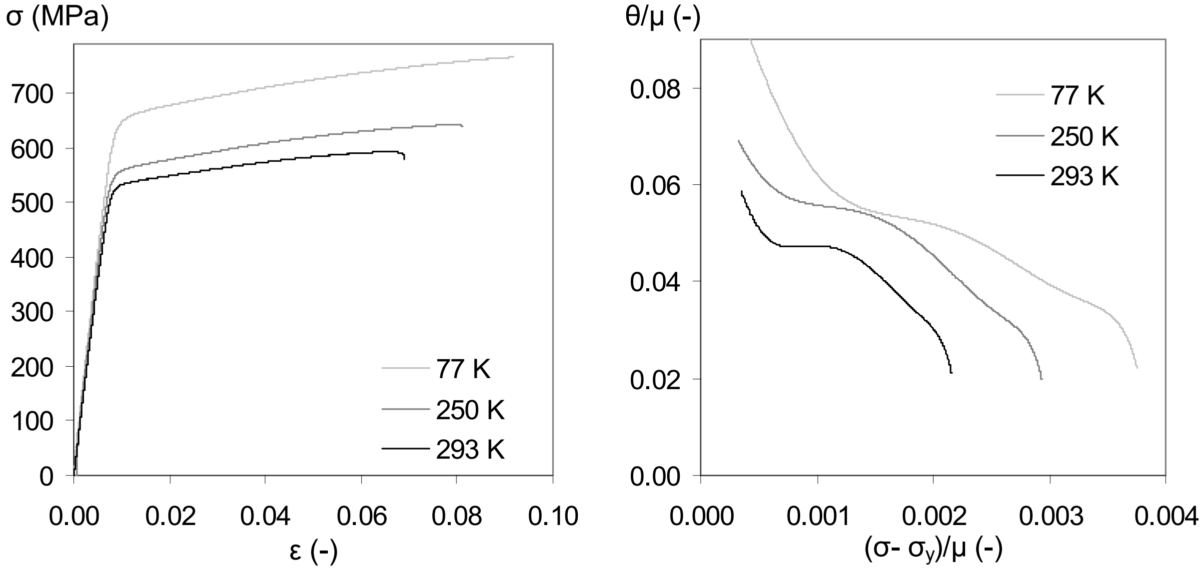

Fig. III.34. Tensile behaviour of T7651 at various temperatures

(a) Tensile curves. (b) Strain hardening curves. $\mu_{77K} = 29.2GPa$, $\mu_{250K} = 28.1GPa$, $\mu_{293K} = 27.7GPa$.

Normalisation by shear modulus μ allows comparing the plastic behaviour, the effect of differential thermal dilatation being separated. Yield stress, UTS and homogeneous elongation increase when lowering the temperature, and sensitivity to temperature is also established for the strain hardening behaviour. A more quantitative approach is given in Fig. III.35.

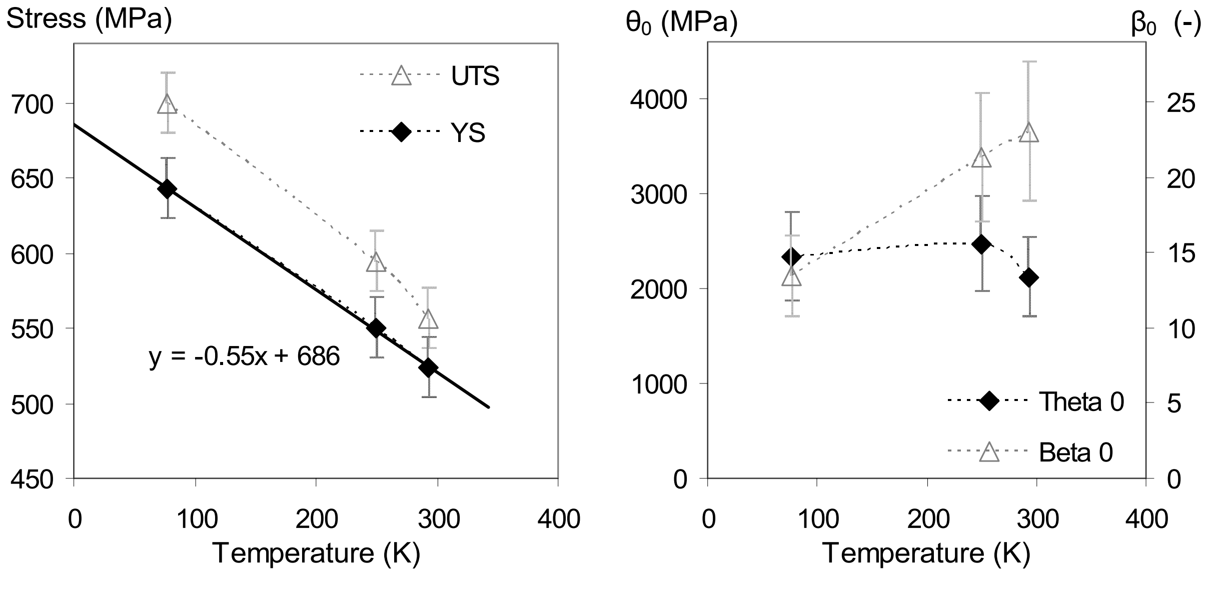

Fig. III.35. Temperature dependency of tensile parameters of T7651

(a) Yield stress and UTS. (b) Strain hardening parameters.

If yield stress σ_y and dynamic recovery rate β_0 are strongly affected by temperature, the storage rate θ_0 is essentially independent of temperature (mean value: 2308 MPa), which are all expected results ([Nes 2002]). This experiment may allow calculating the activation energy ΔG_0 through:

$$\text{(III.67.)}\quad ln\left(\frac{\dot{\varepsilon}_p}{\dot{\varepsilon}_{p0}}\right) = \frac{-\Delta G(\sigma^*)}{k_B T} = \frac{\Delta G_0 - V^*\sigma^*}{k_B T}$$

Where V^* is the activation volume. In other words:

$$\text{(III.68.)}\quad \sigma^* = \sigma - \sigma_\mu = \frac{\Delta G_0}{V^*} - ln\left(\frac{\dot{\varepsilon}}{\dot{\varepsilon}_0}\right)\frac{k_B}{V^*}T$$

The Y-intercept of the $\sigma_y = f(T)$ plot (Fig. III.35) equals $\sigma_y(0K) = \Delta G_0 / V^* + \sigma_\mu$, which means that:

$$\text{(III.69.)}\quad \Delta G_0 = V^*\left(\sigma_y(0K) - \sigma_\mu\right)$$

We are not able to separate the athermal σ_μ from the effective stress contribution σ^* (see chapter I). The tested temperature range is indeed too low to see any saturation of the stress. One can however state that σ_μ is less than the yield stress at 293K: $\sigma_\mu \leq \sigma_{y-293K}$. V^* at yield stress has been measured at ~60b^3 (see Fig. III.42); one can finally state that: $1.4eV \leq \Delta G_0 \leq 6.0eV$.

It has been established that the material is sensitive to temperature. The next point is then to evaluate quantitatively the strain rate sensitivity of the material.

III.C.4.c. Tensile tests at different strain rates

A traditional screw tensile device has been used for most of the experiments, equipped with an extensometer for strain measurements. To higher strain rates tests were performed with a computer controlled servo-hydraulic testing machine, able to reach up to ~4 m/s, but without extensometer. Both results are shown in Fig. III.36.

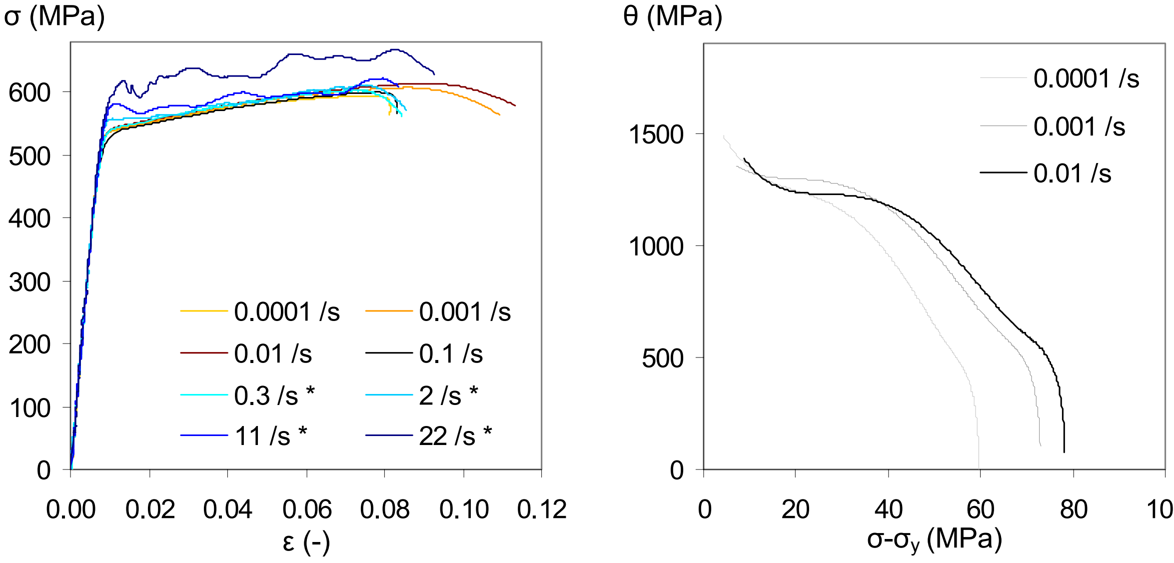

Fig. III.36. Tensile behaviour of T7651 at various strain rates

(a) Tensile curves. (b) Strain hardening curves. Tests performed at room temperature. The stars indicate the specimen strained on the high strain rate machine.

Despite the relatively high range covered by the strain rate, only slight differences are observed between the samples strained between 10^{-4} and 3.10^{-1}/s on the tensile curve. The strain hardening curves are easier to distinguish.

The results performed at higher strain rates (but without extensometer) are more clearly separated. Nevertheless their shape is not classical: they first exhibit a high apparent yield stress, followed by an oscillating regime before collapse. Experiments performed on aluminium alloys with Hopkinson bars show a similar behaviour [Djapic 2000], even though they see this effect at strain rates higher than the strain rates reached in our case. The authors attribute this to the propagation of a plastic stress wave, which over-evaluates the material's yield stress. They propose a method to correct the apparent stress signal into true signal. Evolution of the main tensile parameters is shown in Fig. III.37, separating standard from high strain rate tests.

Yield stress is very slightly increasing in the low strain rates tests and increases drastically in the high strain rate tests. This behavioural change in the apparent yield stress is probably an artefact, as explained in the previous paragraph. The actual yield stress (that we have not been able to calculate at high strain rates) is probably less sensitive to strain rate and should follow a standard logarithmic law (shown by the arrows in Fig. III.37). If one only considers the slow strain rate experiments, the small yield stress variation seems to show a very limited effect of strain rate on tensile behaviour, as expected in 7xxx alloys (see for instance [Johansson 2006, Djapic 2000]).

Concerning the strain hardening parameters, the expected general tendency is also found: storage term θ_0 is more or less constant and the recovery rate β_0 decreases with strain rate.

The results presented here were normalised by the initial yield stress measured by hardness measurements in the specimen grips and while measuring the temperature in the room, to minimise experimental variability. Indeed a lot of the experiments performed did not fit perfectly the general tendency and slightly diverge, and we think that the very small sensitivity to strain rate was hidden by experimental variability. To minimize this, strain rate jump tests will be performed. Indeed in that case, the experimental conditions are constant: same sample; steady temperature.

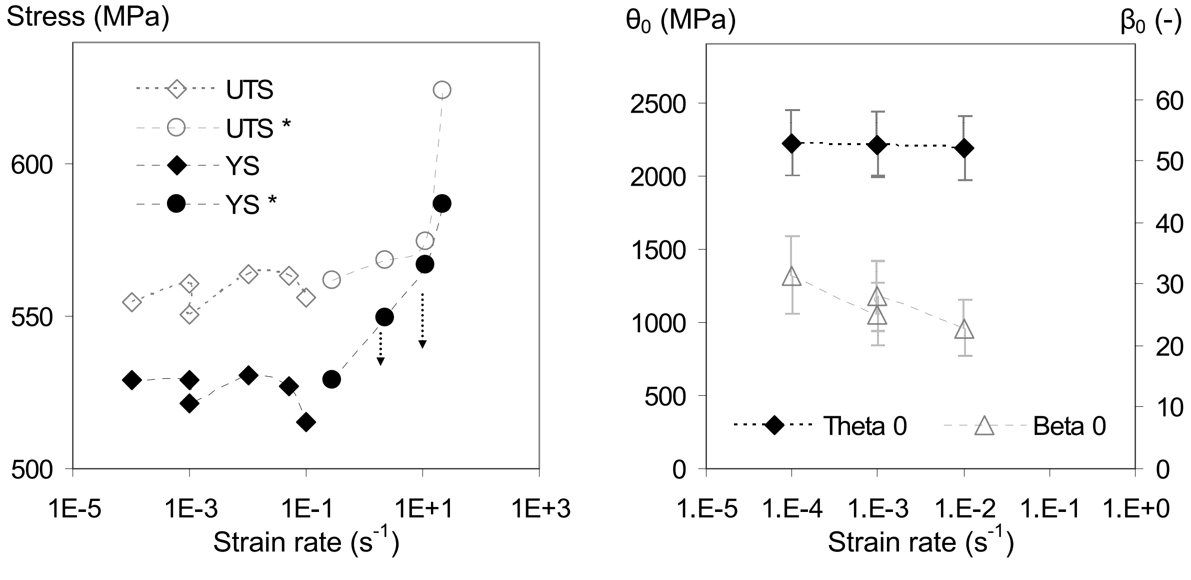

Fig. III.37. Strain rate dependency of tensile parameters of T7651

(a) Apparent yield stress and UTS. The stars indicate the specimen strained on the high strain rate machine; arrows the yield stress correction; the black curve the expected tendency. (b) Strain hardening parameters. 293K.

III.C.4.d. Strain rate jump tests

Fig. III.38 presents strain rate jump tests performed at two temperatures: room temperature and 77K.

In this case a clear strain rate sensitivity is identified, whatever the test temperature. For the two temperatures, stress jumps of $\pm 10 \pm 5\, MPa$ are observed for a strain rate variation of two orders of magnitude.

At room temperature (curve (a)), one first observes a stress jump, followed by a transient parabolic regime (decreasing after jumps and growing after drops); then a steady-state (growing) regime. The low temperature test (curve (b)) directly shows the steady-state regime. The difference between both may be explained by the variation of the n parameter with temperature, governing the recovery rate (see equation (III.13.)). The transient regime is necessary to accommodate the dislocation structure to the new strain rate. Once the equilibrium is reached, the standard hardening mechanisms takes place.

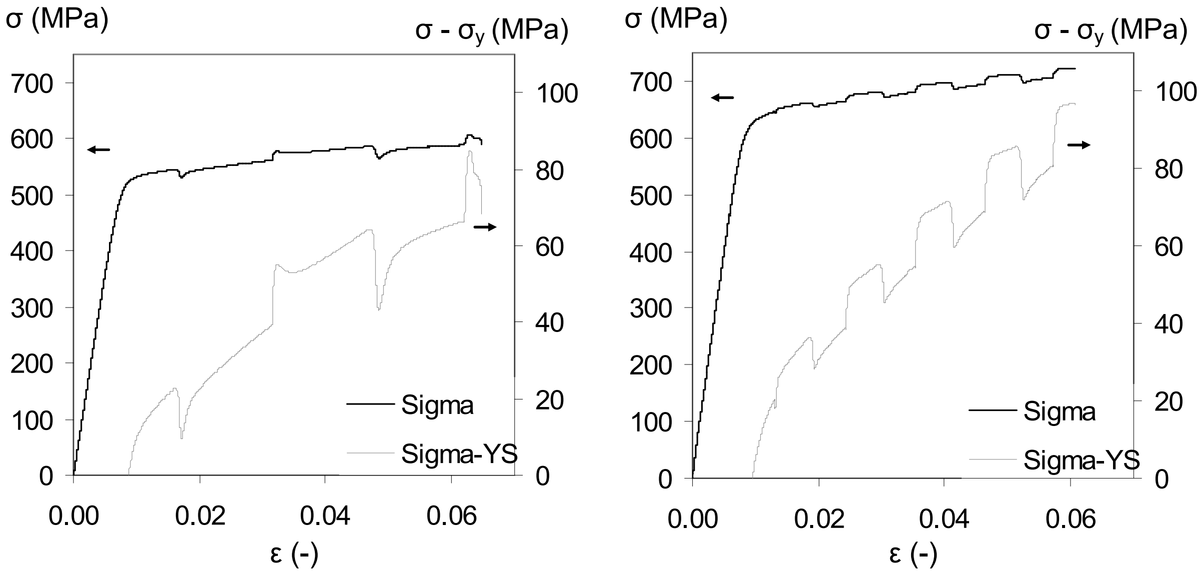

Fig. III.38. Strain rate jumps performed on T7651 at two temperatures

(a) 293K; strain rate varied between 10^{-2} and 10^{-4}/s. (b) 77K; strain rate varied between 10^{-2} and 10^{-4}/s.

The effect of the strain rate jump magnitude is investigated on figure Fig. III.39: the strain rate is varied between 10^{-3} and 10^{-4}/s in case (a) and 10^{-3} and 10^{-5}/s in case (b).

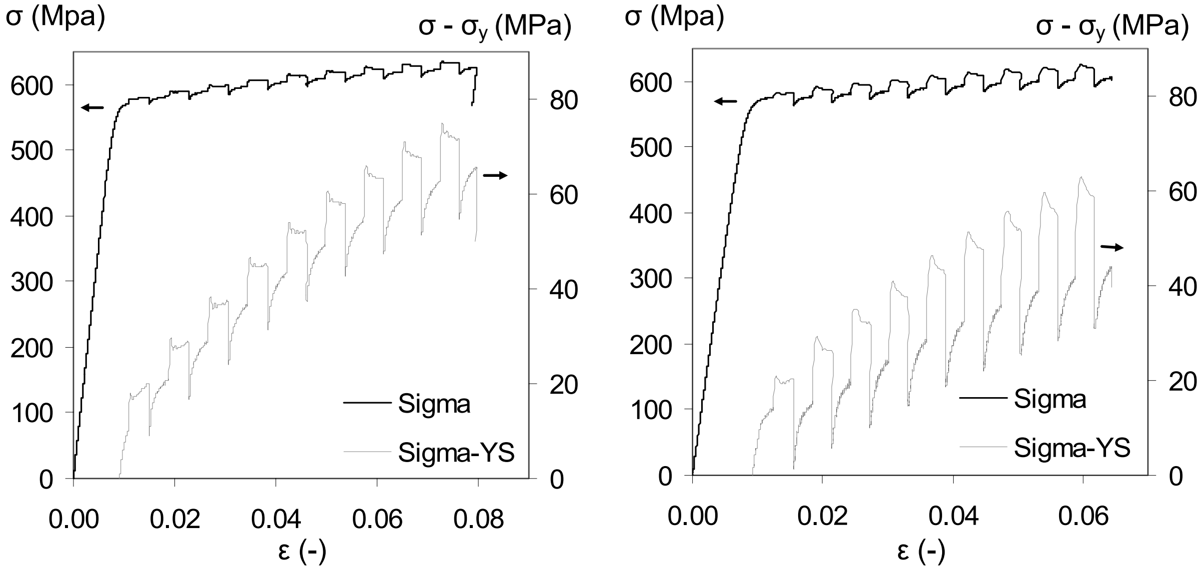

Fig. III.39. Strain rate jumps performed on T7651 at two strain rates

(a) Strain rate jumps from 10^{-3} to 10^{-4}/s; ε_{offset}=0.4%. (b) Strain rate jumps from 10^{-3} to 10^{-5}/s; ε_{offset}=0.3%. 293K.

The instantaneous stress jump $\Delta\sigma_i$ is measured exactly at the stress jump time, and accounts for the total dislocation density, supposed equal during the jump. The steady-state regime stress jump $\Delta\sigma_s$ is determined by extrapolating the flow curve after the transient following the strain rate jump to the moment of the jump, as made by Picu [Picu 2005]. Fig. III.40 presents both results for three different experimental conditions, varying the strain rate and temperature.

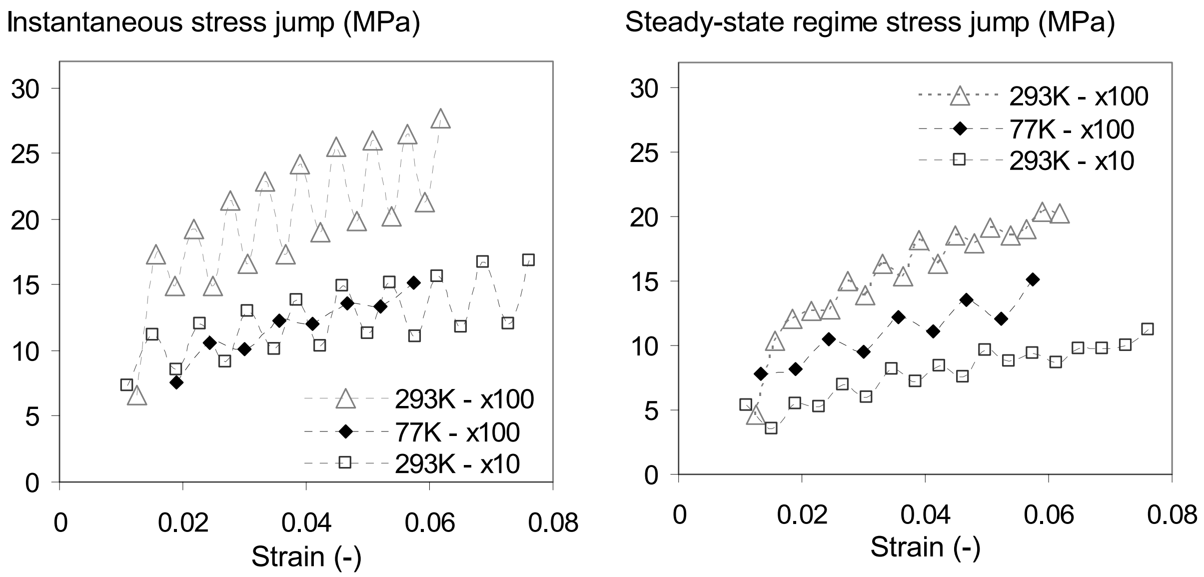

Fig. III.40. Stress jump evolution during strain rate jumps of T7651

(a) Instantaneous stress jump. (b) Steady –state regime stress jump. "x10" and "x100" correspond to the strain rate jump magnitude.

The study of the results presented in Fig. III.40 reveals the following trends:

1. The stress jumps are about twice as large when the strain rate jump is 10 times larger,
2. Decreasing the temperature decreases the stress jump magnitude,
3. The order of magnitude of the two measurements ((a) and (b)) is about the same, but the instantaneous stress jump is somewhat higher than the steady-state measurements. Moreover, the difference between the "positive" stress jumps (increase of the strain rate) and the "negative" ones tend to be diminished for the steady-state regime measurements.
4. The stress jump magnitude grows with deformation,

Point 1 is due to the logarithmic nature of the flow stress/strain rate relationship this will be developed along the next section. Points 2 and 4 will be explained in III.C.4.e.iii. Concerning point 3, the difference between the instantaneous measurement and the "steady-state regime" measurement of the stress jump is due to the different dislocation structure present in both cases (see III.C.4.a).

The instantaneous stress jump $\Delta\sigma_i$ will be used from now. Indeed, the steady-state measurements are sensitive to the transient necessary to establish the steady-state regime[3].

III.C.4.e. Activation volume

i. Definition

The activation volume V^* is defined by the area swept by a dislocation (see Fig. III.41) during a unit duration multiplied by the Burgers vector b. If Λ is characteristic of the obstacle size and L of the "free arm" of the dislocation, it can be expressed in a first approximation ($L >> \Lambda$) as:

(III.70.) $V^* = bA^* = bL\Lambda$

---

[3] We chose in these experiments to perform the strain rate jumps at periodic Δε offsets, to investigate the variation of the instantaneous stress jumps (effect of constant dislocation microstructure) with strain. To measure the "actual" steady-state regime, one should have chosen a larger Δε offset.

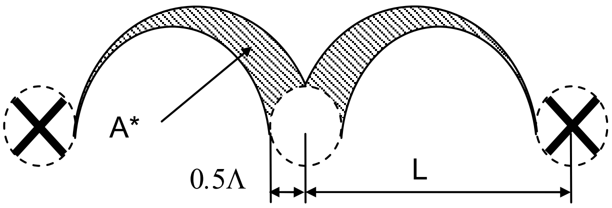

Fig. III.41. Definition of the activation volume

A is the area swept by the dislocation pinned by two obstacles (crosses) to bypass the central obstacle (circle).*

ii. Apparent activation volume

The apparent activation volume V, proportional to V^*, is calculated from the strain rate jump tests as made by Wang et al. [Wang 2006b]:

(III.71.) $$V = k_B.T\frac{ln\,\dot{\varepsilon}_1 - ln\,\dot{\varepsilon}_2}{\Delta\sigma}$$

Kocks [Kocks 1975] calculated that the apparent activation volume is proportional to the average inter-precipitate distance. More generally it depends on the average inter-obstacle distance, as shown by the evolution with strain of the stress jump magnitude in Fig. III.40. Fig. III.42 shows the evolution of the apparent activation volume with the dislocation density ρ or the inter-dislocation distance L_ρ, respectively approximated by:

(III.72.) $$\rho = \left(\frac{\sigma_f - \sigma_y}{M\alpha\mu b}\right)^2$$

(III.73.) $$L_\rho = 1/\sqrt{\rho}$$

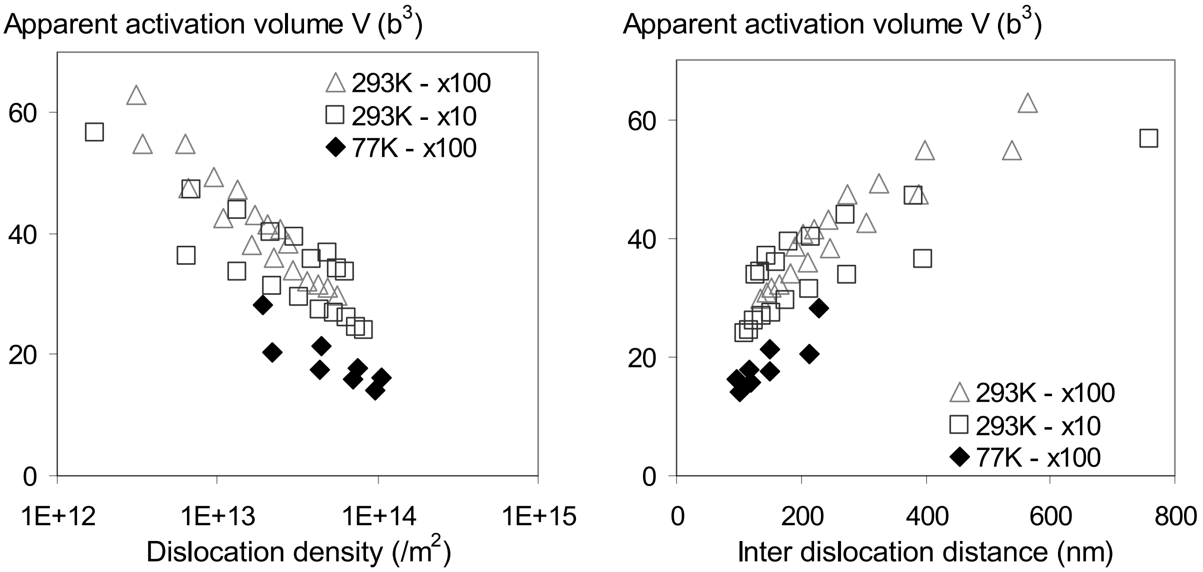

Fig. III.42. Activation volume of T7651

(a) As a function of dislocation density ρ. (b) As a function of inter-dislocation distance L.

As expected, activation volume decreases with dislocation density. The two experiments performed at room temperature follow exactly the same behaviour: the activation volume is not sensitive to the strain rate itself, but to the microstructure. This closes issue “1” tackled in page 98. The experiment performed at lower temperature follows a similar behaviour but the activation volume is shifted towards lower levels. These two points ($V = f(\rho)$ and $V = f(T)$) will be discussed in the next section.

iii. Interpretation

- Evolution of activation volume with strain

Dislocation/dislocation interaction and depinning is not thermally activated: the activation volume reflects the precipitate depinning so that $\Lambda \sim R$. In the absence of dislocations, the only obstacles are precipitates and the “free arm” L (see Fig. III.41) is equal to L^*, the effective inter-precipitate distance along the dislocation line ($L^* = kL$). When dislocations are introduced, L will be only a fraction of L^*. This can be expressed in term of probability. The probability of not having a dislocation between the precipitates is $p_i = e^{-\upsilon}$ where $\upsilon = \rho(L^*)^2 = \rho(kL)^2$, the average number of dislocations “breaking” the free arm. Finally the expression of the mean free arm becomes:

$$\text{(III.74.)} \quad L = p_i L^* + \overline{p}_i \frac{L^*}{1+\upsilon} = L^*\left(e^{-\upsilon} + \frac{1-e^{-\upsilon}}{1+\upsilon}\right)$$

Therefore the activation volume can be written as:

$$\text{(III.75.)} \quad V = V_\infty \left(e^{-\upsilon} + \frac{1-e^{-\upsilon}}{1+\upsilon}\right)$$

Fig. III.43 compares the experimental apparent activation volume measured at room temperature to this simple model. The tuneable model parameters are V_∞ and k, which relates the mean inter-precipitates distance to the effective distance along the dislocation line. This simple model describes well the decrease of the experimental activation volume when dislocation density increases, and the agreement between the model and the experimental results is very satisfactory ($V_\infty = 60b^3$ and $k = 9$).

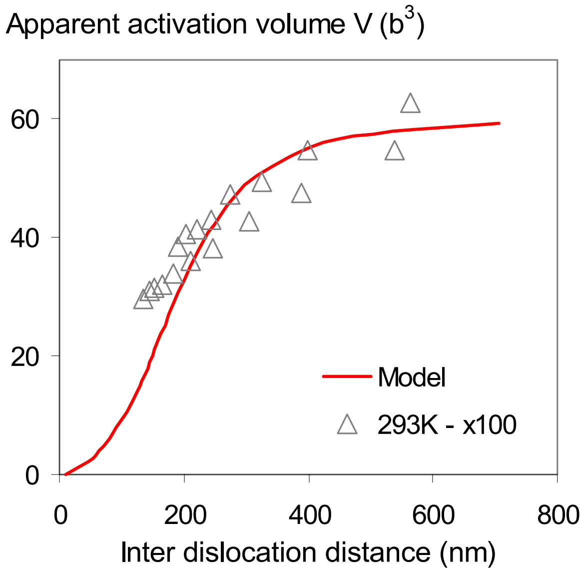

Fig. III.43. Activation volume: comparison between model and experiment

Model parameters are the one measured on T7651 in III.C.1.a. L=27nm, R=4.5nm.

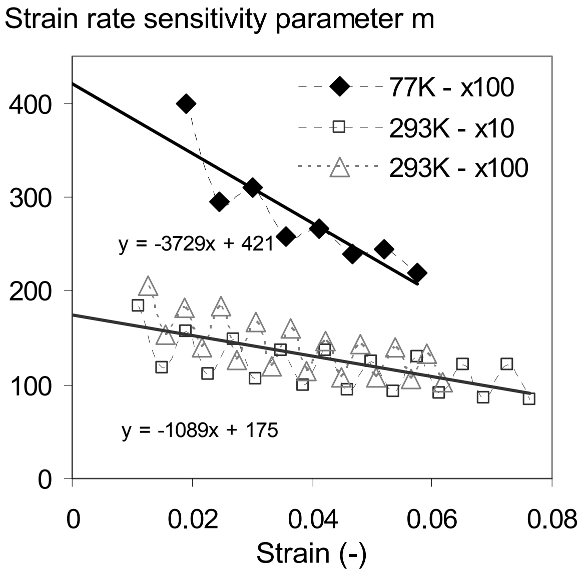

Fig. III.44. Strain rate sensitivity as a function of strain

- Effect of temperature on activation volume

The origin of the activation volume is the possibility to overcome the energy barrier with the help of the thermal energy $k_B T$ (cf. chapter I or Fig. III.45). When temperature is lower the effective stress necessary to overcome the obstacle is higher, but the effective obstacle size Λ is smaller. The consequence is that the activation volume is smaller (see equation (III.70.)).

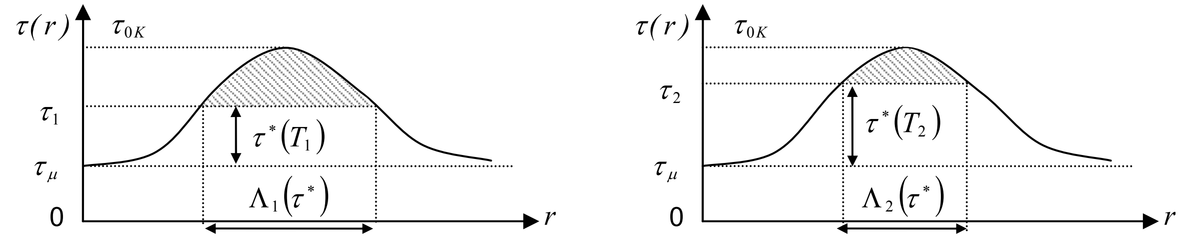

Fig. III.45. Thermal activation of obstacle bypassing

Comparison between two temperatures: T_1 (a) and T_2 (b) with T_1>T_2.

III.C.4.f. Strain rate sensitivity

Following the same approach as Picu et al. [Picu 2005], we determined the strain rate sensitivity parameter with the different experiments through the reverse of equation (III.30.):

$$m = \frac{ln(\dot{\varepsilon}_1/\dot{\varepsilon}_2)}{ln(\sigma_{f1}/\sigma_{f2})} \quad \text{(III.76.)}$$

The evolution of the strain rate sensitivity factor with strain is plot in Fig. III.44. The sensitivity of the yield stress at room temperature is given by the Y-intercept of the curve: m=175.

III.D. Modelling

III.D.1. Yield stress model

III.D.1.a. Solid solution contribution

It is possible to evaluate the contribution of solid solution to yield stress from the as-quenched tensile curve (Fig. III.25), whose yield stress can be written: $\sigma_y(AQ) = \sigma_{LF} + \sigma_{GB} + \sigma_{ss}(AQ) = 150\,MPa$. If one supposes $\sigma_{LF} + \sigma_{GB} = 10\,MPa$ [Deschamps 1999b], one obtains: $\sigma_{ss}(AQ) \approx 140 MPa$. A further hypothesis is made: the contributions of the different solute elements are embedded in a single term, so that: $\sigma_{ss} = KC_{SS}{}^{2/3}$. As $C_{ss}(AQ) = 7.25\%$, one obtains: $K = 805\,MPa$, which is comparable to the one evaluated in [Deschamps 1999b] for copper-free 7xxx alloys ($K = 840\,MPa$).

This calculation is based on strong hypothesis. Neither the grain size, nor the initial solute solution concentration have been varied and their exact contribution to yield stress is not known. The Hall-Petch contribution is taken from the literature, although the grain and sub-grain size, and subsequently σ_{GB} may be slightly different ($\sigma_0 = 28MPa$ in [Teixeira 2008]). Moreover the different solute elements are supposed to have the same contribution. However, if this difference had been considered, the exact matrix composition (which changes during aging; see [Marlaud 2008]) would have been required.

III.D.1.b. Precipitates contribution

As presented in chapter I, the yield stress follows two different evolution laws, whether the material is under-aged or over-aged (see Fig. III.19): respectively

(III.77.) $\sigma_{y-ua} = \sigma_{ss} + \sigma_{0-ua} + \sigma_{P-ua} = \sigma_{ss} + \sigma_{0-ua} + K_{ua} \times M\mu\sqrt{f_v R/b}$ (Under-aged)

(III.78.) $\sigma_{y-oa} = \sigma_{ss} + \sigma_{0-oa} + \sigma_{P-oa} = \sigma_{ss} + \sigma_{0-oa} + K_{oa} \times M\mu b\sqrt{f_v}/R$ (Over-aged)

Therefore plotting the evolution of the modelled σ_{P-ua} and σ_{P-oa} as a function of the experimental yield stress minus the contribution of solid solution will allow the determination of the parameter set $\{\sigma_{0-X};K_X\}$, for each of the two temper groups. The result of this calculation is shown in Fig. III.46, where R and f_v are the measured precipitate radius and volume fraction (see III.C.1).

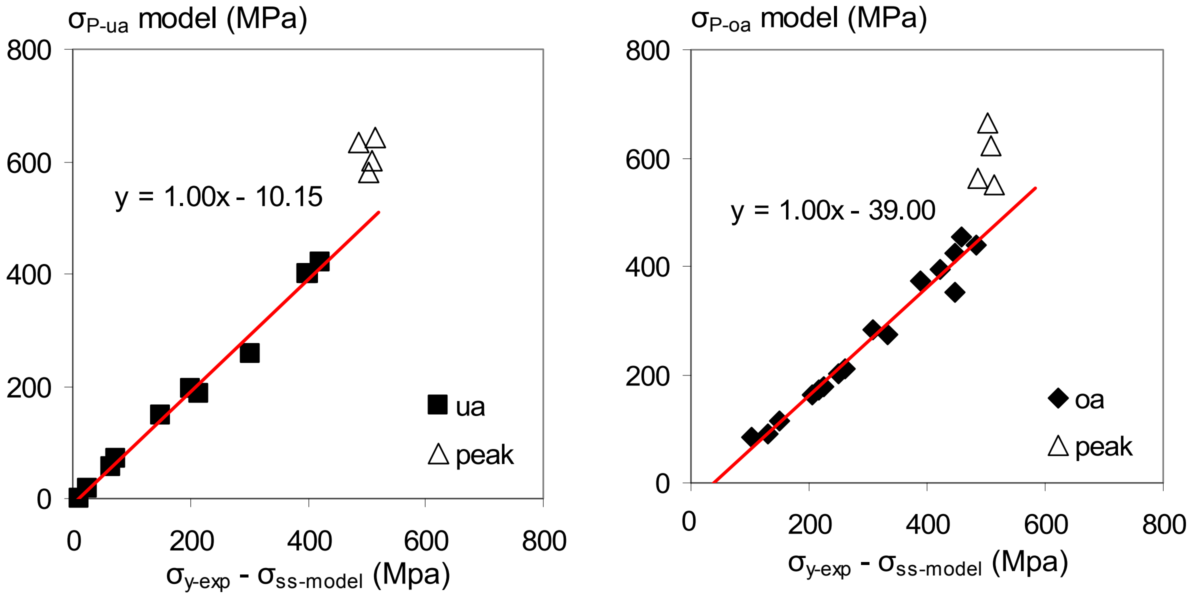

Fig. III.46. Modelled precipitate contribution vs. experimental yield stress

(a) Under-aged model. (b) Over-aged model. “ua” and “oa” stand for “under-aged” and “over-aged” specimen.

A clear separation between under-aged and over-aged materials is observed, and the proposed model fits well the experimental data. The model parameters are given in Table III.5 (supposing $M = 2$):

Parameter	K	σ_0
ua	0.013	10 MPa
oa	0.590	39 MPa

Table III.5. Yield stress model parameters

In the under-aged materials, yield stress can be seen as: $\sigma_y(X) = \sigma_{LF} + \sigma_{GB} + \sigma_{ss}(X) + \sigma_{P-ua}(X)$, where X corresponds to a given temper (or precipitation state). To simplify the approach, we did not separate between the contributions of GP zones and shearable precipitates: those two contributions were included in a single term: σ_{P-ua}. Although simple, this approach seems to be well adapted to our case. There is indeed a very good agreement between the modelled σ_0 value and the expected value.

Concerning the over-aged-materials, the theoretical Orowan law, based on geometrical considerations, supposes $K_{oa} \approx [0.6;0.7]$ (see Chapter I or [Deschamps 1999b]), which is very close to the measured value (0.59). The measured σ_0 is larger than expected (39 instead of 10 MPa). One explanation may be that all the precipitates have been supposed as non-shearable after the peak. A second one is that kinematic hardening (Orowan storage) already induced a flow stress increase at 0.2% plastic strain.

III.D.1.c. Summary

The final expression for yield stress is given in (III.79.). The experimentally measured yield stress is compared to this model in Fig. III.47, using the following transition radius: $R_{trans} = 3.3nm$. Fig. III.47.b. shows the high precipitates contribution during artificial aging (always above 60%). Agreement between the model and the experiment is quite good, even if the peak strength is somewhat overcome by the model. It has been supposed that the whole precipitate population is shifting instantaneously from one mechanism (shearing) to another (bypassing). The use of a particle size distribution instead of a mean radius or the model proposed by Shercliff and Ashby [Shercliff 1990] would solve this issue.

$$\text{(III.79.)}\quad \sigma_y = \sigma_0 + \sigma_{ss} + \sigma_P = 10 + 805\times C_{ss}^{2/3} + \begin{cases} 0.013\times M\mu\sqrt{f_v R/b} & (ua) \\ 29 + 0.59\times M\mu b\sqrt{f_v}/R & (oa) \end{cases}$$

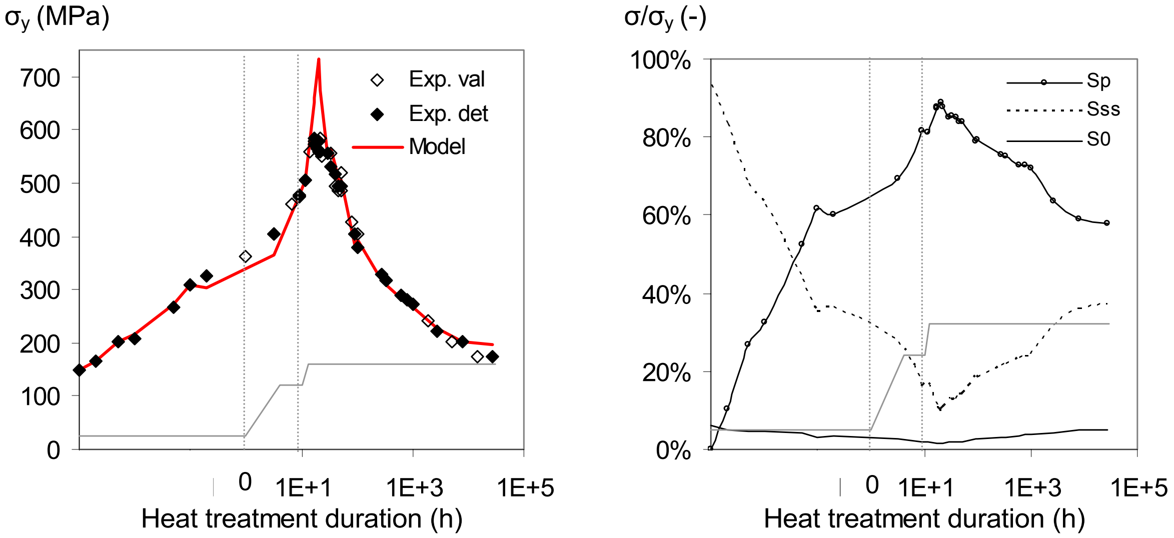

Fig. III.47. Modelled vs. experimental yield stress

(a) Overall model. (b) Relative contributions of precipitates, solid solution and grain boundaries. Experimental data composed of both data used for the determination of the model parameters "det" and validation data ("val"). Values for R, f_v and C_{ss} measured by SAXS; see III.C.1

III.D.2. Strain hardening model

III.D.2.a. Introduction

The KME model described in III.B would predict the behaviour shown in Fig. III.48. It can be compared to the experimental behaviour (Fig. III.49), observed both in our alloy and in 6xxx alloys [Simar 2006].

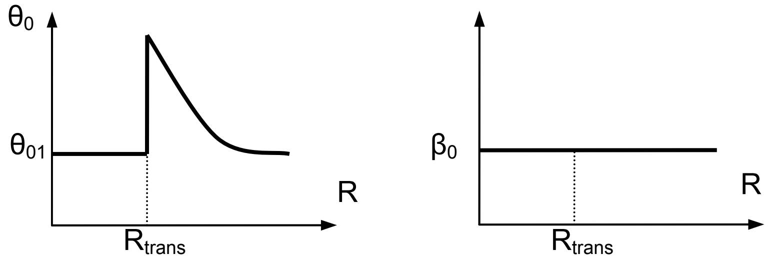

Fig. III.48. Schematic evolution of the strain hardening parameters in the KME model

This plot is presented as a function of the precipitate size R. R_{trans} is the shearing-Orowan transition

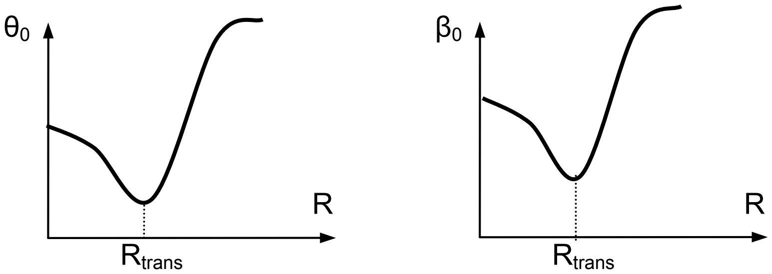

Fig. III.49. Schematic evolution of the strain hardening parameters observed experimentally

This plot corresponds to Fig. III.26 and Fig. III.27, presented as a function of the precipitate size R, during artificial aging. R_{trans} is the shearing-Orowan transition.

A number of striking and important discrepancies are visible:

- The decrease of the storage parameter θ_0 with increasing precipitate radii for shearable precipitates is not captured,
- The continuous increase of θ_0 after the transition is modelled by an instantaneous step followed by a continuous decrease,
- The decrease of the dynamic recovery term β_0 until the transition radius is not described,
- The increase of β_0 for non-shearable precipitates until a saturation value is also not described.

Based on these discrepancies, a more detailed and accurate description of the storage process is obviously required. Moreover, it has been established that kinematic hardening takes place. A new model for over-aged materials, exposed in III.D.2.b, will consider these two points.

III.D.2.b. New strain hardening model

This model for over-aged material is based on the KME model modified by Simar [Simar 2006] for isotropic hardening and on Proudhon's [Proudhon 2008] model for kinematic hardening.

i. Physical basis for isotropic hardening: dislocation density evolution

The density of moving dislocations ρ_m depends on the plastic strain as follows:

(III.80.) $$\frac{\partial \rho_m}{\partial \varepsilon_p} = M\left(k_1\sqrt{\rho_m} - k_2\rho_m\right)$$

k_2 can be expressed in term of critical annihilation distance between two moving dislocations y (interplane distance) [Deschamps 1996]:

(III.81.) $$k_2 = 2y/b$$

Its value depends on the configuration: if the lattice is strongly strained by the presence of a dislocation loop stored around a non-shearable precipitate located in between (see case (b) on Fig. III.50), the annihilation distance is larger (i.e. annihilation happens more easily) than when no obstacle is standing between the two dislocations (case (a)) [Simar 2006].

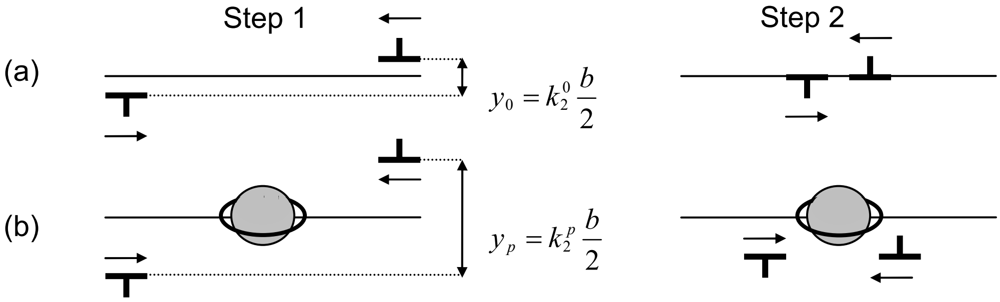

Fig. III.50. Dynamic recovery mechanisms

(a) Dislocations only. (b) Dislocations and a precipitate. (c) Dislocations and a precipitate surrounded by a dislocation loop. After step 2, dislocation annihilation will take place.

Following Simar, we will introduce an efficiency factor φ accounting for the fact that a loop left around a bypassed precipitate may well become unstable, and that it will be more likely to remain stable if the precipitate is larger. Different mechanisms can explain self-annihilation of Orowan loops, such as dislocation cross slip (more frequent at higher temperature) or shearing of the precipitate by an initially stored dislocation loop due to an increase of the stress (cf. Fig. III.51), as proposed by [Bréchet 1989].

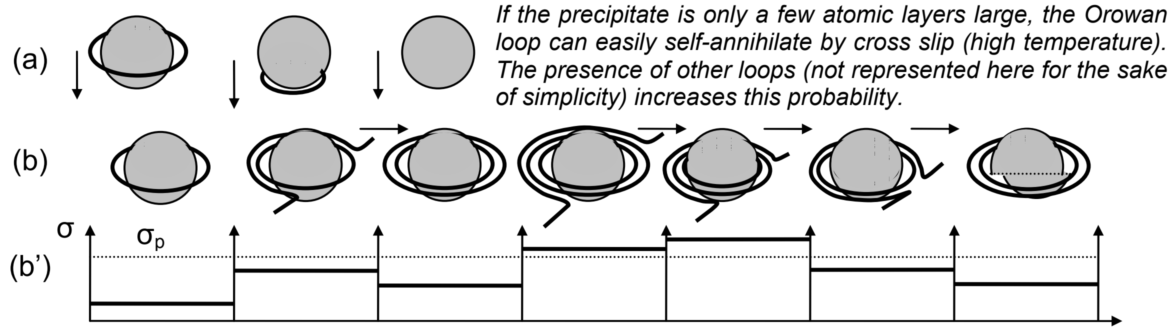

If the precipitate is only a few atomic layers large, the Orowan loop can easily self-annihilate by cross slip (high temperature). The presence of other loops (not represented here for the sake of simplicity) increases this probability.

In this example, if the applied stress is high enough (step 4 where a third Orowan loop is forming around the precipitate), the precipitate will be sheared: in this example, only 2 loops can be stored around the precipitate)

Fig. III.51. Self-annihilation mechanisms

(a) Cross slip on a small precipitate. (b) Shear due to stress increase. (b') Stress applied on precipitate.

$exp(-l_0\varphi/L)$ is the probability for two moving dislocations to annihilate without being "helped" by a precipitate surrounded by an Orowan loop (direct annihilation; see case (a)). In this expression, L is the mean distance between precipitates and l_0 the mean distance between two moving dislocations.

Finally, k_2 can be expressed as the sum of a first term, proportional to k_2^0, taking into account the proportion of the dislocations from the matrix which annihilate by pair in the case where only these two dislocations are considered (see case (a)) and a second term, proportional to k_2^p, which includes the dislocations which annihilate by pair due to an interaction with a dislocation loop stored around a non-shearable precipitate located in between (case (b)):

$$\text{(III.82.)} \quad k_2 = k_2^0\, exp\left(-\frac{l_0\varphi}{L}\right) + k_2^p\left[1 - exp\left(-\frac{l_0\varphi}{L}\right)\right]$$

If one considers that L has the following form:

$$\text{(III.83.)} \quad L = \sqrt{2\pi/3} \times r\Big/\sqrt{f_v}$$

Then:

$$\text{(III.84.)}\quad k_2 = k_2^0\left[exp\left(-\sqrt{\frac{3}{2\pi}}\frac{\sqrt{f_v}\,l_0\varphi}{r}\right)\right] + k_2^p\left[1 - exp\left(-\sqrt{\frac{3}{2\pi}}\frac{\sqrt{f_v}\,l_0\varphi}{r}\right)\right]$$

This process explains the progressive increase of β_0 just after the peak-aged condition; for more details, see [Simar 2006]. In the case of shearable precipitates, where the storage efficiency coefficient φ is equal to zero, k_2 is equal to k_2^0. When precipitates grow, storage efficiency increases and the second part of the expression becomes predominant, until it reaches its maximum when the precipitates become incoherent ($\varphi = 1$). It finally decreases when precipitates are far apart (large coarsening) and direct dislocation annihilation dominates the dislocation annihilation mediated by precipitates. l_0 is equal to $l_0 = \sqrt{1/\rho_m}$.

ii. Physical basis for hardening: number of loops stored around precipitates

In the Proudhon model, the number of loops which can be stored around precipitates is related to the total plastic strain through an expression suggesting the saturation of the Orowan loops number at n^*:

$$\text{(III.85.)}\quad \frac{\partial n}{\partial \gamma_p} = \frac{2r}{b}\left(1 - \frac{n}{n^*}\right)$$

The loops formation rate is maximal at the beginning of plastic deformation and tends to zero when deformation is sufficient to generate n^* loops. It seems quite obvious that the maximal number of loops stored around a precipitate should be precipitate size dependent, simply because they are more stable around a larger precipitate that around a smaller one. Integration of (III.85.) and generalisation to multiple slip systems, gives the evolution of n with strain:

$$\text{(III.86.)}\quad n = n^*\left(1 - exp\left(-\frac{2rM}{bn^*}\varepsilon_p\right)\right)$$

iii. Overall work hardening behaviour

We have in the two previous sections developed a model with two internal variables: ρ to account for the forest dislocations and n for the dislocation loops stored around non-shearable precipitates. Kinematic hardening is governed by n while ρ and n control isotropic hardening. In the following, we will explicit those two contributions and the way to combine them to have a complete description.

- Isotropic contribution

Inspired from the Rauch model [Rauch 2007], the isotropic contribution to strain hardening σ_{iso} takes into account both density of forest and mobile dislocations ρ, and the dislocation density stored around non-shearable precipitates ρ_P.

$$\text{(III.87.)}\quad \sigma_{iso} = \alpha\mu bM\sqrt{\rho + \rho_P}$$

Where ρ_P is proportional to the number of loops effectively stored around one precipitate $n.\varphi$, the precipitate density $3f_v/4\pi r^3$ and the length of a loop stored around a precipitate of radius r, $2\pi r$:

$$\text{(III.88.)}\quad \rho_P = n.\varphi.2\pi r.\frac{f_v}{(4/3)\pi r^3} = n.\varphi\frac{3.f_v}{2r^2}$$

Finally, the isotropic contribution to flow stress is equal to:

$$\text{(III.89.)}\quad \sigma_{iso} = \alpha\mu bM\sqrt{\rho + n.\varphi\frac{3.f_v}{2r^2}}$$

- Kinematic contribution

The kinematic contribution to strain hardening has the same form as in the Proudhon model:

(III.90.) $\sigma_{kin} = f_v E_P \varepsilon_p^*$

In our approach, ε_p^* has been modified in order to take into account the Orowan loops instability: this term is proportional to the number of loops effectively stored around one precipitate $n.\varphi$:

(III.91.) $\sigma_{kin} = f_v E_P \dfrac{bn}{2rM}\varphi$

- Combined model

The constitutive law has to take into account 5 different contributions:

(III.92.) $\sigma_f = f\left(\sigma_{iso}, \sigma_{kin}, \sigma_P, \sigma_0, \sigma_{ss}\right)$

Where σ_{iso} accounts for the isotropic contribution, σ_{kin} is the kinematic component, σ_P is the contribution of non-shearable precipitates, σ_0 is the sum of the lattice friction and the Hall-Petch effect and σ_{ss} the solid solution hardening term.

As dislocations and precipitates do have different densities ($\rho << N$), but a force of the same order of magnitude, a quadratic addition must be considered between the hardening contributions of the precipitates $\sigma_P = \sigma_y - \sigma_0 - \sigma_{ss}$ and the work hardening by dislocations σ_{iso} (see equation (III.89.)). In the case of a simple tensile test, the flow stress finally becomes:

(III.93.) $\sigma_f = \sigma_0 + \sigma_{ss} + \sigma_{kin} + (\sigma_P{}^2 + \sigma_{iso}{}^2)^{1/2}$

iv. Summary

(III.94.) $\sigma_f = \sigma_0 + \sigma_{ss} + f_v E_P \dfrac{bn\varphi}{2rM} + \left(\sigma_P{}^2 + \left(\alpha\mu bM\sqrt{\rho + n.\varphi\dfrac{3.f_v}{2r^2}}\right)^2\right)^{1/2}$

Where the dislocation densities ρ and n respectively evolve with strain as:

(III.95.) $n = n^*\left(1 - exp\left(-\dfrac{2rM}{bn^*}\varepsilon_p\right)\right)$

(III.96.) $\dfrac{\partial\rho}{\partial\varepsilon_p} = M\left(k_1\sqrt{\rho} - k_2\rho\right)$

(III.97.) $k_1 = \dfrac{2\theta_0}{M^2\alpha\mu b}$

(III.98.) $k_2 = k_2^0\left[exp\left(-\sqrt{\dfrac{3}{2\pi}}\dfrac{\sqrt{f_v}\,l_0\varphi}{r}\right)\right] + k_2^p\left[1 - exp\left(-\sqrt{\dfrac{3}{2\pi}}\dfrac{\sqrt{f_v}\,l_0\varphi}{r}\right)\right]$

φ is supposed to evolve linearly between R_{trans} and R_{trans2}.

III.D.2.c. Comparison: model vs. experiments

i. Material parameters

Table III.6. summarises the microstructural features and yield stress of each of the tempers used for the determination of the model parameters (see Fig. III.18).

Temper	R_G (Å)	f_v (-)	σ_y (MPa)
SAHT21h	39	6.0%	573
SAHT45h	60	6.0%	510
SAHT280h	108	6.0%	337
T7651	52	6.0%	555
T7651+24h@210°C	188	5.7%	427
T7651+72h@210°C	243	5.7%	204
T7651+240h@210°C	258	5.7%	174

Table III.6. Tempers and precipitate features used for tensile and Bauschinger tests

ii. Model parameters

Table III.7 presents the model parameters optimised to fit the tensile curves, and the origin of those values. The only tuneable parameters are n^*, M, α and y_P. The other parameters come either from the literature of have been measured experimentally. Among those parameters, k_1, the dislocation storage parameter, is supposed constant and calculated with equation (III.97.) at peak strength. Similarly, the critical annihilation distance when only dislocations are considered y_0 (see Fig. III.50.a) is calculated from:

(III.99.) $y_0 = b\beta_{0-min}/M$

In which $\beta_{0-min} = 4$ is β_0 at peak strength (see Fig. III.27). k_2^0 and k_2^P are respectively calculated as

(III.100.) $k_2^P = 2y_P/b$

(III.101.) $k_2^0 = 2y_0/b = 2\beta_{0-min}/M$

Parameter	Significance	Value	Unit	Origin
b	Burger's vector	0.284	nm	-
μ	Matrix shear modulus	27	GPa	-
M	Taylor's factor	2	-	Fitted in III.D.1.b
n^*	Maximum number of Orowan loops around a precipitate	9	-	Fitted in Fig. III.52
R_{trans}	Precipitate shearing/bypassing transition radius[4]	3.3	nm	Fig. III.13 + Fig. III.19
R_{trans2}	Precipitate coherency/incoherency transition radius	15.0	nm	Fitted in Fig. III.52
E_P	Precipitate’s Young modulus	59	GPa	[Deschamps 1997]
α	Parameter of the Taylor law	0.2	-	Fitted in Fig. III.52
θ_{0-min}	θ_0 if no Orowan loops stored (peak)	974	MPa	Fig. III.26
y_0	Annihilation distance between two moving dislocations (cf. Fig. III.50.a)	0.57	nm	Calc. from eq. (III.99.)
y_P	Annihilation distance between two moving dislocations helped by an Orowan loop (cf. Fig. III.50.b)	10	nm	Fitted in Fig. III.52
σ_0	Stress contribution of HP, SS	39	MPa	See eq. (III.79.)

Table III.7. Model parameters

---

[4] $R_{trans} = 3.3nm$ is effectively the actual transition radius. However, for the calculation of the precipitate storage efficiency parameter φ, a corrected value has been used: $\varphi = (R - kR_{trans})/(kR_{trans} - R_{trans2})$ with $k = 0.8$. It allows a better description of the experimental results, in the case of temper SAHT21

iii. Tensile tests modelling

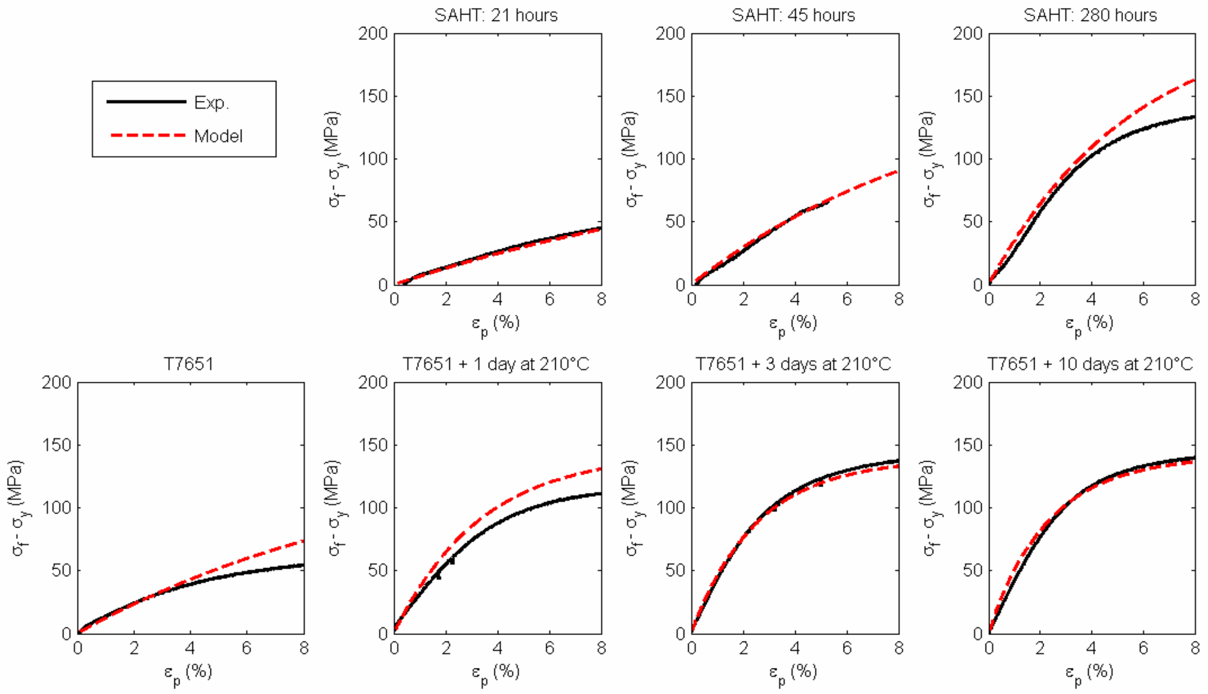

Fig. III.52. Experimental tensile curve compared to the strain hardening model

III.D.2.d. Discussion

i. Model parameters

The experimental results (black curve on Fig. III.52) and the model (red curve) are in good agreement: the general strain hardening model presented in III.D.2.b.iv associated with the parameter set reported in Table III.7 describes well the tensile behaviour of the over-aged materials.

The values of the tuneable parameters are in the expected range. A parametric study presents their respective influence in appendix A.III.4. The critical value found for annihilation helped with Orowan loops, y_P is ~20 times more than the value for direct annihilation y_0. This is slightly less than $y_P = 22nm$, the value evaluated by Simar. However this parameter does not affect very deeply the results (see appendix A.III.4). We found that $n^* = 9$ gives the best fit of the tensile curve, while Proudhon [Proudhon 2008] proposed $n^* = 60$. However their material is a low solute content 6xxx alloy with long precipitates (for Proudhon: fv=1.9%, r=6.6nm, l=300nm), very different from our high precipitate volume fraction 7xxx alloy with small ellipsoidal precipitates. Note that the evolution of the precipitate storage efficiency parameter φ has been slightly modified (see note 4 in page 98) as compared to the Simar model. The evolution law of this parameter was however not presupposed.

ii. Difference with former models

As already said, this model is based on the Simar approach for isotropic hardening and on the Proudhon approach for kinematic hardening. The main differences are listed hereunder:

- We have combined the two approaches to describe the role of precipitation both on isotropic and kinematic hardening. Notably, we take into account the kinematic contribution in the uniaxial tensile test, which was not achieved previously.
- Contrarily to Simar, we only focused this model on over-aged material, neglecting in that way dynamic precipitation for tempers that would have a large solute supersaturation.
- Simar used Estrin's storage term accounting for Orowan loops storage around non-shearable precipitates ($1/bL$, see eq. (III.35.)) and modified it, introducing the precipitate-size dependant

parameter φ, accounting for the stability of the loops. In our case, the initial Kocks and Mecking formalism is kept (see eq. (III.15.)) to describe the evolution of the mobile dislocation density, and Orowan loops storage is considered in a separated equation (see equations (III.87.) and (III.88.)). However, the exact form of the Simar expression ($\partial\rho_{total}/\partial\varepsilon_p = M\left(k_1\sqrt{\rho} + \varphi/bL - k_2\rho\right)$ can be found in our model, provided the effective inter-precipitate distance is written as (see appendix A.III.3. for details):

(III.102.) $$L = \frac{r}{3.f_v}\frac{n^*}{n^* - n}$$

This form is different from the purely geometrical expression of the inter-precipitate distance (see equation (III.37.) and appendix A.III.2). In particular L becomes a strain-dependant parameter (included in n). Physically, this means that the additional Orowan storage term φ/bL decreases when strain increases (i.e. when n increases) and becomes ineffective when $n = n^*$.

- We used the same model as Proudhon for kinematic hardening: the number of Orowan loops that can be stored around a precipitate saturates at n^* (see eq (III.85.)), chosen constant.
- A quadratic addition law (see eq. (III.93.)) for the different contributions is relatively standard [Gomiero 1992b, Deschamps 1999b].

iii. Comments on the experimental results

It has been necessary to include a parameter representative of the “effective yield stress”, to correct the measured $\sigma_{0.2}$ yield stress, for the slightly over-aged materials (SAHT21, SAHT45, T7651). This parameter is necessary to overcome the elastic-plastic transition, which is not fully representative of the plastic behaviour of the material. The stress offset for each temper has been chosen so as to establish a steady-state regime; those values are reported in the next table.

Temper	$\sigma_{0.2}$ (MPa)	$\Delta\sigma$ (MPa)	σ_y (MPa)
SAHT21h	573	18	594
SAHT45h	510	10	520
T7651	555	10	565

Table III.8. Yield stress correction for each temper

iv. Description of strain hardening curves

The nature of the global strain hardening does not allow establishing an analytical expression for the storage and dynamic recovery terms. However, a numerical calculation can be done. The experimental strain hardening curves $\theta = \partial\sigma_f/\partial\varepsilon = f(\sigma_f - \sigma_y)$ are compared to the modelled ones.

Agreement between the model and the experimental result is not perfect, but the general tendency seems to be correct. For a more quantitative comparison, the experimental and modelled strain hardening parameters will be compared in Fig. III.54. Measuring a mean slope on these curves may be criticised, but this approach allows us to compare the model to the experimental results quantitatively.

The model predicts correctly the initial storage evolution and the annihilation rate in the slightly over-aged materials, but foresees a decrease of those parameters in the most over-aged tempers (the ones with precipitates above the critical radius for loss of coherency), which was not explicitly observed experimentally in our case.

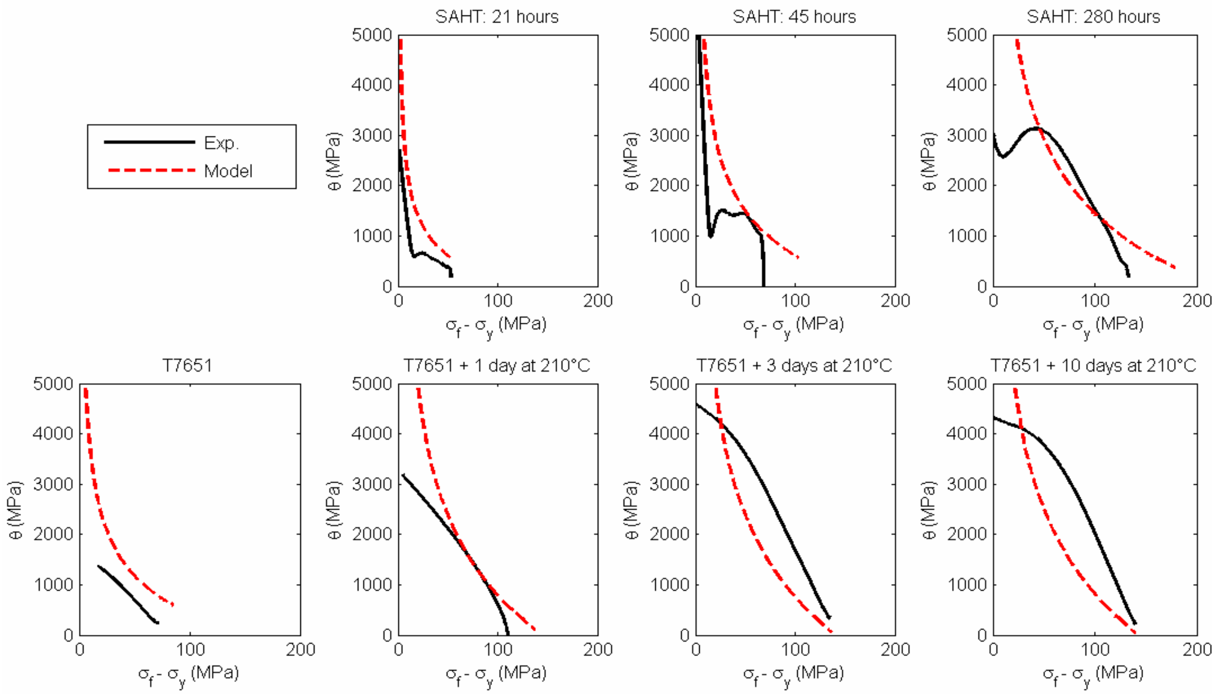

Fig. III.53. Experimental strain hardening curves vs. modelled curves

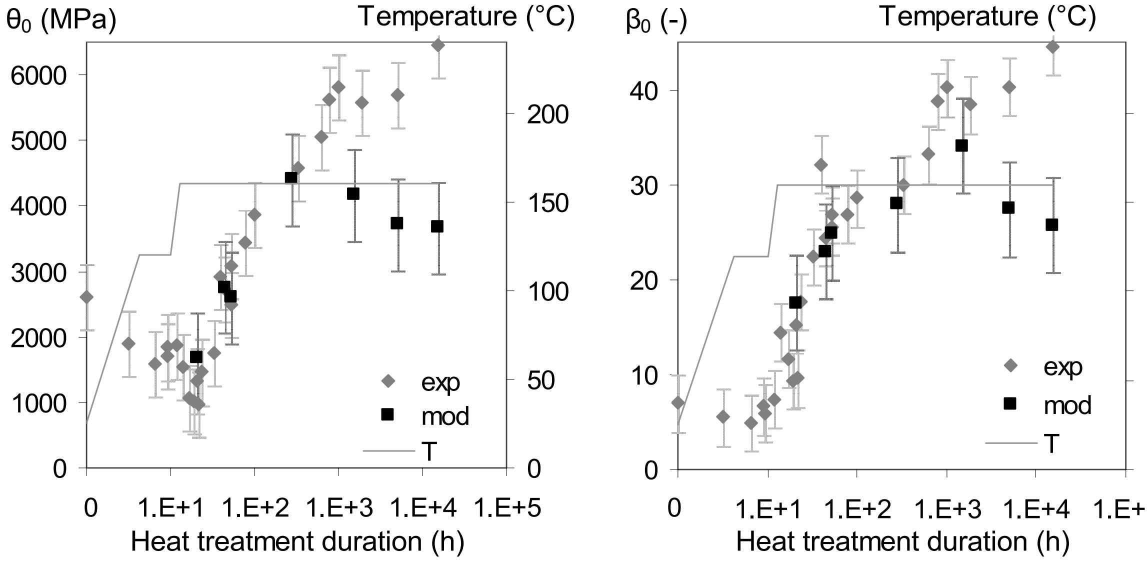

Fig. III.54. Experimental strain hardening parameters vs. modelled results

Data calculated from Fig. III.53. Tempers aged at 210°C are represented with equivalent aging duration at 160°C.

v. Description of the Bauschinger tests

The kinematic strain hardening model is compared to the Bauschinger stress measured for different reverse plastic strain offset values (ε_{RPS}) in Fig. III.53. The model is here calculated assuming a full irreversibility that leads to a direct relation between the back stress and the Bauschinger stress.

The agreement between the model and the experimental results is not very good, even if it is acceptable for the largely over-aged materials. In that case, $\varepsilon_{RPS} = [1\% ; 2\%]$ seem to be correctly described by the modified Proudhon model. For less over-aged materials, the model supposes a lower stability of the Orowan loops (low φ value), which is not fully representative of the experimental results.

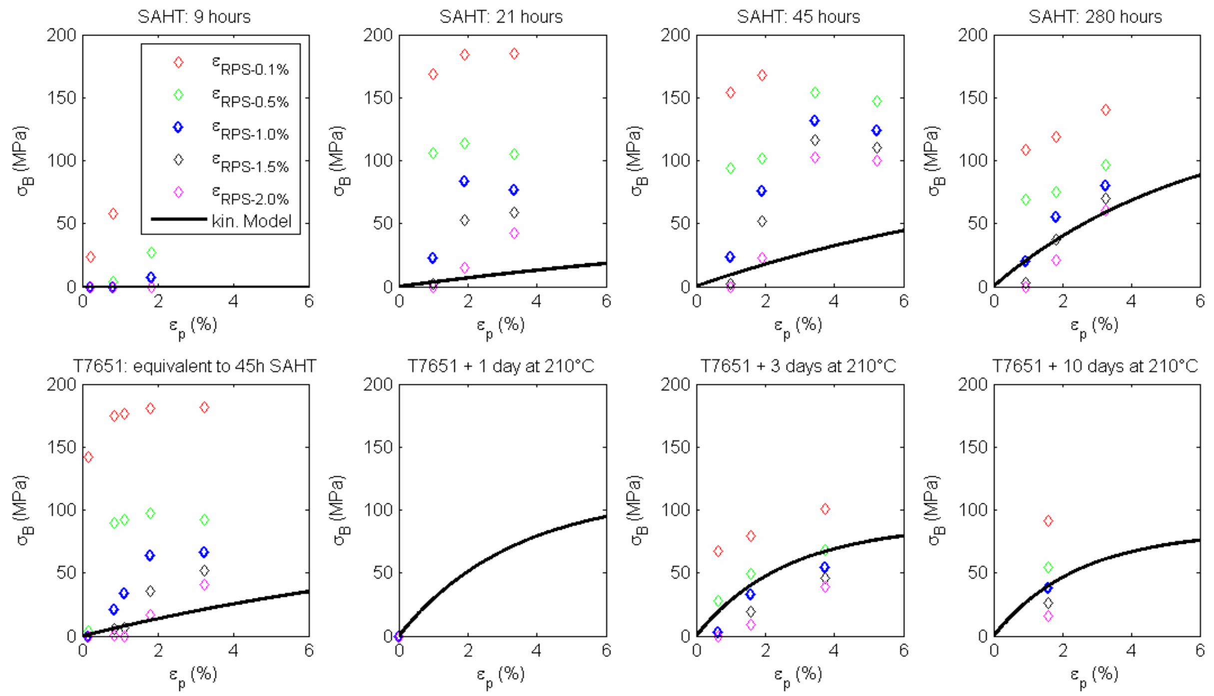

Fig. III.55. Experimental Bauschinger stress vs. kinematic strain hardening model

No Bauschinger data available for T7651+1day@210°C

It has been explained in III.C.3.b.iii that the kinematic hardening σ_{kin} term does not correspond to the Bauschinger stress σ_B measured by the Bauschinger tests, as the non-shearable precipitates contribution to yield stress may change when the material is loaded in the reverse direction. As proposed in III.C.3.b.iii, this can be included in the model using a parameter χ expressing the reversibility of the dislocation path during reverse loading:

$$\text{(III.103.)}\quad 2\sigma_B = \sigma_f^{Forward} - \sigma_f^{Reverse} = \sigma_y(1-\chi) + 2\sigma_{kin}$$

The value of χ is a difficult question that reflects a collective behaviour of dislocations. It probably depends on the Orowan loops density (which depends on both the density and size of non-shearable precipitates and the deformation), as well as the interactions between mobile dislocations and obstacles. It also certainly depends on the intrinsic ability of dislocations for changing planes and thus having irreversible back and forth motions. Discrete Dislocations Simulations should help to shed some light on the parameters controlling χ. However it is possible to determine it empirically for each case, as done in Table III.9.

Temper	SAHT21	SAHT45	SAHT280	T7651	72h@210°C	240h@210°C
$\sigma_{B-0.1\%}$	0.4	0.3	0.45	0.4	0.6	0.4
$\sigma_{B-1\%}$	0.75	0.65	0.85	0.85	1	1
$\sigma_{B-2\%}$	0.9	0.75	0.95	0.95	-	-

Table III.9. Evaluated mean χ value for each temper

No clear tendency can be found concerning the evolution of χ with ageing duration. However, as expected, the “free recovery” parameter χ evolves with the reverse strain level, going from $\chi \approx 0.4$ for $\varepsilon_{RP} = 0.1\%$ to values close to 0.9 for larger reverse deformation. This tends to prove that the dislocation path is reversible and the dislocations loops stored during the forward stage are recovered by the mobile dislocations coming with opposite Burgers vectors.

vi. Influence of strain rate

The strain rate jumps tests presented in III.C.4.d, allow establishing the influence of strain rate on yield stress for T7651 material, using equation (III.104.), the reverse form of equation (III.76.):

$$\text{(III.104.)}\ \sigma_y = \sigma_{y0}\left(\frac{\dot{\varepsilon}}{\dot{\varepsilon}_0}\right)^{1/m}$$

The experimental data from constant strain rate tensile tests (already presented in III.C.4.c) are compared to this model in Fig. III.56, using the following parameters: m=175 (see Fig. III.44.), $\dot{\varepsilon}_0 = 10^{-3}s^{-1}$, $\sigma_{y0} = 529MPa$.

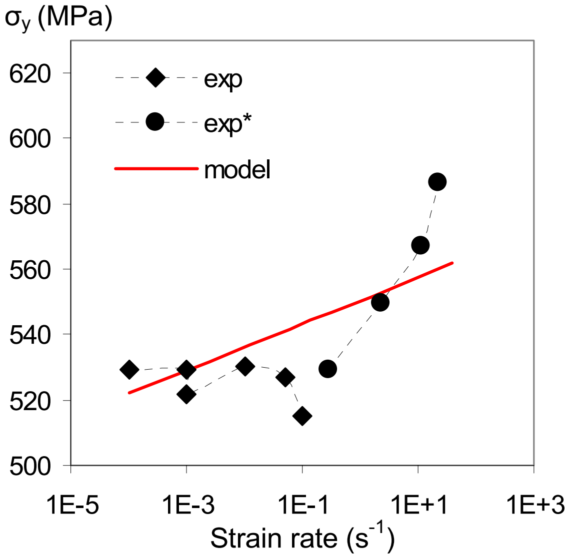

Fig. III.56. Modelled vs. experimental yield stress evolution with strain rate

"exp" correspond to low strain rate tensile tests and "exp" to high strain rates experiments.*

The order of magnitude of the predicted effect is that a change in strain rate of 4 orders of magnitude results in a change of 40 MPa of yield strength, that is a relative change of 6%. This predicted change is in the right range as that coming from the experiments, even though the materials tested in the slow strain rate tensile tests did show a lower (if not absent) influence of strain rate.

III.E. Conclusion

SAXS measurements have been used exclusively to characterise the microstructure of a wide range of materials, obtained throughout various heat treatments (III.C.1). This technique has proven its ability to provide quantitative and absolute information about the main precipitation features. The results have been used as input parameters in the strain hardening model.

Tensile tests have been performed to study the global strain hardening behaviour of those materials. Following the Kocks and Mecking approach, the evolutions of three parameters representative of the strain hardening behaviour with the ageing treatment has been investigated. Those parameters are the yield stress, the initial strain hardening rate and the dynamic recovery rate. The evolution of those parameters (see III.C.2.d) is similar to the one observed by A. Simar [Simar 2006] in 6xxx alloys.

H. Proudhon [Proudhon 2008] showed that the presence of non-shearable precipitates generates kinematic strain hardening. Following his approach, we performed Bauschinger tests to differentiate between isotropic and kinematic strain hardening (III.C.3). The physically-based model modified from Proudhon’s model (III.D.2.b) describes correctly the experimental results, especially for the highly over-aged tempers. However, kinematic strain hardening remains difficult to understand in detail, due to experimental issues and to a lack of knowledge of the complex microplastic phenomena taking place during the strain reversal. We have proposed a mechanism to explain (at least qualitatively) this microplastic behaviour.

Tensile tests at low temperature have shown that the material is sensitive to strain rate (III.C.4.b).

However this strain rate sensitivity cannot easily be described by standard tensile tests performed at different strain rates, the experimental variability being higher than the measurable effect (III.C.4.c). This required strain rate jump tests (III.C.4.d), which allowed us to quantify the effect of strain rate on the tensile behaviour (III.C.4.f). Moreover, a simple semi-phenomenological model has been proposed to explain the evolution of activation volume evolution with strain, which showed a good agreement with the experimental results (III.C.4.e.iii).

A well established and simple yield stress model has proven its ability to describe accurately the results measured experimentally (III.D.1).

A new strain hardening model has been developed for particle-strengthened over-aged materials. This model (III.D.2.b) unifies Simar’s model for isotropic hardening [Simar 2006] and Proudhon’s model [Proudhon 2008] for kinematic hardening. It modifies the initial Kocks, Mecking and Estrin approach and includes two internal variables, respectively the forest dislocations and the Orowan loops. It correctly describes the experimental tensile curves (III.D.2.c.iii), even if some discrepancies still remain (III.D.2.d).

Chapter IV. Microstructural evolution during laser forming treatment

Summary

This chapter investigates the effect of laser beam forming on the precipitation state and the resulting mechanical properties of temper T7651, throughout experimental and modelling work.
These effects have been first characterized experimentally, before being modelled, throughout the following procedure. The process is analysed as a local non isothermal treatment, and the induced temperature distribution is modelled by finite elements modelling. It is used as an input parameter to model the evolution of the local precipitation state during laser forming. These results are compared to the SAXS measurements performed on laser beam formed T7651 parts. Finally, these data, input into the strength model developed in chapter III, allow predicting the local mechanical properties changes induced by the laser treatment.

Outline

IV.A. Introduction

IV.A.1. Laser forming

IV.A.1.a. Generalities

Laser forming (LF) generally uses a loosely focused laser beam (Fig. IV.1) to induce thermal stresses into the depth of a work-piece (Fig. IV.2), and finally deform plastically the material (Fig. IV.3) [Dearden 2006].

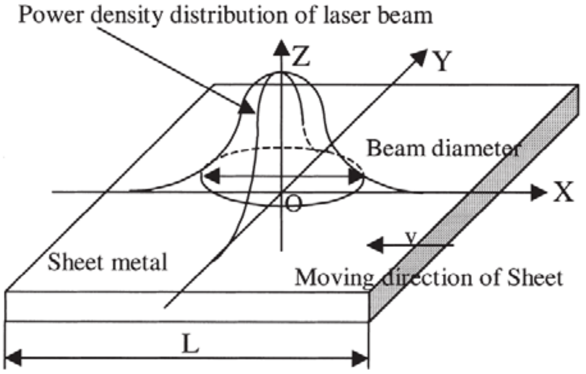

Fig. IV.1. Power density distribution in the laser forming beam

[Hu 2001]

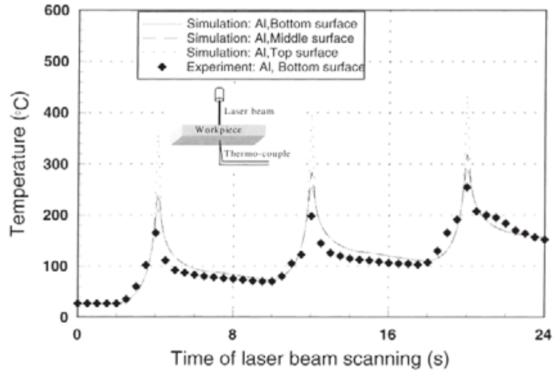

Fig. IV.2. Temperature profile

[Hu 2001] Temperature evolution during 3 passes (Aluminium, P=500 W, v=10 mm/s, T=1.5 mm).

The path of the laser is dependent on the desired forming result [Watkins 2001]. In case of steep temperature gradient across the sheet thickness (so-called "temperature gradient mechanism"), the material will bend. On the opposite, a lower gradient will cause either buckling or upsetting, depending on the sheet thickness (see Fig. IV.3). The main process parameters are the laser power, the laser beam size and its scanning velocity. Various passes may be necessary to obtain the required shape (see Fig. IV.4).

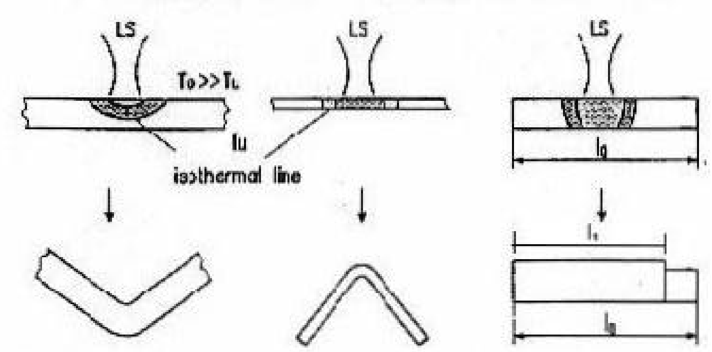

Fig. IV.3. Schematic effect of LF process parameters on component shape

[Watkins 2001] Temperature gradient (left), buckling (middle) and upsetting mechanisms (right).

LF can be either employed to form metallic components or to correct part distortion, as shown in Fig. IV.4. By contrast to conventional forming techniques, it requires no mechanical contact, does not suffer from the 'spring back' effect associated to mechanical forming, and offers many of the advantages of process flexibility and automation associated with other laser processes.

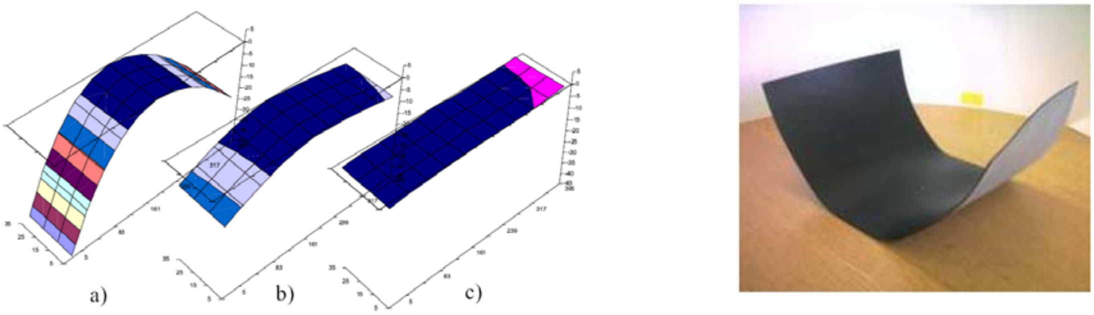

Fig. IV.4. Correction and forming by laser forming

[Dearden 2006] (a) Iterative distortion removal of a distorted component; respectively as received (~45mm max deflection); after 9 and 14 passes. Material: AA5251 400x40x2mm; Process parameters: 900W; 5mm diameter; speed 50-80mm/s. (d) Reverse process: laser formed part, from flat sheet.

IV.A.1.b. Current issues

A large amount of literature is dedicated to the study of laser forming [Hu 2001, Dearden 2006, Shen 2006, Labeas 2008], most of it targeted at the prediction of the optimal process parameters to obtain the required component shape, using finite element modelling. The complex numerical processing includes a laser beam heat flux model to predict the temperature distribution in the component and a thermo–structural analysis including temperature-dependent properties (thermal and mechanical) of the material to predict part distortion.

However, to our knowledge no study exists on the effect of this process on modifying the material's microstructure and on the afferent mechanical properties, although it involves relatively high temperatures. As shown for instance in Fig. IV.2, the material is subjected to a non isothermal treatment with temperatures above 100°C and punctually up to ~300°C, that is high enough to provoke microstructural changes in the material, and subsequently mechanical properties changes.

Concerning this second point (microstructural changes involved by laser forming), this process can be compared to some extent (in the sense of the non isothermal history) to welding techniques such as metal inert gas welding (MIG) [Nicolas 2004], tungsten inert gas welding (TIG) [Preston 2004], laser beam welding [Hu 2006] or friction stir welding (FSW) [Dumont 2006], on which a more abundant literature can be found. The expected effect of such a thermal process is well summarised in [Dumont 2006]: "for age-hardening alloys, the different high-temperature exposures and deformation paths characteristic of the weld and near-weld region are expected to have a profound effect on the magnitude and distribution of the hardening precipitates, depending on their nature, coherency, size and volume fraction. Accordingly, the following may occur: complete dissolution, partial dissolution and/or coarsening of existing precipitates, nucleation and growth of new precipitates. This local evolution of microstructure leads to heterogeneous mechanical properties of the welded joint".

IV.A.2. Scientific objectives

The objectives of this work are to provide quantitative information about the effect of laser forming on the local precipitation microstructure and the related mechanical properties. This includes both experimental and modelling approach, to predict the microstructural and mechanical properties changes induced by the laser treatment.

Laser beam formed T7651 parts will be investigated by SAXS and microhardness (IV.C). A class precipitation model (IV.B) will allow the prediction of the precipitation evolution during the laser treatment, effecting as a local non-isothermal treatment (IV.D). These results, combined with the strength model presented in chapter III, will allow predicting the final mechanical properties (IV.E).

IV.B. Literature review: modelling of precipitation kinetics

IV.B.1. Introduction

Three ways of implementing classical nucleation and growth theories for precipitation are presented and discussed by Perez et. al in [Perez 2008]. They distinguish the “mean radius approach” from the multi-classes approaches: the “Euler-like” and the “Lagrange-like” multi-class approaches (see Fig. IV.5). In the mean radius approach (see for instance [Deschamps 1999b]), the precipitate size distribution is simply described by its mean value, which simplifies the calculations. In our case, a multi-class approach is required, to account for the complex evolution of the particle size distribution during the anisothermal heat treatment generated by the laser. The same choice has been made by various authors ([Myhr 2000], [Nicolas 2002], [Simar 2006]) for similar anisothermal heat treatments.

It has been decided to use a Lagrange-like class model, implemented in a software modified from the PreciSo software developed by Perez and Acevedo [Perez 2007, Acevedo 2007].

IV.B.2. Precipitation model

IV.B.2.a. Generalities

i. Lagrange-like class model

The principle of this model is the following. The precipitate size distribution is discretised into classes of size dR_i, accounting N_i precipitates of mean radius R_i. The driving force for precipitation is the supersaturation of the matrix solid solution. At each timestep, a new precipitate class of radius slightly above R^* (critical radius for nucleation) is created (nucleation). During the same time increment, the radius of each class (that contains a fixed number of precipitates) evolves (growth or dissolution), as represented in Fig. IV.5.b. This whole may be described by 3 main equations: a nucleation law, a growth rate law and a continuity equation.

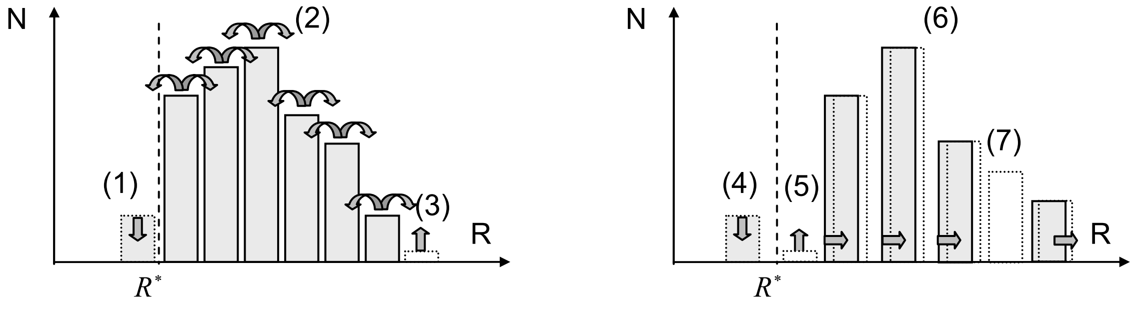

Fig. IV.5. Principle of the class model

(a) Euler- vs. (b) Lagrange-like multi-class models. (1,4): a class below the critical radius for nucleation disappears. (2) Particles flux from one class to the neighbour class. (3, 5): a new class is created. (6): radius evolution in each class. (7): insertion of a new class to minimize the interclass distance.

Coarsening takes place in the later stages of precipitation and leads to an evolution in $R \propto t^{1/3}$ in the bulk (see chapter I), and is accelerated when dislocations are present. Coarsening is naturally accounted for in the class models by the inclusion in the growth equation of the size dependent Gibbs-Thomson (or capillarity) effect.

ii. Simplifications

For the sake of simplicity, the material is described as a pseudo ternary alloy: only magnesium and zinc are considered in the aluminium matrix. Moreover, the precipitate composition is supposed to be stœchiometric and constant during heat treatment: the whole precipitate distribution is seen as $MgZn_2$ precipitates, although the literature has revealed that the reality is more complex (see chapter I). In this model copper atoms are considered as equivalent to zinc atoms, so that $X_{Zn*} = X_{Zn} + X_{Cu}$ and $X^p_{Zn*} = 2X^p_{Mg}$.

iii. Diffusion equation

Precipitation kinetics is controlled by solute diffusion in the matrix, a thermally activated mechanism. The diffusion coefficient D_x of one species in a given matrix is expressed by:

$$\text{(IV.1.)} \quad D_x = D_{0x}\, exp\left(\frac{-Q_{Dx}}{R_B.T}\right)$$

D_{0x} is the diffusion pre-factor, Q_{Dx} the activation energy for diffusion and R_B the universal gas constant.

IV.B.2.b. Nucleation law

i. Nucleation

The nucleation rate can be expressed as a function of an Arrhenius law:

$$\text{(IV.2.)} \quad \frac{\partial N_n}{\partial t} = N_0.Z.\beta^*.exp\left(\frac{-\Delta G^*}{R_B T}\right) exp\left(-\frac{\tau}{t}\right)$$

ΔG^* is the energy barrier for nucleation, N_0 the density of nucleation sites ($= 1/V^\alpha_{at}$) and $\beta^{*^{-1}}$ the critical attachment rate, that is the inverse of the mean time necessary for a solute atom near a precipitate of radius R^* to be attached to it (see Fig. IV.6). This duration can be expressed, for one species x , as:

$$\text{(IV.3.)} \quad \beta_x{}^* = \frac{4\pi R^{*^2}.D_x.X^\alpha_x}{a^4}$$

Where a is the matrix lattice parameter and X^α_x the (atomic) solute fraction in the matrix. The mean duration β^* considers the two constituents of the precipitates, Mg and Zn :

$$\text{(IV.4.)} \quad \beta^{*^{-1}} = \beta_{Mg}{}^{-1} + 2.\beta_{Zn}{}^{-1} = \frac{a^4}{4\pi R^2}\left(\frac{1}{D_{Mg}X^\alpha_{Mg}} + \frac{2}{D_{Zn}X^\alpha_{Zn}}\right)$$

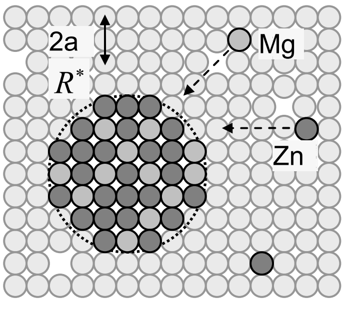

Fig. IV.6. Schematic of a $MgZn_2$ precipitate in an Al matrix

In equation (IV.2.), the second exponential term accounts for the probability to create a new nuclei, an incubation period τ being considered:

$$\text{(IV.5.)} \quad \tau = \frac{1}{2\beta^* Z^2}$$

Z is the Zeldovitch factor, given by:

(IV.6.) $$Z = \frac{V^{p}_{at}}{2\pi R^{*2}}\sqrt{\frac{R_0}{2V^{p}_{at}}}$$

V^p_{at} is the precipitates molar volume, R^* is a critical radius for dissolution (see equation (IV.22.)) and R_0 is the so-called capillarity radius, given by (γ_i the precipitate/matrix interface energy):

(IV.7.) $$R_0 = \frac{2\gamma_i V^p_{at}}{k_B T}$$

ii. Heterogeneous nucleation

ΔG^* (see equation (IV.2.)) will be considered as the energy barrier for heterogeneous nucleation. It has been said in chapter I that nucleation is favoured on heterogeneous sites: dislocations, precipitates, dispersoïds… Accounting for the lower energy barrier for nucleation may be written in the following form:

(IV.8.) $$\Delta G^* = \alpha_h \frac{\Delta G_0}{S^2}$$

α_h is an adjustable parameter accounting for heterogeneous nucleation and decreasing the energy barrier for heterogeneous nucleation. The Gibbs-free energy ΔG_0 is equal to:

(IV.9.) $$\Delta G_0 = \frac{4}{3}\pi R_0{}^2 \gamma_i$$

S is the matrix supersaturation, given by:

(IV.10.) $$S = ln\left(X^{\alpha}_{Mg}\right) + 2\,ln\left(X^{\alpha}_{Zn}\right) - ln\,K^{\infty}_{MgZn2}$$

In which $K^{\infty}_{MgZn_2}$ is the precipitates solubility product, calculated from the equilibrium solute fractions:

(IV.11.) $$K^{\infty}_{MgZn2} = X^{\alpha-\infty}_{Mg}.\left(X^{\alpha-\infty}_{Zn}\right)^2$$

IV.B.2.c. Growth rate law

i. Growth rate

The growth rate of a given precipitate of radius R is given by (equivalently for magnesium):

(IV.12.) $$\left.\frac{\partial R}{\partial t}\right|_{Zn} = \frac{D_{Zn}}{R}\frac{X^{\alpha}_{Zn} - X^{i}_{Zn}}{\alpha.X^{P}_{Zn} - X^{i}_{Zn}}$$

Where D_{Zn} is the species diffusion rate and α the atomic volume ratio between the matrix and the precipitates: $\alpha = V^{\alpha}_{at} / V^{p}_{at}$.

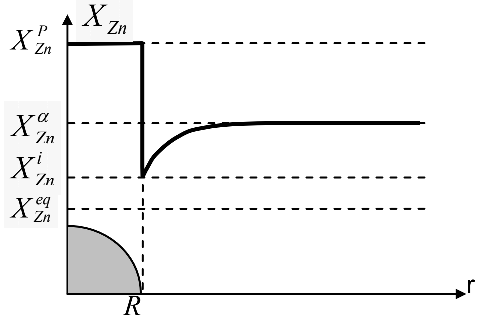

Fig. IV.7. Zinc concentration as a function of the distance from the precipitate

The precipitate composition is supposed constant (r<R). Then it varies between the interface (r=R) and far from the precipitate, up to a steady value in the matrix (r>>R).

As can be seen on Fig. IV.7, X_{Zn}^{α} and X_{Zn}^{P} express the Zinc concentration in the matrix and in the precipitates and X_{Zn}^{i} the concentration at the precipitate/matrix interface. In the case of a binary alloy, its value would be given by the Gibbs-Thomson equation, X_{Zn}^{eq} being the equilibrium solute concentration at the interface:

(IV.13.) $$X_{Zn}^{i} = X_{Zn}^{eq}\, exp\left(\frac{R_0}{R}\right)$$

In our case, the composition at the interface is calculated from the solubility product:

(IV.14.) $$K_{MgZn2} = X_{Mg}^{i}.\left(X_{Zn}^{i}\right)^2$$

ii. Solubility product

The solubility product depends on the Gibbs-free energy expression ΔG_0 , ΔH_0 and ΔS_0 being respectively the entropy variation and the free enthalpy related to the formation of the precipitates:

(IV.15.) $$ln\, K_{MgZn2}^{\infty} = \frac{\Delta G_0}{R_B T} = \frac{\Delta S_0}{R_B} - \frac{\Delta H_0}{R_B T}$$

The Gibbs-Thompson effect tends to dissolve the smaller precipitates, whose surface is large as compared to their volume (see [Perez 2005]). It is accounted in the solubility product as:

(IV.16.) $$K_{MgZn2}(R) = K_{MgZn2}^{\infty}\ exp(R_0/R)$$

iii. Growth and dissolution

“True” growth is not the only phenomenon considered in equation (IV.12.): depending on the precipitate/matrix interface concentration, the precipitates may grow or dissolve:

- If $X_{Zn}^{\alpha} > X_{Zn}^{i}$ the precipitate will dissolve,
- If $X_{Zn}^{\alpha} < X_{Zn}^{i}$ the precipitate will grow,

IV.B.2.d. Continuity equation

In our case (Lagrange-like approach), the size evolution of one class during a time step Δt is given by:

(IV.17.) $$R_i(t+\Delta t) = R_i(t) + dR_i/dt\,\Delta t$$

IV.B.2.e. Model implementation

i. Discretisation

The total number of precipitates is given by:

(IV.18.) $$N = \sum_i N_i$$

Where N_i is the precipitate number (percent volume) in a class of radius $R_i \pm \Delta R/2$. The mean radius and the precipitate volume fraction are calculated using respectively:

(IV.19.) $$\overline{R} = \frac{1}{N}\sum_i N_i R_i$$

(IV.20.) $$f_v = \frac{4}{3}\pi \sum_i N_i R_i^{\,3}$$

If X_{Zn}^{α} and X_{Zn}^{0} are respectively the current and nominal solute fraction in the matrix, and X_{Zn}^{P} the solute content in the precipitate, the mass balance is given by:

(IV.21.) $$X_{Zn}^{\alpha} = \left(X_{Zn}^{0} - f_v X_{Zn}^{P}\right)/\left(1 - f_v\right)$$

ii. Time and class management

An auto adaptive time step Δt is used, to optimise the time consumption and the precision of the calculations (see [Perez 2008] for details).

A minimum number of classes has to be kept, to insure an accurate description of the particle size distribution. For that purpose, a new class is artificially created if the distance between two neighbouring classes is higher than ΔR_{max} (see [Perez 2008] for details).

A class will disappear if the precipitates size is smaller than this critical radius: $R < R_0 \times A$, where A is a tuneable parameter.

iii. Nucleation and dissolution

Heterogeneous nucleation is considered in decreasing the energy barrier for nucleation throughout the α_h parameter (see IV.B.2.b.ii). Nucleation will stop when the driving force is zero, i.e. when $X^{\alpha}_{Mg} = X^{eq}_{Mg}$.

The Gibbs-Thomson effect is responsible for the instability of the smaller precipitates. The critical radius below which precipitates will dissolve ($R < R^*$) or grow ($R > R^*$) is defined as:

$$\text{(IV.22.)}\quad R^* = R_0 / S$$

iv. Solving the growth equation

Two further equations are required to solve equation (IV.12.), the two unknowns being the Zinc and the Magnesium concentrations at the interface X^i_{Zn} and X^i_{Mg}. The first equation is given by an equivalent expression giving the growth rate considering Magnesium atoms:

$$\text{(IV.23.)}\quad \left.\frac{\partial R}{\partial t}\right|_{Mg} = \frac{D_{Mg}}{R}\frac{X^{\alpha}_{Mg} - X^i_{Mg}}{\alpha.X^P_{Mg} - X^i_{Mg}}$$

The second equation is given by the precipitates solubility product K_{MgZn2}:

$$\text{(IV.24.)}\quad K_{MgZn2} = X^i_{Mg}.\left(X^i_{Zn}\right)^2$$

As $X^P_{Zn} + X^P_{Mg} = 1$, the simplification made in IV.B.2.a.ii concerning the precipitates composition can be written as: $X^P_{Mg} = 1/3$ and $X^P_{Zn} = 2/3$. Then equations (IV.12.) and (IV.23.) are equal, which means that:

$$\text{(IV.25.)}\quad D_{Mg}\left(2\alpha/3 - X^i_{Zn}\right)\left(X^{\alpha}_{Mg} - X^i_{Mg}\right) = D_{Zn}\left(\alpha/3 - X^i_{Mg}\right)\left(X^{\alpha}_{Zn} - X^i_{Zn}\right)$$

If one replaces X^i_{Mg} by its expression derived from equation (IV.24.), one finally obtains a one-variable polynomial expression which allows the calculation of the Zinc concentration at the interface X^i_{Zn}, and finally to solve equation (IV.12.):

$$\text{(IV.26.)}\quad A.{X^i_{Zn}}^3 + B.{X^i_{Zn}}^2 + C.X^i_{Zn} + D = 0$$

In which:

$$\text{(IV.27.)}\quad \begin{aligned} A &= D_{Zn}\,{}^{\alpha}\!/_{3} - D_{Mg}X^{\alpha}_{Mg} \\ B &= D_{Mg}\,{}^{2\alpha}\!/_{3}\,X^{\alpha}_{Mg} - D_{Zn}\,{}^{\alpha}\!/_{3}\,X^{\alpha}_{Zn} \\ C &= D_{Mg}K_{MgZn_2} - D_{Zn}K_{MgZn_2} \\ D &= -D_{Mg}\,{}^{2\alpha}\!/_{3}\,K_{MgZn_2} + D_{Zn}.K_{MgZn_2}X^{\alpha}_{Zn} \end{aligned}$$

IV.C. Experimental

IV.C.1. Laser processing

IV.C.1.a. Introduction

To study the effect of laser forming on precipitation and mechanical properties, “model” specimens have been processed and provided by the EADS common research center in Germany. The specimens are 150x76x5 mm plates of T7651 base material. They have been subjected to the following process: first, surface milling; then laser processing itself (see Fig. IV.8). 3 seconds after this process, they were quenched into liquid nitrogen, where they were stored to prevent any natural aging, until both microhardness and SAXS measurements were carried out.

IV.C.1.b. Process parameters

The specimens were swept by the laser beam as presented in Fig. IV.8.b. The laser lines were made sequentially, the laser parameters for each of the three specimens being presented in Table IV.1.

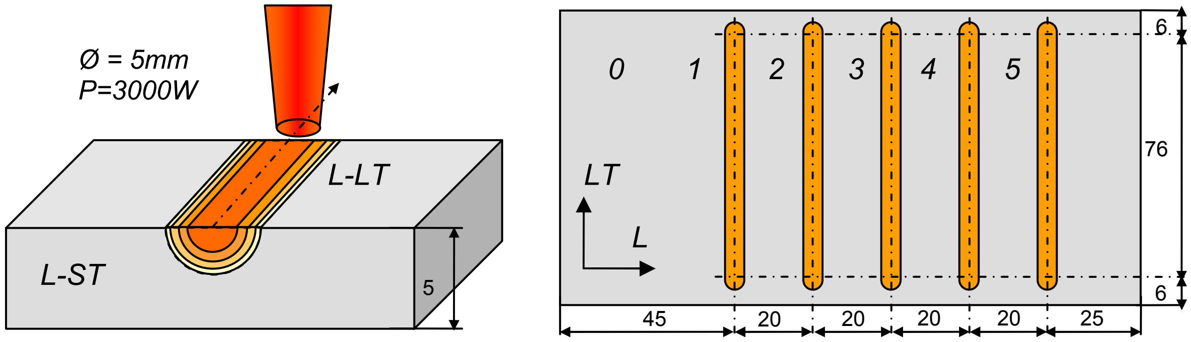

Fig. IV.8. Specimen and laser processing

(a) Schematic of laser processing and local temperature heating. (b) Whole specimen and laser lines. In that case 5 laser lines were made (labeled from “1” to “5”). “0” is the area far from the laser lines. Time duration between end of each line and beginning of next line is 10 seconds. The specimen is quenched into liquid nitrogen 3 seconds after end of last line.

The laser parameters are reported in Table IV.1. The beam diameter and the power remained constant; the velocity and the number of laser lines have been varied. The specimen that received the highest heat input is the specimen #2 (1/3 more than specimen #1, the laser velocity being smaller). It should be therefore the most affected specimen and for this reason it will receive more attention.

Specimen	Line number	Velocity	Beam diameter	Power
1	5	15 mm/s	5 mm	3000
2	5	10 mm/s	5 mm	3000
3	1	10 mm/s	5 mm	3000

Table IV.1. Laser parameters for each specimen

IV.C.2. Mechanical properties mapping

Transverse (L-ST plane) and surface (L-LT plane) Vickers microhardness measurements (weight: 100 g) have been performed to map out the local mechanical properties in the laser processed specimens presented in IV.C.1. Note that the specimens have been mirror polished before performing these measurements. A complete set of results will be presented for specimen #2, the most affected one.

IV.C.2.a.Area 0 measurements

Surface measurements have been performed far from the laser area along the L direction (see Fig. IV.8.b), to investigate whether the whole material has been affected by the laser process or not.

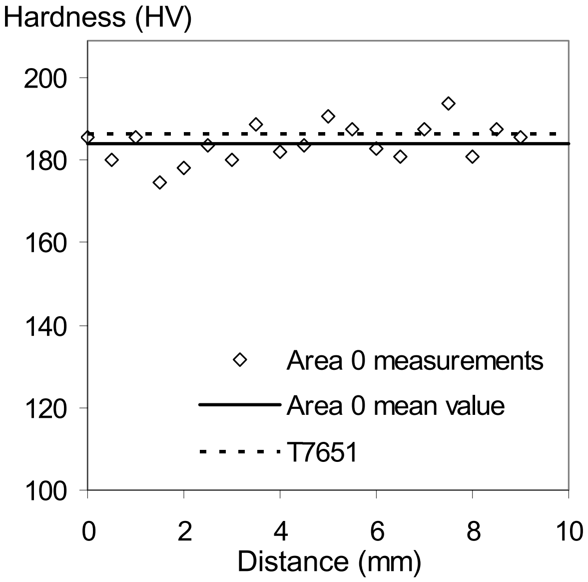

Fig. IV.9. Microhardness mapping of specimen #2, area 0

Fig. IV.9 shows that the mechanical properties are homogeneous on the surface, with an average hardness of 184 HV. This is slightly smaller than the hardness value of the parent T7651 material (186 HV), but this difference is not significant. It can be therefore considered that far from the laser lines the material is not affected at all by the laser treatment.

IV.C.2.b.Laser lines measurements

Fig. IV.10 shows the hardness profile along the L direction (see Fig. IV.8) of specimen #1, laser line #1, measured either on the top surface of at various depths in the transverse L-ST plane.

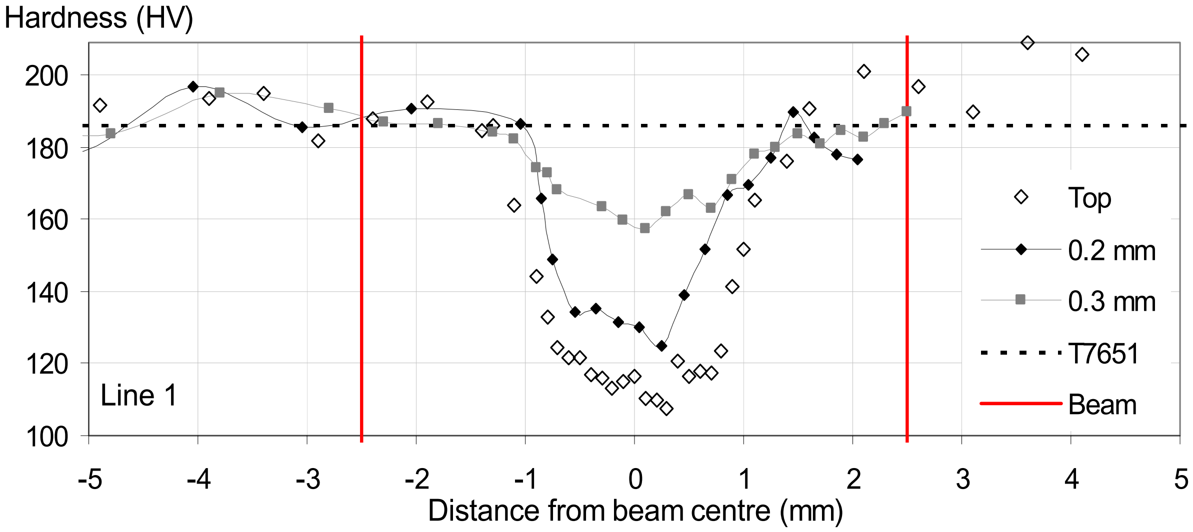

Fig. IV.10. Microhardness mapping of specimen #1, line 1

“Top” is the surface measurement; 0.2 and 0.3 are the surface offsets from the surface. “T7661” is the reference hardness value of the base T7651 material. “Beam” represents the laser beam width.

The same results for the laser lines #1, #3 and #5 of specimen #2 (higher power, as compared to specimen #1) is presented in Fig. IV.11. This allows plotting a complete mechanical properties map, as made on Fig. IV.12.

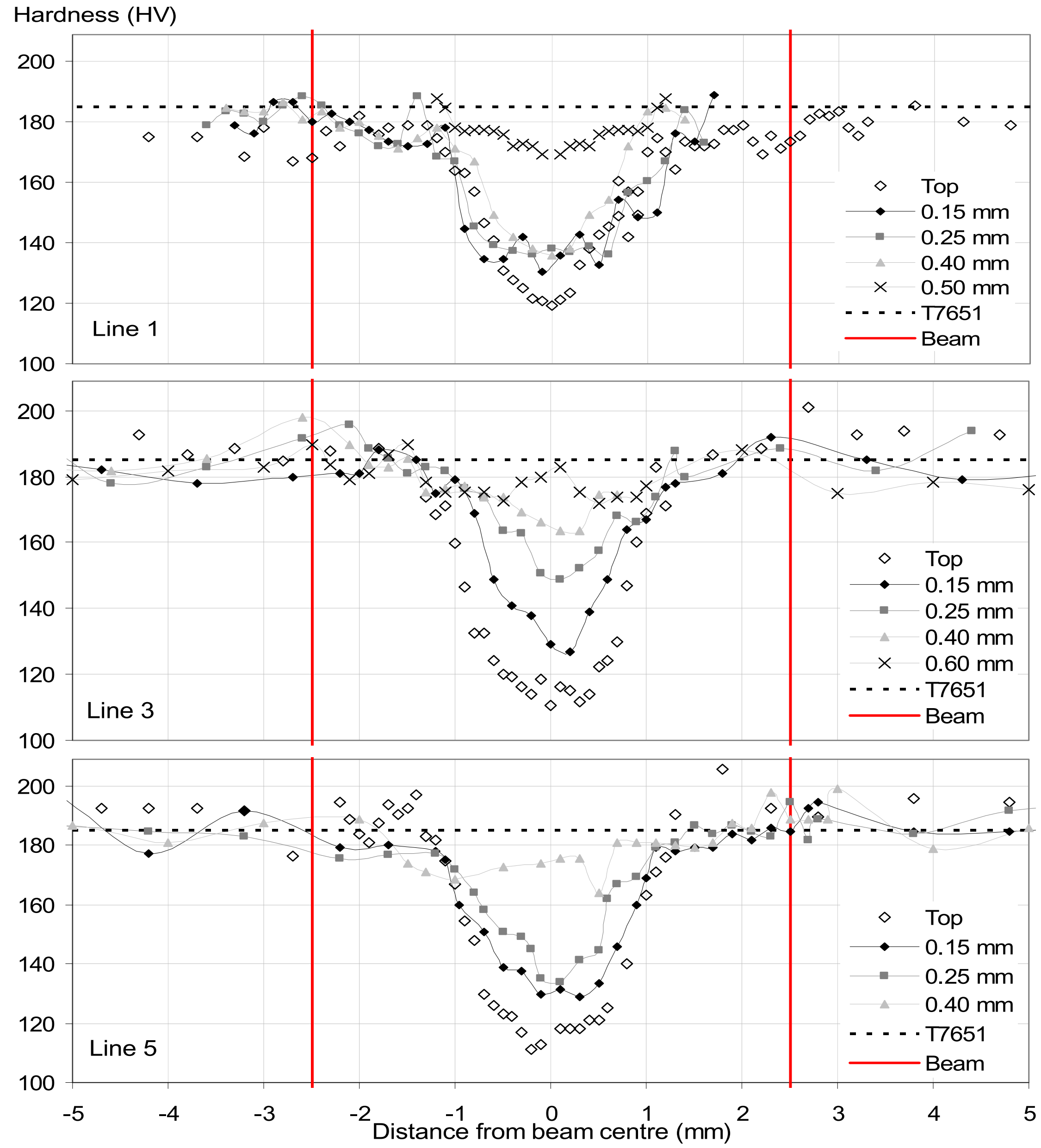

Fig. IV.11. Microhardness mapping of specimen #2

Measurements performed in the centre of: (a) the first, (b) the third, (c) the fifth laser line. “Top” is the surface measurement; 0.15, 0.25, 0.4 and 0.6 are the surface offsets from the surface. “T7661” is the reference hardness value of the base T7651 material. “Beam” represents the beam width.

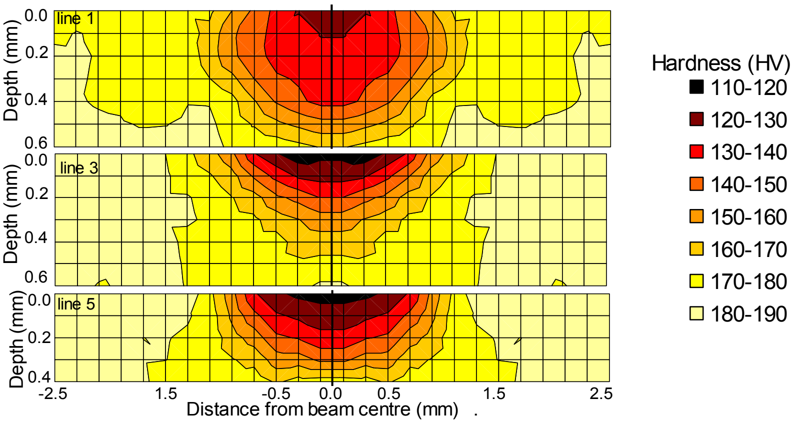

Fig. IV.12. Microhardness map of specimen #2

Laser lines 1 (a), 3 (b) and 5 (c). Mean values calculated between symmetrical points.

From these measurements, the following statements can be made:

- Far from the beam centre, the hardness value is close to the hardness of the base material.
- In a finite area around the beam centre, the mechanical properties are different from the parent material properties. This area will be called the apparent heat affected zone (HAZ). This zone is about 4 to 5 mm width, which corresponds to the beam diameter and about 0.6 mm deep.
- The mechanical properties generally follow an inversed bell-shaped curve in the HAZ with a drop in the centre (up to 65 HV losses), even if a slight increase can be observed in some cases in the centre (line #3, 0.40mm depth) or at the edges of the HAZ (for instance line #5, top).
- The three different laser lines seem to show slightly different behaviors. First, the peak values of the top measurements are ordered as a function of the line number: it goes deeper in line #5 than in lines #3 and #1. Then, values are more centered in the first lines than in line #5.
- Despite their different laser treatment (different laser velocity), samples #1 and #2 do not present significantly different behaviors. The only noticeable point is the lower depth of the affected zone for the lowest treated specimen (#1). Indeed, 0.3mm under the surface, the central point has lost 25 HV as compared to the base material properties, while it has lost 45 HV for the specimen #2.

More generally it can be said that these profiles are very similar to ones measured in the heat affected zone of welded components [Nicolas 2002, Myhr 2004, Simar 2006]. This laser forming process is indeed very comparable to laser welding (or more generally to welding). The microstructure is affected by the local heat treatment. Two phenomena may have happened, depending on the temperature range reached during the laser treatment: either a local fusion of the material, or precipitation evolution (dissolution and/or growth and/or coarsening).

IV.C.3. Microstructure mapping

IV.C.3.a. Grain microstructure

The grain microstructure has been investigated with an optical microscope after mirror polishing. One can notice in Fig. IV.13 a brighter zone characteristic of the heat affected zone, surrounded by a grey zone, which corresponds to the non affected zone. This colour change tends to show that some precipitates have been dissolved in the HAZ. The sub-grains are highly distinguishable on the whole micrograph and no trace of fusion (e.g. solidification) can be found. It can be concluded from this observation that the changes of mechanical properties during laser processing are probably due to precipitation phenomena.

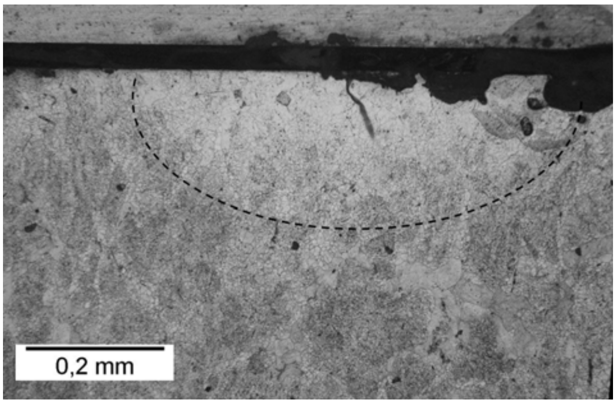

Fig. IV.13. Optical micrograph of specimen #2

Transverse cut. The top grey area is a counter sample and black area is glue. The major grey area in the bottom is the specimen. The dashed line limits the highly affected from the less affected zone.

IV.C.3.b. Precipitation state

i. Specimens

The specimens that have been investigated by microhardness have been cut into 100 µm thick samples (see Fig. IV.14). For instance to obtain the second slice, located at 100 µm (± 50 µm, i.e. [-50;-150 µm]) below the initial specimen surface, it has been necessary to remove by mechanical polishing 50 µm from the top surface and 4.85 mm from the bottom face. As the X-Ray beam size is about 0.2 by 0.2 mm wide, this allows mapping more accurately the local precipitate microstructure than in the case of transverse measurements.

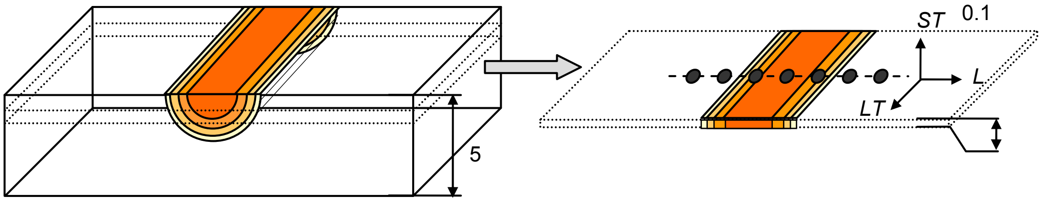

Fig. IV.14. Schematic of the SAXS specimen

(a) Base specimen. (b) 100 µm slice. Each point represents a SAXS measurement.

ii. SAXS results

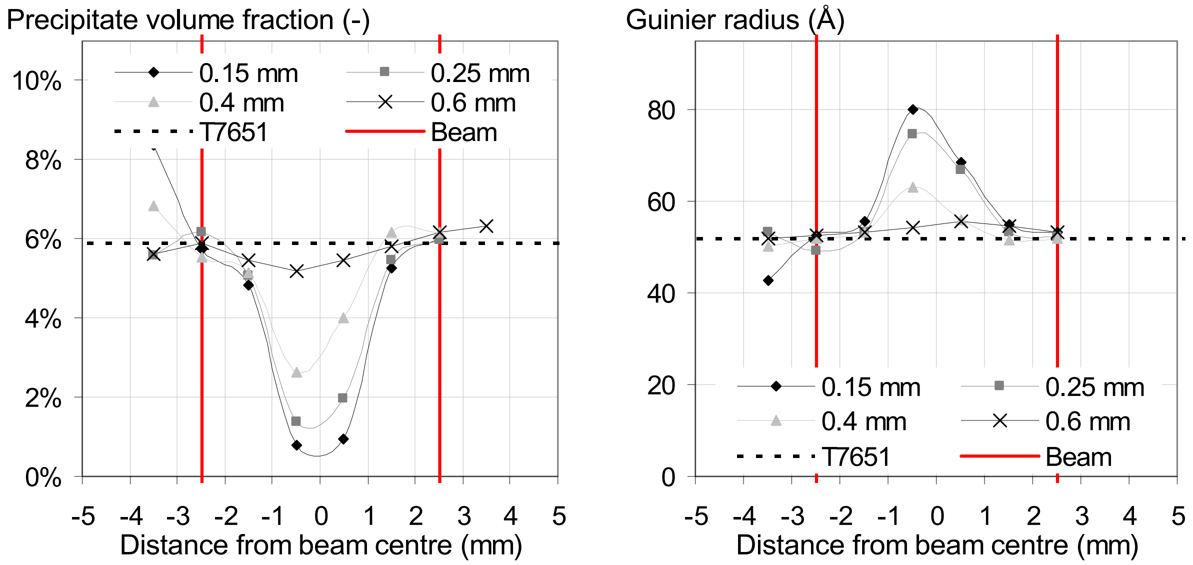

Fig. IV.15. SAXS measurements performed on specimen #2, line 3

(a) Precipitate volume fraction. (b) Guinier radius.

The corresponding 2D precipitation maps are presented in Fig. IV.16.

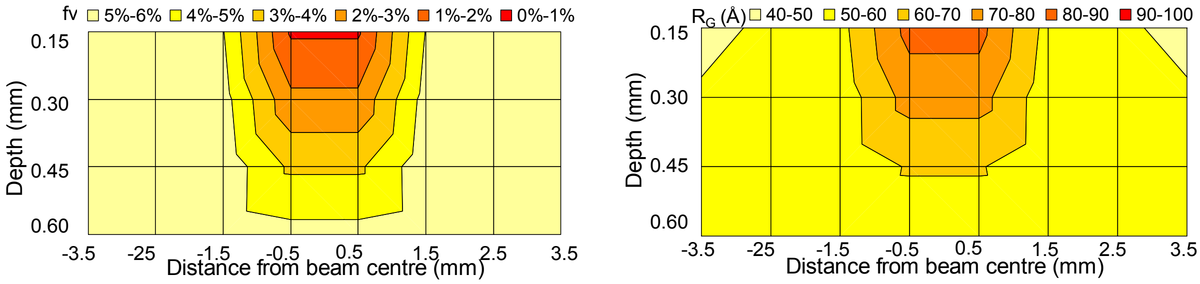

Fig. IV.16. Precipitation map of specimen #2, line 3

(a) Precipitate volume fraction. (b) Precipitate Guinier radius. Mean values calculated between symmetrical points.

These results show a similar behavior as the ones observed for microhardness mapping: the closer one comes to the beam centre, the most affected is the precipitate microstructure. The precipitate volume fraction diminishes and is probably 0 in the near subsurface, while the precipitate mean size increases, meaning that the smaller precipitates are dissolved during the laser treatment. The measurements performed far away from the laser beam centre are identical to the parent T7651 material (volume fraction = 5.9%; Guinier radius = 52 Å). The non affected zone is about 5 mm large and slightly more than 0.6 mm deep.

IV.C.4. Conclusion on experimental results

It has been shown in IV.C.2 that the local mechanical properties are affected by the laser treatment, close to the laser beam. The affected zone is about 0.6 mm deep and 2.5 mm wide from the laser beam centre. Outside of this zone, the material has kept the parent material properties.

The SAXS results presented in IV.C.3.b show similar behaviour. If one superimposes the hardness map and the precipitation state map (see Fig. IV.17), one can see that there is a very good agreement between the loss of mechanical properties and the precipitation dissolution. This confirms that the loss of mechanical properties is attributed to the partial dissolution of the precipitates.

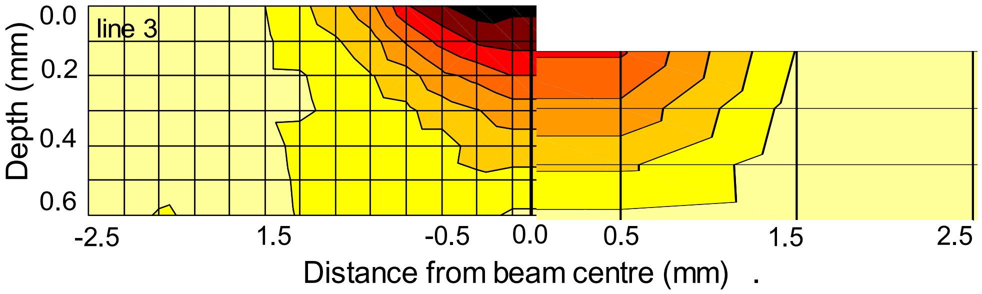

Fig. IV.17. Superimposition of hardness and precipitate volume fraction maps

(a) Microhardness map (from Fig. IV.12). (b) Precipitation volume fraction map (SAXS measurements; see Fig. IV.16)

There is a very strong properties gradient in the affected zone, which will require a very accurate modelling procedure to predict correctly the evolution of the precipitation state during the laser treatment.

IV.D. Modelling

IV.D.1. Introduction

The overall procedure for modelling the effect of laser processing on precipitation can be divided into 3 main stages. First, the temperature profile in the specimen during laser treatment has to be modelled. Then the precipitation model has to be calibrated. Finally, the temperature profile calculated previously will be used as an input for the precipitation model, and the predicted result compared to the experimental results presented previously. This whole strategy is summarised in Fig. IV.18.

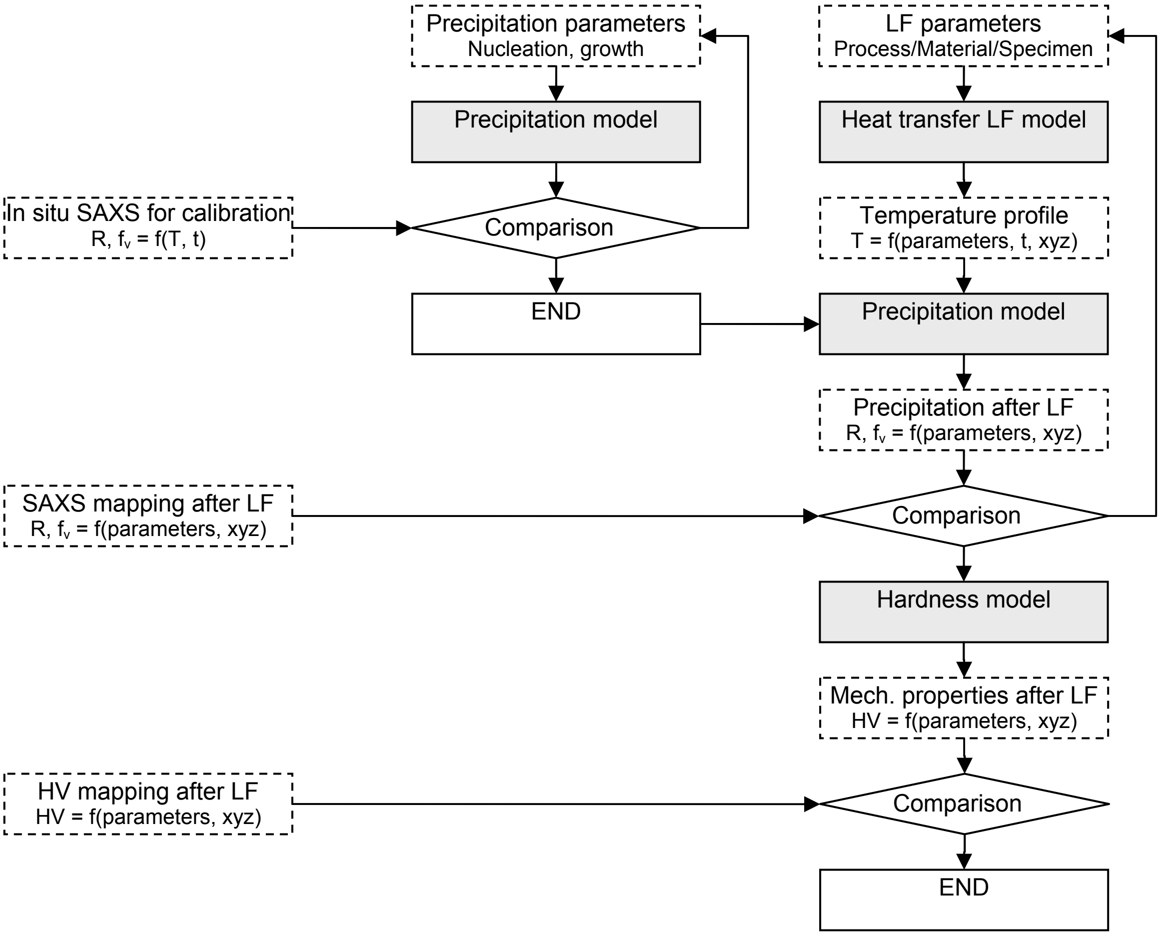

Fig. IV.18. Algorithm: modeling the effect of laser processing on precipitation

In the first column are represented theexperimental tasks; the second one concerns the calibration of the precipitation model; the third one the overall modeling process. In grey the different models.

IV.D.2. Temperature profile calculation

IV.D.2.a. Introduction

Temperature distribution and temperature evolution was computed by Patras University, a partner in the COMPACT project, using a laser beam heat flux model, such as the one presented in [Labeas 2008]. For their Finite Element Model, they meshed the specimen with SHELL131 elements of the ANSYS code (see Fig. IV.19.b). It is a 3-D layered shell element with in-plane and through-thickness thermal conduction capability. The element has four nodes with up to 32 temperature degrees of freedom at each node. Ten layers through-the-thickness of the 5mm plate have been considered. The meshes are refined in the near-beam area (see Fig. IV.19.a).

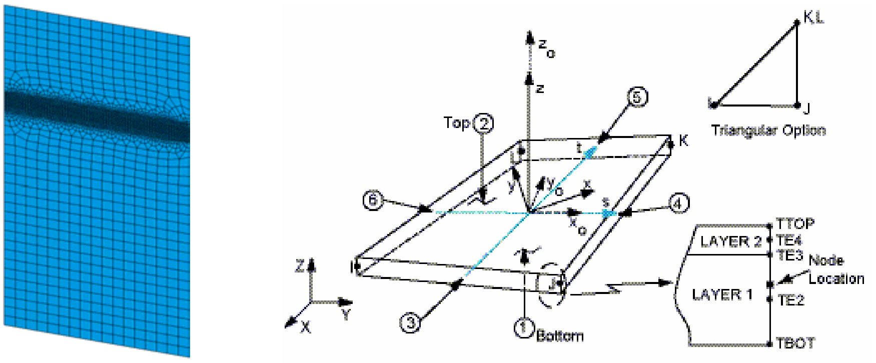

Fig. IV.19. Plate meshing and element geometry

(a) Plate meshing, showing a refined mesh in the near-beam area. (b) SHELL131 element of ANSYS

The different parameters entering the laser beam heat flux model can be divided into 3 families: process parameters (beam power, diameter, scanning velocity and distance from material), material parameters (thermal conductivity, heat capacity and density) and specimen parameters. This third family includes the specimen geometry but also the material absorption coefficient, which mainly depends on the material surface state (colour and roughness).

This last parameter is difficult to evaluate accurately, and would have required a specific calibration (in situ measurements with a pyrometer or thermocouples for instance), which has not been made. Therefore it has been chosen to calculate the temperature distribution for different values of the absorption coefficient (between 0.1 and 0.2) and to evaluate the value of the effective absorption coefficient by an inverse methodology: the experimental precipitation state measured on the laser treated part is compared to the modelled precipitation state, resulting from the computed temperature profile.

IV.D.2.b. Results

i. Initial results

An example of the evolution of the temperature distribution on the top surface during laser processing is shown on Fig. IV.20. In that case the absorption coefficient (AC) is chosen at 0.10, which generates a maximum temperature of ~420°C, in the middle of the laser beam.

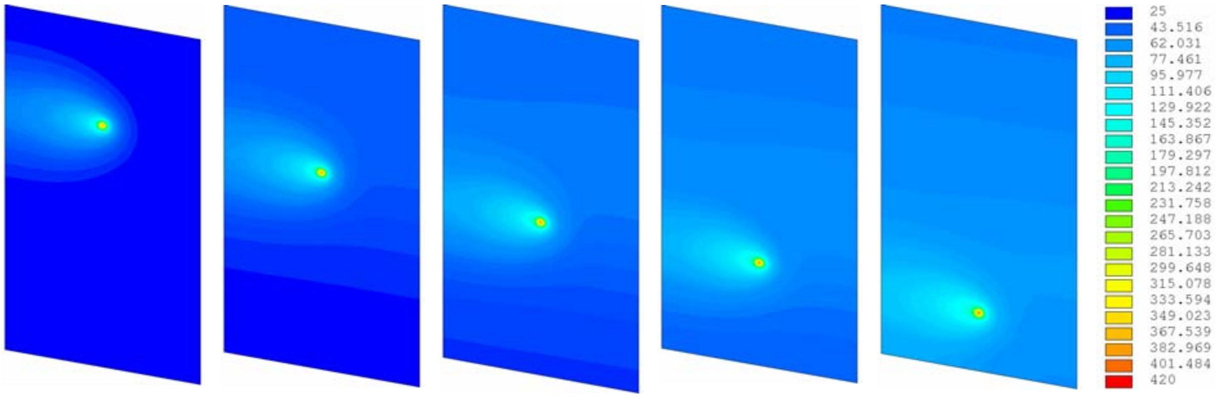

Fig. IV.20. Evolution of temperature distribution during laser processing

Temperature calculated on the top surface of specimen #2 with AC=0.1. On each figure, the laser beam is in the middle of the laser line.

At first sight, one can notice an increase of the mean plate temperature between the first and the last laser lines, which goes from ~25°C to ~70°C. This effect will be seen more clearly in the following figures, where more quantitative data will be available.

ii. Qualitative analysis of the temperature profiles

Fig. IV.21 shows the evolution of the temperature of some relevant locations during the whole laser process: on the surface, in the middle of laser lines 1, 3 and 5 (Fig. IV.21.a) and for different depths in the centre of laser line 1 (Fig. IV.21.b). From this figure, the following statements can be made:

- The temperature at a given point rises sharply when the laser beam approaches. The reached peak temperature, above 160°C[1], is probably high enough to destabilise the precipitates. This stage lasts less than 1s, after which the temperature goes back to lower values (less than 100°C) when the laser beam goes away. Then, a second temperature increase can be observed when the laser beam is at the middle of the second laser line (and respectively for the other lines).
- The mean plate temperature increases during the whole process, going from room temperature to ~60°C. As a consequence, the peak temperature from one laser line to another also rises.
- The heat transfer occurs very rapidly and there is almost no delay (about 0.1s) between the laser beam passage and the peak temperature. This is due to the high thermal conductivity of aluminium (about 1000 J/kg/K [Compact 2007]).
- There is a high temperature gradient in the depth of the specimen in the near-peak area (see Fig. IV.21.b). The temperature profile is very steep and reaches high values in the top surface (in that case: 374°C), but less than 160°C in the middle of the plate and even less in the bottom of the plate (5mm under the top surface). This gradient decreases and disappears very soon after the peak: in less than 1s, the temperature is homogeneous in the depth.

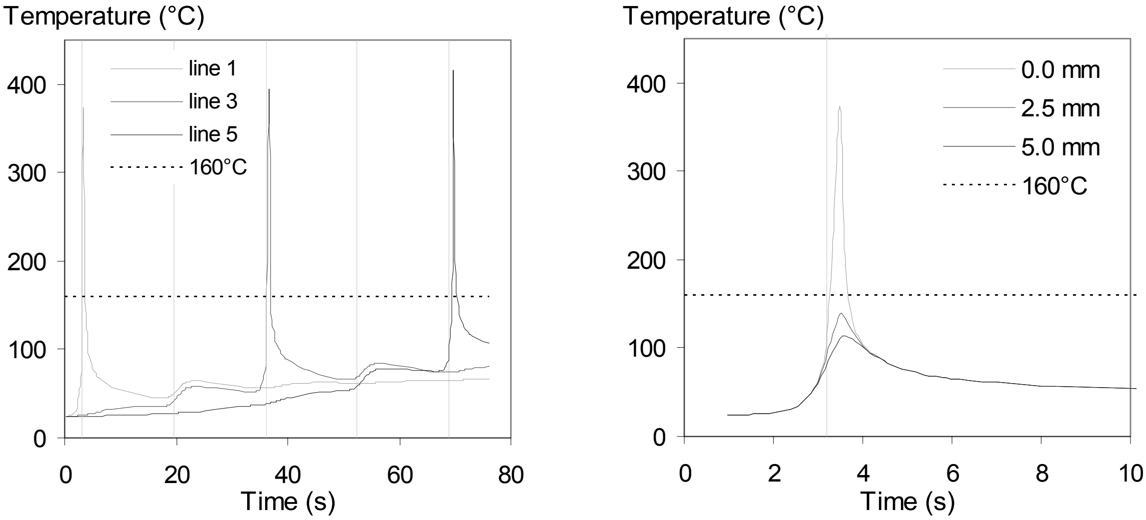

Fig. IV.21. Temperature profiles at various locations

(a) Surface measurements, centre of lines 1, 3 and 5 (LT=0, L=0, ST=0). (b) Comparison between top, middle and bottom surface measurements in the centre (LT=0, L=0) of line 1. Plate #2, AC=0.1. The vertical grey lines indicate the time at which the laser beam crosses the LT=0 position, for each line.

To summarise, it can be said that laser processing generates a short, intense, heterogeneous and highly non-isothermal heat treatment. The temperature gradient mainly affects the peak temperature, the rest of the temperature profile being identical, whatever the distance from the laser beam centre. Moreover the peak temperature of the different laser lines increases (see Fig. IV.21.b). The temperature outside of the near-peak area is probably too low (and the timescale small) to affect the precipitation state significantly. On the contrary, the temperature in the very sub-surface is enough to affect precipitation and will require special attention.

---

[1] For the sake of simplicity, and in a first qualitative analysis, the final temperature of the T7651 treatment (i.e. 160°C) will be considered as the critical temperature, able to destabilise the microstructure.

iii. Qualitative analysis of the temperature distribution at peak

For that purpose, the temperature distribution in the close area under the surface (1 mm deep, 2.5 mm wide) has been calculated for lines 1, 3 and 5 of specimen #2 (Fig. IV.22). As the peak temperature is probably the main parameter controlling the extent of the modification of the precipitation state, these calculations are carried on at the time where the temperature has reached its maximum value.

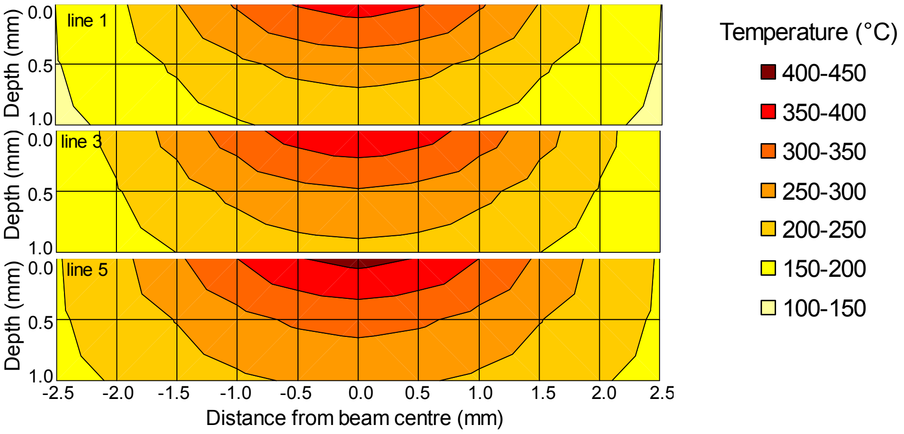

Fig. IV.22. Temperature distribution at maximum temperature

Temperature distribution at maximum temperature for (a) line 1, (b) line 3, (c) line 5, in the centre of the lines (LT=0) (respectively at 374°C at 3.4s, 395°C at 36.6s, 417°C at 69.8s). Plate #2, AC=0.1.

One can see the progressive increase of the peak temperature as the laser process goes on: the maximum temperature reached in line 1 is 374°C, while it goes up to 417°C in line 5. The “deeply” heat affect zone (temperature above 250°C) remains less than 1mm deep and 4mm large.

iv. Correlation between peak temperature and mechanical properties

This temperature distribution is compared to the mechanical properties maps in Fig. IV.23. It is not possible to perform a real quantitative analysis of these results, but it already confirms what has been observed previously. The higher is the temperature, the stronger will be the effect on the mechanical properties and the deeper the hardness drop. When the peak temperature is less than 250°C, the mechanical properties are almost not affected (hardness remains above ~170-180 HV).

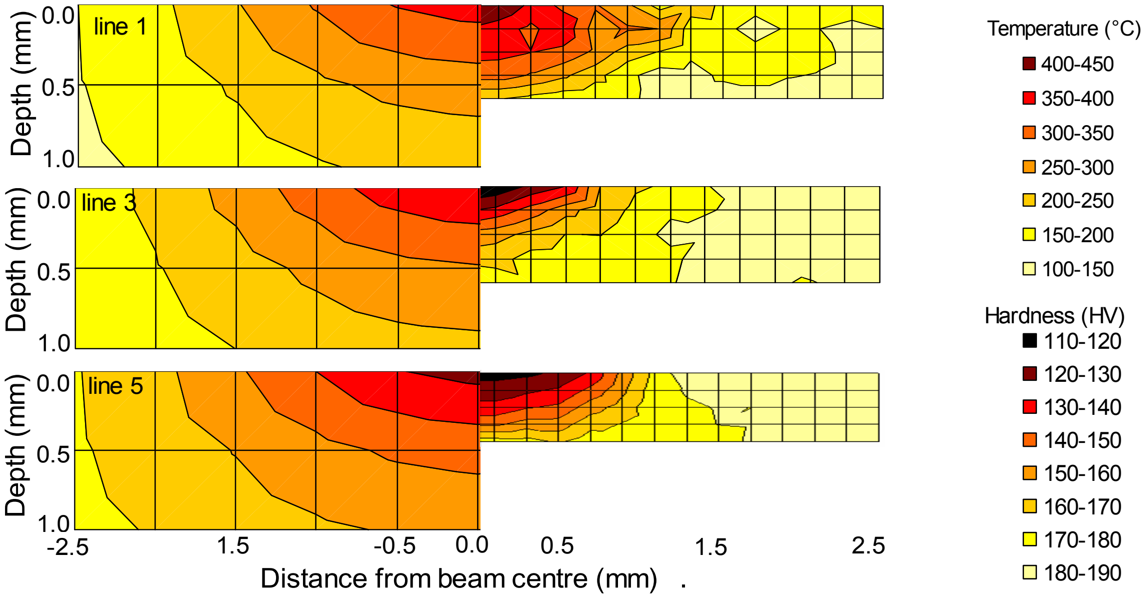

Fig. IV.23. Superimposition of temperature and hardness maps

Laser lines 1 (a), 3 (b) and 5 (c) of plate #2. Temperature (left) vs. microhardness map (right).

v. Temperature profiles at some relevant locations

The temperature profiles of some relevant points of are presented in Fig. IV.24. They will be used in the precipitation kinetics modelling.

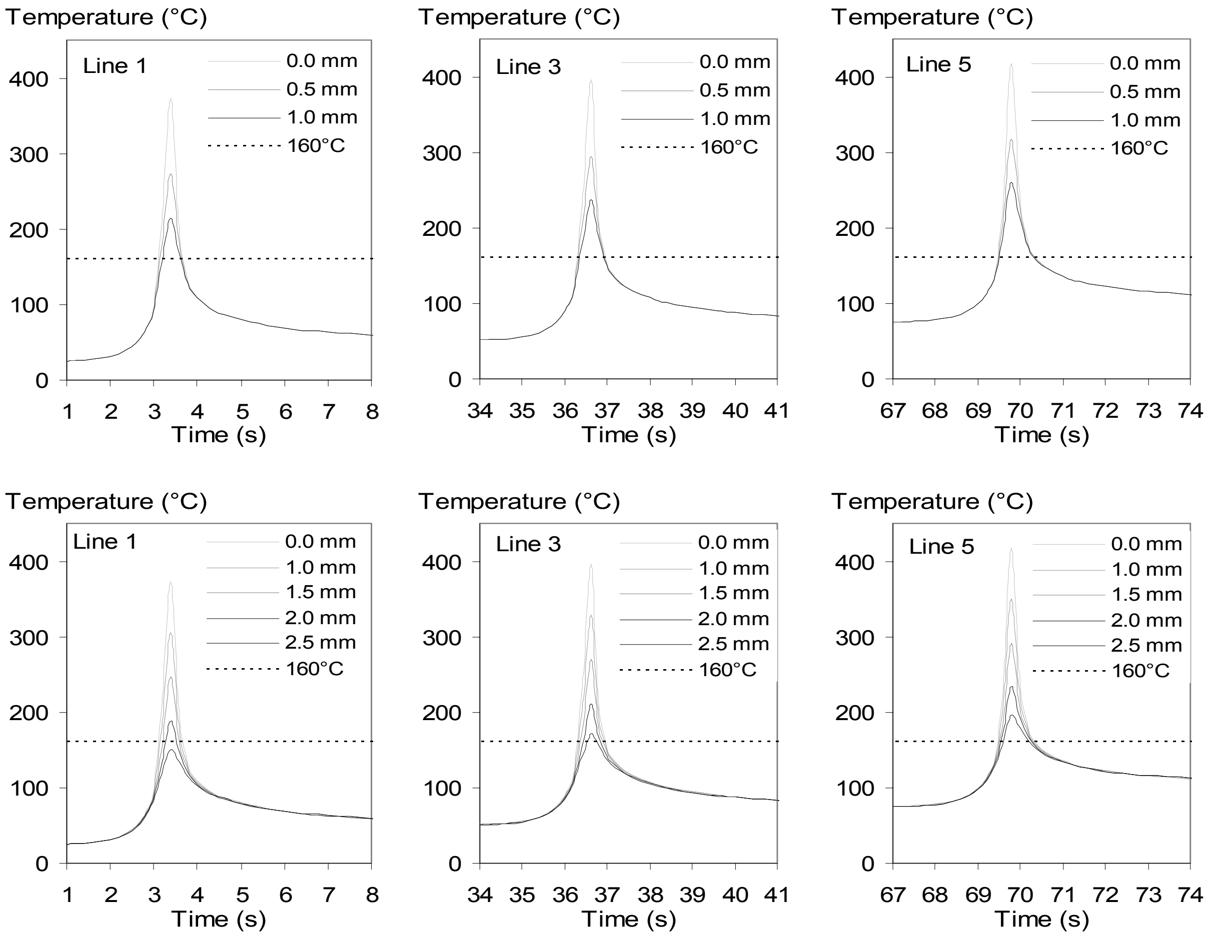

Fig. IV.24. Temperature profiles at some relevant locations

(a, b, c): Centre of the lines (L=0), various depths (ST direction). (d, e, f): Top surface (ST=0), various distances from beam centre (ST direction). Temperature calculated in the centre (LT=0) of the first (a, d), third (b, e) and fifth (c, f) laser lines of specimen #2 with AC=0.1.

vi. Influence of the absorption coefficient

The same calculations have been performed with absorption coefficients of 0.125, 0.15 and 0.20, instead of 0.10. Two examples corresponding to two different locations are plot in Fig. IV.25.

One can notice that the absorption coefficient plays a quite significant role on the peak temperature, but also on the average plate temperature. For laser line 5 for instance, the peak temperature varies from 416°C for AC=0.10 to 785°C for AC=0.20. This high temperature would have overcome the material fusion temperature, which is not the case, according to our observations (see Fig. IV.13).

As this coefficient is not known precisely, it will be necessary to investigate the effect of the various temperature profile results (which correspond to the different absorption coefficients) on the precipitation modelling, and to calculate its value by an inverse method.

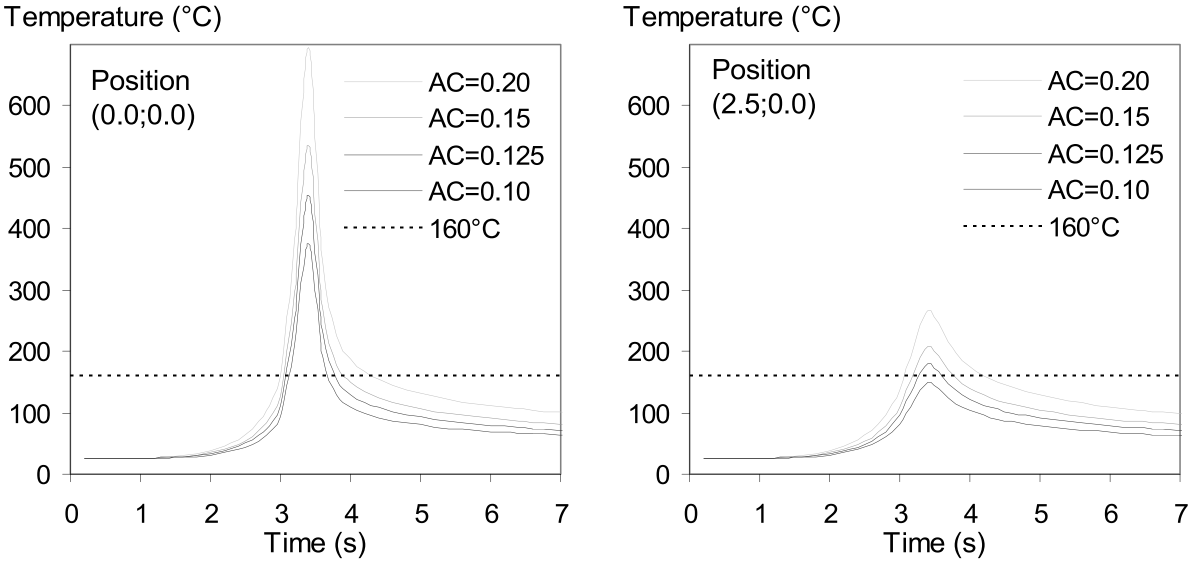

Fig. IV.25. Influence of absorption coefficient on temperature profiles

(a) Centre of the laser beam (L=0). (b) 2.5mm away from the beam centre (L=2.5). Centre of laser line #1, surface measurements (LT=0, ST=0).

IV.D.3. Precipitation model calibration

IV.D.3.a. Introduction

It has been shown in chapter III that SAXS measurements allow a quantitative description of the precipitate state, in particular to determine the mean precipitates size (Guinier radius) and the volume fraction. This technique is therefore very accurate to adjust the model parameters. For that purpose, in situ SAXS experiments have been carried out on temper T7651: isothermal heat treatments for the model calibration itself and controlled heating rate reversions for the model validation. Then the non-isothermal heat treatments corresponding to the laser forming treatment will be applied to the model and compared to the measurements performed on laser treated components and presented in IV.C.3.

IV.D.3.b. Experiments

i. Set-up and treatments

The high photon flux available at ESRF allows measuring the precipitation evolution with a good signal/noise ratio at relatively high acquisition frequency, which is very suitable for performing in situ reversion experiments. In that case, 0.5s long images have been acquired.

T7651 thin specimens have been subjected to isothermal heat treatments at various temperatures: from 200°C to 340°C (typical heating ramp: 5-10°C/s), and heating ramps at 0.8 and 1.6°C/s.

ii. Experimental results

The evolution of the precipitate volume fraction and Guinier radius during isothermal treatment at 240°C are shown in Fig. IV.26, as well as the measured temperature profile.

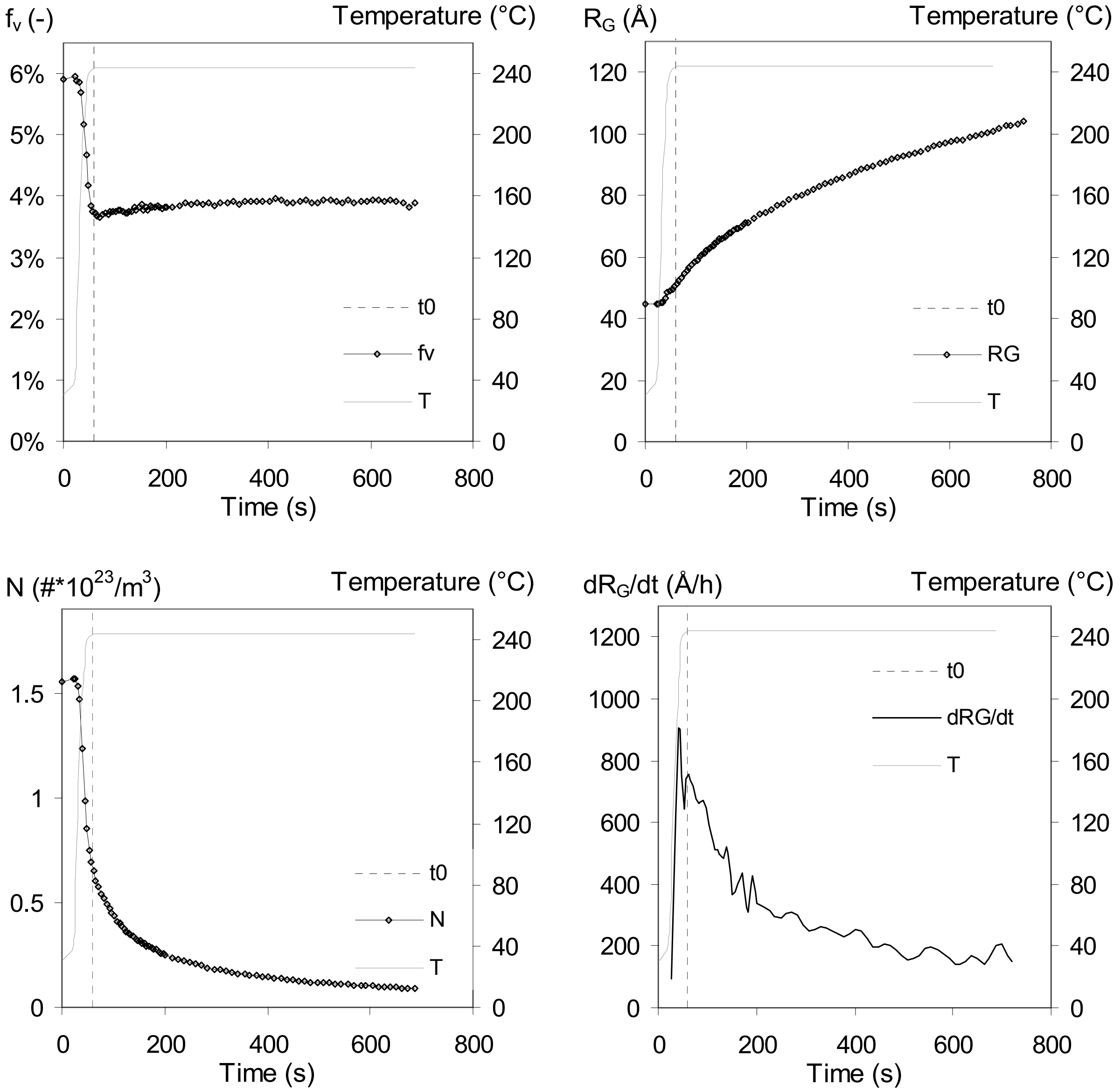

Fig. IV.26. Precipitation evolution: SAXS measurements during reversion at 240°C

(a) Precipitate volume fraction. (b) Precipitate Guinier radius. (c) Precipitate number density. (d) Precipitate growth rate. t0 corresponds to the time at which the temperature is stabilized (~57s). Temperature in grey.

It has to be noticed that the temperature does not reach instantaneously the target temperature (here: 240°C): about 60s are required to stabilise the temperature at this level. During this heat treatment, composed of a heating ramp and an isothermal treatment, the precipitation evolves as follows:

- As soon as the temperature exceeds 160°C, the precipitate volume fraction drops sharply. At the same time the apparent precipitate growth rate is very high (about 1000 Å/h). This corresponds to a brutal dissolution of the smaller precipitates. The temperature rise effectively increases the critical radius for nucleation R^* and the sub-critical precipitates are dissolved.
- The temperature goes on to increase, leading to the dissolution of a larger number of precipitates. At some point, the precipitate volume fraction reaches a minimum value, after which it increases again. This probably corresponds to precipitate growth: the solute atoms from the formerly dissolved (small) precipitates are now in a supersaturated solid solution, and diffuse towards the larger precipitates, still stable at 240°C.

- The precipitate volume fraction goes towards a saturation value[2], corresponding to the equilibrium value at 240°C. Coarsening probably takes place, the precipitate number density being still decreasing.

The same results are presented in Fig. IV.27, for the various reversion treatments listed in the introduction of this section.

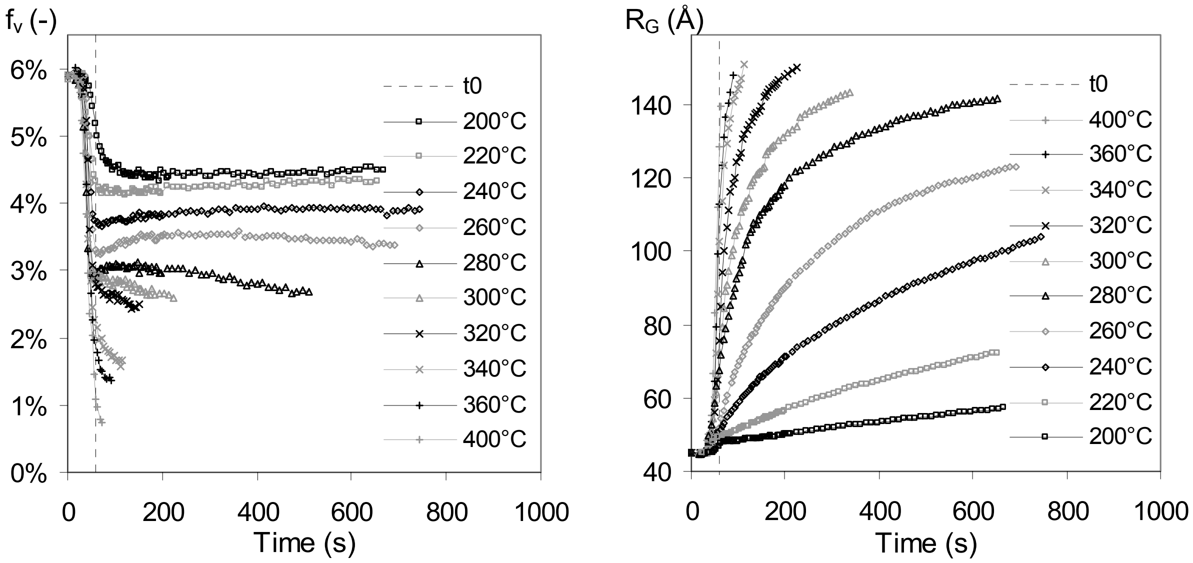

Fig. IV.27. Precipitation kinetics measurements during reversion

(a) Precipitate volume fraction. (b) Precipitate Guinier radius. t0 represents the average time at which the temperature is stabilized (60s).

The following statements can be made:

- The higher is the reversion temperature, the most rapid will be the precipitation kinetics, thermal activation enhancing diffusion (see equation (IV.1.)). On the other hand the very high average precipitate growth rate at high temperature is probably also due to the high dissolution rate, the precipitate critical radius R^* being increased and the solid solution greatly enriched. Note that for the highest temperatures, the SAXS signal became rapidly incomplete (diffusion peak displaced towards the very small angles and hidden by the beamstop) and did not authorised further measurements.
- The higher is the reversion temperature, the lower goes the precipitate volume fraction. The equilibrium value is indeed lower at higher temperature, but this is not as simple, as it will be explained in the next point.
- Two kinds of behaviour can be observed. If the reversion temperature is below 260°C, the precipitate volume fraction follows the behaviour presented in the previous paragraph. On the other hand, at higher temperatures, no increase of the precipitate volume fraction is observed. The apparent precipitate volume fraction is always decreasing. On the one hand, this is partly attributed to the SAXS signal loss (see note 2). On the other hand, this temperature corresponds to the stability domain of the η' precipitates (about 250°C; see chapter I), and both effects (experimental artefact and real dissolution) probably happen simultaneously.

---

[2] At the end of the heat treatment, the measured volume fraction decreases. This experimental artefact, already discussed in chapter III, is explained by the partial loss of the SAXS signal in the small scattering angles. This effect is deeper in the high temperature heat treatments, the signal loss appearing more rapidly (see Fig. IV.28).

IV.D.3.c. Modelling reversion experiments

i. Initial material properties

The SAXS results already presented in chapter III concerning the precipitate measurements made on temper T7651 are reported on Fig. IV.28. This (lognormal) precipitate size distribution will be used as initial state for the precipitation model.

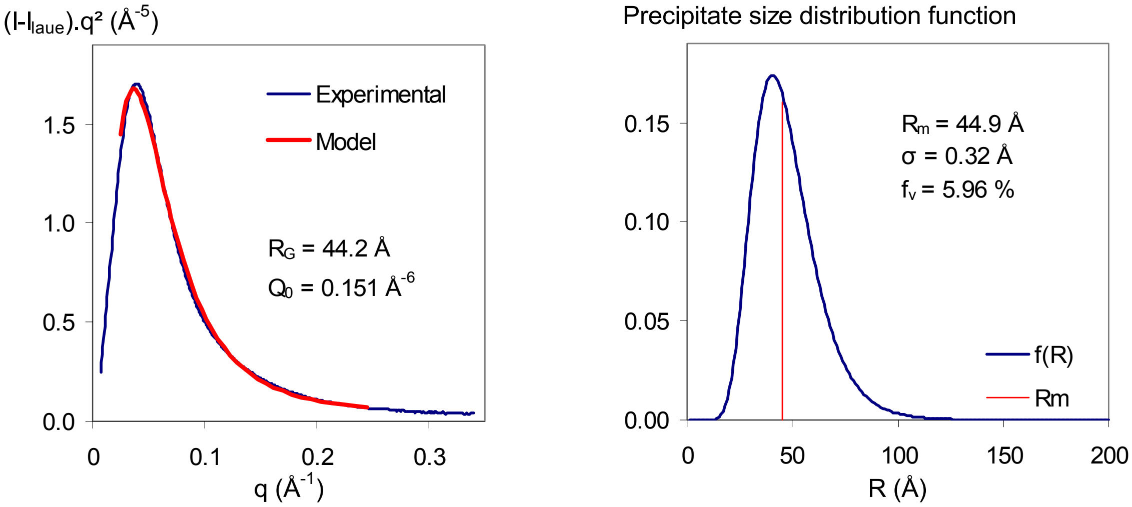

Fig. IV.28. SAXS signal and precipitate size distribution of T7651

(a) Kratky plot (experimental data and model). (b) Corresponding particle size distribution.

ii. Modelling

The reversion experiments presented in Fig. IV.27 have been used to fit the model. Fig. IV.29 presents an example of the complete modelling on one of them (isothermal treatment at 240°C).

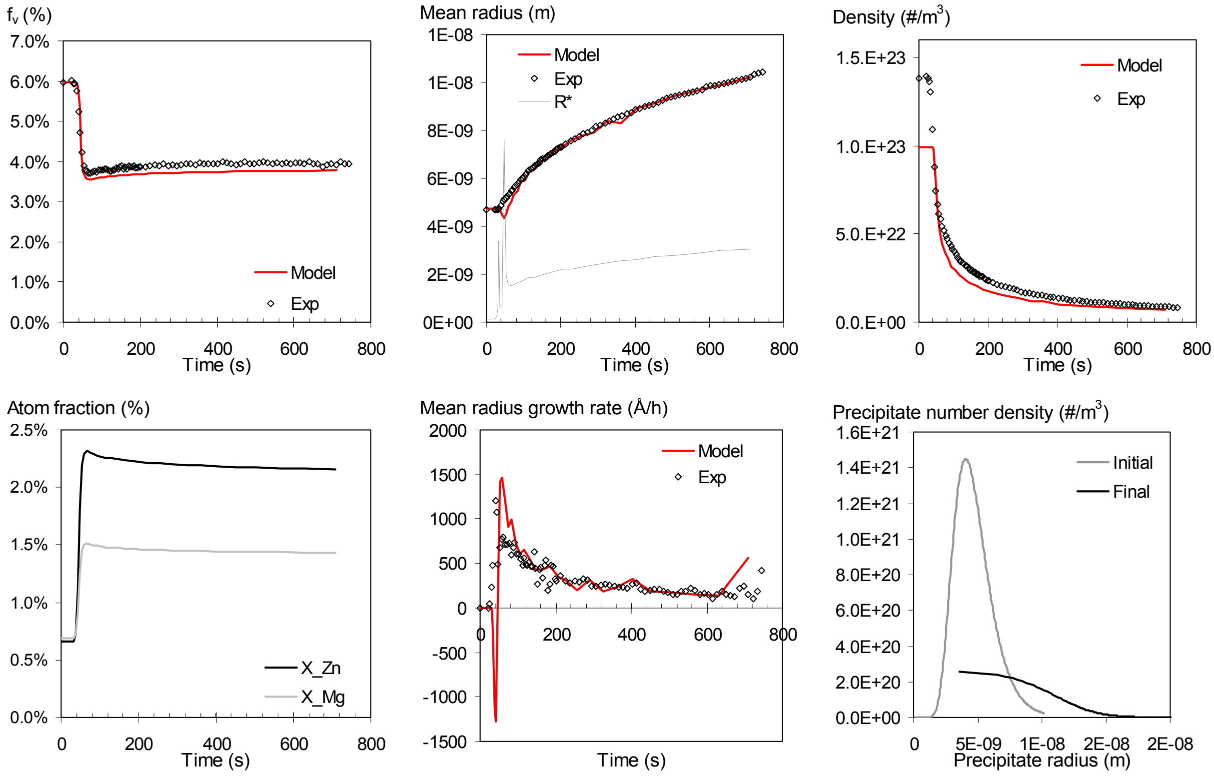

Fig. IV.29. Precipitation kinetics modelling during reversion at 240°C

(a) Precipitate volume fraction. (b) Precipitate mean radius. (c) Precipitate number density. (d) Atom fraction in the matrix. (e) Radius growth rate. (f) Initial and final precipitate size distributions.

The same model has been applied to the other heat treatments; the computed results are compared to the experimental results (Fig. IV.27) in Fig. IV.30.

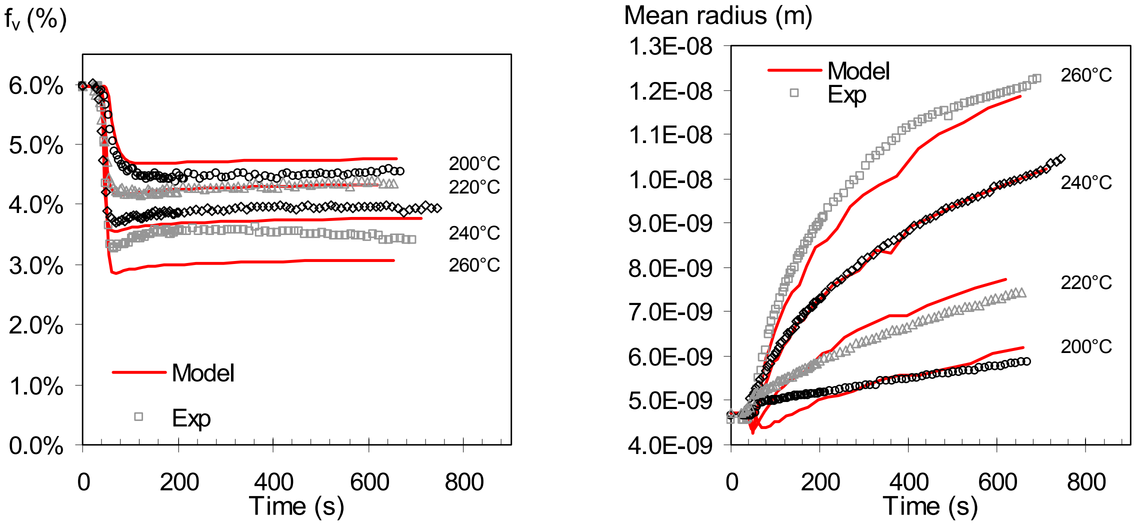

Fig. IV.30. Precipitation kinetics modelling during reversion at various temperatures

(a) Precipitate volume fraction. (b) Precipitate mean radius.

Agreement between the model and the experimental data is very good, both on the thermodynamic aspects (to which the dissolution stage and the equilibrium volume fraction are related) and the kinetic aspects.

iii. Model parameters

The model parameters are summarized in Table IV.2.

Parameter	Significance	Value	Unit	Comparison
k_B	Boltzmann constant	$1.38\ 10^{-23}$	$m^2.kg.s^{-2}.K^{-1}$	-
R_B	Universal gas constant	8.34	$J.mol^{-1}.K^{-1}$	-
D_{0Mg}	Diffusion coefficient	$1.3\ 10^{-8}$	$m^2.s^{-1}$	(*)
Q_{Mg}	Activation energy for diffusion	85.3	$KJ.mol^{-1}$	88.3 (*)
D_{0Zn}	Diffusion coefficient	$1.3\ 10^{-7}$	$m^2.s^{-1}$	(*)
Q_{Zn}	Activation energy for diffusion	85.3	$KJ.mol^{-1}$	88.3 (*)
V_{at}^{α}	Matrix atomic volume	1.13^{-29}	m^3	-
a_{α}	Lattice parameter	4.04^{-10}	m	-
M_{α}	Molar weight	26.982	$g.mol^{-1}$	-
V_{at}^{p}	Precipitates atomic volume	$1.13\ 10^{-29}$	m^3	-
ρ_p	Precipitate volume density	5206	$kg.m^{-3}$	-
γ_i	Precipitate surface energy	0.5	$J.m^{-2}$	0.65 (*)
α_h	Heterogeneous nucleation coefficient	0.3	-	(*)
ΔS_0	Free enthalpy	59.8	$KJ.mol^{-1}.K^{-1}$	75 (*)
ΔH_0	Entropy variation	15.8	$J.mol^{-1}$	21.4 (*)

Table IV.2. Precipitation model parameters used to describe reversion experiments

The star refers to the values found by [Nicolas 2002] in a T7 copper-free 7xxx alloy

iv. Discussion and validation

The model parameters that have been optimized are close to the values found in the literature (see the review made by [Nicolas 2002], who simulated the welding of a copper-free 7xxx aluminium alloy). Q_{Zn} and Q_{Mg} are slightly lower than her values, which may be surprising. Indeed, our alloy contains copper, known to diffuse less rapidly than zinc [Marlaud 2008]: as copper is assimilated to zinc in our model, this should increase Q_{Zn}. However, contrary to [Nicolas 2002], our alloy has been deformed before aging. Thus, it contains a higher dislocation density, which tends to decrease the activation energy for diffusion. For instance, according to [Jannot 2006], the activation energy for diffusion of copper in an aluminium matrix is 98 KJ.mol^{-1} in the bulk and 80 KJ.mol^{-1} in a dislocation core. Similarly, while $Q_{Zn}^{bulk} \approx 120$ and $Q_{Mg}^{bulk} \approx 130$ KJ.mol^{-1} [Nicolas 2002], they are decreased by a factor ~0.5 to ~0.75 in dislocation cores [Picu 2004]. Moreover, those values are known to decrease with increasing solute concentration [Varadarajan 1992], and the solute content is higher in our case.

The free enthalpy and entropy variation values, smaller than those proposed by [Nicolas 2002], can be also explained by the different precipitates compositions. To validate the model, calculations have been performed during constant heating ramps and compared to experimental results (Fig. IV.31).

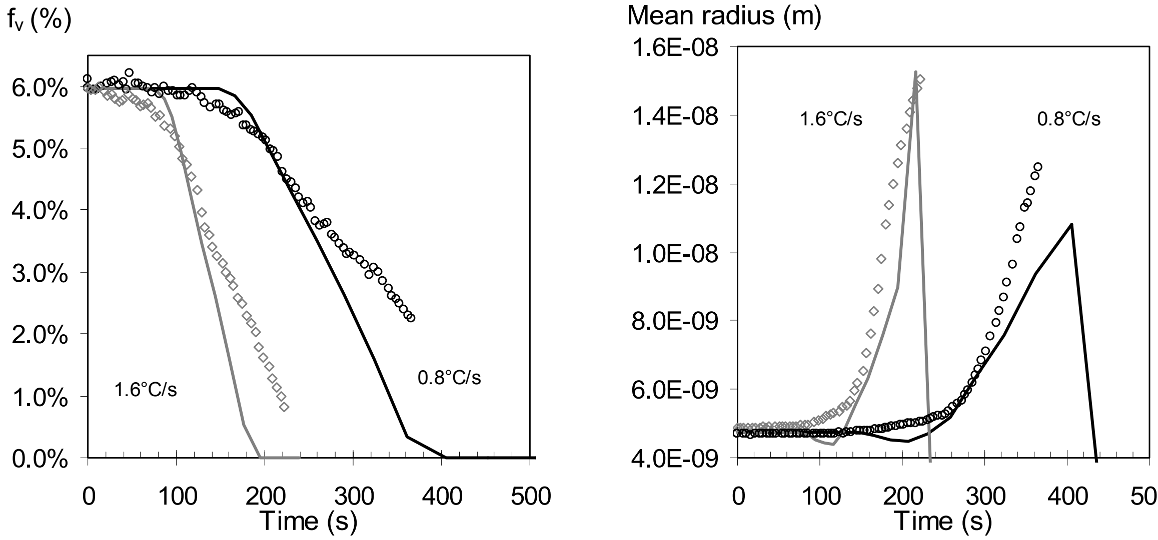

Fig. IV.31. Precipitation kinetics modelling during heating ramps

(a) Precipitate volume fraction. (b) Precipitate mean radius. For sake of comparison, the temperatures at the radius peaks are respectively of 370°C (0.8°C/s) and 402°C (1.6°C/s).

The results show good agreement with the experiments, even if the kinetics is slightly over-estimated. Moreover, the model predicts a complete dissolution of the precipitates, while the SAXS signal still goes on to increase. Indeed, very large η precipitates (in particular the ones present on grain boundaries or on dislocations) are far more stable than the η' precipitates, which are effectively dissolved at these temperatures (about 330°C). To cure this discrepancy and to optimise the model, one could introduce two families of precipitates with different solubility products.

Even if not perfect, the evolutions of the precipitate size and volume fraction are correctly described by the model. It will now be computed to simulate the effect of a highly non isothermal history, namely the laser treatment, on precipitation.

IV.D.4. Modelling precipitation evolution during laser forming

IV.D.4.a. Determination of the laser absorption coefficient

The central point located 0.5 mm below the surface of laser line #3 of specimen #2 will be used to fit the absorption coefficient. At this location, both the temperature profile and the precipitates parameters (see Fig. IV.15, provided an interpolation of the measured values) are known. Moreover, contrary to the surface, where all the precipitates have been dissolved, there is still ~4.0% of the precipitate volume fraction left. The precipitate Guinier radius is equal to 58 Å.

The different temperature profiles calculated with the different laser absorption coefficients will be applied to the model, and compared to this experimental result in Fig. IV.32.

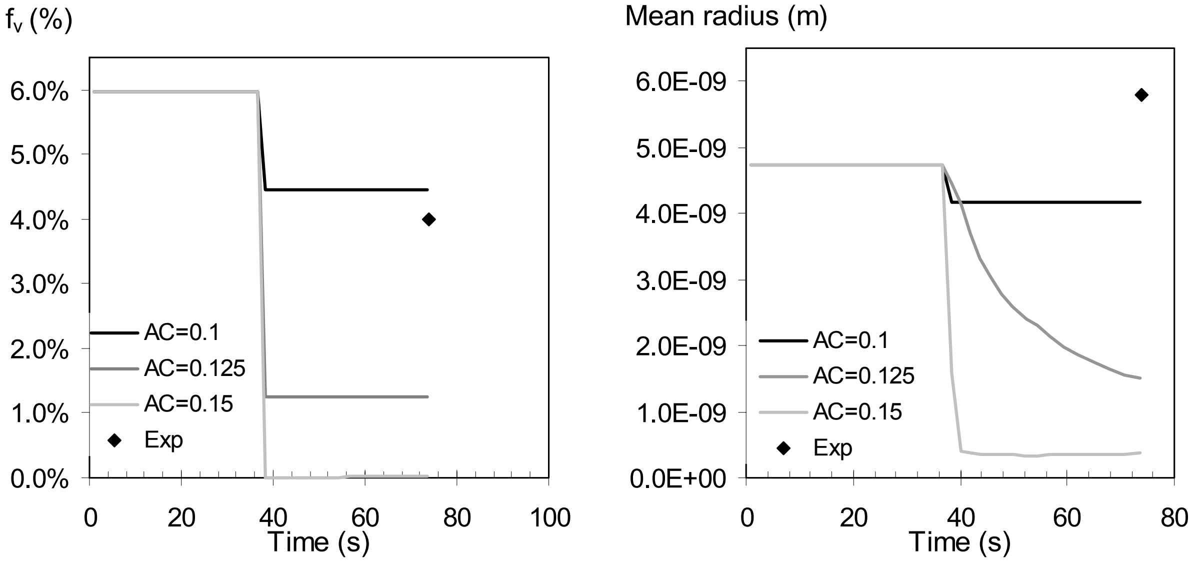

Fig. IV.32. Effect of laser absorption coefficient on the modelling of precipitation kinetics

(a) Precipitate volume fraction. (b) Precipitate mean radius. Specimen #2, laser line #1

The precipitate volume fraction decreases at the position of the temperature peak. An increasing absorption coefficient dissolves a larger part of the volume fraction, the peak temperature being higher (Fig. IV.25). One obtains the best agreement between the model and the experiment for AC=0.1.

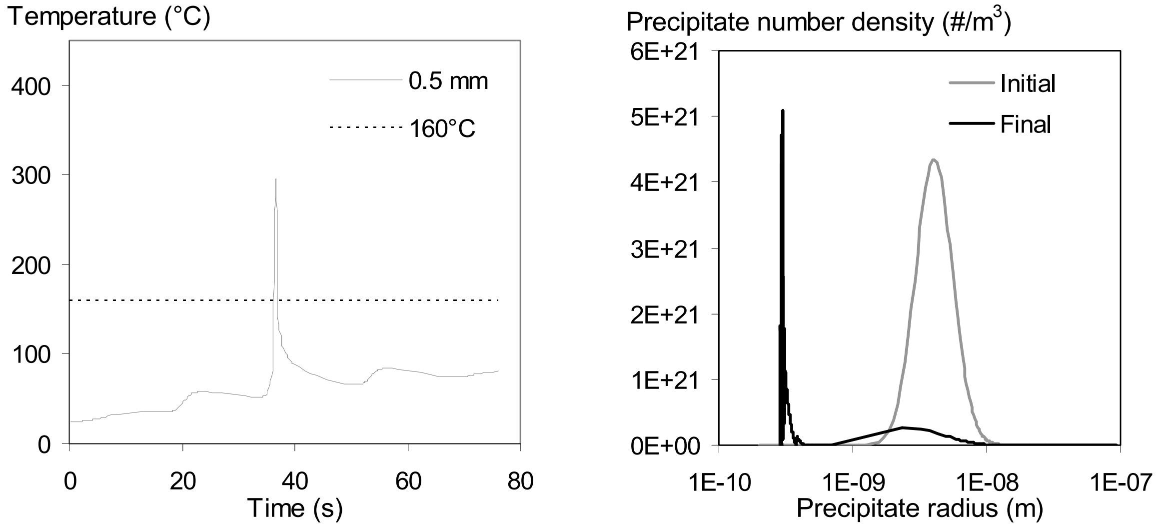

Fig. IV.33. Example of a calculated temperature profile and precipitate size distribution

(a) Temperature profile calculated in the centre of laser specimen #2, Laser line #3, 0.5 mm deep, with AC=0.1. (b) Precipitate size distribution calculated before and after the treatment at surface point.

Concerning the evolution of the precipitate radius, whatever the absorption coefficient, the model predicts a decreasing precipitate radius, whereas an increase has been measured by SAXS. The model predicts that the whole particle size distribution is shifted to the left, but also the nucleation of very small precipitates after the main temperature peak (see Fig. IV.33.a), which tends to shift even more the mean precipitates size towards lower values (see Fig. IV.33.b).

However, despite this discrepancy, that will be discussed later, the modelling of a complete microstructure will be carried out, using the absorption coefficient which gave the best result: AC=0.1.

IV.D.4.b. Prediction of the precipitate microstructure after laser forming

The model has been run with various temperature profiles (see Fig. IV.24), corresponding to 18 points (i.e. 36 symmetrical points) in the transverse section of laser line #3 of specimen #2. Fig. IV.34 and Fig. IV.35 compare the resulting precipitation maps (bottom) to the experimental precipitation maps, reconstructed from SAXS measurements (already presented in Fig. IV.16).

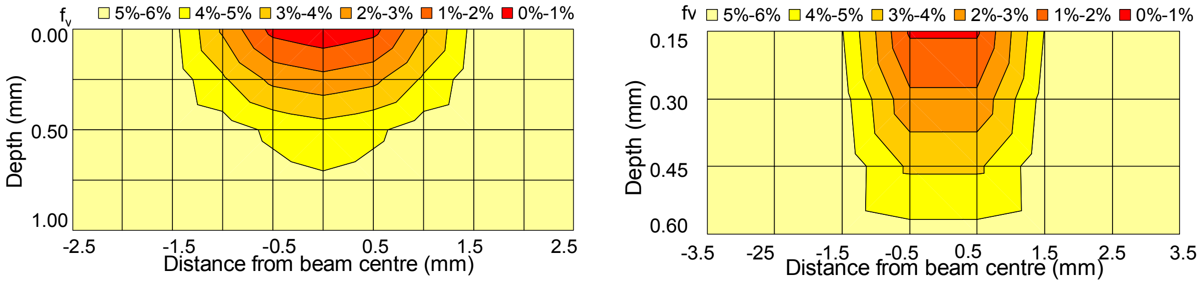

Fig. IV.34. Comparison between modelled and measured precipitate volume fraction maps

Specimen #2, line 3, A=0.1. (a) Modelled precipitate volume fraction. (b) Precipitate volume fraction measured by SAXS. Note that the area is different (1x5 mm² vs. 0.6x7 mm²).

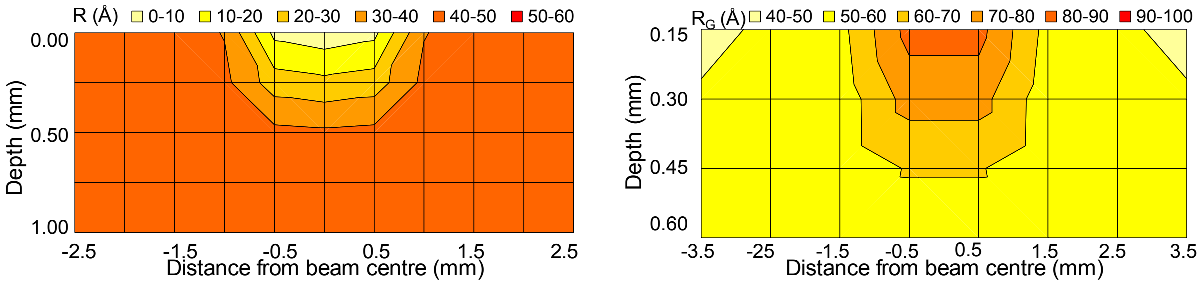

Fig. IV.35. Comparison between modelled and measured precipitate radius maps

Specimen #2, line 3, A=0.1. (a) Modelled mean radius. (b) Guinier radius measured by SAXS. Note that the areas differ, as well as the scales of the modelled and experimental precipitate radii.

In both cases (i.e. Fig. IV.34 and Fig. IV.35), there is a correct agreement in the dimension of the heat affected zone. In terms of microstructural gradient, the modelled precipitate volume fraction corresponds very well to the experimental result. On the other hand, the modelled mean precipitate size and the Guinier radius do not correspond at all, as already reported in IV.D.4.a.

IV.E.Discussion

IV.E.1. Model validation

The agreement between the model and the experiments is imperfect. On the one hand, there is a remarkable agreement concerning the experimental and the modelled volume fraction (see comparison in Fig. IV.36); on the other hand the state of precipitation predicted by the model has a much finer scales than the experimental one

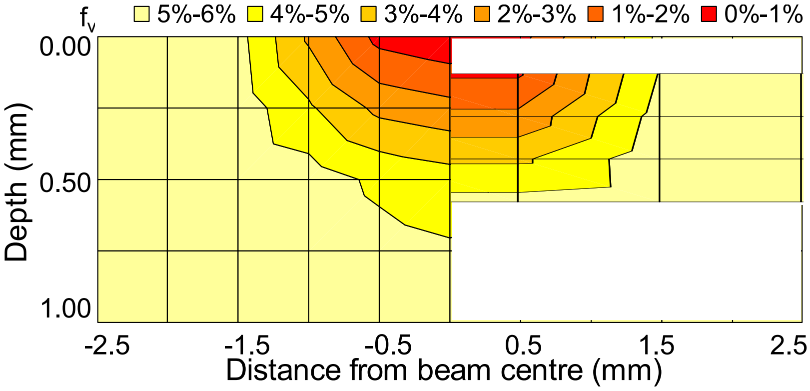

Fig. IV.36. Superimposition of the measured and modelled precipitate volume fraction maps

Modelled (left) vs. volume fraction measured by SAXS (right). From Fig. IV.34

Two reasons can explain this discrepancy on the size, with still a good agreement on the volume fraction: either the model needs to be improved, or the experimental data are not reliable.

The model predicts on the one hand the (partial) dissolution of most of the precipitates; on the other hand the nucleation of fine precipitates; both effects tend to decrease the precipitate mean size. The nucleation effect, which theoretically accounts for a small precipitate volume fraction (about 0.002%) does affect very significantly the precipitate mean size for the most critical heat treatments (i.e. at the surface, in the centre of the laser beam), where a large fraction of the precipitate volume fraction is dissolved. This effect is probably overestimated and could be improved, provided new investigations on the (delicate) issue of the nucleation conditions.

Then, modelling the effect of laser forming on precipitation has required a large number of processing steps: finite element modelling of the temperature profiles generated by the laser treatment, experimental characterization of precipitation, precipitation model calibration, before the final modelling. This complex procedure is source of errors, which multiply along the process.

The reliability of the experimental data may be discussed as well. Indeed, the model predicts the nucleation of small precipitates after the peak, during the last 40s of the treatment (at ~70°C, see Fig. IV.33.a). If GP zones have effectively precipitated during this stage, this was not measured by SAXS. Indeed, the experimental set-up did not allow measuring very small precipitates, their signal being embedded in the Laue value. This means that the measured Guinier radius is not representative of the whole range of precipitates, and probably overestimates the average precipitate size.

It remains that the volume fraction is accurately described by the model. Therefore if some very small precipitates are not currently experimentally measured, they have to contribute only at a reduced level to the total volume fraction. More local techniques such as TEM or 3D atom probe could give a qualitative indication if this very elusive precipitation is present or not, but would not allow, in a reasonable time, to do the same type of mapping that SAXS allows.

IV.E.2. Modelling the mechanical properties

The effect of the laser treatment on hardness has been measured experimentally in IV.C.2. The objective is now to model this. In chapter III, a model which relates the yield stress to the precipitate radius and volume fraction has been established (see III.D.1), and an empirical relation links the yield stress to hardness (III.C.2). The combination of these two laws allows calculating the expected hardness after laser forming treatment, provided the precipitation state is known.

IV.E.2.a. Modelling the mechanical properties from SAXS data measurements

Fig. IV.37 compares a measured hardness map to a modelled one. In that case, the SAXS results presented in Fig. IV.16 have been used as input parameters into the over-aged yield stress and hardness models. The use of the over-aged model is justified by the fact that the SAXS measurements predict precipitates larger than the critical transition radius (33 Å; see chapter III).

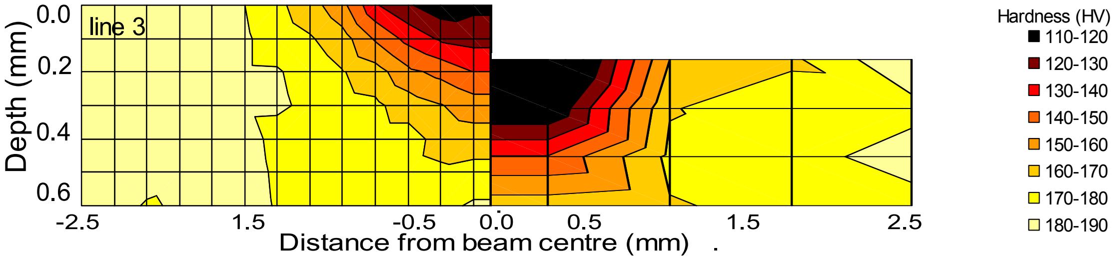

Fig. IV.37. Superimposition of measured and semi-modelled hardness maps

Specimen #2, laser line 3. Measured (left) vs. modelled (right) hardness maps. The modelled results used SAXS data as input parameters.

The predictions of the effect of laser on hardness are overestimated, the material being less affected than what is expected. The general shape and size of the heat affected zone is however respected.

IV.E.2.b. Modelling the mechanical properties from calculated precipitation

Instead of the experimental SAXS results, the modelled precipitation results (see Fig. IV.34 and Fig. IV.35) may been implemented in the same yield stress and hardness models, as done in Fig. IV.38. In that case, a mixed, precipitate size-dependent model is used. Below the transition radius (i.e. according to the precipitation model: in the heat affected zone) the under-aged-model is used, whereas the over-aged model is used far away from the heat affected zone.

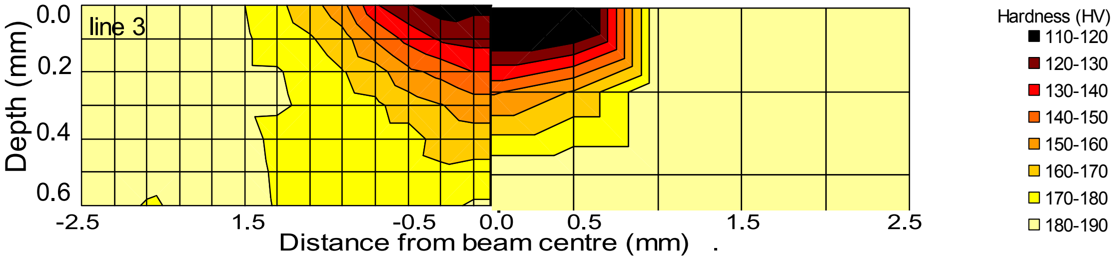

Fig. IV.38. Superimposition of measured and fully-modelled hardness maps

Specimen #2, laser line 3. Measured (left) vs. fully modelled (right) hardness maps.

A really good agreement is found: both the size of the affected zone and the quantitative effect of the laser treatment have been modelled. It may be slightly optimized by using a full precipitate size distribution, instead of a mean radius value, but the calculation is already very good. This finally validates the issue tackled in IV.E.1: precipitation kinetics is accurately predicted by the precipitation model, and the discrepancy between the model and the SAXS measurements on the precipitate size is probably mainly due to experimental issues.

IV.E.3. Effect of post laser treatment on precipitation

Fig. IV.39 compares microhardness measurements performed on the same laser formed specimen, in the as-received state ("LNQ" stands for liquid nitrogen quench) and after 1 year natural aging, to investigate the effect of a simple post-laser treatment on the mechanical properties.

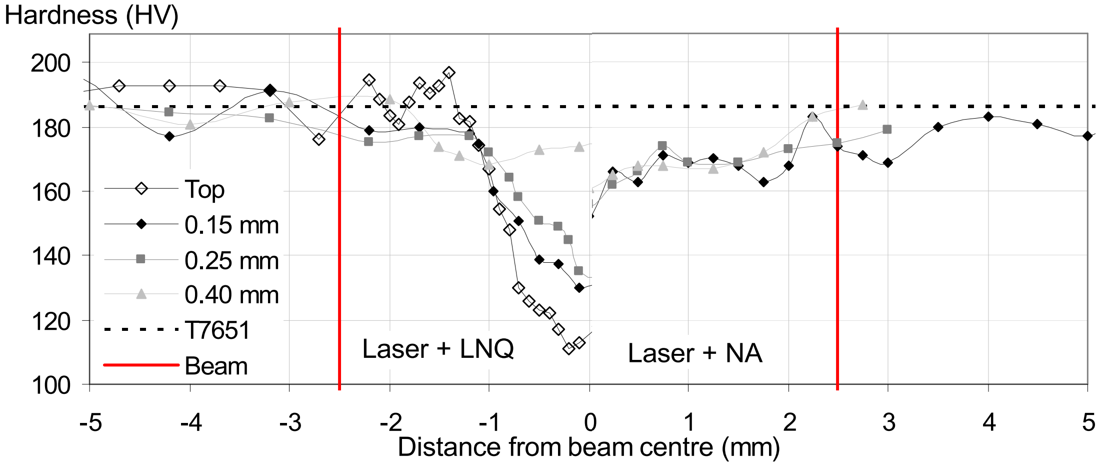

Fig. IV.39. Effect of natural aging on hardness after laser processing

On the left, the hardness measurements performed after laser processing and liquid nitrogen quench. On the right, the same specimen measured after 1 year of natural aging. The grey line in the middle separates the two curves. Note that no data are available in the surface of the NA specimen.

A large proportion of the mechanical properties have recovered during the natural aging treatment. Just after the laser treatment, the hardness was typically 60 to 80% below that of the parent material in the most affected zone (except the surface, which is even lower). After natural aging, the lowest measured hardness is only 80% below this same level. Moreover, the mechanical properties are identical, whatever the depth, while they were obviously depth dependent before this treatment.

The laser forming treatment did effectively dissolve the smaller precipitates, and the mechanical properties were "supported" by the larger remaining precipitates. During natural aging, GP zones have nucleated, grow, and recovered a large part of the mechanical properties. However, they still remain small and cannot constitute sufficient strong obstacles to recover fully the mechanical properties.

IV.E.4. Conclusion

The effect of laser treatment on both the precipitation and the mechanical properties has been evidenced experimentally. Furthermore, these results have been modelled, using a complex multi-stage modelling suite, including finite element modelling of temperature profiles and a class model for modelling of precipitation, combined with a strength model. The developed precipitation model is able to model accurately both isothermal and non-isothermal treatments. The final results present a very good agreement with the experimental results, validating the whole modelling process.

The effect of the laser treatment is to dissolve the precipitates in the very subsurface (typically: 0.6mm deep by 4 mm wide), but the available solute fraction also allows the re-nucleation of new GP zones. Despite this nucleation, the laser treatment is however very detrimental (at least) to the mechanical properties: 50 to 80% of the strength is lost in the affected zone.

However, a long term natural aging treatment, very simple to perform in industrial conditions, is enough to recover a significant part of these mechanical properties.

Chapter V. Microstructural evolution during thermomechanical treatments

Summary

This chapter investigates the effect of the coupling of a thermal and a mechanical treatment on precipitation. This study is mainly based on *in situ* experimental characterization, performed with a specific device developed during this work (TSAXS, see chapter II). This device allows correlating quantitatively the effect of the thermomechanical process parameters (strain rate, strain, temperature, initial state) to the material's response (precipitation state, stress).

The first experimental results concern the simulation of part distortion correction. In this scope, the effects of temperature and stress on creep rate and precipitation kinetics of the fully heat treated T7651 temper have been studied.

The second experimental part is dedicated to the study of age-forming of partially heat treated materials. The effects of different process parameters (namely the initial state, the strain rate and the strain) on precipitation kinetics have been investigated.

On a more fundamental viewpoint, mechanisms have been proposed to explain the enhanced precipitation kinetics observed during stress- and strain-aging. This leads to a new model for the prediction of precipitation kinetics induced by thermomechanical treatments, based on the class model presented in chapter IV.

Outline

V.A. Introduction

V.A.1. Thermomechanical processes

V.A.1.a. Generalities

Some industrial manufacturing processes involve both deformation (or stress) and heating stages; they can be gathered under the general “thermomechanical processes” term. These thermomechanical treatments (TMT) can be divided into two groups[1]: the ones in which deformation and aging treatment are sequential (deformation stage followed by a heat treatment) and the ones where both occur simultaneously.

Among the different “sequential TMT”, one can list pre-stretching (about which some words have been said in chapters I and III) and stretch forming [Cai 2009], followed by an age hardening treatment. Interest into “simultaneous TMT” has been shown recently in the aerospace industry. The friction stir welding joining process (see for instance [Genevois 2006]) and forming processes such as hot forming [Cavaliere 2002] or creep age-forming (CAF; see [Starink 2006, Lin 2006]) are some of those.

V.A.1.b. Age forming

Age forming or creep age-forming (CAF) combines simultaneously strain and heat treatment. It is used in the aerospace industry to process complex-shaped panel components, such as wing skin panels. It is for instance used to form the upper wing skin of A380 airplane [Benett 2009]. In that case the process is generally the following:

- First, a partially heat-treated but fully machined component is loaded (generally elastically) and located by means of a guide system onto a generally concave form tool, whose surface has been designed to compensate the post-process spring-back.
- Next, a vacuum bag is fitted to seal the component against the continuous surface of the form tool, and air is removed from under the bag, creating an atmospheric pressure differential that produces a clamping action, forcing the panel towards the tool surface.
- Finally, the component and tool are loaded into an autoclave with a pressurised air system that forces the panel on to the face of the tool and completes the shape-forming procedure while the panel undergoes heat treatment, which lasts up to 24 hours.

From the manufacturing point of view, the main benefits of creep forming are the accuracy and repeatability that can be achieved, as well as the ability to produce multiple curvatures on thick topologically complex components [Benett 2009]. Moreover, as it combines simultaneous stress relaxation, creep and age hardening, it allows particularly low residual stress levels [Starink 2006]. The reduction of internal stresses enhances resistance to both fatigue and stress corrosion cracking [Lin 2006] which increases the component lifetime.

V.A.1.c. Current issues

i. <u>Effect of TMTs on microstructure</u>

It has already been said in chapter I that TMT affects the microstructure. In the case of sequential TMTs, the effect of the two stages is additive: the deformation modifies the microstructure (dislocation structure, precipitation, eventually grain structure), which will evolve differently during the further aging treatment, as compared to a non-deformed microstructure. In the second case (simultaneous TMT),

---

[1] This chapter will focus on the thermomechanical treatments (TMT) that involve precipitation and will not consider the treatments made before the solution heat treatment, such as the rolling operation.

there may be coupled effects of deformation and temperature and the microstructural evolution is more complex. As reported by [Cavaliere 2002]: “In such conditions the microstructural evolution does not depend only on the applied stress, but is the product of complex interactions between the kinetics of dislocation generation and annihilation, nucleation of new phases and zones, and growth of the precipitates”. The different possible effects will be listed in section V.B.

ii. Effect of TMTs on the final mechanical properties

If TMTs affect the microstructure, they also affect the material properties, in particular the mechanical properties, very sensitive to the precipitate microstructure, as already demonstrated in chapters III and IV. It is therefore of interest to better understand the microstructural mechanisms occurring during TMTs, to target the process parameters on the optimization of the final microstructure.

iii. Heterogeneous TMTs

In case of homogeneous stress/strain in the material, the overall microstructure will evolve similarly in the whole material. On the opposite, a heterogeneous TMT will generate heterogeneous microstructures, and therefore lead to heterogeneous properties in the component.

The Airbus A380 wing skins are up to 33 metres long and 2.8 metres wide, with thicknesses that vary abruptly between 3mm and 28mm [Benett 2009]. In such a complex initial shape, which requires a complex curvature, the component will be subjected to stress and/or strain heterogeneities during the CAF operation. This is illustrated in Fig. V.1, where both mechanical properties and microstructural heterogeneities have been evidenced in a creep-aged component.

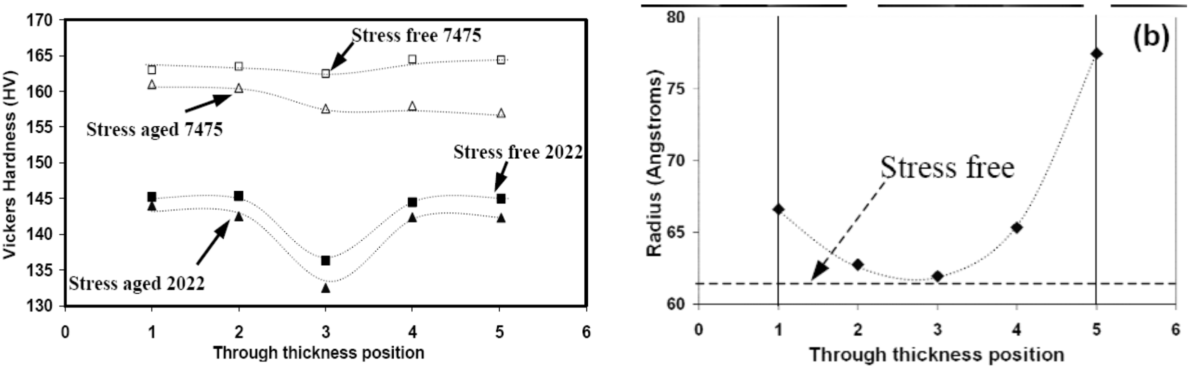

Fig. V.1. Through thickness properties of two aluminium alloys after industrial CAF

[Bakavos 2006b] (a) Microhardness. (b) Guinier radius. 20 mm thick plates were aged formed (bended, the maximum stress being ±185 MPa). The positions from 1 to 5 respectively correspond to outer surface, 1/4, 1/2, 3/4 and inner surface (from tension to compression).

Other industrial treatments, such as part distortion correction treatments, are by nature heterogeneous. To correct slight part distortion at the very end of the manufacturing process, a combination of local forming operation (bending) and heating may be used. This local operation probably modifies locally the microstructure and the resulting properties.

V.A.2. Scientific objectives

It has been shown in chapter III that the precipitate microstructure is the major strengthening component in 7xxx alloys. As a consequence, investigating the influence of TMTs on precipitation is a natural question to address. Various levels of coupling can exist between stress, strain and precipitation, acting on nucleation, accelerated diffusion, precipitate shearing, keeping the material out of equilibrium, … These effects are very poorly understood, and one cannot predict , within the current state of the art, neither the magnitude nor even the direction of microstructure evolution under an external combination of temperature, stress and strain.

A micro tensile and heating device for in situ SAXS measurements has been developed to monitor the evolution of precipitation during various TMTs. This device, presented in chapter II, allows obtaining quantitative information about the effect of the process parameters on precipitation kinetics.

Any combination of TMT process parameters can be achieved with such a device: creep, tensile tests or relaxation tests may be performed, varying the temperature, stress level or the strain rate, as well as the initial temper and the duration of the treatment. In spite of its versatility, and due to time constraints, it has been decided to restrict the study to two kinds of treatments:

- Simulation of post-machining part distortion correction treatments on fully heat-treated AA7449 T7651 components. For this purpose, the effect of moderate temperature and stress level on creep properties and precipitation kinetics will be investigated, on the base T7651 material.
- Age forming of partially heat-treated materials. In this case, the effect of strain rate on precipitation kinetics for various initial tempers will be investigated.

This experimental work will be combined with modelling work, to quantify the effect of the process parameters on precipitation kinetics and to validate the mechanisms.

V.B. Literature review

A brief reminder about the effect of temperature on plasticity and on the precipitates will be given, summarizing what has been developed extensively in chapters **I**, **III** and **IV**. It will be completed by a review of the possible plasticity / precipitation interactions and the possible effects of strain and stress on precipitation, on both the thermodynamic and the kinetic aspects (V.B.1). Finally a literature review of the two TMTs that will be investigated experimentally in this chapter (namely creep and strain aging) will be made in V.B.2.

V.B.1. Generalities

V.B.1.a. Effect of temperature on plasticity

i. Introduction

The mechanical properties vary as a function of the straining temperature, but also of the strain rate, as illustrated in Fig. V.2. This can be explained by the thermal activation of the plasticity mechanisms, and in such a case of a precipitation hardened material, to the destabilization at high temperatures of the initial distribution of hardening precipitates.

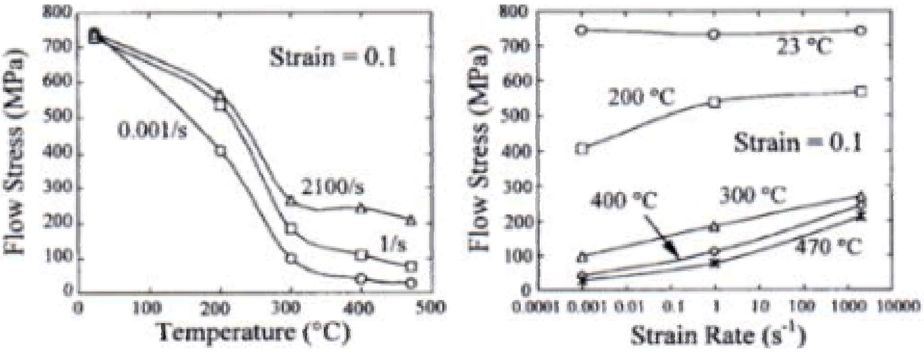

Fig. V.2. Maximum flow stress as a function of temperature and strain rate in AA7075

[Jin 2000]

ii. Basic plasticity mechanisms

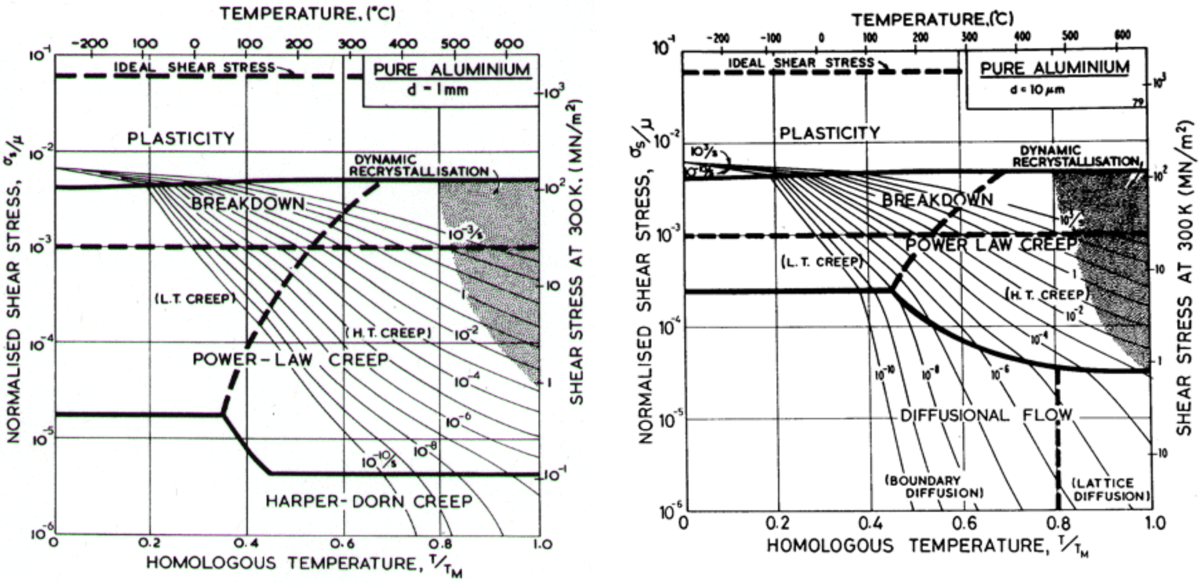

Fig. V.3. Deformation mechanisms map in pure aluminium

[Frost 1982] Two grain sizes are presented: 1 mm (a). 10 μm (b).

At low temperature, plastic deformation occurs through dislocation glide. At higher temperature, dislocation motion is made easier: cross-slip and climb add further degrees of freedom, as compared to simple glide mechanism.

At even higher temperatures, plasticity can take place via individual motion of point defects (vacancies), called “diffusional plasticity.

These plasticity mechanisms are temperature and stress dependent. Frost and Ashby [Frost 1982] have proposed the so-called deformation maps to limit the stress/temperature domains in which each plasticity mechanism dominates, those being valid for a given material and grain size (see Fig. V.3).

iii. Dislocation / particles interactions

As already developed in chapter III, precipitates contribute to increase dislocation storage and add a further strengthening term. However temperature modifies the precipitates / dislocation interactions and the strengthening mechanisms[2]. While in-plane shearing and Orowan bypassing of precipitates are the standard bypassing mechanisms, the higher dislocation mobility at high temperature tends to favour by-passing of precipitates by cross-slip or climb (see for instance [Delmas 2003]).

iv. Overall plastic behaviour in the 100 to 200°C temperature range

In our case, the investigated temperature range is 100 to 200°C. This corresponds to T/Tf~0.5, which means that diffusional flow can safely be considered as negligible: our study can be restricted to dislocation glide and creep. Therefore deformation is the result of the balance between two phenomena: dislocation storage and recovery. On the one hand, when temperature is increased, dislocation storage is decreased, the obstacles by-passing being favoured (see previous paragraph). On the other hand, recovery is thermally activated, that is to say that an increasing temperature tends to decrease the saturation stress.

V.B.1.b. Coupled effect of temperature and stress/strain on precipitation

i. Introduction

Precipitation is affected by temperature, both for thermodynamic and kinetic reasons. Temperature determines the precipitates stability, and therefore controls precipitate nucleation and dissolution. It also enhances diffusion and controls growth and coarsening rates.

Straining (or stressing) the material, either before (in which case it only induces “static effects”) or during (which may induce “dynamic effects”) the heat treatment affects precipitation. Dislocations modify the microstructure, interact with solute atoms and precipitates; stress changes the local equilibriums...This section will consider the main possible interactions of stress/strain with precipitation.

ii. Basic concepts

- Thermodynamic aspects

In a recent paper, Embury, Deschamps and Bréchet [Embury 2003] have proposed a review of the possible plasticity / precipitation interactions. In particular they summarized the thermodynamic effect of these interactions on the free energy diagrams for precipitation (see Fig. V.4).

The “static” free energy diagram for a given temperature is exposed in Fig. V.4.a. The vertical dashed lines respectively represent the solubility limit of the solute atom in the matrix and the precipitate nominal composition, and ΔC the (concentration) stability domain of the precipitates in the matrix.

---

[2] In this section (V.B.1.a), the solute and precipitates are supposed fully stable and no word will be said about the possible precipitation evolution during straining.

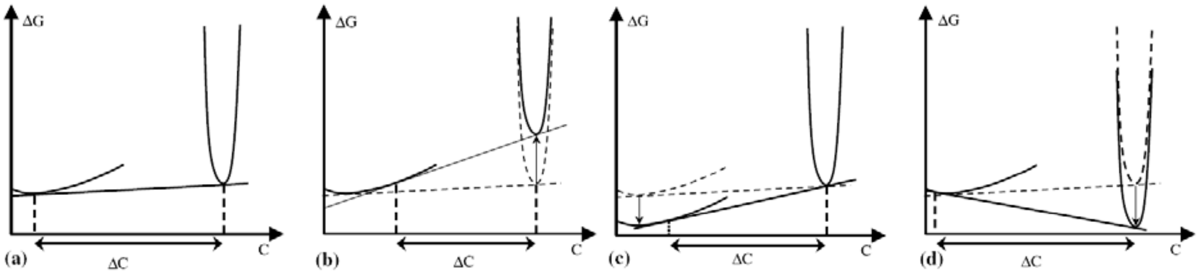

Fig. V.4. Free energy diagrams for precipitation and effect of precipitation

[Embury 2003]. (a) Bulk material. (b) Destabilisation of precipitates by interface creation. (c) Destabilisation of precipitates by locally decreasing the matrix energy due to segregation. (d) Stabilisation of precipitates due to the lowering of elastic energy.

In case (b), the precipitate stability tends to be reduced (i.e. the precipitates dissolve), deformation generating "microstructure refinement", enhancing the Gibbs-Thomson effect. In our case, this microstructure refinement can be understood as the shearing of coherent precipitates, which creates new surfaces. The presence of dislocations around the precipitates may also increase the interface energy, and destabilise them.

In case (c), the destabilisation of precipitates stems from a modification of the solid solution. The authors explain that the free energy curve for the solid solution can be shifted downward due to segregation in the dislocation cores. There would then be a lower driving force to precipitate at dislocation core, even in the absence of any elastic interaction.

Case (d) may happen if precipitation in the volume requires a substantial amount of elastic energy to occur. Indeed the presence of dislocations increases the local elastic stresses.

- Kinetic aspects

The same authors present the different kinetic aspects of strain / precipitation couplings. On the one hand, the vacancies (which governs precipitation kinetics by allowing atomic diffusion; see chapter I) will interact with dislocations, either mobile ones can act as sources of vacancies, or immobile dislocations can be sinks for them. The presence of dislocations may modify diffusion kinetics in the bulk. In addition, dislocations provide short circuits to the bulk diffusion path, in which diffusion is accelerated. Finally, the dislocation motion provides non diffusive transport paths to the solute atoms. This will be developed and illustrated in the following.

iii. Static effects

- Heterogeneous nucleation

Precipitation nucleation is enhanced by the presence of dislocations. They act as heterogeneous nucleation sites by decreasing the energy barrier for nucleation (typically: 30% of the homogeneous nucleation energy barrier). Precipitates also often form directly as a more stable phase on dislocations: directly in the η phase on dislocations, while they nucleate in the metastable η' form in the bulk [Embury 2003]. As a consequence, the presence of dislocations modifies the precipitate density in the material: instead of being homogeneously distributed in the bulk (Fig. V.5.a), precipitates tend to preferentially nucleate on dislocations, as illustrated in Fig. V.5.b.

- Pipe diffusion

The presence of dislocations also modifies the precipitation kinetics, as they favour an accelerated solute diffusion, as compared to classical vacancy diffusion. The activation energy for diffusion is indeed smaller in the dislocation core than in the material bulk; typically 60-80% less [Jannot 2006, Picu 2004]. This effect is known as "pipe diffusion". This effect is illustrated in Fig. V.5.b. and c., where a bipolar particle distribution can be observed: fine precipitates in the bulk and coarser precipitates on dislocations. Another consequence can be found on the morphology of the precipitates: the solute segregation in the dislocation core tend to generate elongated precipitates [Deschamps 1999a].

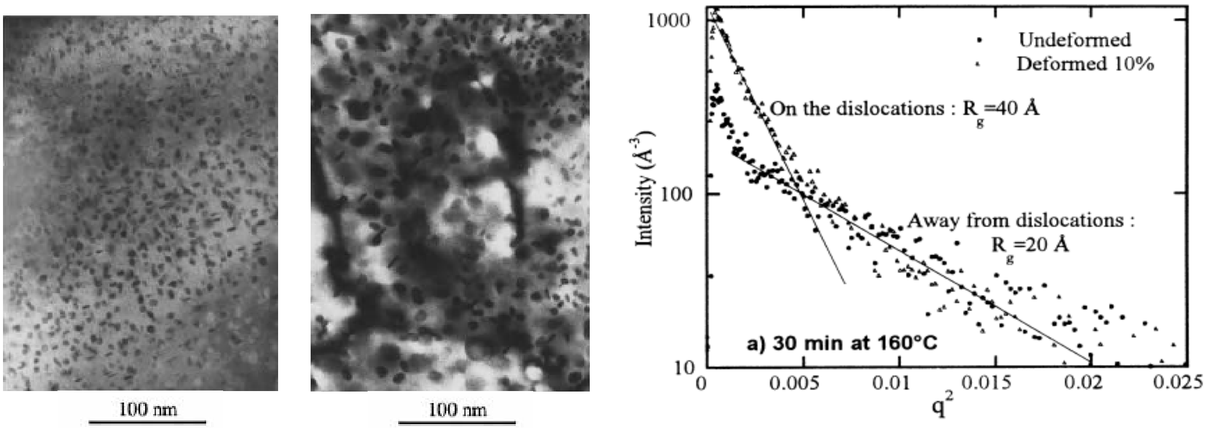

Fig. V.5. Effect of pre-deformation on precipitation in AA7xxx

[Deschamps 1999a]. (a, b):TEM micrograph of an artificially aged AA7xxx alloy (1 hour at 160°C) with no pre-stretching (a) ; with 10% pre-deformation (b). (c) SAXS signal after 30 min of artificial aging at 160°C of non deformed and deformed specimens. At high scattering vector values (smaller precipitates), the two signals coincide perfectly. At low q values, the deformed specimen exhibits a higher scattered intensity, characteristic of larger precipitates.

iv. Dynamic effects

- Dynamic strain aging and plasticity induced precipitation

Dynamic strain aging (see for instance [Hörnqvist 2006]) refers to solute segregation on moving dislocations, while plasticity induced precipitation refers to precipitation occurring during deformation. Mobile dislocations tend to drag highly mobile solute atoms, which may precipitate when the dislocations are momentarily stopped by obstacles. Those precipitates constitute new obstacles on which the dislocation is pinned, and tend to increase the dislocation storage term (see for instance [Simar 2006]). This phenomenon may be responsible for plastic instabilities in the stress-strain curve [Estrin 1989], the intermittent pinning and unpinning stages affecting the overall strain rate. It depends on the solute atom vs. dislocation mobility: it is therefore temperature and strain rate dependent.

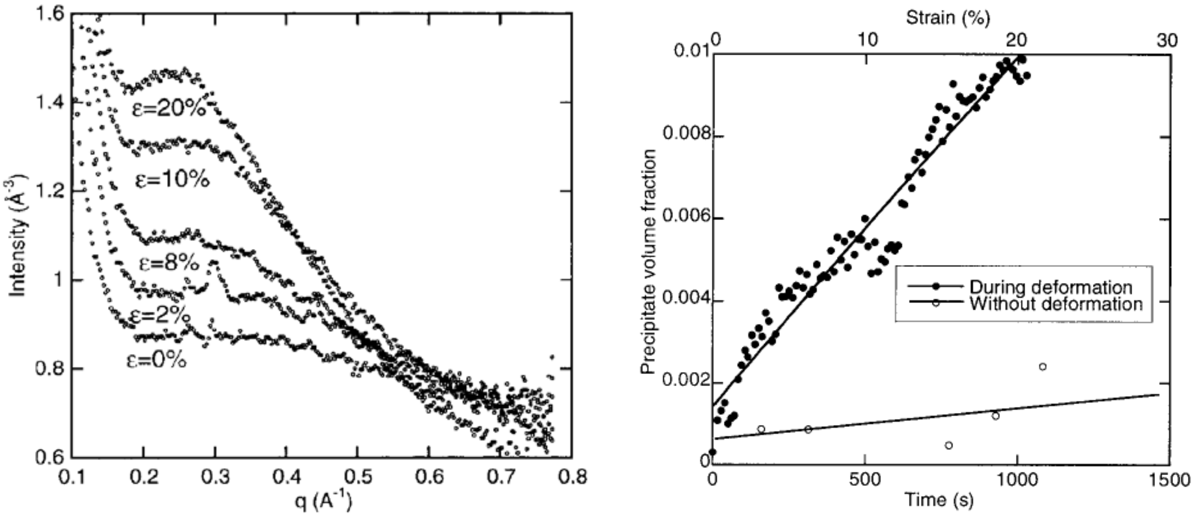

Fig. V.6. Effect of strain on precipitation in as quenched AA7010

[Deschamps 2003b]. (a) SAXS spectra measured at different strain levels. (b) Evolution of the precipitate volume fraction with and without strain. In situ SAXS measurements performed during deformation at room temperature. In (a), the shift of the intensity peak towards the left characterises a precipitate size increase; the growing area under the curve demonstrates a growing volume fraction.

Fig. V.6.a presents the effect of room temperature deformation on the precipitation kinetics of as-quenched AA7xxx specimens. It clearly shows that straining the material greatly enhances the kinetics of precipitation, which is attributed by the authors to dynamic precipitation. Actually this phenomenon may be present in nucleation, growth and coarsening stages, depending on the solute content in the matrix [Deschamps 1999c].

- Plasticity induced dissolution

Precipitate shearing leads to the creation of new interfaces, which tend to destabilize the precipitate equilibrium (Gibbs-Thompson effect), and possibly dissolve the precipitate [Zhu 1997, Embury 2003]. This so-called “strain-induced dissolution” may be observed on the stress-strain curves, characterised by a “pseudo Portevin Le Châtelier effect”.

This effect has been recently experimentally demonstrated by Loo et al. [Loo 2008] using Nuclear Magnetic Resonance (NMR). Artificially aged Al-Cu alloys containing both GP zones and metastable θ' particles were rolled up to different strain levels (0% to 70%) at room temperature. The NMR spectra is related to the copper distribution in the different phases (matrix, GPz and θ' precipitates; see Fig. V.7.a), and the peak analysis allows quantifying the copper content in them (Fig. V.7.b).

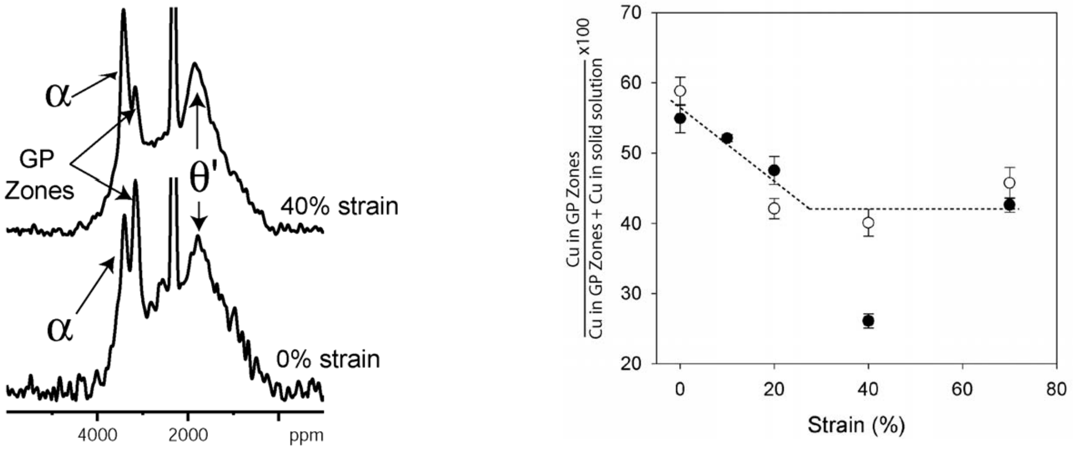

Fig. V.7. Strain-induced precipitation in AA2xxx monitored by NMR

[Loo 2008]. (a) Effect of a 40% room temperature deformation on the NMR spectra. (b) Quantification of the relative copper content in GP zones after various imposed rolling strains.

The analysis of larger metastable precipitates is not made by the authors, since they focus their attention on the analysis of the GP zones. In the heat treated and unrolled condition, about 60% of the copper not present in the θ' precipitates is present in GP zones (Fig. V.7.b). This proportion diminishes gradually up to 40% during straining, showing a flux of the copper atoms from GP zones to solid solution, that is to say a dissolution of the GP zones, and saturates after ~30% straining. Two competing phenomena indeed take place: on the one hand, the shearing dissolves the GP zones; on the other hand, as the matrix supersaturation increases, it favours re-precipitation.

v. Effect of elastic stress

Elastic stresses may also modify precipitation. Depending on the precipitate elastic properties and molar volume as a function of the matrix, an applied stresses will either stress positively or negatively the precipitates. As a consequence, it may prevent, delay or accelerate precipitation, and modify the precipitate morphology, some directions of growth being favoured, as compared to energetically less favoured directions. This effect is illustrated in Fig. V.8 in a 2xxx series alloy: in that case, the presence of a compressive stress has modified the precipitates morphology by preventing growth in the loading (compression) direction and enhancing growth in the perpendicular direction.

In 2xxx Al-Cu alloys, the needle-shaped precipitates are known to show a large mismatch with the matrix, de to the small size of the Cu atoms. As a consequence, the external load greatly modifies the elastic stresses at the precipitate/matrix interface. In 7xxx alloys, on the contrary, the presence of both small (Zn) and large (Mg) atoms enable precipitation with low elastic mismatch and less effect of an external stress on the precipitate morphology is expected.

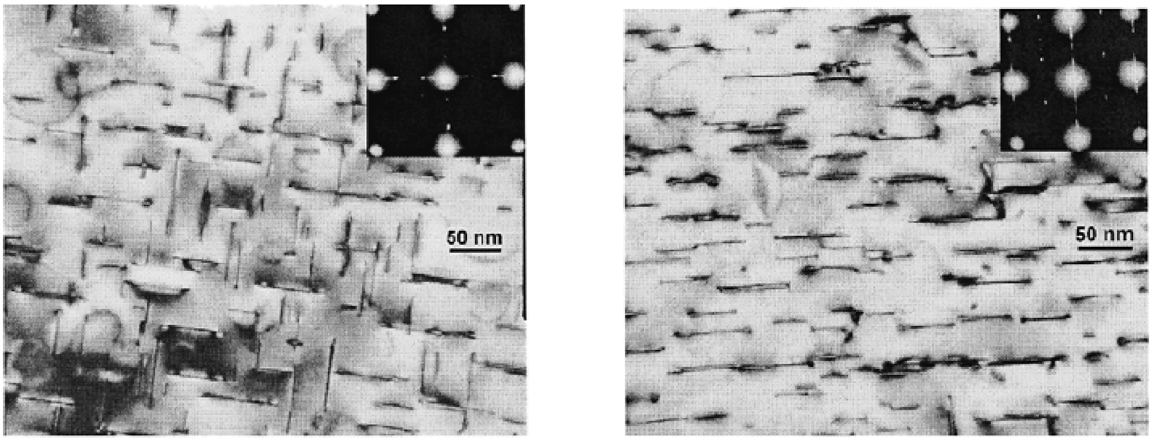

Fig. V.8. Effect of stress aging on the θ''/θ' precipitate microstructure of a AA2xxx

[Zhu 2001a] Bright-field TEM images of Al–4Cu single crystals aged at 180°C for 31 h under compressive stress of (a) 0 MPa and (b) 64 MPa. Stress applied along the vertical direction.

V.B.2. Effect of TMTs on microstructure and properties

Once these basic mechanisms have been explained, this section will review the consequences of hot creep and strain forming, the two thermomechanical treatments that will be investigated in this chapter, on the microstructure and mechanical properties.

V.B.2.a. Creep forming

Zhu and Starke [Zhu 2001a, 2001b, 2001c] performed creep tests on as quenched 2xxx aluminium alloys, varying the creep stress between 0 and ~150 MPa. They monitored the Vickers hardness in situ, and also investigated the precipitate morphology by ex situ TEM.

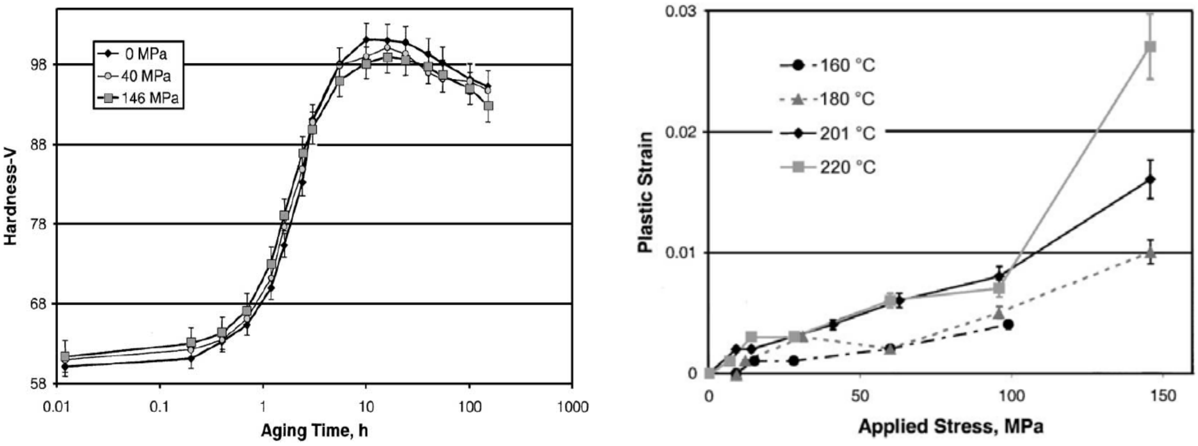

Fig. V.9. Effect of stress aging on the mechanical properties of a AA2xxx

[Zhu 2001c]. (a) Evolution of hardness monitored in situ during stress aging of polycrystalline Al–4Cu specimens at 201°C. (b) Effect of temperature and creep stress on plastic strain after "creep peak aging" (about 11h) of Al-4Cu single crystals specimens.

Their main results are the following:

- Elastic stress has little impact on the overall kinetics of the aging processes (see Fig. V.9.a).
- A relatively high stress (around yield stress level, which is less than 100 MPa) is required to see a significant material flow under creep (see Fig. V.9.b).
- Aging under applied stress generates an alignment of the precipitates (see Fig. V.8). Compressive stress leads to a perpendicular θ / θ' plate dominated precipitate structure whereas tensile stress favours formation of parallel plates. Moreover, the stress-orienting effect depends on the applied stress, temperature and alloy composition.

Bakavos and Prangnell [Bakavos 2006a, Bakavos 2006b] have recently investigated the effect of creep age forming on the precipitate microstructure and properties of an AA7475 alloy by TEM and (ex situ) SAXS measurements. They compared the response of a stress-free specimen to a specimen stressed at 245 MPa during a two stages artificial aging treatment (108°C and 160°C; initially: naturally aged temper).

The available dataset (see Fig. V.10) does not allow establishing a significant effect of stress aging on precipitation kinetics. However, it seems that precipitation is somewhat accelerated during the second heating stage at 160°C; at the very end of the treatment, a 6% difference can be observed. If one considers the effect of stress aging on the precipitate radius (see Fig. V.11), the difference remains also small. However, its evolution during aging is coherent with the hardness curve, representative of a shearing-bypassing transition. In the under-aged condition, the stress-aged specimen present smaller precipitates and is softer than the stress-free aged specimen; it remains softer in the over-aged condition, but this is explained by a higher precipitate size.

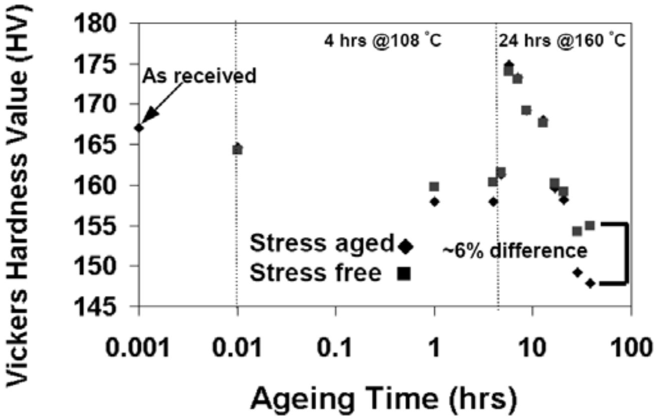

Fig. V.10. Effect of stress aging on the mechanical properties of AA7475

[Bakavos 2006a] 245 MPa stress.

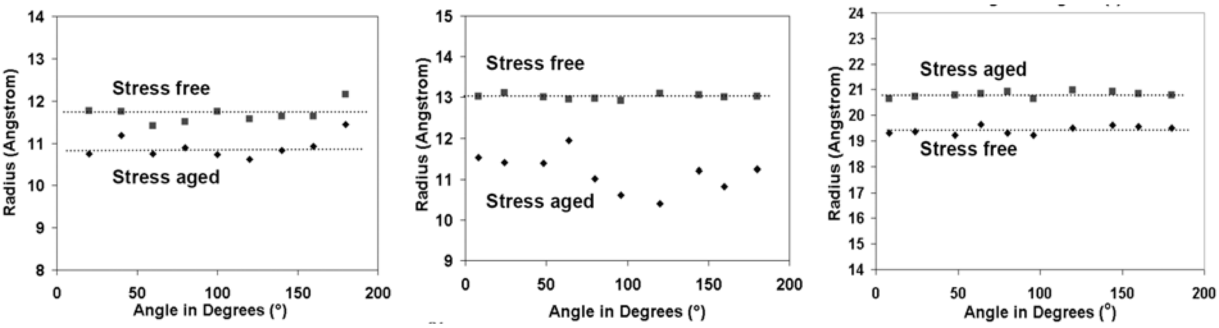

Fig. V.11. Effect of stress aging on the precipitate radius of AA7475

[Bakavos 2006a] The Guinier radius has been measured by SAXS, after various treatment durations (see also Fig. V.10): respectively 0.01 h @ 108°C (a), 4 h @ 108°C (b) and 0.01 h @ 160°C (c). The angle represents the angle towards the load direction (90°).

In Fig. V.11.b, the radius difference as a function of the angle tends to demonstrate a preferential orientation of GP zones, such as the phenomena observed in AA2xxx alloys. The authors explain that stress lead to the nucleation of oriented plate-like GPII zones, while the stress-free specimen only exhibit spherical GPI zones. Then, during the second heating ramp (Fig. V.11.c), these GPII zones are dissolved, while spheroïdal η' particles precipitate, isotropically oriented

V.B.2.b. Strain forming

i. Sequential stages: deformation followed by aging

The presence of dislocations, which decrease the energy barrier for nucleation, favours heterogeneous nucleation. Growth and coarsening are also enhanced, solute diffusion being faster along dislocations. However the consequence of pre-deformation on the precipitate microstructure can be very different. In 7xxx alloys, the precipitates will be coarser and the particle size distribution wider (see Fig. V.5.b and c). The exact opposite effect can be found in 2xxx Al-Cu-Mg alloys: pre-deformation generally leads to a much higher precipitate number density of finer precipitates (see Fig. V.12, [Wang 2008, Tolley 2006]).

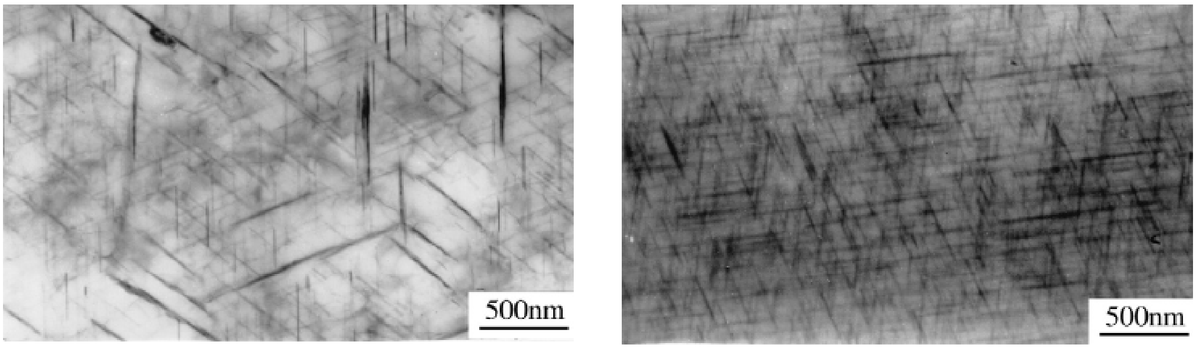

Fig. V.12. Effect of pre-deformation on S' precipitates in AA2618

[Wang 2008]. (a) Peak-aged non pre-deformed material (20 hours at 200°C). (b) Peak-aged 10% pre-deformed material (4 h at 200°C), in which a much higher precipitate density is found.

This difference between 2xxx and 7xxx alloys can be explained by the difference in term of nucleation barrier. In 7xxx alloys, η' precipitates mainly nucleate heterogeneously on GP zones, and the probability to nucleate on dislocations is only slightly higher: the presence of dislocations has a limited impact on nucleation. On the contrary, in AA2xxx alloys, the transition phase S' generally nucleates homogeneously [Dubost 1991], and heterogeneous nucleation is much highly favoured.

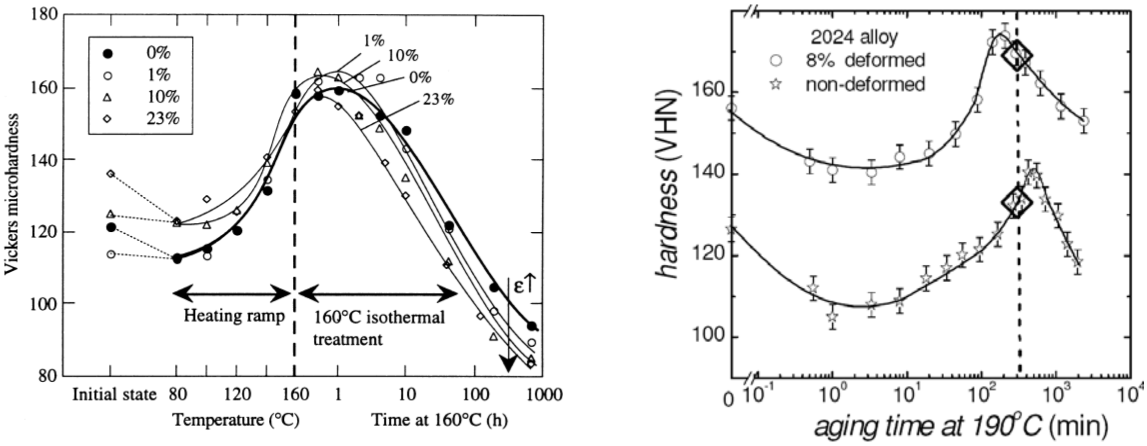

Fig. V.13. Effect of pre-deformation on hardness evolution of two alloys during artificial aging

(a) [Deschamps 1999a] aging of AA7xxx at 160°C. (b) [Tolley 2006] Aging of AA2024 at 190°C. In both cases kinetics is enhanced but the effect on the peak value is opposite.

As a consequence, precipitation kinetics is always enhanced with deformation and the hardness peak is reached sooner (see Fig. V.13). On the other hand the hardness peak value can be either increased or decreased. Indeed, while pre-stretching is generally detrimental to hardness in 7xxx alloys (see Fig. V.13.a), it ameliorates the performance of 2xxx alloys (see Fig. V.13.b). This is explained by the reasons exposed in the previous paragraph: a much higher precipitate density of fine precipitates optimizes the material strength (Orowan strengthening).

ii. Simultaneous stages: deformation and aging

It has been said in chapter III that there is generally a negative sensitivity of stress to temperature. In other words, the stress-strain curve is generally shifted towards lower values when the temperature is increased. However, there are some cases, associating precipitation evolution during straining, where the opposite effect is found, as for instance illustrated in Fig. V.14.a.

Hörnqvist [Hörnqvist 2006] investigated the effect of low temperatures strain aging (in that case: from -20°C to 60°C; see Fig. V.14) on the stress-strain behaviour of a 7xxx alloy. The naturally aged temper exhibits an abnormal behaviour: the higher is the temperature, the greater are the yield stress and the strain hardening rate. The same tests performed on peak-aged temper present a standard sensitivity.

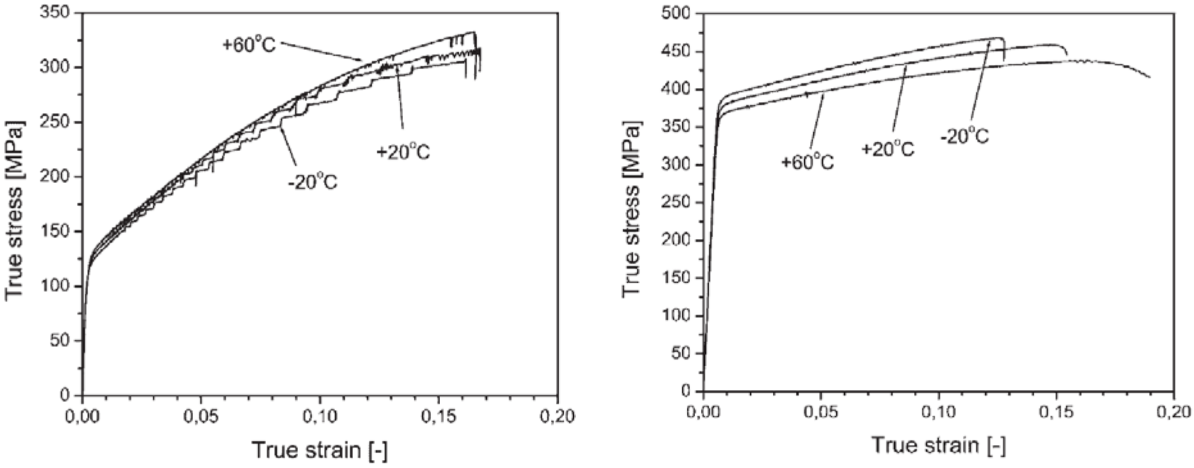

Fig. V.14. Effect of intermediate temperature on stress/strain curves of AA7030

[Hörnqvist 2006] (a) Naturally-aged temper. (b) Peak-aged temper.

In the naturally aged temper, the growth of the GP zones improves the precipitates contribution to flow stress (shearing mechanism). As a consequence, the higher is the temperature, the most rapidly will grow the precipitates and the higher will be the material strength. On the contrary, after the peak strength, the Orowan bypassing mechanism dominates, and a more rapid growth of the precipitates at higher temperature is detrimental to the material strength. One can also notice the presence of PLC effect, which can be partly attributed to dynamic strain aging.

At higher temperature, the interactions may be even more different. Cavaliere [Cavaliere 2002] investigated the effect of hot forming on stress/strain behaviour of AA2xxx by torsion testing. The effects of the forming temperature and the strain rate are presented in Fig. V.15.

The author noted the following behaviour: in the low temperature regime (here: 150–200 °C), the stress/strain curves monotonically increase up to fracture; at intermediate temperatures (200–300 °C) the curves increase up to the peak followed by a moderate decrease in equivalent stress. In the high temperature regime, the stress drop becomes more and more pronounced, and it transforms into a continuous reduction in σ, approaching zero. The effect is less pronounced when the strain rate is increased. Similar results have been obtained by [Yi 2007] on AA7050.

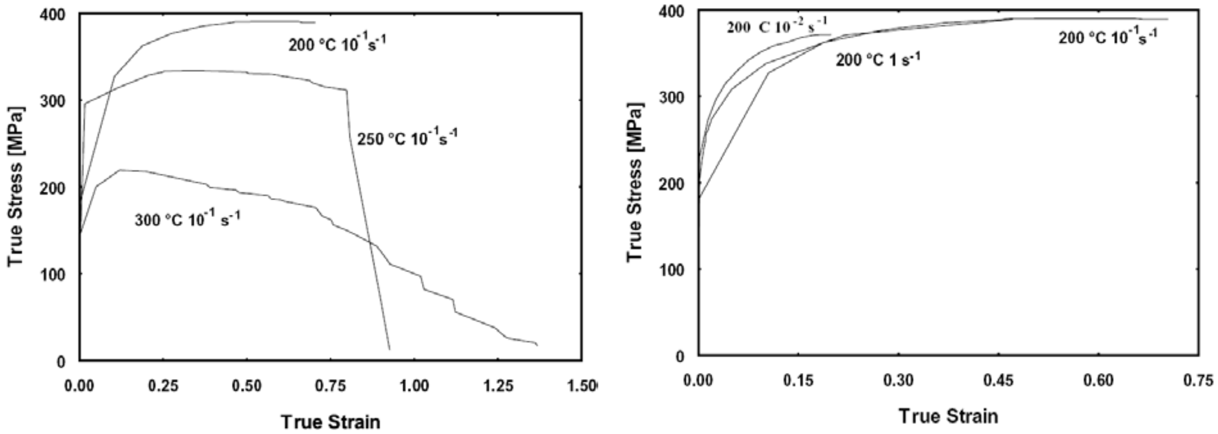

Fig. V.15. Effect of temperature and strain rate on stress/strain curves of AA2618

[Cavaliere 2002]. (a) Effect of temperature. (b) Effect of strain rate. Equivalent stress-strain curves measured by torsion testing of an as-quenched temper.

At intermediate temperature (150°C-200 °C), the GP zones nucleate and grow (in particular through dynamic precipitation) and strengthen the material during straining. Moreover, the dislocation structure evolves “classically”, in the sense that recovery is only slightly enhanced, which leads to classical stress-strain behaviour. One can add that a lower strain rate lets more time for precipitation to occur, and therefore promotes the strengthening effect of the precipitates. At high temperature (above 300°C), the mechanisms governing plasticity are modified (see V.B.1.a): dynamic recovery is enhanced, promoting work softening. Moreover, precipitation is limited, the critical radius for nucleation being very high, and strain-induced dissolution phenomena probably occur, decreasing even more the precipitate contribution to flow stress.

iii. Difference between sequential and simultaneous age forming

The differences between sequential and simultaneous straining on precipitation kinetics are compared in Fig. V.16. The first specimen group was exposed to a rapid strain aging stage (typical duration: 10 s) at high temperature (250°C to 350°C), along with various levels of strain (from 0 to 50%), after which it was rapidly cooled. The second specimen group was pre-strained at room temperature up to a similar level, after which it was exposed to a similar artificial aging treatment in salt bath.

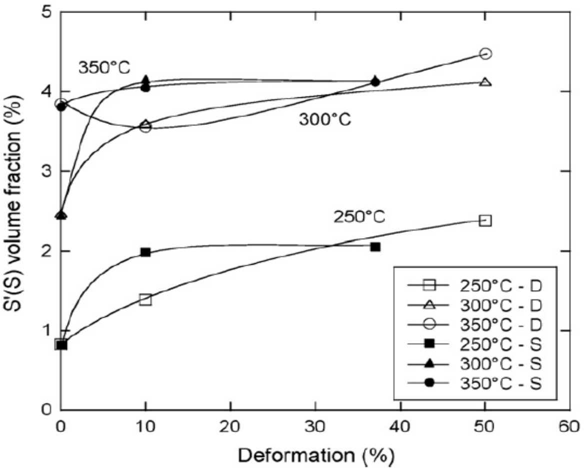

Fig. V.16. Effect of sequential and simultaneous TMT on precipitation kinetics

[Genevois 2006]. AA2024 T351. Precipitate volume fraction of the S'/S phase measured by Differential Scanning Calorimetry. Dynamic precipitation experiments (“D” symbols) performed on a Gleeble thermomechanical apparatus. Static precipitation experiments (“S” symbols): compression tests followed by heat treatments of identical duration.

At intermediate deformation levels, (10% deformation), the precipitates volume fraction is systematically higher in the static case, that in the dynamic case. The authors propose two interpretations of this enhanced kinetics. First, the whole deformation is applied initially in the static case, whereas it occurs progressively along the heat treatment in the dynamic case. The dislocation density in the pre-deformed material is already high before the heat treatment occurs, which increases the number of heterogeneous nucleation sites at the beginning. Moreover, as the specimens have been deformed at room temperature in the static case, dynamic recovery was limited, contrary to the dynamic case, where it was emphasized. This also tends to increase the dislocation density and to promote precipitation.

At higher strain, the volume fraction is almost identical in both cases, whatever the temperature considered. To explain this, the authors assume that the dislocation density is probably the same, the dislocations initially present after pre-stretching being partly recovered during the heating stage.

V.B.3. Partial conclusion

Precipitation is affected by TMTs on both thermodynamic and kinetic aspects, whether the straining and heating stages happen sequentially or simultaneously. The precipitate microstructure may be affected as well, throughout heterogeneous nucleation, enhanced growth along dislocations, strain-induced precipitation or dissolution, or orientation effects. The dislocation density itself is also affected: if temperature tends to increase the dislocation mobility and therefore to favour dynamic recovery, simultaneous precipitation may also limit this mobility.

The different examples presented in this section illustrate the complexity of the precipitation/plasticity interactions occurring during thermomechanical treatments. Precipitation and plasticity mechanisms both depend on temperature and their coupling is complex to comprehend and to reveal experimentally. In the last example for instance (see Fig. V.16), the effect of strain aging on precipitation kinetics has been established, but it has not revealed a real dynamic mechanism, related to the motion of dislocation (dynamic strain aging or strain induced dissolution).

The effects of these dynamic mechanisms can be hidden into effects which may be due to static phenomena too, and conventional techniques are generally not sufficient to reveal them unambiguously[3]. It has been shown (Fig. V.7) that complex experimental techniques allow uncovering these mechanisms. The straining and heating TSAXS device (see chapter II) has been developed during this PhD partly to answer this question: it will allow establishing quantitatively the effect of the TMT parameters on precipitation kinetics, but also revealing the mechanisms occurring.

---

[3] Mechanical tests, easier to implement, can also provide information about dynamic precipitation phenomena, the stress-strain curves generally exhibiting plastic instabilities. It is however an indirect technique.

V.C. Experimental results

V.C.1. Introduction

Two kinds of experiments have been performed, to simulate two different industrial TMTs.

The first group of experiments is related to post-machining part distortion correction of aeronautical components. In that case, creep experiments have been performed on the fully heat treated T7651 material, varying both creep stress and temperature. The first objective is to measure the creep performance of the material and the conditions in which post-machining part distortion may be corrected. The second objective is to investigate the effect of creep conditions on precipitation kinetics. This can be used as a tool to optimize the part distortion treatment.

The second group of experiments is related to the age forming process of partially heat treated pre-machined components. In that case, various initial heat treatments have been performed, followed by creep aging and strain aging experiments. The objective is to investigate the effect of the process parameters on precipitation kinetics.

These thermomechanical treatments have been performed on the TSAXS device at ESRF, to measure simultaneously and quantitatively the material's mechanical behaviour and the effect of the TMTs on precipitation.

V.C.2. Creep on T7651 material

V.C.2.a. Thermomechanical treatment

Creep stress and temperature are varied in the following range: respectively for the applied stress between 0[4] and yield stress value, and for the temperature from 120 to 180°C. The TMT sequence consists in:

- A first rapid heating stage (about 2 minutes), during which the stress is maintained at 20 MPa.
- A rapid elastic loading stage at controlled strain rate (~1 minute).
- The creep test itself, which typically lasts 20 to 40 minutes.
- A cooling stage, during which stress is maintained at 20 MPa.

V.C.2.b. Creep behaviour

Fig. V.17 presents the different kinds of experiments that have been performed. In Fig. V.17.a, creep stress is maintained ~10% below the yield stress level, once yielding has been observed. This allows measuring the materials yield stress with a good precision on the same sample on which the creep test is carried out, at the TMT temperature. Then other experiments have been performed at lower creep stress values (see Fig. V.17.c). In some cases, the creep stress has been varied during the experiment (see Fig. V.17.e). Since the number of experimental variables is minimized, it allows obtaining more reliable data, as compared to constant creep stress tests performed on different specimens.

The analysis of the creep signal allows measuring the material's yield stress as a function of temperature, as plotted on Fig. V.18.a. It also allows measuring its resistance to creep or creep rate

---

[4] Instead of imposing "0 MPa", it has been chosen to impose "20 MPa" to insure that no compression of the specimens will occur during the test. This very small stress value probably affects neither creep, nor precipitation.

(see Fig. V.18.b), expressed as the strain rate generated by a specific applied stress, for a given temperature: $\dot{\varepsilon}(T,\sigma)$.

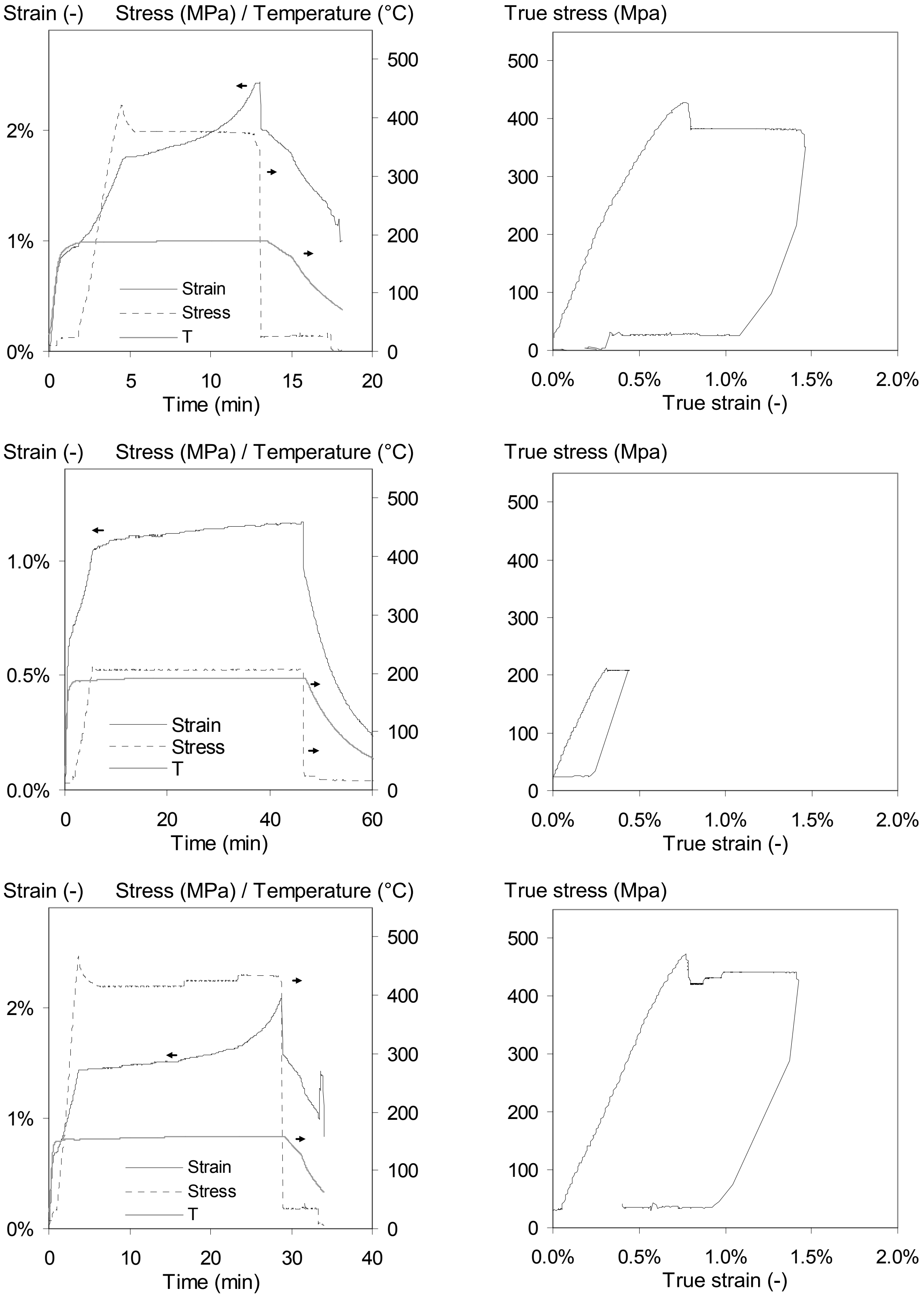

Fig. V.17. Selected creep tests

(a, c, e) Temperature, stress and total strain evolutions versus time. (b, d, f) True stress-strain curves, thermal strain being removed. (a, b): Stress applied once yield stress has been overcome. (c, d): stress applied below yield stress. (e, f): Creep stress has been varied along the heat treatment.

Fig. V.18.a presents a rupture in the yield stress evolution with temperature: yield stress decreases more slowly in the room temperature range (20°C to 120°C) than in the hot temperature range (120°C-190°C). Between 120°C and 180°C, it decreases linearly from ~500 MPa to ~400 MPa.

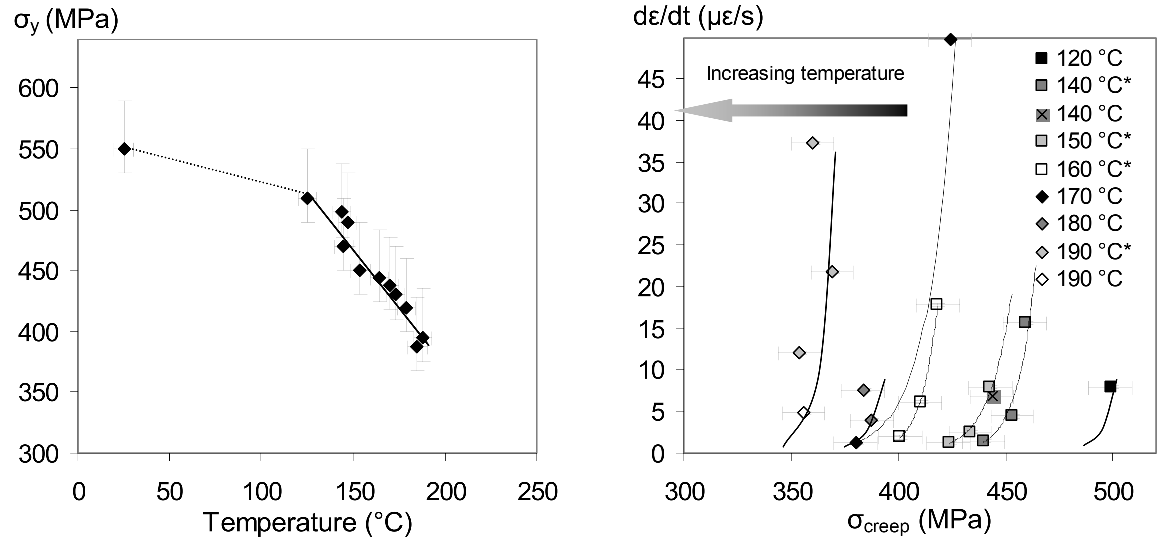

Fig. V.18. Yield stress and creep behaviour of T7651 as a function of temperature

(a) Yield stress as a function of temperature. (b) Creep rate as a function of temperature and stress. In Fig. (a) yield stress is measured from the creep experiments (see Fig. V.17), which explains the large error bars. In Fig. (b), creep rate is measured in the steady-flow regime, before catastrophic flow occurs. The stars in the legend are associated to the creep rates measured on a single specimen, to which various creep stresses have been applied sequentially (see Fig. V.17.e).

Fig. V.18.b shows that creep rate increases with both stress and temperature, following an exponential law. Stress and thermal activation favour the dislocation mobility, which flow more easily. A simple view is that the lower is the temperature, the higher has to be the creep stress to observe the same deformation rate. At 120°C for instance, about 500 MPa is required to see flow of 8 με/s, while the same deformation rate only requires 420 MPa at 160°C.

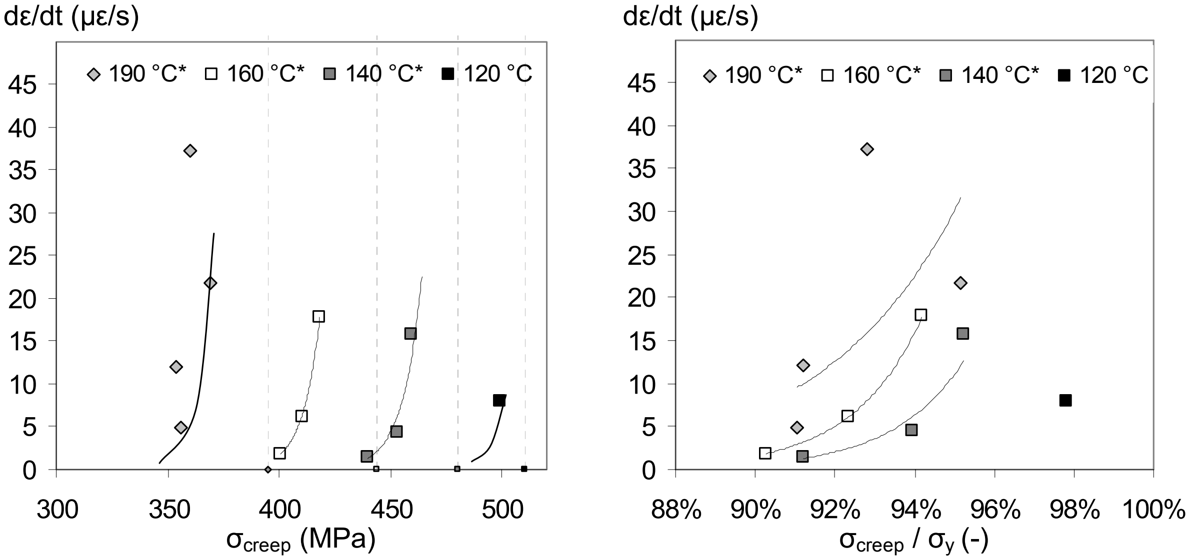

Fig. V.19. Effect of creep stress related to yield stress on creep rate

(a) Creep rate evolution with stress for selected temperatures compared to yield stress (vertical dashed lines). (b) Creep rate as a function of the creep stress / yield stress ratio.

Zhu and Starke ([Zhu 2001c]; see Fig. V.9.b) noted that a significant strain could be achieved only at relatively “high creep level”. To check this point, creep stress has been related to yield stress in Fig. V.19. For instance to see a 8 µε/s flow, a creep stress ratio of 98% is required at 120°C, versus a 93% ratio at 160°C. More generally, one can say that in the investigated time and temperature range, a significant material flow is observed for creep ratios above ~90%.

V.C.2.c. Precipitation kinetics

160°C is the temperature used for the final treatment of the T7651 material. As a consequence, the effect of creep below and above this threshold may be different, and the two cases will be considered.

i. Effect of creep above 160°C

Fig. V.20 presents the effect of a creep stress on the evolution of the precipitate size and volume fraction at 180°C. For the sake of comparison, a stress-free specimen is aged in the same conditions.

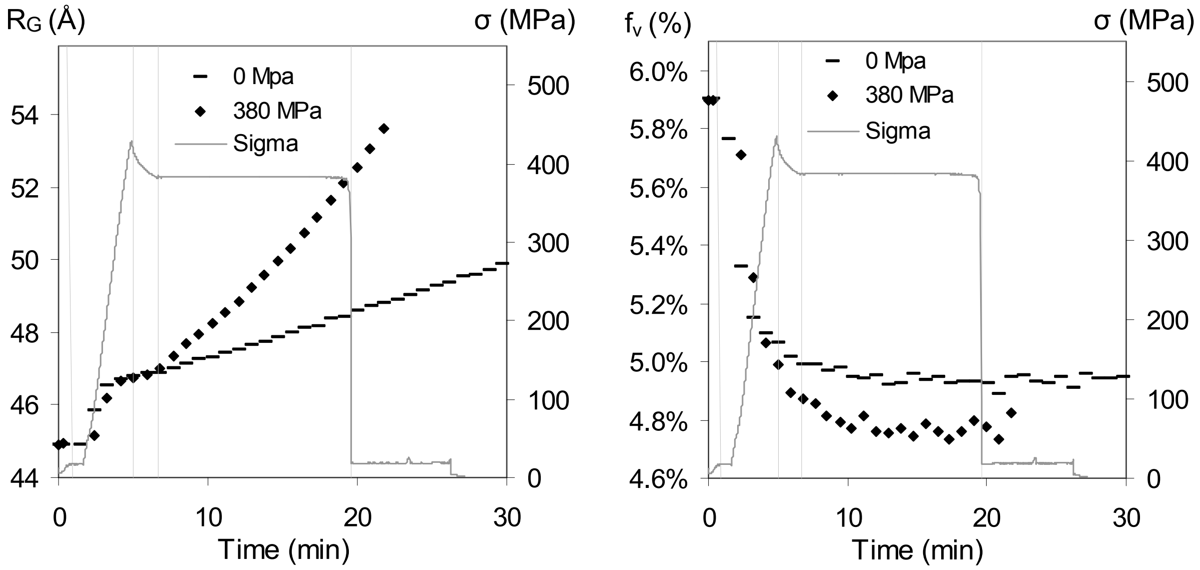

Fig. V.20. Effect of creep on precipitation kinetics at 180°C

(a) Guinier radius. (b) Precipitate volume fraction. Stress evolution of the specimen creep-aged at 380 MPa in grey. The vertical lines limit the TMT stages: the first one is the end of the heating ramp; the second one the end of the constant strain rate loading stage; the last 2 limit the creep stage.

The analysis of Fig. V.20 gives the following results:

- At the beginning, the precipitate mean size increases rapidly from ~45 to 46.5 Å, while the precipitate volume fraction decreases from 5.9% to about 5%. The rapid heating stage tends to destabilize the smaller precipitates (see chapter IV and discussion in V.C.3.c.iv). There is however a delay between the temperature peak (~1 min; see the grey vertical line) and the beginning of dissolution (~ 2 min).
- Then, the precipitate mean size grows at a constant rate for both specimens (stress-free and stress-aged), up to a certain stage, where it starts to accelerate. No clear effect is observed during the relaxation stage, but the precipitate radius begins to increase more rapidly as soon as the constant creep stress is applied.
- Simultaneously, the precipitate volume fraction seems to be also affected, being slightly smaller once load is applied. However, this may be an experimental artefact: the high precipitate growth rate tends to shift more rapidly the SAXS signal toward the low scattering vector values, hiding sligthly the spectra behind the beamstop.

- When the specimen is unloaded, the precipitates seem to grow at the same rate as during creep. This tends to prove that the static effect (i.e. the presence of dislocations itself) dominates the precipitate growth rate, rather than the dislocation motion. However, only a few data points are available and the tendency is difficult to establish clearly.

Fig. V.21 presents similar results, for specimens aged at 190°C at various stress levels: a stress-free specimen (0 MPa), a specimen stressed at ~60% of the yield stress value (206 MPa; see Fig. V.17.c and d) and a third one stressed at 375 MPa, whose stress profile is reported on the same figure.

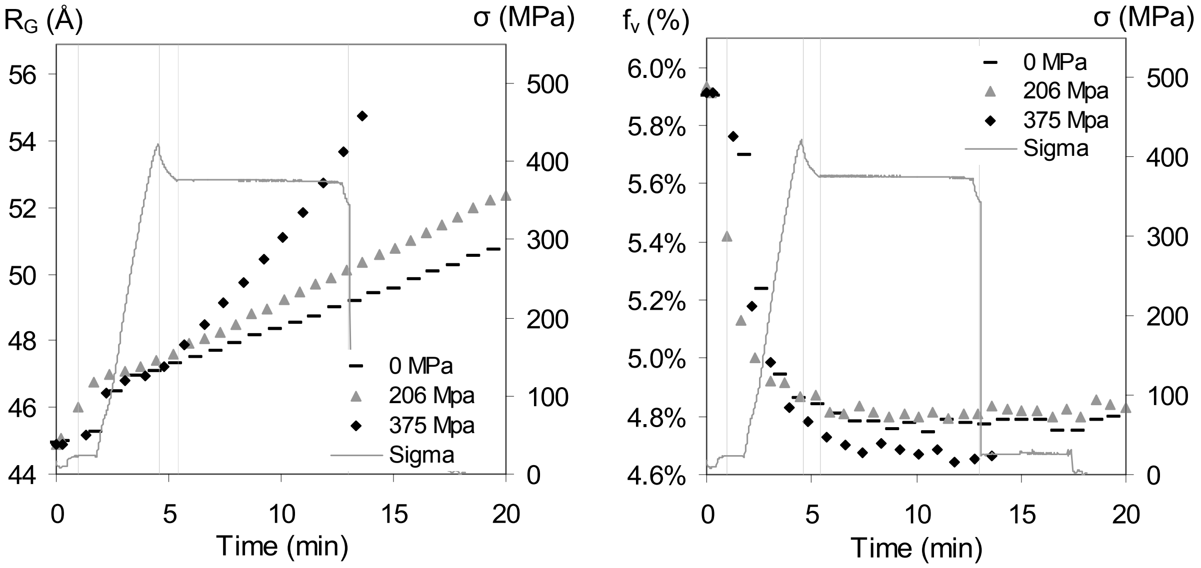

Fig. V.21. Effect of creep on precipitation kinetics at 190°C

(a) Guinier radius. (b) Precipitate volume fraction. Stress of the specimen aged at 375 MPa in grey.

Results similar to the ones observed at 180°C are observed. However, in that case, where different creep stress experiments are available, one can note that a lower creep stress diminishes greatly the precipitate growth rate, while the precipitate volume fraction is apparently not affected. This can be checked by comparing the evolution of the precipitate growth rate to the strain, as done in Fig. V.22.

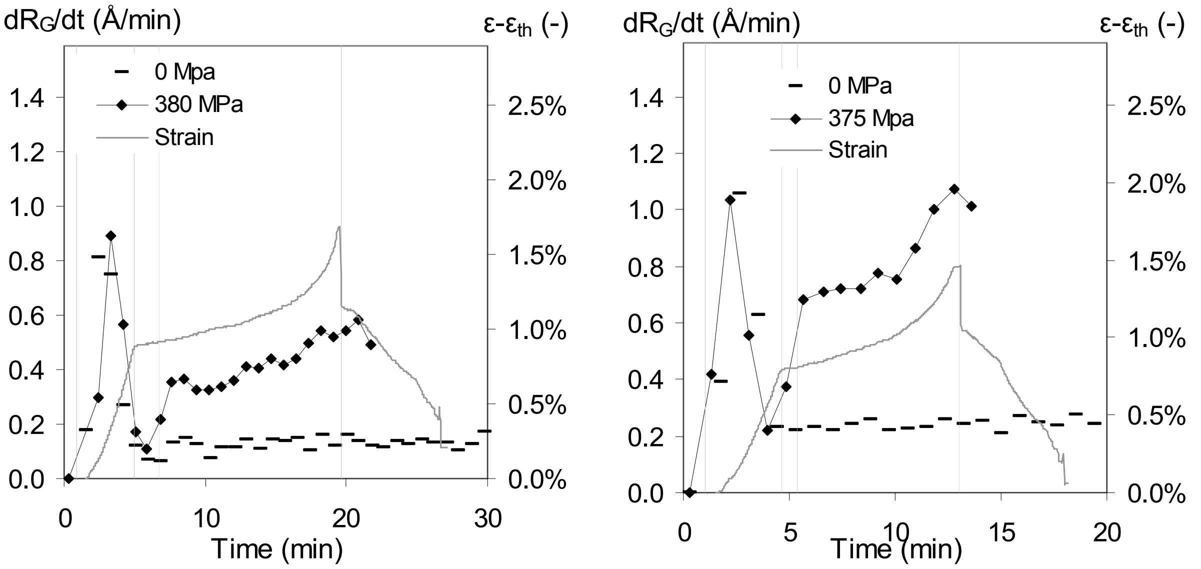

Fig. V.22. Effect of strain on the precipitate growth rate

(a) Radius growth rate at 180°C. (b) Radius growth rate at 190°C. In that case the strain is the sum of the plastic and elastic strains: thermal dilatation has been deduced from the total strain.

While the precipitate growth rate remains constant in the stress-free specimen (about 0.15 Å/min at 180°C and 0.22 Å/min at 190°C), it actually grows continuously when strain increases. Moreover it always remains about 300% higher as compared to the stress-free aged specimen.

Fig. V.22 tends to show that the growth rate depends on strain. To check whether it is also strain rate dependent or not, the precipitate growth rate is compared to the strain rate in Fig. V.23.

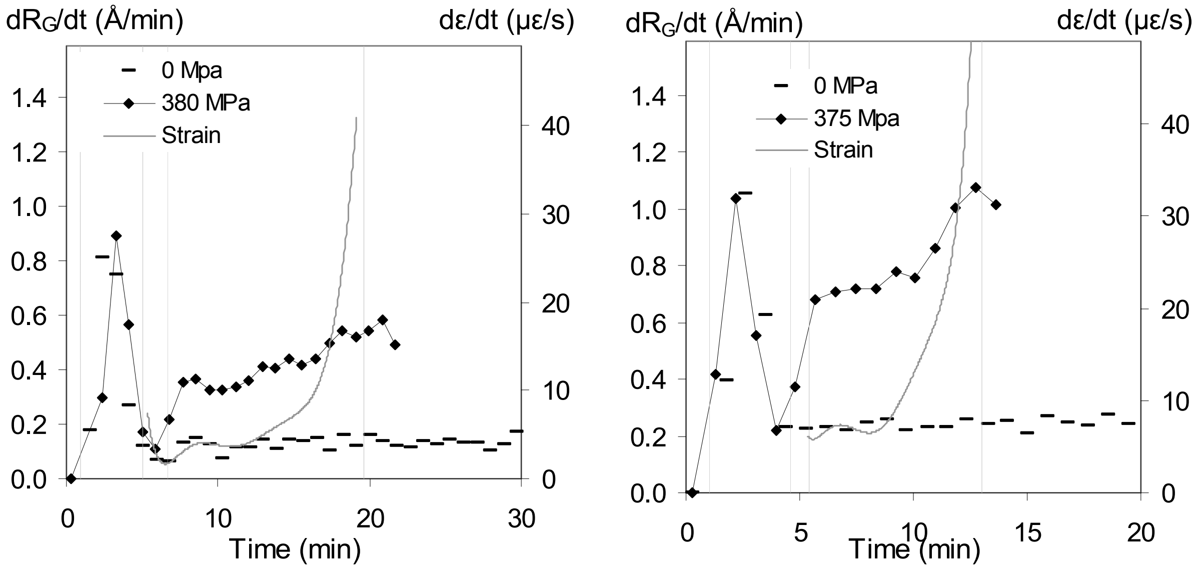

Fig. V.23. Effect of strain rate on the precipitate growth rate

(a) Radius growth rate at 180°C. (b) Radius growth rate at 190°C.

No obvious relation between creep rate and precipitate growth rate is observed, which tends to evidence that the precipitate growth rate is more sensitive to strain than to strain rate. However, at a lower stress value (206 MPa; see Fig. V.24), the opposite behaviour is found. While strain only slightly increases, the apparent precipitate growth rate decreases, in conjunction with the strain rate decrease. However, since at such small stress the behaviour is very similar as without applied stress, this result may be not necessarily significant.

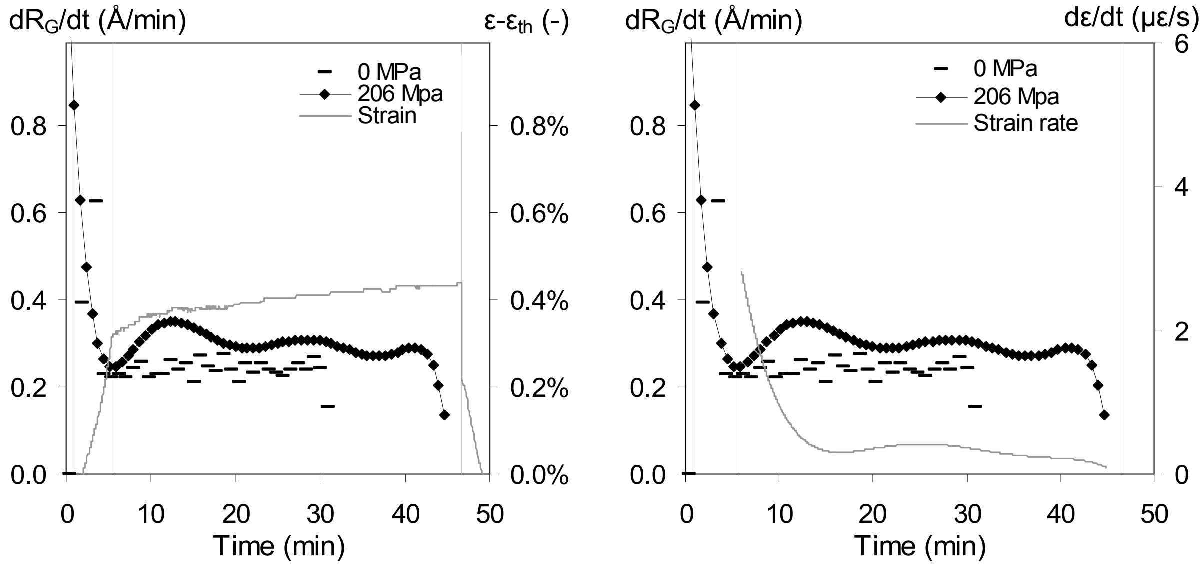

Fig. V.24. Effect of strain rate on the precipitate growth rate

(a) Radius growth rate at 180°C. (b) Radius growth rate at 190°C.

ii. Effect of creep at 160°C and below 160°C

Fig. V.25 and Fig. V.26 present the evolution of the precipitate Guinier radius and volume fraction during multi-stage creep tests at respectively 160°C and 140°C.

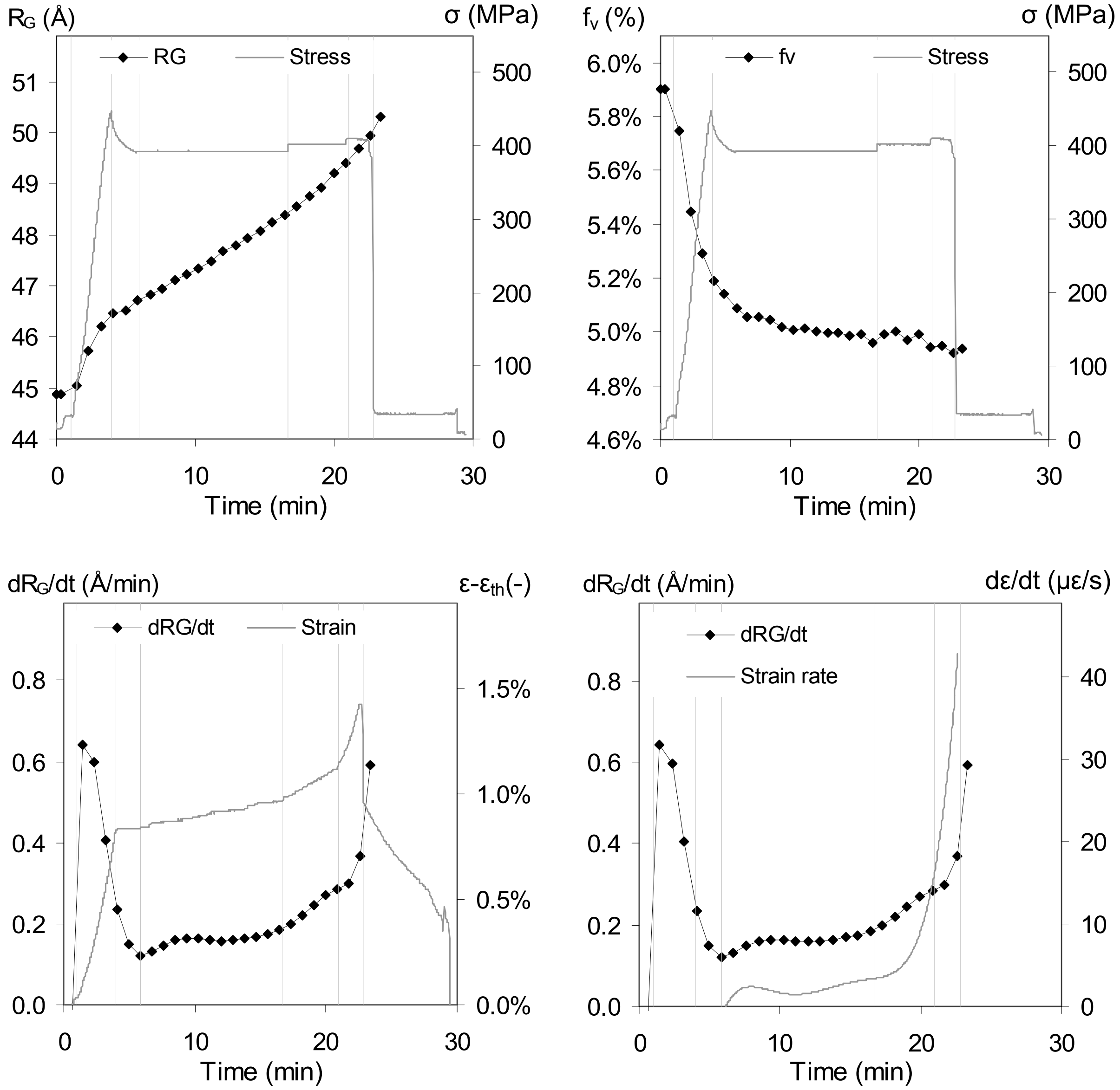

Fig. V.25. Effect of creep on precipitation kinetics at 160°C

(a) Guinier radius vs. stress plot. (b) Precipitate volume fraction vs. stress. (c) Precipitate growth rate vs. strain. (d) Precipitate growth rate vs. strain rate. The vertical lines limits to the TMT main stages: the first one is the end of the temperature ramp; the second one the end of the constant strain rate loading stage; the 4 others the various constant stress limits.

Each time the stress increases, the precipitate growth rate rises as well. For instance it grows from a mean value of ~0.16 to ~0.26 Å/min when stress increases from 392 to 402 MPa. The precipitate volume fraction decreases continuously, but this effect is probably mainly due to an experimental artefact, and will not be considered as effectively occurring.

As previously evidenced at higher temperature, the precipitate growth rate seems to be more related to the stress level or to the strain (Fig. V.25.c) than to the strain rate (Fig. V.25.d).

At 140°C, as at higher temperature, the precipitate growth rate still depends on the creep stress value. For instance it goes from 0.04 to 0.057 Å/min when the stress increases from 431 to 443 MPa.

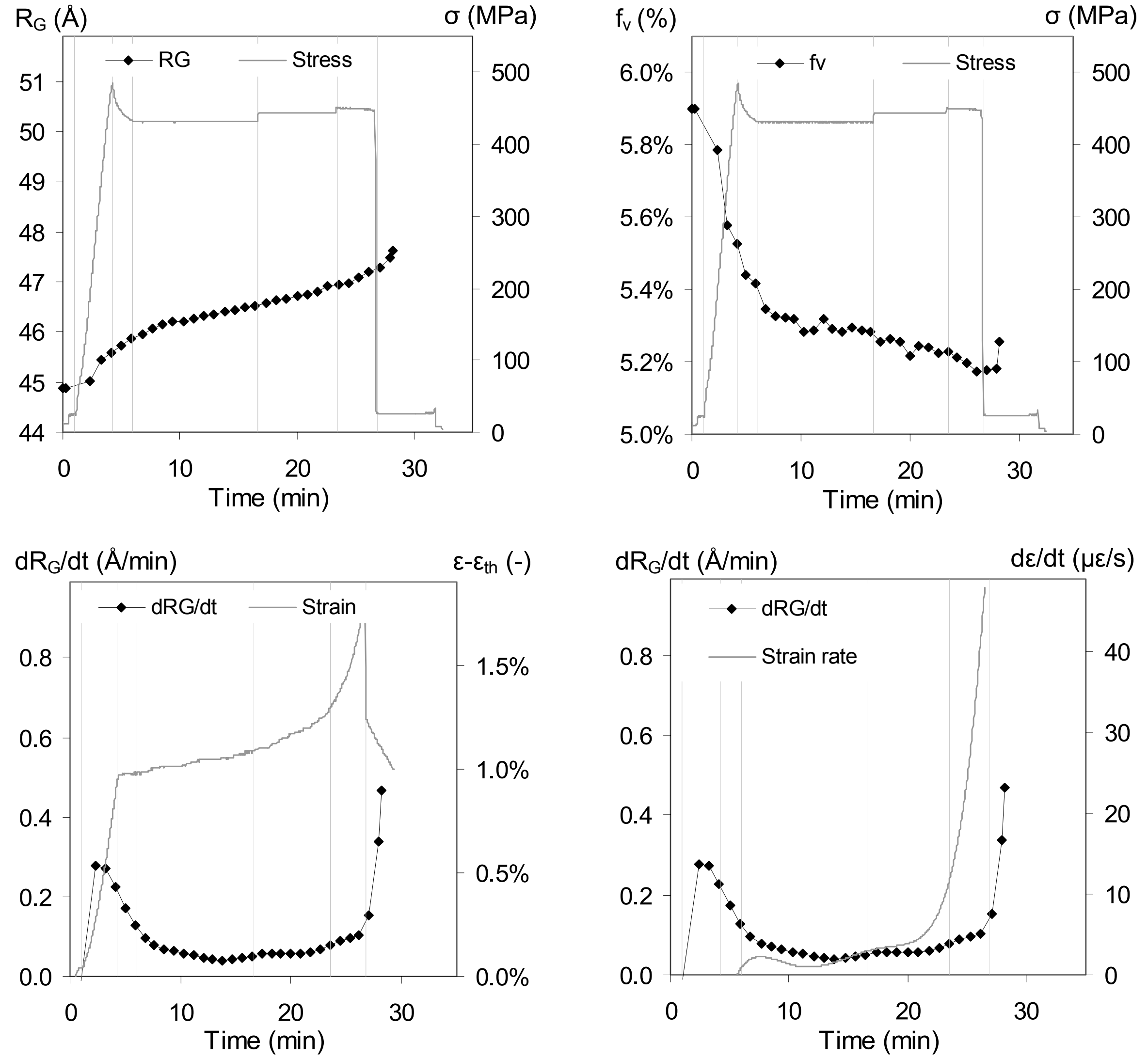

Fig. V.26. Effect of creep on precipitation kinetics at 140°C

(a) Guinier radius vs. stress plot. (b) Precipitate volume fraction vs. stress. (c) Precipitate growth rate vs. strain. (d) Precipitate growth rate vs. strain rate.

V.C.2.d. Conclusion on creep-age forming

i. Sensitivity of radius growth rate

It is possible to calculate a parameter characteristic of the sensitivity of precipitate growth rate to stress variation:

$$\text{(II.1.)}\quad \delta = \frac{\Delta \dot{R}_G / \dot{R}_G}{\Delta \sigma / \sigma}$$

The effect of temperature on this sensitivity parameter is presented in Table V.1. This table won't be considered for a thorough quantitative analysis, due to a limited number of experimental data and debatable measurements. However, the fact that the precipitate growth rate sensitivity to stress increases with temperature is interesting. In particular, it shows that even if the temperature is below the temperature of the T7651 treatment (160°C), the precipitate microstructure is unstable and affected by creep.

Temperature (°C)	140	150	160
Sensitivity	15	23	25

Table V.1. Precipitate growth rate sensitivity to stress as a function of temperature

The precipitate growth rate sensitivity apparently depends more on the strain level than on the strain rate. It tends to show that static effects (i.e. dislocation density) mainly control the growth rate, more than dynamic effects (i.e. dislocation motion). One element to explain this is certainly the fact that these straining tests have been carried out at very low strain rates (straining lasted about 20 minutes).

ii. Industrial considerations

Creep forming of fully heat treated AA7449 T7651 components requires a relatively high creep level to be effective: typically a creep level about 10% below the yield stress level. Increasing the temperature allows diminishing either the duration or the creep stress value of the forming operation.

In the considered 140-190°C temperature range, the microstructure is affected, even if the creep forming operation takes place below 160°C, the temperature of the previous T7651 heat treatment. The higher are the temperature and the stress values, the most affected will be precipitation kinetics.

The microstructure being affected by creep age forming, the final mechanical properties after a part distortion correction treatment would be the result of a time/temperature/creep stress balance.

V.C.3. Strain age-forming

V.C.3.a. Thermomechanical treatment

The overall TMT is composed of two stages: an initial heat treatment to design the initial temper, and a real TMT, in which a stress and/or a strain aging treatment are imposed (see Fig. V.27).

The initial heat treatment follows the standard aging heat treatment presented in chapter II: solution heat treatment, water quench and natural aging followed by artificial aging at 120°C and 160°C (see Fig. V.27.b). This treatment has been interrupted after various durations, to generate 5 different partially heat treated groups of specimens (see Fig. V.27.b) for the further TMT. Groups 1 to 4 are under-aged and group #5 is slightly over-aged.

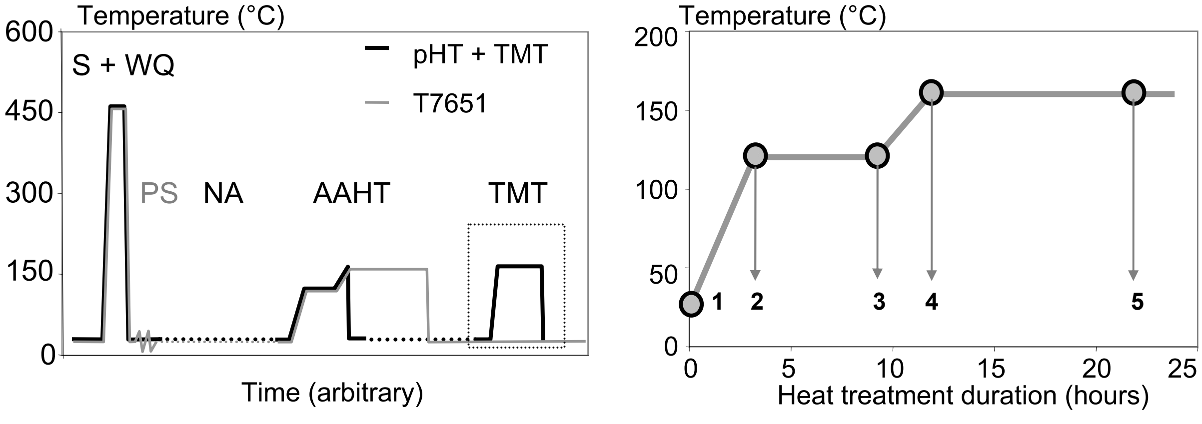

Fig. V.27. Overall TMT and initial partial heat treatment

(a) Overall thermomechanical treatment. (b) Initial partial heat treatment and definition of the 5 initial tempers. In Fig. (a), "S" stands for "solution heat treatment", "WQ" for "water quench", "PS" for "pre-stretching", "NA" for "natural aging", "AAHT" for "artificial aging heat treatment" and "TMT" for "thermomechanical treatment". The black curve corresponds to the treatment performed in this chapter: a partial heat treatment following the T7651 heat treatment (grey curve), followed by a TMT.

The number of possible variations for this type of heat treatments is enormous. For the effective thermomechanical stage, it has been decided to fix the temperature at the level of the previous partial heat treatment, to limit the number of TMT variables only to strain and strain rate. For instance the partially heat treated material #3 (see Fig. V.27.b), whose heat treatment has been interrupted after 6 hours at 120°C, will be subjected to tensile tests at 120°C.

Once the specimen is set in the tensile device and the SAXS chamber under vacuum, the exact TMT sequence is the following (see also Fig. V.28):

- 1: Rapid heating stage (~1 minute) up to testing temperature, during which load is controlled at 0. At the end of this stage, strain is set at 0 to remove thermal dilatation.
- 2a: Rapid elastic stage (~1 minute) at constant strain rate, up to about 80-90% of yield stress. It has been chosen to fix an identical elastic straining stage for all the specimens of one group, to only focus on the effect of the (further) plastic deformation on precipitation.
- 2b: Constant strain rate straining, up to a certain strain threshold. Both the effects of strain rate and strain limit are investigated.
- 2c: Once the strain target is reached, a relaxation stage takes place (at constant overall strain). The duration of this stage is set so that the overall TMT lasts about 30 minutes.
- 3: Rapid cooling stage (~2 minutes) down to room temperature, during which load is controlled at 0 to prevent specimen fracture.

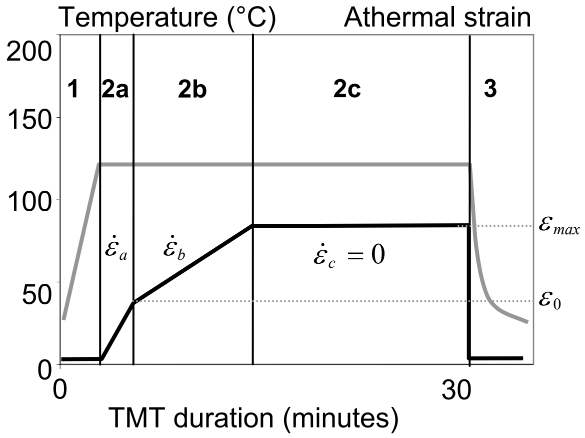

Fig. V.28. Schematic of the TMT

Temperature in grey (set at 120°C in this example). Strain in black. The vertical lines show the limits of the different TMT stages listed before.

V.C.3.b. Effect of strain aging on precipitation and properties: qualitative study

Before investigating quantitatively the effect of the process parameters (strain, strain rate, initial state) on precipitation kinetics, a detailed qualitative study of one experiment will be carried on. Both the mechanical response (i.e. stress-strain curve) and the precipitation response to a thermomechanical treatment will be investigated.

i. Tensile behaviour as a function of temperature

Fig. V.29 compares the tensile behaviour of two specimens: the first one has been deformed at 25°C on a standard tensile machine; the second one at 160°C on the TSAXS device. These under-aged specimens have been subjected to the same partial heat treatment, interrupted at stage #4 of the standard artificial aging treatment (see Fig. V.27.b).

One can notice major differences between the two curves:

- First, even if the exact yield stress value is not known[5], it is definitely lower at high temperature.

---

[5] The yield stress has not been determined precisely, because of the difficult interpretation of the stress-strain curves (in particular the transient regime). It is however definitely lower than at room temperature (for specimen #43: $\sigma_y \in [300;400]$

- Then, a transient regime appear in the high temperature test (between arrows “1” and “2”), during which the apparent strain hardening rate remains high. This is not observed at room temperature.
- Finally[6], the strain hardening rate in the steady-state regime (between “2” and “3”) is much lower.

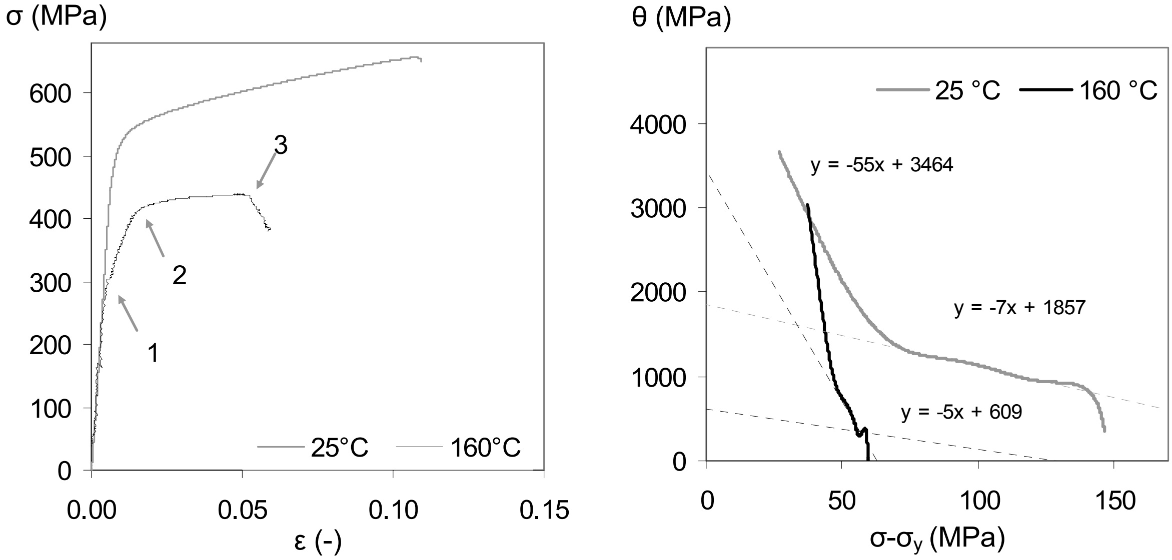

Fig. V.29. Effect of temperature on the stress-strain behaviour of specimen group #4

(a) Tensile curves. (b) Strain hardening curve. The specimen deformed at 160°C is the TSAXS specimen #43. The specimen deformed at room temperature is a standard tensile specimen (see chapters II and III). The yield stress of #43 has been evaluated at 380 MPa.

Before going further into the interpretation of these differences, it is first important to underline that the two experiments were not performed in the same conditions. The room temperature test was performed with a standard tensile specimen, on a standard tensile machine equipped with an extensometer (see chapter II for details), whereas the high temperature test was performed on the TSAXS device and corresponds to specimen #43 (see Table V.2).

The lower yield stress is probably due both to thermal activation of precipitate/dislocation overcoming, and to a lower dislocation density (enhanced dynamic recovery), giving a reduced forest hardening. This also explains the lower strain hardening rate in the third regime. In that present case, contrary to what has been observed in Fig. V.14.a, the precipitate growth during strain aging is not sufficient to balance significantly the enhanced dynamic recovery.

The remaining issue is the cause of the transient observed after the initial linear stage. A possible hypothesis is an experimental artefact due to an experimental issue. The transient (observed on all the specimens; see Fig. V.33) may be related to the specimen geometry. It could have happened, that the central section (see Fig. V.30) has plastified at ~300 MPa (which explains the first transition, shown by the first arrow on Fig. V.29). Then this section has work hardened, transferring progressively the plastic deformation to the larger specimen’s section, which finally yielded at ~400 MPa (second arrow). However, the second section is 5/3 larger than the central section, and moreover, a microscopic study of the deformed surface specimens revealed that plastic deformation was restricted to the central section (see Fig. V.30). It is not unreasonable to think that this transient behaviour may be also due to precipitation events. A similar phenomenon has been found in the literature ([Cavaliere 2002]; see Fig. V.15), but in that case, the acquisition frequency of these experiments may be debatable.

---

[6] The stress decrease after the third arrow corresponds to the relaxation stage, and won’t be considered here.

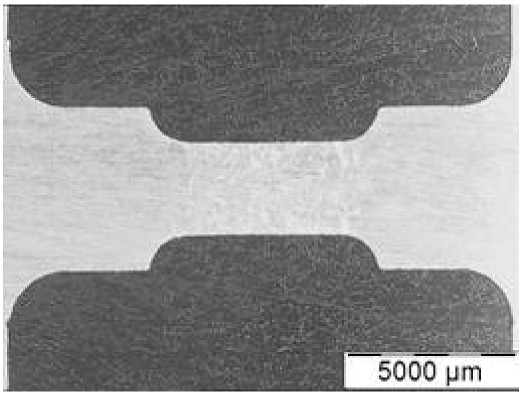

Fig. V.30. Tensile specimen #43 after straining

The central section is the only area where traces of deformation bands are found.

ii. Effect of straining on precipitation kinetics

It has been shown in V.C.2 that creep does accelerate precipitation, as compared to a stress-free specimen. One will now investigate the effect of straining on precipitation by comparing the SAXS results of a stress-free aged specimen (#40) to the strained specimen #43 in Fig. V.31.

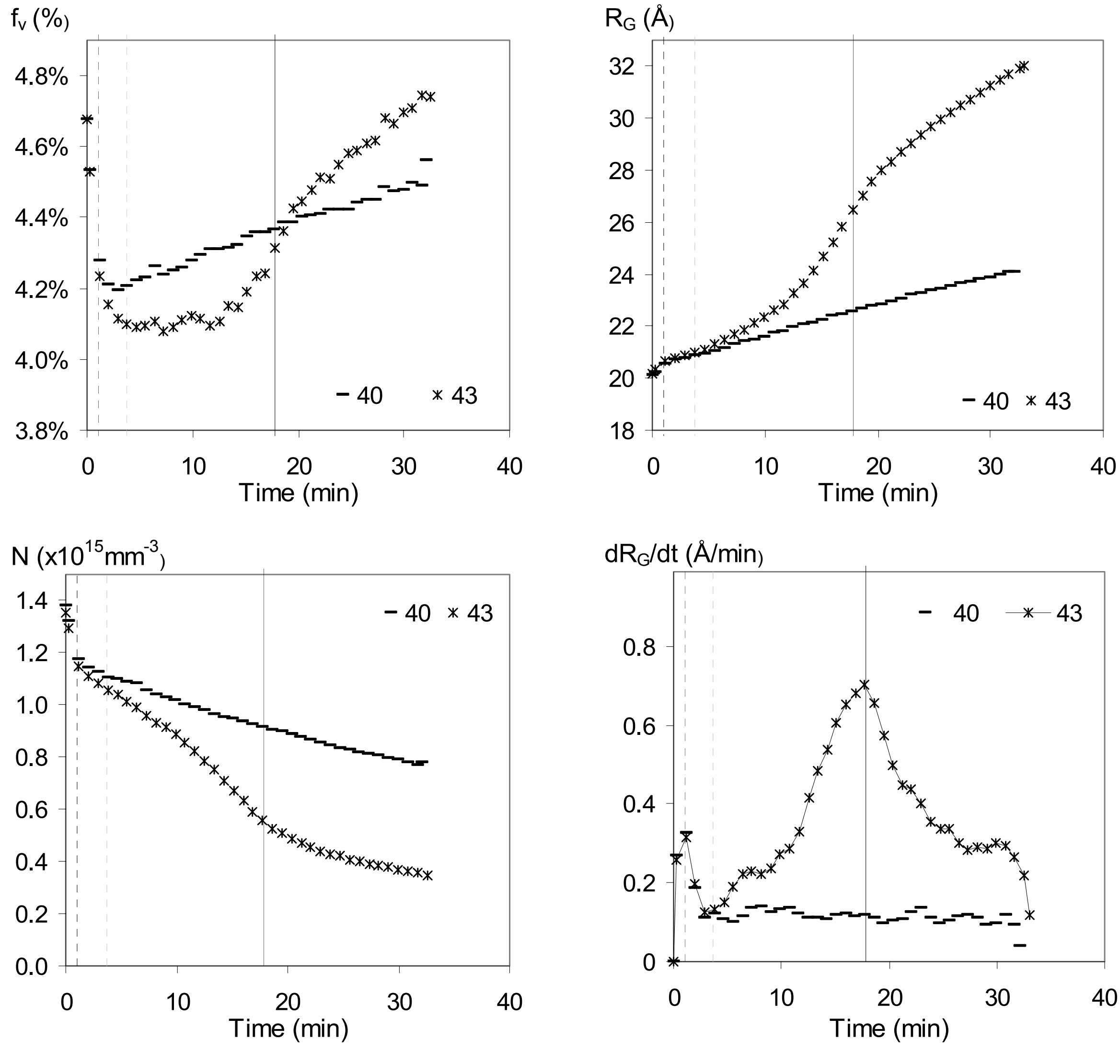

Fig. V.31. Effect of straining on precipitation kinetics of specimen group #4

(a) Precipitate volume fraction. (b) Precipitates Guinier radius. (c) Precipitate number density. (d) Precipitate radius growth rate. The vertical lines respectively indicate: the end of the temperature ramp (dashed black), the strain rate transition 2a/2b (dashed grey) and the straining/relaxation transition 2b/2c (full).

- Stress-free specimen

Right at the beginning of the experiment, the undeformed sample (black dashed line) presents a dissolution stage, where the precipitate volume fraction looses 15% within 1 minute, while the precipitate size remains approximately constant, resulting in a decrease of the particle number density.

Then, a second step of continuous and constant increase of the precipitate size and volume fraction and a decrease of the number density shows that precipitation has entered into a regime of coarsening. This coarsening is relatively slow, the precipitate radius evolving from 1.9 to 2.3 nm in the 30 minutes of the test duration.

- Strained specimen

While the behaviour of the strained specimen is similar to the one of the reference sample during the dissolution step (up to the grey dashed line), it rapidly exhibits different precipitation behaviour afterwards. The precipitate volume fraction remains at a lower level for some time, after which it increases more rapidly than the volume fraction of the stress-free specimen.

The precipitate radius is strongly affected by straining: while the precipitates of the stress-free specimen grow at a constant rate of ~0.11 Å/min, the precipitate growth rate of the strained specimen always remains at a higher level. Moreover it follows a bell-shaped curve which seems to be correlated to the thermomechanical treatment. It begins to diverge at the location of the strain rate transition (vertical grey dashed line); then the growth rate increases during plastic deformation, and reaches a maximum at the end of the straining stage (vertical black line). It finally decreases during the relaxation stage. All these observation are compatible with an assumption of enhanced diffusion due to the presence of dislocations.

V.C.3.c. Effect of the process parameters on precipitation during strain aging of temper #4

Let investigate now the effect of the various process parameters.

i. <u>Imposed TMT</u>

Seven partially heat treated specimens of group #4 have been strained at 160°C at different strain rates, and up to different plastic strain levels. A reference sample (#40) was not strained; specimens #41, #42 and #43 were strained at relatively low strain rate (~5.10^{-5}.s^{-1}); the second group (#44, #45, #46) was strained more rapidly (~25.10^{-4}.s^{-1}). The imposed TMT (i.e. the strain-time signal) is represented in Fig. V.32 and the corresponding TMT parameters are reported in Table V.2.

Temper	Sample	Plastic strain	Strain rate (s^{-1})	Strain duration (h)
#4	40	0.0%	0.0	0.00
	41	2.6%	2.7 10^{-5}	0.36
	42	4.0%	5.9 10^{-5}	0.26
	43	4.6%	6.0 10^{-5}	0.30
	44	0.5%	17.8 10^{-5}	0.07
	45	2.2%	21.8 10^{-5}	0.10
	46	4.6%	37.1 10^{-5}	0.10

<u>Table V.2. TMT conditions of group #4 specimens</u>

The more slowly strained specimens (Fig. V.32.a) were deformed at identical strain rate during the first “high strain rate stage” (2a), after which they were subjected to a lower strain rate deformation. The rapidly strained specimens (Fig. V.32.b) were deformed at constant strain rates during the whole straining stage. The duration of the straining stages is different for each specimen; the idea was, to obtain comparable deformations in the two groups: about 2%, 4% and 6%. One can notice (arrows in Fig. V.32.a) a steady-state deformation regime, during which the strain rate remains constant.

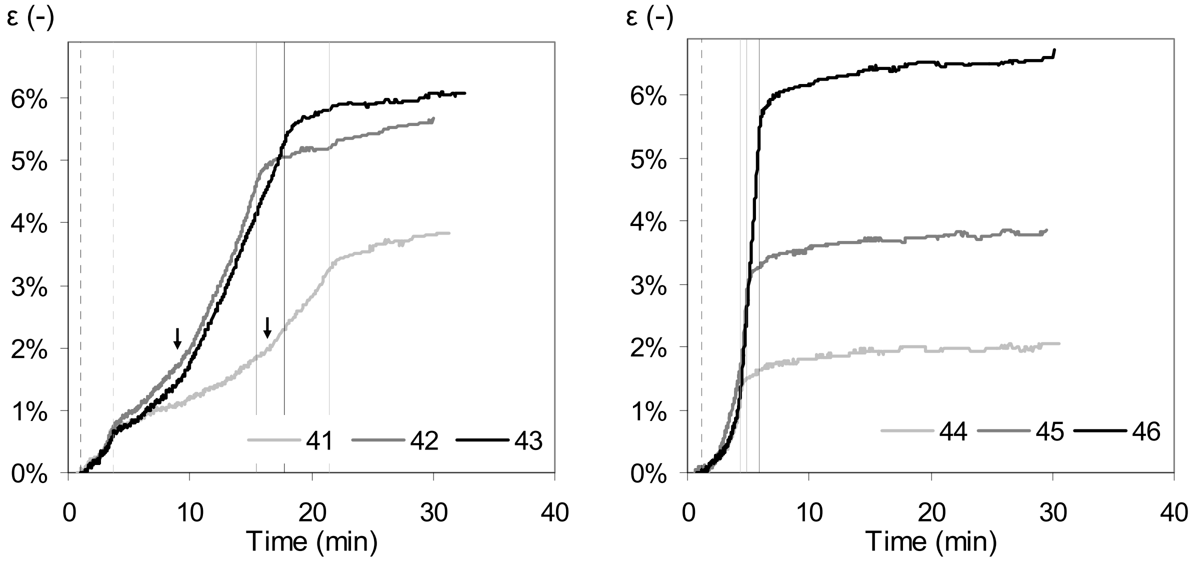

Fig. V.32. Strain-time curves of specimen group #4

Slowly (a) and rapidly (b) strained specimens. The vertical lines respectively indicate: the end of the temperature ramp (dashed black), the strain rate transition 2a/2b (dashed grey) and the straining/relaxation transitions 2b/2c (full). The arrows indicate the beginning of the steady-state deformation regime.

ii. Stress-strain behaviour

The corresponding stress-strain curves are represented on Fig. V.33.

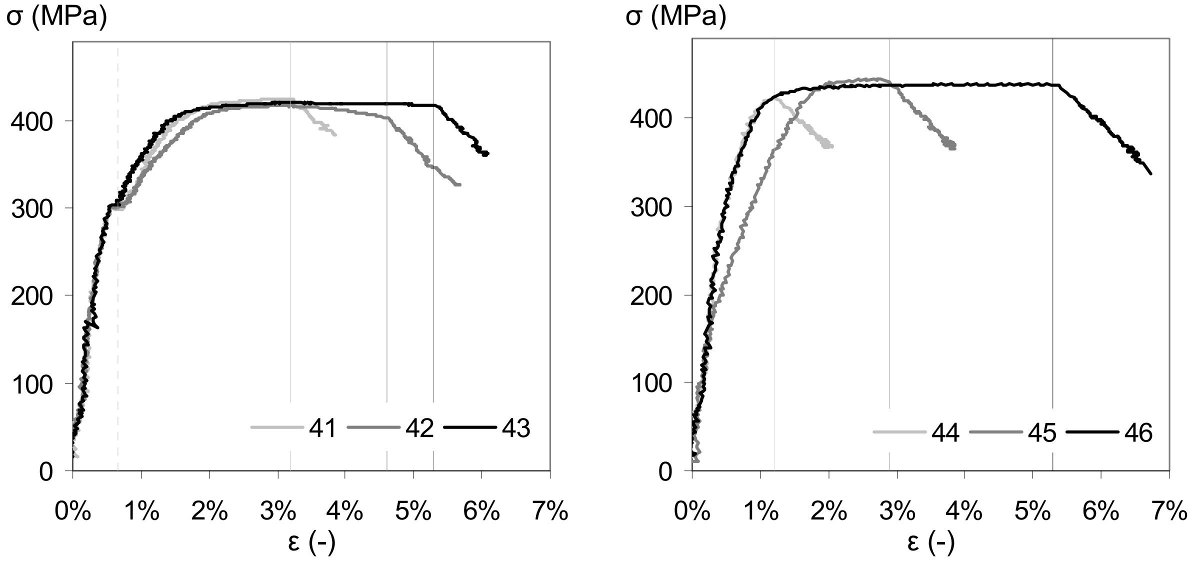

Fig. V.33. Stress-strain curves of specimen group #4

Slowly (a) and rapidly (b) strained specimens. The vertical lines respectively indicate: the strain rate transition 2a/2b (dashed grey) and the straining/relaxation transitions 2b/2c (full).

The behaviour observed in V.C.3.b.i (in particular the transient regime) is similar in each specimen. One can add that the steady-state deformation regime observed in Fig. V.32 corresponds to a saturation of stress. The value of the saturation stress seems to be lower for the slowly strained specimens (~420 MPa) than for the more rapidly strained specimens (~435 MPa). This difference may be however too small to be interpreted, due to the relatively large error bars of the experiments.

iii. Precipitation kinetics

The evolution of the most important parameters measured during the tests, both in terms of mechanical response (stress, strain rate) and of precipitate microstructure are reported on Fig. V.34.

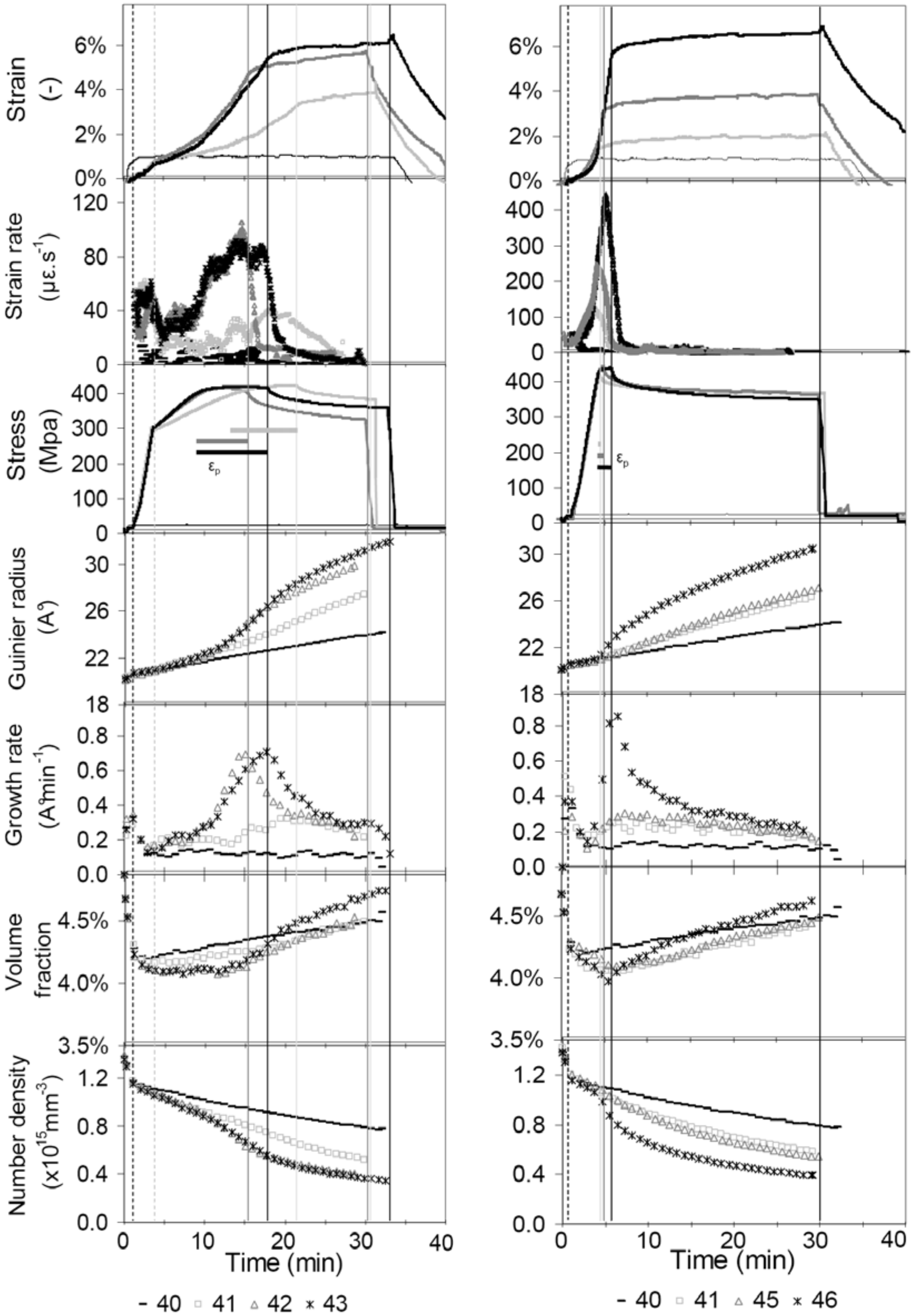

Fig. V.34. Effect of straining on precipitation kinetics - temper #4

Slowly strained specimens (left); more rapidly strained specimens (right). The vertical lines respectively indicate: the end of the temperature ramp (dashed black), the strain rate transition 2a/2b (dashed grey) and the straining/relaxation transitions 2b/2c (full). The apparent plastic deformation[7] duration ε_p is represented on the stress (3rd) figure.

---

[7] The apparent plastic deformation is measured as the difference between the strain at the end of the straining stage and the strain at which stress is no more linear.

iv. First analysis

- General behaviour

All the specimens present a precipitation response similar to the one presented in V.C.3.b.ii. This behaviour is summarized in Fig. V.35.

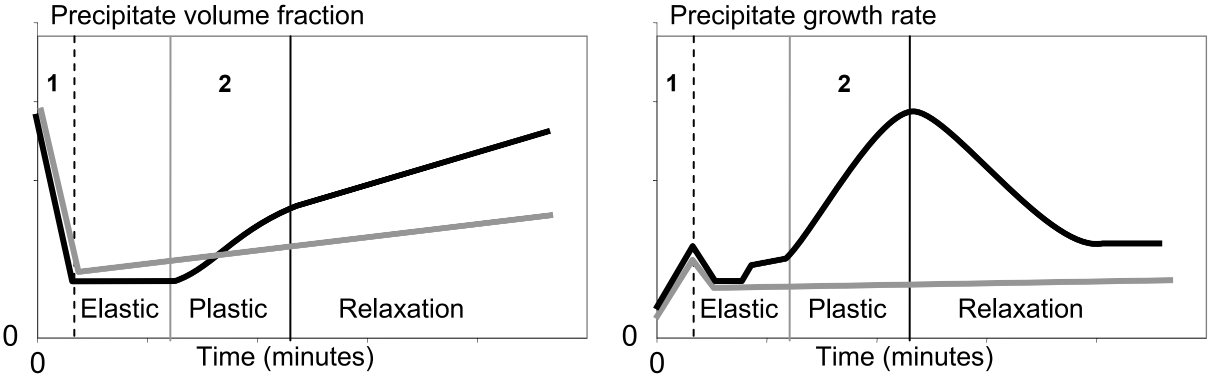

Fig. V.35. Schematic evolution of the main precipitation parameters during straining

(a) Precipitate volume fraction. (b) Precipitate growth rate. The grey curve represents the stress-free material; the black line the material subjected to the TMT. The vertical lines limit the different stages.

During the heating stage, about 0.5% of the precipitate volume fraction initially present in the material dissolves. Then, while it undergoes reversion slowly and constantly for the stress-free specimen, it remains lower during the elastic stage, and progressively increases during the plastic stage. Finally it grows at a constant rate during relaxation.

The precipitate growth rate is even more affected. It begins to differ from the stress-free specimen behaviour at the very end of the elastic stage: as already observed during the creep tests in V.C.2, a stress, even if it is lower than the yield stress, tends to increase the kinetics of precipitation. Then, while plastic deformation occurs, the precipitate growth rate increases, up to a maximum, located at the end of the straining stage. It then decreases as soon as deformation is stopped, and tends to saturate at levels which remain significantly higher than the ones observed for the stress-free case.

If it is clear why the precipitate growth rate peak is positioned at the end of the straining stage, its level remains more difficult to comprehend. It seems however that it is related both to the strain (a higher strain tends to promote a higher growth rate) and to the strain rate too. Both a larger strain and a larger strain rate lead to a higher dislocation density, and therefore to a faster solute diffusion helped by pipe diffusion.

Before discussing further the origin of the enhanced precipitation kinetics during straining, one will first analyse the initial microstructure and the effect of the heating stage.

- Initial microstructure and effect of the heating stage

As already observed during the creep tests in V.C.2, a significant fraction of the precipitates is dissolved during the heating ramp. A fine analysis of the SAXS spectra will provide information about the effective microstructure at the beginning of the straining stage.

On Fig. V.36, the position of the intensity peak (top arrow) is shifted towards the low scattering vector values during the whole duration of the heat treatment. This explains the continuous increase of the Guinier radius during the experiment (Fig. V.34). During the straining and relaxation stages (hell grey curves labelled #10 to #40), the growth of the Guinier radius is accompanied by a shift of the whole spectra towards lower scattering angles. On the contrary, during the heating stage (black and dark grey curves), the diffusion signal in the low scattering vectors range (left arrow) does not change at all, while the spectra at higher scattering vectors (right arrow) shifts very rapidly. These two points respectively mean a full stability of the larger precipitates and dissolution of the smaller precipitates.

This demonstrates that secondary GP zones have nucleated during the intermediate storage stage (between the end of the heat treatment and the TMT treatment; typically 2 weeks). The larger particles which precipitated during the aging treatment are not affected by the heating stage, contrary to the GP zones, not stable enough to support the high heating rate.

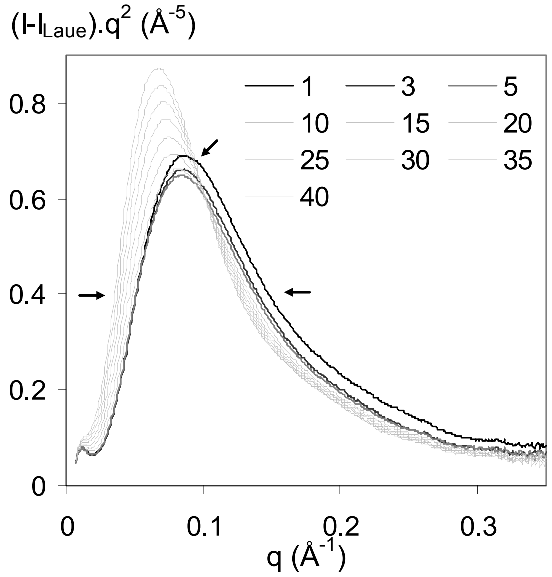

Fig. V.36. SAXS spectra evolution during TMT of specimen #44

The numbers indicate the image number. #1 is the initial state; #5 corresponds to the beginning of the straining stage, during which there is approximately one image every minute.

Thus, the microstructure at the beginning of the TMT consists of metastable η' precipitates and a mildly supersaturated solid solution (about 3% of the atomic fraction). We will in the following discuss the origin of the enhanced precipitation during the TMT.

v. Discussion: mechanisms responsible for the enhanced precipitation during the TMT

It has been evidenced the precipitate growth rate increases continuously during the straining stage, and remains at a very significant level during the relaxation stage. Several mechanisms can be invoked to explain this behaviour:

- Nucleation of new precipitates aided by the presence of dislocations or their movement (dynamic nucleation),
- Diffusion of solute to pre-existing precipitates, accelerated by the presence of dislocations or their movement (static or dynamic growth),
- Acceleration of particle coarsening by the presence or the movement of dislocations (static or dynamic coarsening).

The reality of these mechanisms in the tested conditions will be evaluated in the following.

- Dynamic nucleation

The precipitate number density always decreased during the different TMT tests. Although it cannot be ruled out that some re-nucleation of a stable phase can happen at the expense of a dissolving metastable phase, it is unlikely that re-nucleation is the main mechanism explaining the effect of stress in the current conditions of initial heat treatment.

- Static growth and coarsening after plastic straining

At the end of the relaxation following the plastic strain at constant strain rate, the precipitate growth rate converges to one common value, higher in the case of the deformed samples than for the unstrained sample. Moreover, this value is observed to be proportional to the total applied plastic strain, as shown in Fig. V.37. A reasonable assumption is that the total plastic strain is directly related to the dislocation density at the end of the constant strain rate stage. From these accumulated dislocations results an accelerated solute transport via pipe diffusion, and thus an accelerated growth.

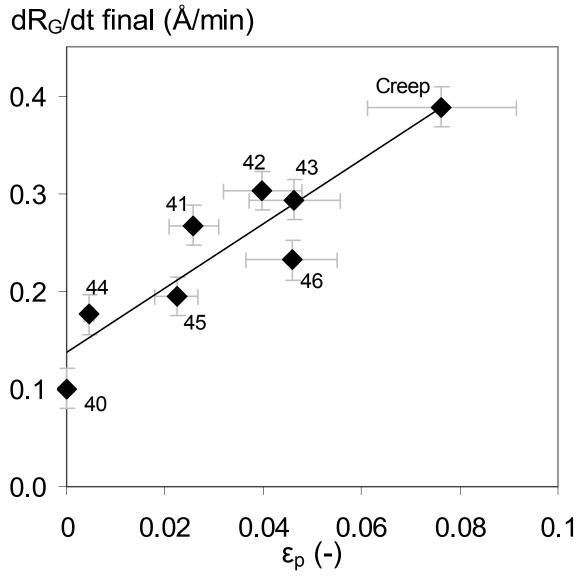

Fig. V.37. Final precipitate growth rate as a function of the apparent plastic strain in group #4

The final growth rate is measured at the end of the relaxation stage. The apparent plastic strain is the strain measured at the end of the straining stage minus the strain at the apparent yield stress.

- Dynamic growth and coarsening during plastic straining

The maximum precipitate growth rate, observed in conjunction with the highest strain rate, happens at constant volume fraction, and thus translates in a fast decrease of the precipitate number density. Therefore, we observe a clearly defined stage of dynamic coarsening during plastic strain, related not only to the presence of dislocations, but mainly to their motion through the material.

One could argue that this may be simply due to a static effect: due to work hardening, the dislocation density increases during the staining stage, which accelerates the kinetics of precipitation; it then decreases during the relaxation stage, due to recovery. Nevertheless, the precipitate growth rate rapidly decreases as soon as the plastic strain rate is reduced: there is no delay and this decrease is quite significant. If precipitation kinetics were only determined by static effects, it would have required an instantaneous recovery of a large number of dislocations. This is unlikely to happen in such a short timescale, and tends to confirm that there is a dynamic effect of the dislocations on precipitation evolution.

Several dynamic mechanisms have been invoked in V.B.1.b.iv which can explain this accelerated coarsening. One is transport of solute by the moving dislocations in the form of a Cottrell atmosphere. One possibility is an accelerated loss of coherency of the precipitate interfaces due to their interaction with dislocations, resulting in a decrease of the equilibrium concentration of solute and thus to an enhanced coarsening kinetics. It is however not possible to discriminate between them at this point.

Dynamic precipitation can also be responsible for the high work hardening rates observed in Fig. V.29.b. In the present case, a storage higher[8] than 3500 MPa (±500 MPa) were measured during the TMT, well above the values of 1000-2000 MPa expected from only dislocation storage. The rationale of this explanation is clearly that precipitates are initially in an under-aged state, and thus that the flow stress increases when the precipitate size increases. Thus, the precipitate size growth during the tensile test results in an additional contribution to the flow stress, which translates into a high strain hardening rate [Simar 2006].

- Effect of strain and strain rate on the precipitate growth velocity

It is suspected that both the stain and the strain rate do influence the precipitate growth rate. The relative influence of these two parameters will be evaluated in Fig. V.38.

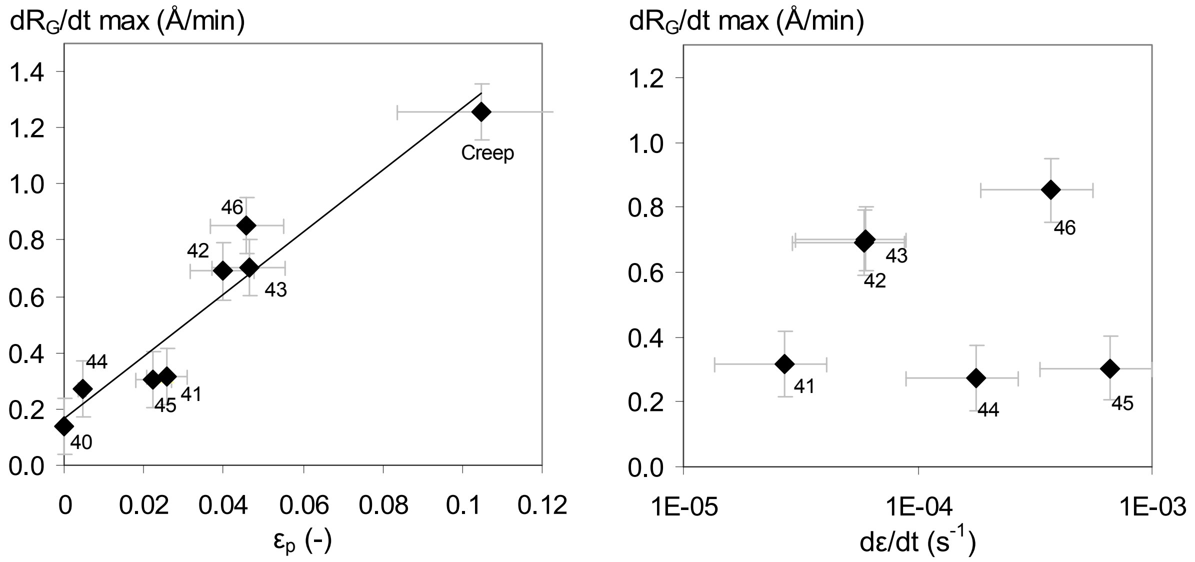

Fig. V.38. Maximum precipitate growth rate as a function of the TMT parameters in group #4

(a) Maximum precipitate growth rate as a function of the apparent plastic strain. (b) Maximum precipitate growth rate as a function of the strain rate.

As suspected, a clear dependence of the maximum precipitate growth rate on the plastic strain is demonstrated: the more deformed is the specimen, the higher is the precipitate growth rate. The effect of the strain rate is less evident, and requires a finer analysis.

Specimens #42 and #43 were deformed at the same strain rate, but the strain duration was longer for specimen #43, which means that it was subjected to a much higher plastic strain (1%). The consequences are that the peak is shifted on the time axis (see Fig. V.34), but the maximum growth rate is equal.

Samples #41 and #45, as well as samples #43 and #46 were deformed up to the same strain level (respectively: about 2.5% and 4.6%) but with different strain rates (about 10 times faster for the second group). Both the maximal level and the mean value of the growth rate are close.

From these results, it appears that in the investigated range (which is relatively narrow in terms of strain rate), dynamic coarsening of precipitates is mostly controlled by the level of strain, whereas the strain rate seems to have a second order influence.

---

[8] As the exact yield stress value is difficult to establish, the work hardening rate has been calculated considering a yield stress varying from 300 MPa to 380 MPa. This induces $\theta_0 \in [3500;8000]$

V.C.3.d. Effect of the initial temper

Similar experiments have been performed on the different tempers presented in Fig. V.27.

i. Precipitation kinetics during straining of temper #5

The over-aged temper #5 has been aged 10 hours at 160°C before being deformed in situ on the TSAXS device. The results of these experiments are shown in Fig. V.39.

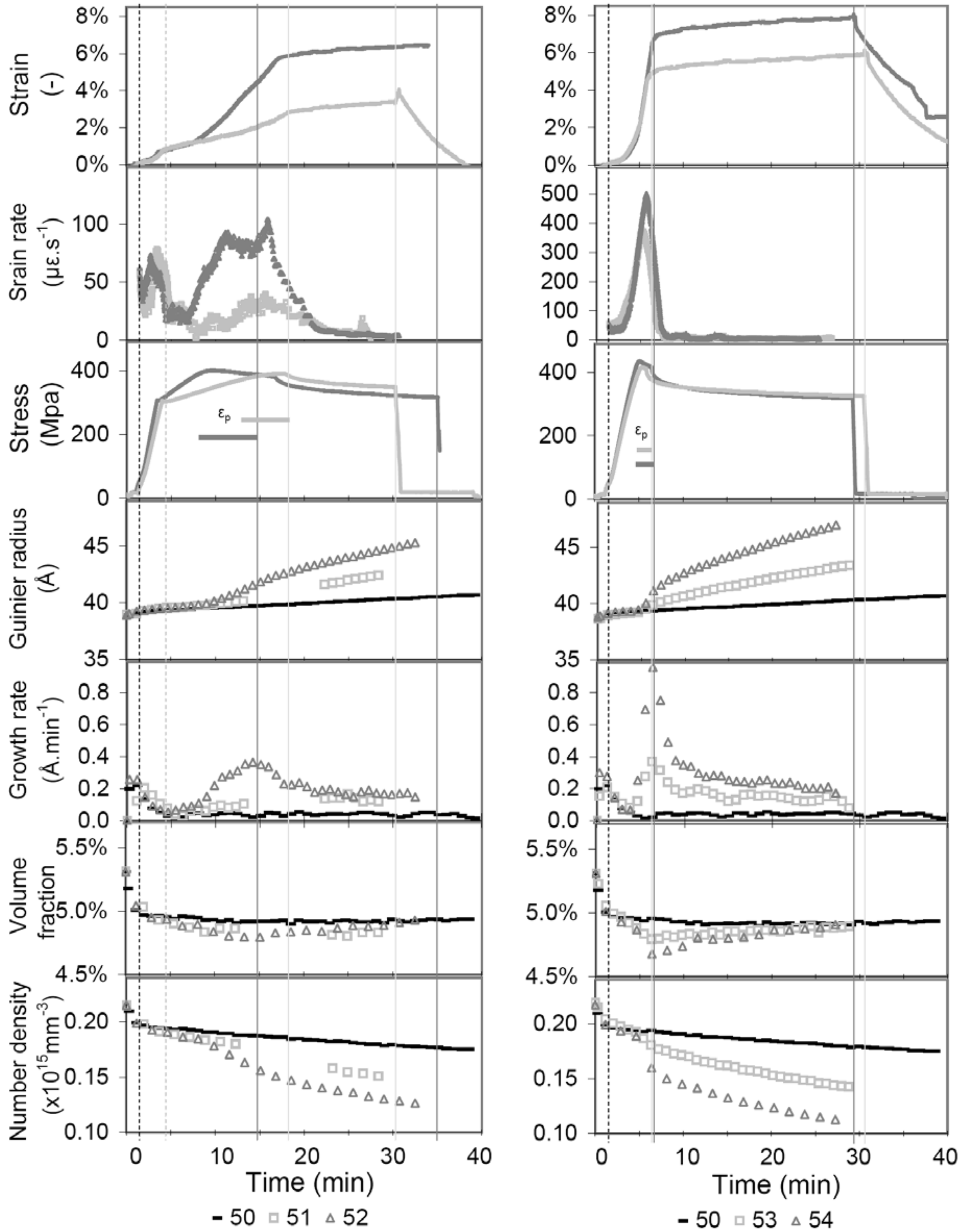

Fig. V.39. Effect of straining on precipitation kinetics- temper #5

Specimen #50 is stress-free aged.

ii. Analysis of precipitation kinetics in temper #5

Results similar to the ones presented in V.C.3.c for temper #4 are observed in Fig. V.39. The precipitate volume fraction is slightly lower during some time in the strained specimens, after which it recovers and meets the volume fraction of the stress-free specimen. The most striking effect is found on the precipitate radius evolution: straining accelerates precipitation kinetics once the apparent yield stress is overcome. Moreover, the maximal precipitate growth rate occurs at the end of the straining stage (see the fifth figure) as soon as relaxation begins, the precipitate growth rate drops. It decreases progressively and finally stabilises at a constant rate, higher than the stress-free aged specimen.

As already observed, it seems that a higher strain tends to promote a higher precipitate growth rate. To check this point in a more objective approach, the influence of the process parameters - namely the apparent plastic strain and the strain rate - on precipitation kinetics will be investigated in Fig. V.40.

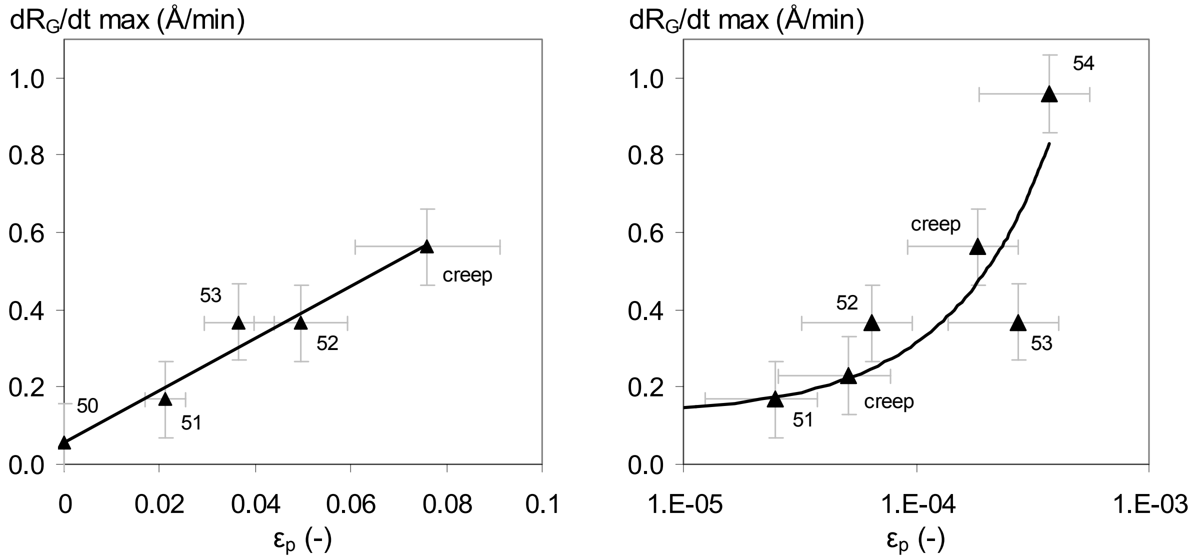

Fig. V.40. Maximum precipitate growth rate as a function of the TMT parameters in group #5

(a) Maximum precipitate growth rate as a function of the apparent plastic strain. (b) Maximum precipitate growth rate as a function of the strain rate.

There is a good correlation between the maximum precipitate growth rate and the plastic strain (Fig. V.40.a). The maximum precipitate growth rate seems to be also dependent on the with the strain rate, according to Fig. V.40.b. However, the fact that the higher strain rate experiments also correspond to the higher strain experiments (see labels on both figures) does not allow discriminating between both effects.

iii. Quantitative study: influence of the initial temper on the precipitate growth rate

Similar experiments have been performed on tempers #1, #2 and #3. Unfortunately, due to some experimental issues (not adequate camera/specimen distance) for the naturally aged temper (#1), the results are not exploitable. Before investigating the effect of strain, one will first analyse the evolution of precipitation kinetics in the different stress-free aged specimens.

Fig. V.41 compares the Guinier radii evolutions of the different stress-free aged specimens #20, #30, #40 and #50. The initial radius size grows logically with the temper, but it is interesting to notice that the growth rate of the tempers #2 and #4 (triangles) are higher than the growth rates of tempers #3 and #5 (squares). These last two tempers have been aged a few hours at the TMT temperature (respectively 6 hours at 120°C and 10 hours at 160°C), and are therefore close to the equilibrium volume fraction. Contrarily, tempers #2 and #4 were aged only up to the end of a heating ramps (respectively up to 120°C and up to 160°C), which means that they are far from the equilibrium volume fraction, and that the solute supersaturation is higher: the solute supersaturation effect dominates the temperature effect on precipitation kinetics.

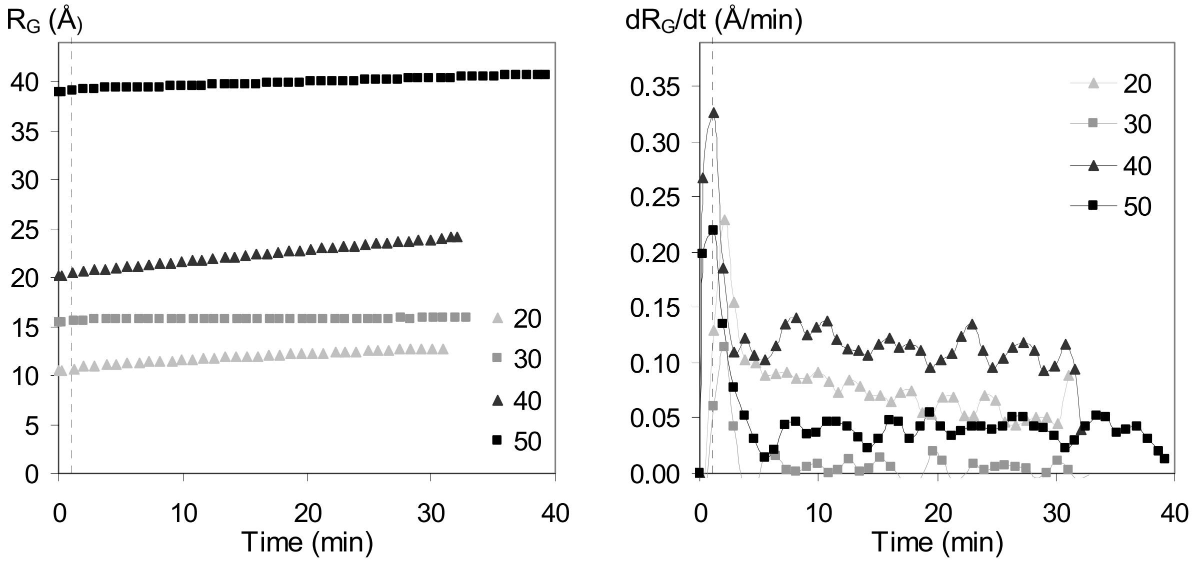

Fig. V.41. Evolution of the precipitates during stress-free aging: effect of initial temper

(a) Guinier radius evolution. (b) Precipitate growth rate. Specimens #20 and #30 aged at 120°C; specimens #40 and #50 aged at 160°C

iv. Quantitative study: influence of the initial temper and strain on the precipitate growth rate

One will now consider the influence of straining on the precipitate growth rate, for each of the initial tempers. The maximum precipitate growth rate (reached at the end of straining), and the final precipitate growth rate (reached at the end of the relaxation stage), seem to be accurate parameters to describe this effect. The influence of strain on these two parameters is shown in Fig. V.42.

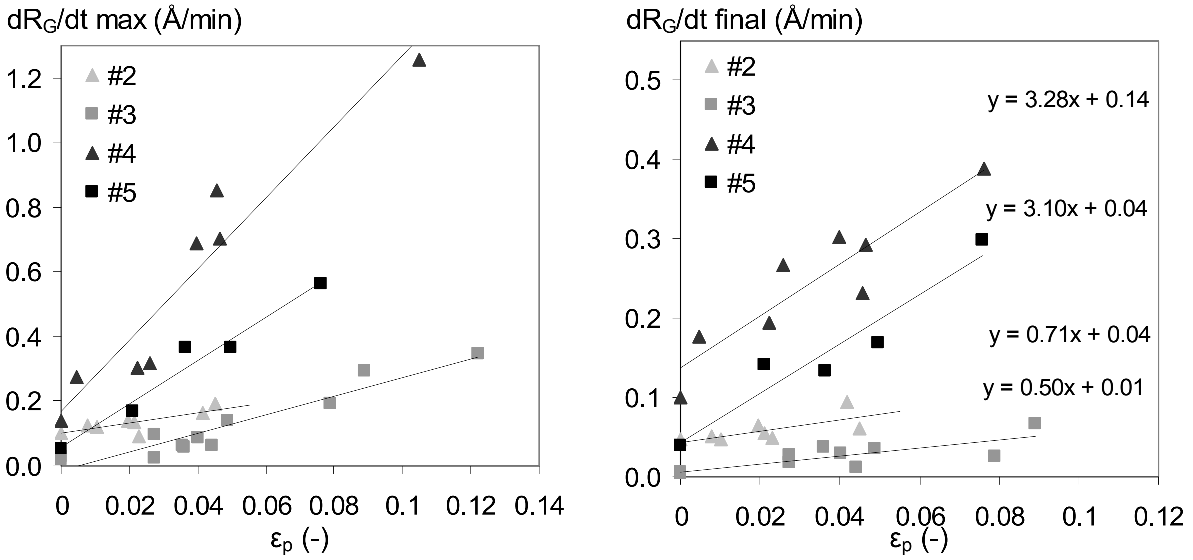

Fig. V.42. Influence of strain on the precipitate growth rate for different initial tempers

(a) Maximum precipitate growth rate as a function of the apparent plastic strain. (b) Final precipitate growth rate as a function of the apparent plastic strain. Specimen groups #2 and #3 aged at 120°C; specimen groups #4 and #5 aged at 160°C

The following statements can be made:

- For each of the different tempers, the higher is the strain, the higher is the precipitate growth rate.
- The tempers aged at 160°C (black) exhibit a higher sensitivity of the precipitate growth rate to strain that the tempers aged at 120°C (grey).
- Moreover, the tempers aged at the same temperature do present the same sensitivity of the final growth rate parameter to plastic strain (Fig. V.42.b).

The first point has been already discussed and can be justified by the increasing dislocation density, favouring enhanced diffusion via dislocation cores (pipe diffusion).

The second and third points are more striking. In Fig. V.41, it has been shown the solute supersaturation effect dominates the temperature effect on precipitation kinetics; in other words, the precipitates grow more rapidly in the tempers with the highest solute content, namely tempers #2 and #4, (represented by triangles), as compared to the tempers aged at higher temperature. Fig. V.42 shows that straining does affect very significantly the precipitate growth rate, so that this order is modified. The sensitivity of the precipitate growth rate to strain is larger at higher temperature, and this effect widely dominates the solute supersaturation effect. This may be striking, because for a given strain, the higher is the temperature, the lower is the dislocation density. However, the difference between the two temperatures may be not large enough to modify significantly the recovery process.

V.C.3.e. Conclusion on strain aging

We have shown a clear influence of deformation on precipitation the precipitate growth rate and the volume fraction, demonstrating a probable thermodynamic effect and an evident kinetic effect. It has been in particular established that the precipitate growth rate, rises all along the plastic strain stage.

Strain is the major parameter governing the kinetics of precipitation. However, dynamic precipitation processes, which are related to the density of moving dislocations, are also operating during the stage of constant strain rate in the plastic regime, and their influence is also apparent in the behaviour during the relaxation step. The global picture which emerges is that total dislocation density affects precipitation: coarsening is permanently accelerated by the presence of dislocations during the relaxation stage (thus the influence of the strain), but the transport of solute seems to depend also on dislocation velocity (thus the influence of strain rate).

The major macroscopic consequence of this microstructural evolution enhanced by deformation, from a mechanical viewpoint, is a very large apparent strain hardening rate, much larger than the one observed at room temperature.

All the different initial tempers investigated behave similarly under straining. However, the sensitivity of precipitation kinetics to straining is highly dependent on the temper. It is possible to predict (to some extent) the evolution of precipitation kinetics during straining, using the results presented in Fig. V.42.b, which may be of interest to optimize industrial age-forming treatments.

V.D. Discussion and modelling

V.D.1. Mechanisms affecting precipitation during TMT

This point has been developed along the analysis of the creep and strain aging experiments. It has been established that straining and/or stressing the material during aging influences precipitation. There is probably a thermodynamic effect of these TMTs, the precipitate volume fraction being generally lower in the stressed than in the stress-free aged specimens. However this remains difficult to comprehend, due to experimental issues. The most spectacular effect is an increase of the precipitate growth rate during straining and/or stressing.

The question of the dynamic nature of this kinetic effect remains difficult to answer. It seems that the kinetic effects measured during the creep tests performed on temper T7651 are mainly related to static effects. The straining tests, on the contrary, tend to show that dynamic effects are also present.

Our conclusions are that both the dislocation density and the dislocation motion seem to affect precipitation kinetics during TMT. Static effects seem to be dominant when the strain rate is low (creep tests) and dynamic effects seem to play a role during faster TMTs (higher strain rate tests).

V.D.2. Modelling precipitation kinetics during TMT

V.D.2.a. Precipitation model

The class model presented in chapter IV will be used to predict the effect of a thermomechanical treatment on precipitation kinetics. However, the existing model simply considers the effect of heat treatment; and requires therefore some modifications, to account for the TMT parameters.

As the thermodynamic effect of straining on precipitation has not been clearly evidenced, one will only focus on the description of the kinetic effect. Thus, the simplest approach is to replace the standard (temperature dependent) diffusion parameter $D(T)$ by an effective diffusion coefficient D^*, characteristic of the effect of the thermomechanical process parameters on precipitation.

It is assumed that the enhanced kinetics is due to both a static and a dynamic effect. For the sake of simplicity, it has been decided to relate the plastic strain to the static effect, and the strain rate to the dynamic effect. Since for low strain the dislocation density is linear with strain, it is reasonable to assume that the pipe diffusion contribution should be linear with strain. Since the “ballistic transport” should be proportional to both the moving dislocation density and to their velocity, it is reasonable to assume that the ballistic effect is proportional to the strain rate. Therefore a reasonable phenomenological expression for the effective diffusion coefficient will be in the form: $D^* = D(T, \varepsilon, \dot{\varepsilon})$, so that:

$$\text{(II.2.)} \quad D^* = D(T, \varepsilon, \dot{\varepsilon}) = D_0 \, exp\left(\frac{-Q}{RT}\right)\left(1 + D_1\varepsilon + D_2\dot{\varepsilon}\right)$$

In which D_1 and D_2 are respectively the contributions of strain and strain rate to atomic diffusion.

V.D.2.b. Model calibration

The SAXS results of specimen #40 (see in Fig. V.31), a stress-free aged specimen, will be used to calibrate the model. The experimental and modelled results are compared in Fig. V.43.

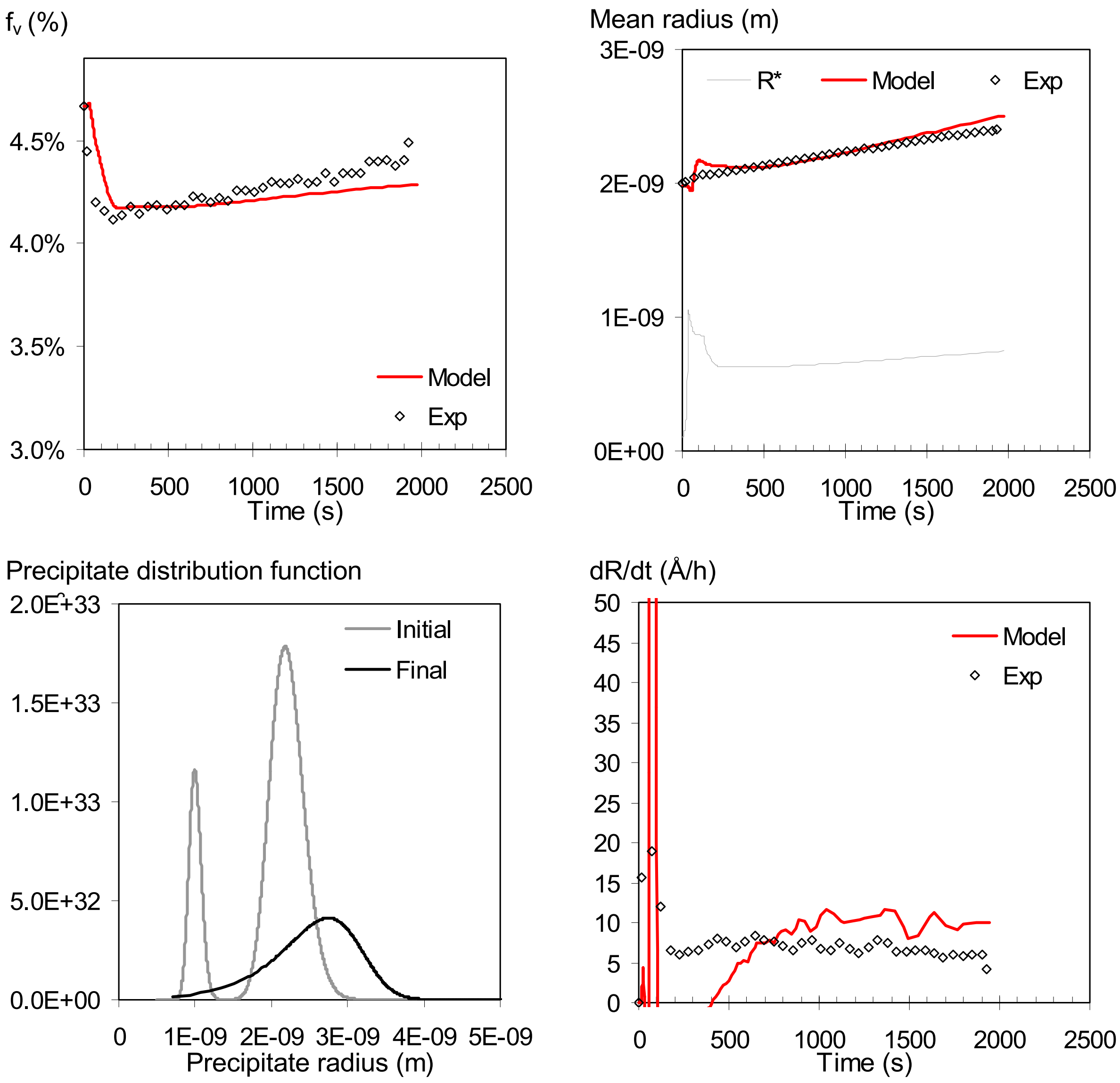

Fig. V.43. Precipitation model calibration on specimen #40

(a) Modelled vs. experimental volume fraction evolution. (b) Experimental Guinier radius vs. modelled mean radius. (c) Initial vs. final precipitate size distribution. (d) Experimental vs. modelled precipitate growth rate.

A small volume fraction (~0.1%) of small particles has been included in the initial particle size distribution, to account for the GP zones which have nucleated during the intermediate storage stage. This slightly improved the results, even if the dissolution stage is not fully described by the model. To have an even better agreement, one could introduce different thermodynamic and structural properties to this second population; this point has been already discussed in chapter IV.

However, our objective is mainly to model the evolution of the precipitate growth rate during the isothermal treatment. In that case, the agreement between the model and the experiment is very satisfactory for this given objective.

V.D.2.c. Model parameters

The model parameter values determined in chapter IV for the T7651 temper are reported in column three of Table V.3, to be compared to the values of temper #4 (column four).

The free enthalpy value has been slightly decreased, as compared to T7651 temper. This can be justified by the fact that less stable precipitates are present in the initial #4 temper, as it mainly consists in fine η' precipitates (see chapter III).

The activation energy for diffusion is slightly higher than for temper T7651. Two reasons can explain this (see discussion in IV.D.3.c.iv): on the one hand, the initial solute content is higher; on the other hand, fewer dislocations are present, as the material has not been subjected to pre-stretching.

Parameter	Significance	T7651 values	Temper #4 values	Unit
D_{0Mg}	Diffusion coefficient	1.3 10^{-8}	-	$m^2.s^{-1}$
Q_{Mg}	Activation energy for diffusion	85.3	88.5	$KJ.mol^{-1}$
D_{0Zn}	Diffusion coefficient	1.3 10^{-7}	-	$m^2.s^{-1}$
Q_{Zn}	Activation energy for diffusion	85.3	88.5	$KJ.mol^{-1}$
γ_i	Precipitate surface energy	0.5	-	$J.m^{-2}$
α_h	Heterogeneous nucleation coefficient	0.3	-	-
ΔS_0	Free enthalpy	59.8	53.2	$KJ.mol^{-1}.K^{-1}$
ΔH_0	Entropy variation	15.8	-	$J.mol^{-1}$

Table V.3. Precipitation model parameters for tempers T7651 and #4

In the central column are reported the values determined in chapter IV for the temper T7651. The parameters that have been modified to fit the temper #4 results (Fig. V.43) are reported in column four.

V.D.2.d. Results: modelling of precipitation kinetics during straining

The initial precipitate size distribution presented in Fig. V.43.c and the model parameters reported in Table V.3 will be input in the model, as well as the thermomechanical treatment corresponding to the experimental treatment presented in Fig. V.34. It includes a thermal, a strain and a strain rate profile.

The strain and strain rate diffusion parameters (respectively D_1 and D_2; see equation (II.2.)) will be fitted on the experimental (SAXS) data presented on the same figure. Fig. V.44 presents the thermomechanical treatment corresponding to specimen #45 test (a) and the effect of the TMT on the effective diffusion coefficients (b). The result on precipitation kinetics is shown in Fig. V.45, where both the modelled and the experimental radius evolution are plot.

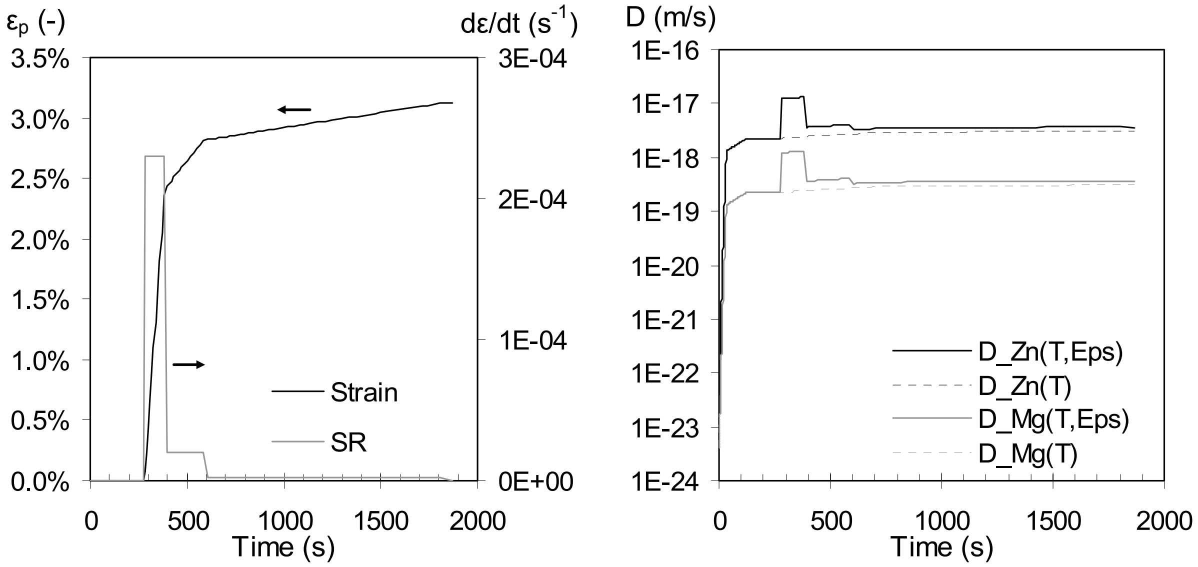

Fig. V.44. Modelling of precipitation kinetics of specimen #45: TMT parameters

(a) Thermomechanical treatment. (b) Effect of the TMT on the effective diffusion coefficients.

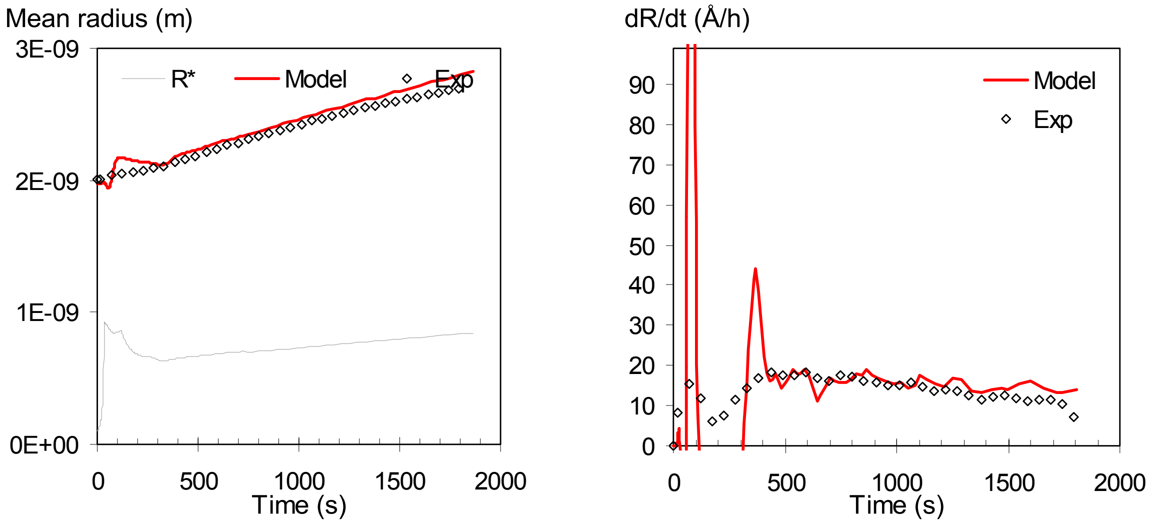

Fig. V.45. Modelling of precipitation kinetics of specimen #45: results

(a) Guinier radius and modelled mean radius evolution. (b) Precipitate growth rate evolution.

In that case, the following parameter set has been fitted: $D_1 = 5$ and $D_2 = 1.9\times 10^4\ s$. To validate this modelling approach, a second calculation is performed to simulate TMT #43 (Fig. V.46).

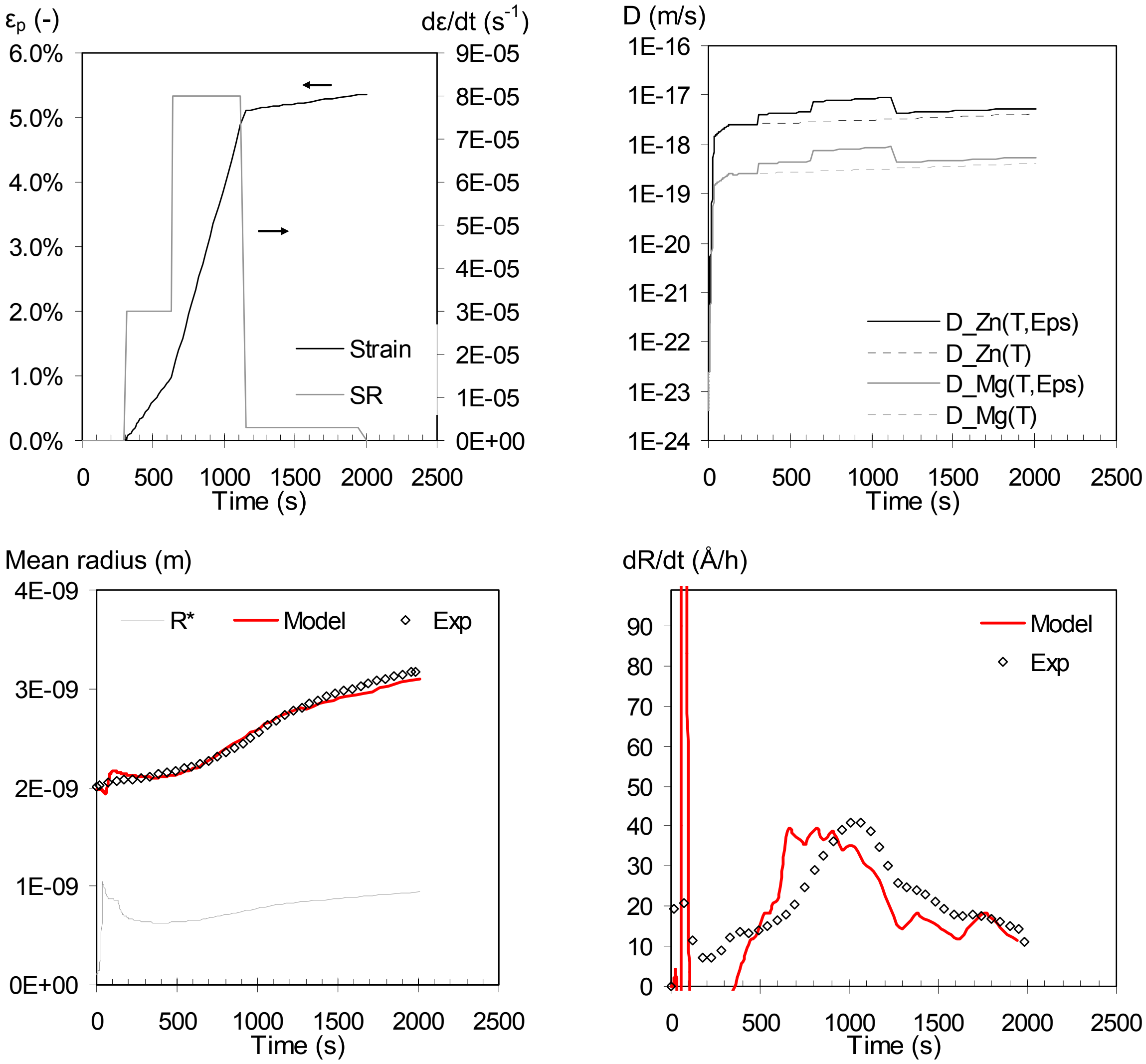

Fig. V.46. Modelling of precipitation kinetics of specimen #43

(a) Thermomechanical treatment. (b) Effect of the TMT on the effective diffusion coefficients. (c) Guinier radius and modelled mean radius. (d) Precipitate growth rate.

V.D.2.e. Discussion

The agreement of the model to the experimental data is very satisfactory: both the kinetics and the range of the straining effect of on the precipitate growth rate are well described.

This validates the very simple approach used to model the effect of straining on precipitation kinetics. Using stress instead of strain would have been a more physical approach, as stress could be related to the dislocation density, which is probably the determining parameter. However, the fact that both the temperature and the precipitation state evolve continuously during the experiment, would make the calculation of the dislocation density very delicate, and the small strain under consideration allow the present approximation.

V.D.3. Conclusion

The TSAXS device developed during this PhD has proven its ability to simulate accurately thermomechanical treatments, while measuring in situ the evolution of precipitation kinetics. It therefore allows a very fine analysis of the effects of the TMT parameters on precipitation.

The couplings between straining (or stressing) and precipitation has been evidenced and quantified. Both treatments tend to increase the kinetics of precipitation, in the considered tempers. It appears that the precipitate growth rate presents a positive sensitivity to stress, strain and strain rate.

This result is of interest for industrial applications: thermomechanical treatments inducing a gradient either in the stress, the strain or the strain rate, will lead to heterogeneous precipitation microstructure, and therefore to heterogeneous properties.

Empirical relations have been found between the process parameters (initial temper and strain) and the evolution of the precipitates mean size. This allows predicting the evolution of the precipitate growth rate during a given TMT, which could be of interest to optimize industrial practices.

Moreover this effect has been modelled, by integrating a very simple modelling approach to account for the TMT parameters, to the class model presented in chapter IV.

On a more fundamental view point, our conclusion is that this accelerated precipitation kinetics is probably mainly due to a static effect, related to the presence of dislocations. However, a contribution of the dislocation motion (dynamic effect) is also probably present, in particular if the strain rate is high enough.

Chapter VI. Conclusions and perspectives

Summary

This chapter summarises the main results obtained throughout this PhD: respectively the effect of precipitation on strain hardening properties (Chapter III); the impact of laser forming on the precipitate microstructure and mechanical performance (Chapter IV) and the effect of thermomechanical treatments on precipitation (Chapter V). It also develops the perspectives opened by this work, on both the scientific and the applicative points of view.

VI.A. Conclusion

The study of the couplings between precipitation and plasticity during thermomechanical treatments for part distortion correction has been achieved, based on three main components: instrumental development, material characterization, and modelling. Instrumental development was required to answer complex industrial issues. Material characterization, which included mechanical tests and microstructural characterization (mainly SAXS (Small-Angle X-Ray Scattering)) was used to evaluate the microstructural mechanisms and to feed the models. Physically-based models have been developed to predict the effect of the thermomechanical treatments on the material properties.

VI.A.1. Strain hardening model for shot peening

The effect of the precipitation microstructure on the strain hardening behaviour has been evidenced experimentally. From this, a physically-based strain hardening model has been proposed to model the mechanical behaviour of particle-strengthened over-aged materials. This model unifies Simar's model for isotropic hardening [Simar 2006] and Proudhon's model [Proudhon 2008] for kinematic hardening. It modifies the initial Kocks, Mecking and Estrin approach and includes two internal variables, respectively the forest dislocations and the Orowan loops. It correctly describes the experimental tensile curves of a wide range of metallurgical tempers, even if some discrepancies still remain. It also provides a framework for the analysis of the Bauschinger effect.

This model can be implemented into a finite elements code, to model complex strain paths and strain rate dependant experiments, such as shot peening.

VI.A.2. Effect of laser forming on microstructure and properties

The relations between the laser forming treatment, its effect on the microstructure and the final material properties have been established, both by experimental means (SAXS and hardness) and by modelling. The effect of the laser treatment is to dissolve the precipitates in the very subsurface, which is detrimental to the local mechanical properties. However, a simple natural aging treatment, easy to perform industrially, allows recovering the major part of the initial properties.

The developed size-class precipitation model is able to simulate the effect of both isothermal and non isothermal heat treatments on precipitation. Simulating the effect of laser forming on precipitation has required a large number of modelling steps: finite element modelling of the temperature profiles generated by the laser treatment, experimental characterization of precipitation, precipitation model calibration, before the final modelling. Despite this complex modelling route, source of errors, the final result fits very well to the experimental measurements performed on laser processed specimens.

VI.A.3. Effect of TMTs on precipitation

The micro tensile and heating device for in situ SAXS experiments (TSAXS) developed during this PhD has appeared to be a very powerful tool to simulate a wide variety of thermomechanical treatments (TMTs), while measuring quantitatively their effect on precipitation.

Straining or stressing the material during aging, as it is the case during age-forming, enhances precipitation kinetics: the most noticeable effect is an increase of the precipitate growth rate. There are both a static and a dynamic influence of dislocations on precipitation, even if it remains difficult to fully understand their respective weight. This effect has been implemented in the size-class precipitation model, by including a strain and strain rate dependant term in the diffusion coefficient. This simple model describes very well the experimental data.

VI.B. Perspectives

Each of the three experimental chapters opens the way to further investigations, targeted on scientific issues, or to possible exploitation, for engineering purposes.

VI.B.1. Strain hardening model

The research carried out for the establishment of a strain hardening constitutive law showed that some points remain unclear, such as the origin of the transients observed in both the Bauschinger and the tensile curves of over-aged tempers. A phenomenological, but not quantitative model has been proposed. A future work would be to evaluate the reality of this mechanism, and eventually to quantify and model it, which could be achieved throughout discrete dislocations dynamics.

On the more applicative point of view, the new strain hardening model which has been developed can be implemented into finite element analysis, where its ability to describe both isotropic and kinematic hardening can be of interest, in particular to simulate strain path changes. A good validation of this model would be to use it in double bending tests (i.e. bending in one direction and reversely).

VI.B.2. Precipitation model

The results obtained on the effect of laser forming on precipitation is satisfactory, but could be improved. On the first hand, the modelled thermal profiles have been validated by an inverse methodology, which is probably not perfectly precise. A more accurate validation would be to perform direct temperature measurements during the laser treatment. On the second hand, if the physics of the precipitation model is well established, the effect of the numerical model parameters has not been fully investigated, and can probably be optimized. Finally, the model simplifies the microstructure; an improved version would account for two or three precipitates types and their composition evolution, including copper.

In one looks towards possible applications, this model can be used in other cases where non-isothermal treatments are involved, such as welding treatments. In the case of laser forming, this model can be coupled to a temperature and microstructure-dependent constitutive law, to estimate the material's flow due to the laser treatment (whether applied for part distortion correction or for internal stress reduction). However, obtaining a physically-based constitutive law capable of such a description still requires a large amount of work.

VI.B.3. Effect of TMTs on precipitation

It has been clearly evidenced that straining and/or stressing the material does enhance precipitation kinetics. However, one point still remains unclear: in what respect is this effect due to pipe diffusion (i.e. related to the dislocation density, which varies during the TMT), to solute collecting due to the dislocation motion, and to dynamic precipitation (i.e. formation of new precipitates linked to the motion of dislocations). The balance of these three phenomena depends necessarily on the initial state of the material (supersaturation of solute), on temperature and strain rate. To discriminate between static and dynamic effects, one could imagine performing more complex tests, such as tensile tests at increasing (stepped) strain rates, at decreasing strain rates…

The effect of straining on precipitation kinetics has been implemented in the precipitation model by including a strain and strain rate dependant term in the diffusion coefficient. However, if this simple model is enough to model growth or coarsening, it is not to model thermodynamic effects and nucleation. In that case, a more comprehensive model has to be developed, based on dislocation density variations for instance.

The TSAXS device opens a wide range of new possibilities, to quantify the effect of TMTs on precipitation. It may be used for instance to simulate the effective impact of industrial age-forming treatments on precipitation. Another field of investigation would be to characterize the mechanical constitutive law during quenching, while the evolution of precipitation could be measured in situ.

VI.B.4. A more global overview

The different industrial processes (shot peening, laser forming and strain and creep-age forming) have been respectively considered as a pure mechanical treatment, a pure thermal treatment and true thermomechanical treatments.

This simplified view has been chosen to simplify the analysis of the complex microstructural mechanisms operating during these treatments. However, shot peening also induces heat transfers, which may affect precipitation, and laser forming also leads to dislocation restoration.

To be closer from the physical interactions operating during these treatments, a further step would be to reconsider all these industrial processes as true thermomechanical treatments, and to consider, in all these cases, a real coupling between plasticity, precipitation and temperature.

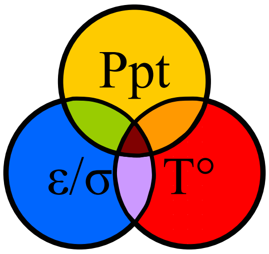

VI.C. Bibliography

[Acevedo 2007] D. Acevedo-Reyes, PhD thesis, Institut National des Sciences Appliquées de Lyon (2007)

[Alekseev 2002] A.A. Alekseev, I.N. Fridlyander, L.B. Ber, Mat. Sci. For. 396-402 (2002), 821-826

[Arsenlis 1999]. A. Arsenlis, D.M. Parks, Acta Mat. 47 (1999), 1597-1611

[Ashby 1970] M.F. Ashby, Phil. Mag. 21 (1970), 399-424.

[Augereau 2007] F. Augereau, D. Laux, L. Allais, M. Mottot, C. Caes, Ultrasonics 46 (2007), 34-41

[Bakavos 2006a] D. Bakavos, P.B. Prangnell, B. Bes, F. Eberl, J.G. Grossmann, Mat. Sci. For. 519-521 (2006), 333-338

[Bakavos 2006b] D. Bakavos, P.B. Prangnell, B. Bes, F. Eberl, S. Gardiner, Mat. Sci. For. 519-521 (2006), 407-412

[Benett] www.bennettmg.co.uk

[Benzerga 2004] A.A. Benzerga, Y. Bréchet, A. Needleman, E. Van der Giessen, Modelling Simul. Mater. Sci. Eng. 12 (2004), 159-196

[Ber 2000] L.B. Ber, Mat. Sci. Eng. A280 (2000), 91-96

[Berg 2001] L.K. Berg, J. Gjonnes, V. Hansen, X.Z. Li, M. Knutson-Wedel, G. Waterloo, D. Schryvers, L.R. Wallenberg, Acta Mat. 49 (2001), 3443-3451

[Boger 2006] R.K. Boger, PhD thesis, Ohio State University (2006)

[Bouabdallah 2006] K. Bouabdallah, PhD thesis, Université Ferhat Abbas, Setif Ufas, Algeria, 2006

[Bréchet 1989] Y. Bréchet, F. Louchet, Acta Met. 37, 9 (1989) 2469-2473

[Bréchet 1995] Y. Bréchet, Y. Estrin, Acta Mat. et Met. 43, 3 (1995), 955-963

[Bréchet 1996] Y. Bréchet, Y. Estrin, Scripta Mat. 35, 2 (1996), 217-223

[Brenner 1991] S.S. Brenner, J. Kowalik, H. Ming-Jian, Surface Science 246 (1991), 210-217

[Brinksmeier 2007] E. Brinksmeier, J. Sölter, C. Grote, CIRP Annals - Manufacturing Technology 56, 1 (2007), 109-112

[Brown 1955] A.F. Brown, Phil. Mag. Suppl. I, 4 (1955), 427-493

[Cai 2009] Z.Y. Cai, S.H. Wang, X.D. Xu, M.Z. Li, Journ. of Mat. Proc. Tech. 209 (2009), 396-407

[Calvet 1938] J. Calvet, P. Jacquet, A. Guinier, Comptes rendus Académie des Sciences 206 (1938), 1972-1974

[Cavaliere 2002] P. Cavaliere, Journal of Light Metals 2 (2002), 247-252

[Charles 1984] J.A. Crane, F.A.A. Crane, “Selection and Use of Engineering Materials”, ed. Butterworths (1984)

[Chenal 1999] B. Chenal, J. Driver, Techniques de l’ingénieur M230 (1999)

[Chinh 2004] N.Q. Chinh, J. Lendvai, D.H. Ping, K. Hono, Journal of Alloys and Compounds 378 (2004), 52-60

[Cina 1992] B. Cina, F. Zeidess, Mat. Sci. For. 102-104 (1992), 99-108

[Clouet 2004] E. Clouet, PhD thesis, Ecole Centrale Paris (2004)

[COMPACT 2004] COMPACT, Sixth framework Programme, Aeronautics and Space, AERO-2003-1.1.1.3b, annex 1: description of work (2004)

[Compact 2007] Compact internal document.

[Curtis 2003] S. Curtis, E.R. De Los Rios, C.A. Rodopoulos, A. Levers, International Journal of Fatigue 25 (2003), 59-66

[Dai 2007] X.Y. Dai, C.Q. Xia, A.R. W, X.M Peng, Mat. Sci. For. 546-549 (2007), 961-964

[Dearden 2006] G. Dearden, S.P. Edwardson, E. Abed, K. Bartkowiak, K.G. Watkins, Laser Institute of America, 599, 99 (2006), Paper 505

[Delmas 2003] F. Delmas, M. Vivas, P. Lours, M.J. Casanove, A. Couret, A. Coujou, Mat. Sci. Eng. A340 (2003), 286-291

[Denkena 2008] B. Denkena, L. De Leon, M. Otte, Proceedings IDE2008 (2008)

[Déprés 2004] C. Déprés, PhD thesis, Institut Polytechnique de Grenoble (2004)

[Deschamps 1996] A. Deschamps, Y. Bréchet, C.J. Necker, S. Saimoto, J.D. Embury, Mat. Sci. Eng. A207 (1996), 143-152

[Deschamps 1997] A. Deschamps, PhD thesis, Institut Polytechnique de Grenoble (1997)

[Deschamps 1998] A. Deschamps, Y. Bréchet, Mat. Sci. Eng. A251 (1998), 200-207

[Deschamps 1998b] A. Deschamps, Y. Bréchet, Scripta Materialia 39, 11 (1998), 1517-1522

[Deschamps 1999a] A. Deschamps, Y. Bréchet, F. Livet, Mat. Sci. Tech. 15, 9 (1999), 993-1000

[Deschamps 1999b] A. Deschamps, Y. Bréchet, Acta Mat.47, 1 (1999), 293-305

[Deschamps 1999c] A. Deschamps, M. Niewczas, F. Bley, Y. Bréchet, J.D. Embury, L. LeSinq, F. Livet, J.P. Simon, Phil. Mag A79, 10 (1999), 2485-2504

[Deschamps 2001] A. Deschamps, D. Dumont, Y. Bréchet, C. Sigli, B. Dubost, Proceedings of the James T. Staley honorary Symposium on Aluminum Alloys, Nov. 2001, ed. M. Tiryakioglu, ASM International (2001), 298-305

[Deschamps 2003a] A. Deschamps, HDR thesis, Institut Polytechnique de Grenoble (2003)

[Deschamps 2003b] A. Deschamps, F. Bley, F. Livet, D. Fabregue, L. David, Phil. Mag 83, 6 (2003), 677-692

[Deschamps 2008] A. Deschamps, G. Texier, S. Ringeval, L. Delfaut-Durut, Mat. Sci. Eng. A, accepted manuscript (2008)

[Develay 1986] R. Develay, Techniques de l'ingénieur M1290, M1291. (1986)

[Djapic 2000] L. Djapic Oosterkamp, A. Ivankovic, G. Venizelos, Mat. Sci. Eng. A278 (2000), 225-235

[Dolan 2004] G.P. Dolan, J.S. Robinson, Journ. of Mat. Proc. Tech.153-154 (2004), 346-351

[Dörr 1999] T. Dörr, M. Hilpert, P. Beckmerhagen, A. Kiefer, L. Wagner, Proceedings ICSP7 (1999), 153-160

[Dubost 1991] B. Dubost, P. Sainfort, Techniques de l'ingénieur M240 (1985)

[Dumont 2003] D. Dumont, A. Deschamps, Y. Bréchet, Mat. Sci. Eng. A356 (2003), 326-336

[Dumont 2004] D. Dumont, A. Deschamps, Y. Bréchet, Acta Mat. 52 (2004), 2529-2540

[Dumont 2005] M. Dumont, W. Lefebvre, B. Doisneau-Cottignies, A. Deschamps, Acta Mat. 53 (2005), 2881-2892

[Dumont 2006] M. Dumont, A. Steuwer, A. Deschamps, M. Peel, P.J. Withers, Acta Mat. 54 (2006), 4793-4801

[Embury 1965] J.D. Embury, R.B. Nicholson, Acta Mat. 13, 4 (1965), 403-417

[Embury 1989] J.D. Embury, D.J. Lloyd, T.R. Ramachandran, Treatise on Mat. Sci. Tech. 31 (1989), 579-601

[Embury 2003] J.D. Embury, A. Deschamps, Y. Bréchet, Scripta Mat 49 (2003), 927-932

[Embury 2006] J.D. Embury, W.J. Poole, D.J. Lloyd, Mat. Sci. For. 519-521 (2006), 71-78

[Estrin 1984] Y. Estrin, H. Mecking, Acta Met. 32, 1 (1984), 57-70

[Estrin 1989] Y. Estrin, L.P. Kubin, J. Mech. Behaviour Mat. 2 (1989), 255

[Estrin 1996] Y. Estrin, in Unified Constitutive Laws of Plastic Deformation, ISBN 0124259707, Ed. Academic Press, A.S. Krausz, K. Krausz: Dislocation Density Related Constitutive Modeling (1996), 69-106

[Estrin 1998] Y. Estrin, Journ. of Mat. Proc. Tech. 80-81 (1998), 33-39

[Estrin 1999] Y. Estrin, S. Arndt, M. Heilmaier, Y. Bréchet, Acta Mat. 47, 2 (1999), 595-606

[Evers 2002] L.P. Evers, D.M. Parks, W.A.M. Brekelmans, M.G.D. Geers, Journal of the Mechanics and Physics of Solids 50 (2002), 2403-2424

[Fleck 2003] N.A. Fleck, M.F. Ashby, J.W. Hutchinson, Scripta Mat. 48 (2003), 179-183

[Forty 1954] A.J. Forty, Advances in Physics, Phil. Mag. 3, 9 (1954), 1-25

[Fratzl 2003] P. Fratzl, J. Appl. Cryst. 36 (2003), 397-404

[Friedel 1964] J. Friedel, Dislocations, ed. Pergamon Press, Oxford (1964)

[Frost 1982] H.J. Frost, M.F. Ashby, Deformation-Mechanism Maps, The Plasticity and Creep of Metals and Ceramics, Pergamon Press (1982)

[Gao 1999] H. Gao, Y. Huang W.D. Nix, J.W. Hutchinson, Journal of the Mechanics and Physics of Solids 36 (1999), 1239-1263

[Gao 2003] H. Gao, Y. Huang, Scripta Mat. 48 (2003), 113-118

[Gao 2007] N. Gao, M. J. Starink, N. Kamp, I. Sinclair, J. Mat. Sci. 42 (2007), 4398-4405

[Genevois 2006] C. Genevois, D. Fabrègue, A. Deschamps, W.J. Poole, Mat. Sci. Eng. A441 (2006), 39-48

[Gerold 1978] V. Gerold, G. Kostorz, J. Appl. Cryst. 11 (1978), 376-404

[Goerdeler 2001] M. Goerdeler, G. Gottstein, Mat. Sci. Eng. A309-310 (2001), 377-381

[Gomiero 1992a] P. Gomiero, F. Livet, Y. Bréchet, F. Louchet, Acta Met. et Mat. 40, 4 (1992), 847-855

[Gomiero 1992b] P. Gomiero, Y. Bréchet, F. Louchet, A. Tourabi, B. Wack, Acta Met. et Mat. 40, 4 (1992), 863-871

[Gröbner 2007] J. Gröbner, L.L. Rokhlin, T.V. Dobatkina, R. Schmid-Fetzer, Journal of Alloys and Compounds 433 (2007), 108-113

[Guagliano 2001] M. Guagliano, Journ. of Mat. Proc. Tech 110 (2001), 277-286

[Guinier 1938a] A. Guinier, Comptes rendus Académie des Sciences 206 (1938), 1374-1376

[Guinier 1938b] A. Guinier, Comptes rendus Académie des Sciences 206 (1938), 1641-1643

[Hansen 2002]. V. Hansen, K. Stiller, G. Waterloo, G. Gjønnes, X.Z. Li, Mat. Sci. For. 396-402 (2002), 815-820

[Hansen 2006] V. Hansen , A. Vevecka-Priftaj, J. Fjerdingena, Y. Langsrud, J. Gjønnes, Mat. Sci. For. 519-521 (2006), 579-584

[Hénon 2006] C. Hénon, G. Pouget, T. Warner, Mat. Sci. For. 519-521 (2006), 693-698

[Hollomon 1945] J.H. Hollomon, Trans Metall. Soc. AIME 162 (1945) 268-290.

[Hörnqvist 2006] M. Hörnqvist, B. Karlsson, Mat. Sci. For. 519-521 (2006), 883-888

[Hu 2001] Z. Hu, M. Labudovic, H. Wang, R. Kovacevic, International Journal of Machine Tools & Manufacture 41 (2001), 589-607

[Hu 2006] B. Hu, I.M. Richardson, Mat. Sci. Eng. A429 (2006), 287-294

[Jannot 2006] E. Jannot, V. Mohles, G. Gottstein, B. Thijsse, Defect and Diffusion Forum 249 (2006), 47-54

[Jin 2000] Z. Jin, W.A. Cassada, C.M. Cady, G.T. Gray, Mat. Sci. For. 331-337 (2000), 527-532

[Johansson 2006] M. Johansson, M. Hörnqvist, B. Karlsson, Mat. Sci. For. 519-521 (2006), 841-845

[Jordon 2007] J.B. Jordon, M.F. Horstemeyer, K. Solanki, Y. Xue, Mech. of Mat. 39 (2007) 920-931

[Kamp 2002] N. Kamp, I. Sinclair, M.J. Starink, Met. and Mat. Trans. A33, 4 (2002), 1125-1136

[Koc 2006] M. Koc¸ J. Culp, T. Altan, Journ. of Mat. Proc. Tech. 174 (2006), 342-354

[Kocks 1975]	U.F. Kocks, A.S. Argon, M.F. Ashby, Prog. Mater. Sci. 19 (1975), 1-288
[Kocks 1976]	U.F. Kocks, Journ. of Eng. Mater. and Tech. 98 (1976), 76-85
[Kocks 2003]	U.F. Kocks, H. Mecking, Prog. Mater. Sci. 48 (2003), 171-273
[Kopp 2002]	R. Kopp, J. Schulz, CIRP annals - Manuf. Tech. 41, 1 (2002), 195-198
[Kozaczek 1999]	K.J. Kozaczek, P.R. Moran, D.S. Kurtz, R. Martin, Proceedings ICSP7 (1999), 313-320
[Kubin 2003]	L.P. Kubin, A. Mortensen, Scripta Mat. 48 (2003), 119-125
[Lagowa 2001]	B.W. Lagowa, I.M. Robertson, M. Jouiad, D.H. Lassila, T.C. Lee, H.K. Birnbaum, Mat. Sci. Eng. A309-310 (2001), 445-450
[Lebyodkin 1996]	M. Lebyodkin, Y. Bréchet, Y. Estrin, L. Kubin, Acta Mat.44, 1 (1996), 4531-4541
[Li 1999]	X.Z. Li, V. Hansen, J. Gjønnes, L.R. Wallenberg, Acta Mat. 47, 9 (1999), 2651-2659,
[Li 2001]	X.M. Li, M.J. Starink, Mater. Sci. Techn. 17 (2001), 1324-28
[Lim 2004]	S.T. Lim, S.J. Yun, S.W. Nam, Mat. Sci. Eng. A371 (2004), 82-90
[Lin 2006]	J. Lin, K.C. Ho, T.A. Dean, International Journal of Machine Tools & Manufacture 46 (2006), 1266-1270
[Loo 2008]	P.T. Loo, T.J. Bastow, A.J. Hill, J. da Costa Teixeira, C.R. Hutchinson, Proceedings ICAA11 (2008)
[Ludian 2007]	T. Ludian, L. Wagner, Mat. Sci. Eng A468-470 (2007), 210-213
[Ludwick 1909]	P. Ludwick, Elemente der Technologischen Mechanik. Springer Verlag, Berlin, 1909
[Maciel 2003]	A. Maciel Camacho, H.V. Atkinson, P. Kapranos, B.B. Argent, Acta Mat. 51 (2003), 2319-2330
[Marlaud 2008]	T. Marlaud, PhD thesis, Institut Polytechnique de Grenoble (2008)
[Marlaud 2008b],	T. Marlaud, A. Deschamps, F. Bley, Proceedings ICAA11 (2008)
[Mecking 1981]	H. Mecking, U.F. Kocks, Acta Met. 29 (1981), 1865-1875
[Meo 2003]	M. Meo, R. Vignjevic, Advances in Engineering Software 34 (2003), 569-575
[Moan 1979]	G.D. Moan, J.D. Embury, Acta Mat. 27 (1979), 903-914
[Mondal 2005]	C. Mondal, A.K. Mukhopadhyay, Mat. Sci. Eng. A391 (2005), 367-376
[Morfin 2006]	I. Morfin, F. Ehrburger-Dolle, I. Grillo, F. Livet, F. Bley, J. Synchrotron Rad. 13 (2006), 445-452
[Morgeneyer 2006]	T.F. Morgeneyer, M.J. Starink, I. Sinclair, Mat. Sci. For. 519-521 (2006), 1023-1028
[Morrison 1992]	J.D. Morrison, J.D. Corcoran, K.E. Lewis, J. Appl. Cryst. 25 (1992), 504-513
[Mughrabi 1975]	H. Mughrabi, “Constitutive Equations in Plasticity”, ed. by A.S. Argon, MIT Press, Cambridge, (1975), 199-250
[Muñoz 2008]	M.A. Muñoz-Morris, I. Gutierrez-Urrutia, D.G. Morris, Mat. Sci. Eng. A493 (2008), 141-147
[Myhr 2000]	O.R. Myhr, Ø. Grong, Acta Mat. 48 (2000), 1605-1615
[Myhr 2004]	O.R. Myhr, Ø.Grong, H.G. Fjær, C.D. Marioara, Acta Mat.52 (2004), 4997-5008
[Nabarro 1947]	F.R.N. Nabarro, Proc. Phys. Soc. 59 (1947), 256-272
[Nes 1995]	E. Nes, T. Furu, Scripta Met. et Mat. 33, 1 (1995), 87-92
[Nes 2002]	E. Nes, K. Marthinsen, Y. Bréchet, Scripta Mat. 47 (2002), 607-611
[Nes 2006]	E. Nes, B. Holmedal, B. Forbord, Mat. Sci. For. 519-521 (2006), 63-70
[Nicolas 2002]	M. Nicolas, PhD thesis, Institut National Polytechnique de Grenoble (2002)

[Nicolas 2004]	M. Nicolas, A. Deschamps, Met. and Mat. Trans. A35 (2004), 1437-1448
[Ortiz 1982]	M. Ortiz, E.P. Popov, Proceedings Royal Society London A379 (1982), 439-458
[Peierls 1940]	R. Peierls, Proc. Phys. Soc. 52 (1940), 34-37 :
[Perez 2005]	M. Perez, Scripta Mat. 52 (2005), 709-712
[Perez 2007]	M. Perez, E. Courtois, D. Acevedo, T. Epicier, P. Maugis, Phil. Mag. Let. 87, 9 (2007), 645-656
[Perez 2008]	M. Perez, M. Dumont, D. Acevedo-Reyes, Acta Mat. 56 (2008), 2119-2132
[Philibert 1998]	J. Philibert, A. Vignes, Y. Bréchet, P. Combrade, “Métallurgie, du minerai au matériau“, ed. Masson, Paris (1998)
[Picu 2004]	R.C. Picu, D. Zhang, Acta Mat. 52 (2004), 161-171
[Picu 2005]	R.C. Picu, G. Vincze, F. Ozturk, J.J. Gracio, F. Barlat, A.M. Maniatty, Mat. Sci. Eng. A390 (2005), 334-343
[Poulose 1974]	P.K. Poulose, J.E. Morall, A.J. McEvily, Met. Trans. 5 (1974), 1393-1400
[Preston 2004]	R.V. Preston, H.R. Shercliff, P.J. Withers, S. Smith, Acta Mat. 52 (2004) 4973-4983
[Proudhon 2008]	H. Proudhon, W.J. Poole, X. Wang, Y. Bréchet, Phil.Mag. 88, 5 (2008), 621-640
[Rauch 1993]	E. Rauch, HDR thesis, Institut Polytechnique de Grenoble (1993)
[Rauch 2007]	E.F. Rauch, J.J. Gracio, F. Barlat, Acta Mat. 55 (2007), 2939-2948
[Robertson 2005]	I.M. Robertson, A. Beaudoin, K. Al-Fadhalah, L. Chun-Ming, J. Robach, B.D. Wirth, A. Arsenlis, D. Ahn, P. Sofronis, Mat. Sci. Eng. A400 (2005), 245-250
[Robinson 2006]	J.S. Robinson, D.A. Tanner, Mat. Sci. For. 524-525 (2006), 305-310
[Robson 2001]	J.D. Robson, P.B. Prangnell, Acta Mat. 49 (2001), 599-613
[Robson 2004]	J.D. Robson, Acta Mat. 52 (2004), 1409-1421
[Robson 2007]	J.D. Robson, P.B. Prangnell, B.J. McKay, C.P. Heason, Mat. Sci. For. 550 (2007), 45-54
[Saada 2005]	G. Saada, Mat. Sci. Eng. A400-401 (2005), 146-149
[Seitz 1950]	F. Seitz, Acta Cryst. 3 (1950), 355-363
[Sha 2004]	G. Sha, A. Cerezo, Acta Mat. 52 (2004), 4503-4516
[Shen 2006]	H. Shen, Y. Shi, Z. Yao, J. Hu, Computational Mat. Sci. 37 (2006), 593-598
[Shercliff 1990]	H.R. Shercliff, M.F. Ashby, Act Met. et Mat. 38, 10 (1990), 1789-1802
[Sigli 2006]	C. Sigli, Mat. Sci. For. 519-521 (2006), 321-326
[Simar 2006]	A. Simar, PhD Thesis, Université Catholique de Louvain-La-Neuve (2006)
[Simar 2007]	A. Simar, Y. Bréchet, B. de Meester, A. Denquin, T. Pardoen, Acta Mat. 55 (2007), 6133-6143
[Simar 2008]	A. Simar, Y. Bréchet, B. De Meester, A. Denquin, T. Pardoen, Mat. Sci. Eng. A486, 1-2 (2008), 85-95
[Simon 1997]	J.P. Simon, S. Arnaud, F. Bley, J.F. Berar, B. Caillot, V. Comparat, E. Geissler, A. de Geyer, P. Jeantey, F. Livet, H. Okuda, J. Appl. Cryst. 30 (1997), 900-904
[Simon 2006]	J.P. Simon, J. Appl. Cryst. 40 (2007), s1-s9
[Srikant 2006]	G. Srikant, N. Chollacoop, U. Ramamurty, Acta Mat. 54 (2006), 5171-5178
[Starink 1999]	M.J. Starink, P. Wang, I. Sinclair, P.J. Gregson, Acta Mat. 47, 14 (1999), 3855-3868
[Starink 2003a]	M.J. Starink, X.M. Li, Met. and Mat. Trans. A34, 4 (2003), 899-911
[Starink 2003b]	M.J. Starink, S.C. Wang, Acta Mat. 51 (2003), 5131-5150
[Starink 2005a]	M.J. Starink, Mat. Sci. Eng. A390, 1-2 (2005), 260-264

[Starink 2005b] M.J. Starink, N. Gao, L. Davin, J. Yan, A. Cerezo, Phil. Mag. 85, 13 (2005), 1395-1417

[Starink 2006] M.J. Starink, N. Gao, N. Kamp, S.C. Wang, P.D. Pitcher, I. Sinclair, Mat. Sci. Eng. A418 (2006), 241-249.

[Sullivan 2008] A. Sullivan, J.D. Robson, Mater. Sci. Eng. A478, 1-2 (2007), 351-360

[Tanaka 2006] M. Tanaka, C. Hénon, T. Warner, Mat. Sci. For. 519-521 (2006), 345-350

[Tanner 2003] D.A. Tanner, J.S. Robinson, Finite Elements in Analysis and Design 39 (2003), 369-386

[Taylor 1934a] G.I. Taylor, Proceedings Royal Society London A145 (1934), 362-387

[Taylor 1934b] G.I. Taylor, Proceedings Royal Society London A145 (1934), 388-404

[Teixeira 2008] J. da Costa Teixeira, D.G. Cram, L. Bourgeois, T.J. Bastow, A.J. Hill, C.R. Hutchinson, Acta Mat. 56 (2008), 6109-6122

[Teixeira 2008b] J. da Costa Teixeira, L. Bourgeois, W. Sinclair, C.R. Hutchinson, Proceedings ICAA11 (2008)

[Tekkaya 2000] A.E. Tekkaya, CIRP Annals - Manufacturing Tech. 49 (2000), 205-208

[Thomson 1999] R. Thomson, L. E. Levine, G. G. Long, Acta Cryst. A55 (1999), 433-447

[Tolley 2006] A. Tolley, R. Ferragut, A. Somoza, Mat. Sci. For. 519-521 (2006), 489-494

[Tsao 2005] C.S. Tsao, U.S. Jeng, C.Y. Chen, T.Y. Kuo, Scripta Mat. 53 (2005), 1241-1245

[Voce 1948] E. Voce, J. Inst. Metals, 74 (1948), 537-562

[Vratnica 2007] M. Vratnica, Z. Cvijović, K. Gerić, Z. Burzić, Mat. Sci. For. 555 (2007), 553-558

[Wang 2006] T. Wang, M.J. Platts, A. Levers, J. of Mat. Proc. Tech. 172 (2006), 159-162

[Wang 2006b] Y.M. Wang, A.V. Hamza, E. Ma, Acta Mat. 54 (2006), 2715-2726

[Wang 2007] S.C. Wang, M.J. Starink, Acta Mat. 55 (2007), 933-941

[Wang 2008] J. Wang, D. Yi, X. Su, F. Yin, Mat. Characterization 59 (2008), 965-968

[Watkins 2001] K.G. Watkins, S.P. Edwardson, J. Magee, G. Dearden, P. French, R.L. Cooke, J. Sidhu, N.J. Calder, AMTC, Seattle (2001), paper 2001-01-2610

[Werenskiold 2000] J.C. Werenskiold, A. Deschamps, Y. Bréchet, Mat. Sci. Eng. A293 (2000), 267-274

[Varadarajan 1992] S. Varadarajan, V.A. Fournelle, Acta Met. Mat. 40, 8 (1992), 1847-1854

[Wheelabrator 2008] www.wheelabratorgroup.com

[Williams 2003] J.C. Williams, E.A. Starke, Acta Mat. 51 (2003), 5775-5799

[Windsor 1988] C.G. Windsor, J. Appl. Cryst. 21 (1988), 582-588

[Yi 2007] Y. Yi, H. Chen, Y.C. Lin, Mat. Sci. For. 546-549 (2007), 1065-1068

[Zaiser 1998] M. Zaiser, P. Hähner, Phil. Mag. A77, 6 (1998), 1515-1529

[Zhen 2002] L. Zhen, Y.X. Cui, W.Z. Shao, D.Z. Yang, Mat. Sci. Eng. A336 (2002), 135-142

[Zhu 1997] A.W. Zhu, Acta Mat. 45,10 (1997), 4213-4223

[Zhu 2001a] A.W. Zhu, E.A. Starke, Acta Mat. 49 (2001), 2285-2295

[Zhu 2001b] A.W. Zhu, E.A. Starke, Acta Mat. 49 (2001), 3063-3069

[Zhu 2001c] A.W. Zhu, E.A. Starke, Journ. of Mat. Proc. Tech. 117 (2001), 354-358

[Zhu 2002] X.K. Zhu, Y.J. Chao, Computers and Structures 80 (2002), 967-976

[Zhu 2006] B. Zhu, Y. Zhang, B. Xiong, Z. Li, F. Wang, H. Liu, Mat. Sci. For. 519-521 (2006), 901-906

[Zhu 2008] Z. Zhu, M.J. Starink, Mater. Sci. Eng. A488 (2008), 125-133

VI.D. Table of illustrations

Chapter I

Chapter II

Chapter III

Chapter IV

Chapter V

VI.E.Table of tables

Chapter I

Chapter II

Chapter III

Chapter IV

Chapter V

VI.F. Appendix

A.III.1. Detailed calculation of the KME kinetic equation

A.III.1.a. Storage term

The time for a dislocation to be pinned τ is equal to the average spacing between obstacles L (forest dislocations, precipitates…) divided by the dislocation velocity on a glide plane υ : $\tau = L/\upsilon$.

Whatever the kind of obstacles to the dislocation motion, the dislocation storage rate is proportional to the mobile dislocation density ρ_m and inversely proportional to this duration; in other words:

(A.III.1.) $\frac{\partial \rho^+}{\partial t} = k \frac{\rho_m}{L/\upsilon}$

The Orowan equation tells us that:

(A.III.2.) $d\gamma = \rho_m b \upsilon dt$

Combining (A.III.1.) with (A.III.2.) directly gives the evolution of the dislocation storage term with strain:

(A.III.3.) $\frac{\partial \rho^+}{\partial \gamma} = \frac{k}{bL}$

This general formula can be applied to different kind of obstacles, the main parameters being the inter-obstacles distance L and the obstacle efficiency k .

A.III.1.b. Dynamic recovery term

The dynamic recovery term can be expressed as the following:

(A.III.4.) $\frac{\partial \rho^-}{\partial \gamma} = \frac{\partial \rho^-}{\partial t} \frac{\partial t}{\partial \gamma}$

The first factor (annihilation rate) is obtained through the following reasoning: a single moving dislocation will annihilate if it comes close enough from another dislocation with an opposite Burgers vector (see Fig. VI.1). The annihilation distance $2R$ is temperature and strain rate dependant. In other words, the characteristic annihilation volume (volume in which a dislocation of length L gliding at a velocity υ during dt is likely to meet a dislocation of opposite sign with which annihilation may occur) is equal to (see Fig. VI.2):

(A.III.5.) $dV = 2RL\upsilon dt$

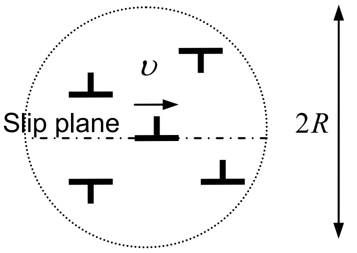

Fig. VI.1. 2D representation of the annihilation volume

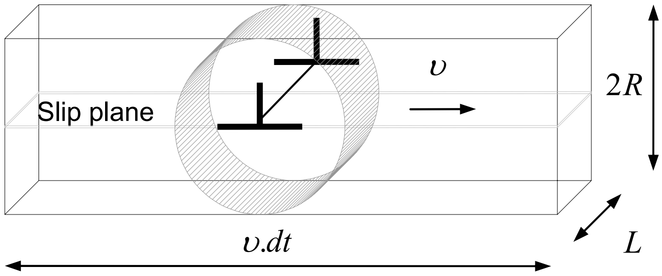

Fig. VI.2. Volume swept by a moving dislocation

The more dislocations there are in the surrounding volume, the higher will be the probability to annihilate: the length of annihilated dislocation is proportional to the total dislocation length present in the characteristic volume: ρdV . Nevertheless, as only dislocations with opposite Burgers vector can annihilate, an efficiency parameter k has to be introduced. The length of annihilated dislocation dL^- in the elementary volume around a mobile dislocation is finally equal to:

(A.III.6.) $dL^- = k\rho dV$

If one considers the volume of the specimen V_t, as a function of the mobile dislocation density ρ_m:

(A.III.7.) $V_t = L_t / \rho_m = nL / \rho_m$

where L_t is the total dislocation length in the material and n the number of elementary volumes, the dislocation density evolution may be written as:

(A.III.8.) $d\rho^- = -ndL^- / V_t$

Combining equations (A.III.5.), (A.III.6.), (A.III.7.) and (A.III.8.), one obtains:

(A.III.9.) $d\rho^- = -2kR\upsilon\rho\rho_m dt$

This expression expresses that the more dislocations there are in the surrounding area, the higher will be the probability to annihilate ($\partial\rho^- / \partial t \propto \rho$) and that each moving dislocation may be subjected to annihilation ($\partial\rho^- / \partial t \propto \rho_m$).

Combining expression (A.III.9.) and the Orowan equation (A.III.2.), (A.III.4.) is finally equal to:

(A.III.10.) $$\frac{\partial\rho^-}{\partial\gamma} = \frac{\partial\rho^-}{\partial t}\frac{\partial t}{\partial\gamma} = \frac{-2kR}{b}\rho$$

This expression is commonly written as:

(A.III.11.) $$\partial\rho^- / \partial\gamma = k_2\rho$$

A.III.2. Relation between R, fv and L

Assuming that n spherical precipitates of radius R are present in a volume $V = 2RX^2$ (see Fig. VI.3), the precipitate volume fraction f_v is equal to:

(A.III.12.) $$f_v = n\frac{4/3\pi R^3}{2RX^2}$$

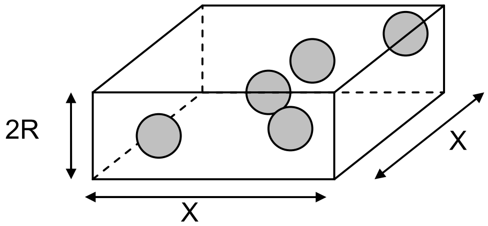

Fig. VI.3. 2D representation of the annihilation volume

The precipitate surface density in one glide plane N_P is defined as the number of precipitates in the plane of surface X^2; in other words: $N_P = n/X^2$. The precipitate volume fraction is then:

(A.III.13.) $$f_v = 2/3\pi N_P R^2$$

The inter-precipitate distance L is equal to $L = 1/\sqrt{N_P}$, that is to say that the expression linking the precipitate volume fraction to the precipitate size and inter-precipitate distance is written as:

(A.III.14.) $$f_v = \frac{2\pi}{3}\frac{R^2}{L^2}$$

A.III.3. Calculation of the effective inter-precipitate distance

The effective inter-precipitate distance may be written in a form different from the purely geometrical expression presented in the previous part:

(A.III.15.) $$L = \sqrt{\frac{2\pi}{3}} \frac{R}{\sqrt{f_v}}$$

This new expression is directly derived from the new strain hardening model, which will bring it together with the initial Estrin model. As the total dislocation density may be written $\rho_{total} = \rho + \rho_P$, its derivative versus deformation is equal to:

(A.III.16.) $$\frac{\partial \rho_{total}}{\partial \varepsilon_p} = \frac{\partial \rho}{\partial \varepsilon_p} + \frac{\partial \rho_P}{\partial \varepsilon_p}$$

The first term, the mobile dislocation density, evolves as:

(A.III.17.) $$\frac{\partial \rho}{\partial \varepsilon_p} = M\left(k_1\sqrt{\rho} - k_2\rho\right)$$

The second term, the Orowan loops density, is equal to:

(A.III.18.) $$\frac{\partial \rho_P}{\partial \varepsilon_p} = \frac{\partial}{\partial \varepsilon_p}\left(n.\varphi\frac{3.f_v}{2r^2}\right) = M\frac{2r}{b}\left(1 - \frac{n}{n^*}\right)\left(\varphi\frac{3.f_v}{2r^2}\right) = \left(\varphi\frac{3.f_v}{r}\right)\frac{M}{b}\left(1 - \frac{n}{n^*}\right)$$

Replacing expressions (A.III.17.) and (A.III.18.) into equation (A.III.16.) gives:

(A.III.19.) $$\frac{\partial \rho_{total}}{\partial \varepsilon_p} = M\left(k_1\sqrt{\rho} - k_2\rho\right) + \frac{M}{b}\varphi\frac{3.f_v}{r}\left(1 - \frac{n}{n^*}\right)$$

Another form of equation (A.III.19.) may be:

(A.III.20.) $$\frac{\partial \rho_{total}}{\partial \varepsilon_p} = M\left(k_1\sqrt{\rho} + \frac{\varphi}{bL} - k_2\rho\right)$$

This is exactly the equation used by Simar in her model (formerly from Estrin), to account for the global dislocation density evolution. The second term, φ/bL, accounts for the storage of Orowan loops and L is the distance between non-shearable precipitates. If one compares equations (A.III.19.) and (A.III.20.), it gives a new form of the effective inter-precipitate distance, defined as:

(A.III.21.) $$L = \frac{r}{3.f_v}\frac{n^*}{n^* - n}$$

n varying with deformation, this effective distance is strain dependant. In other words, as represented in Fig. VI.4, Orowan storage diminishes as deformation goes on, and as soon as the maximal number of Orowan loops is stored ($n = n^*$), this additional storage term becomes ineffective.

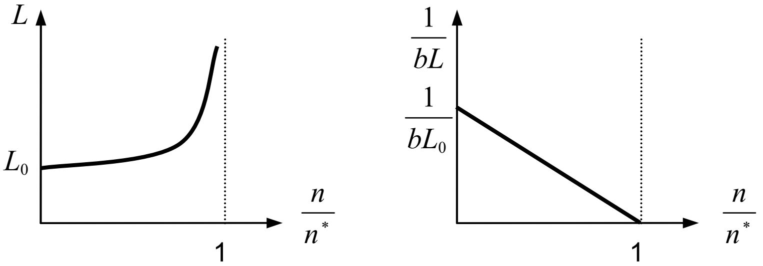

Fig. VI.4. Schematic of the inter-precipitate distance evolution with strain

(a) Inter-precipitate distance. (b) Additional storage parameter.

A.III.4. Parametric study of the global strain hardening model

The influence of the main model parameters is presented in this section. The experimental tensile curves are compared to the model presented in III.D.2, associated to the model parameters presented in Table III.7. In each of the figures presented in this section, one parameter is varied:

φ (Fig. VI.5), the parameter accounting for the stability of Orowan loops as a function of the precipitate size, is either chosen constant, or varying linearly between R_{trans1} and R_{trans2}, after which it remains constant ($\varphi = 1$).

n^* (Fig. VI.6), the maximum number of Orowan loops for one precipitate, is varied between 5 and 15. The value chosen for the model is 9.

y_P (Fig. VI.7), which accounts for the enhanced dislocation annihilation due to Orowan loops, is varied between $y_0 = 0.57nm$ (i.e. there is no influence of Orowan loops) and 100 nm (i.e. the presence of Orowan loops deeply affects annihilation). The value chosen in the model is 10 nm.

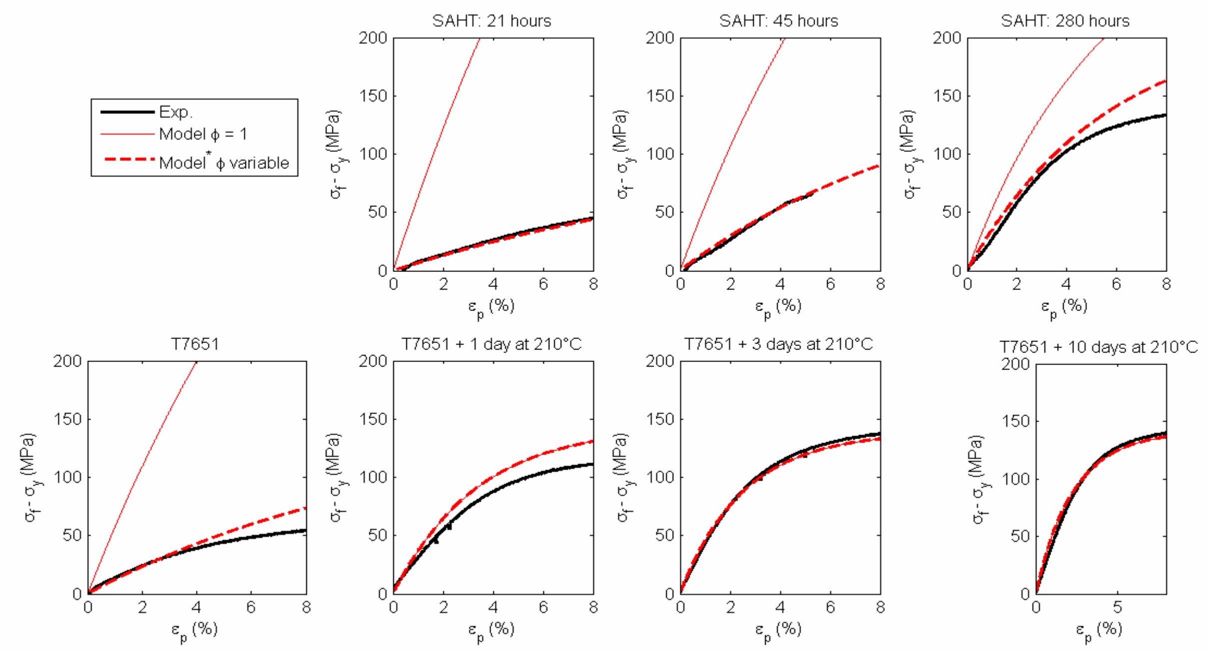

Fig. VI.5. Influence of φ on work hardening

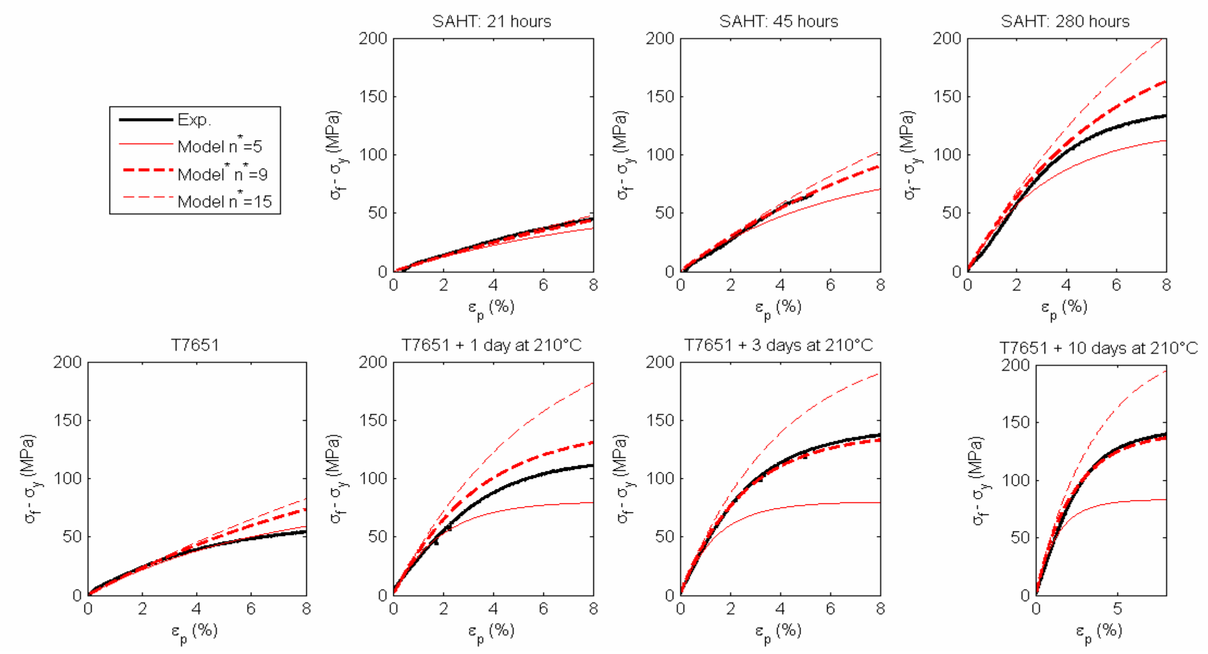

Fig. VI.6. Influence of n* on work hardening

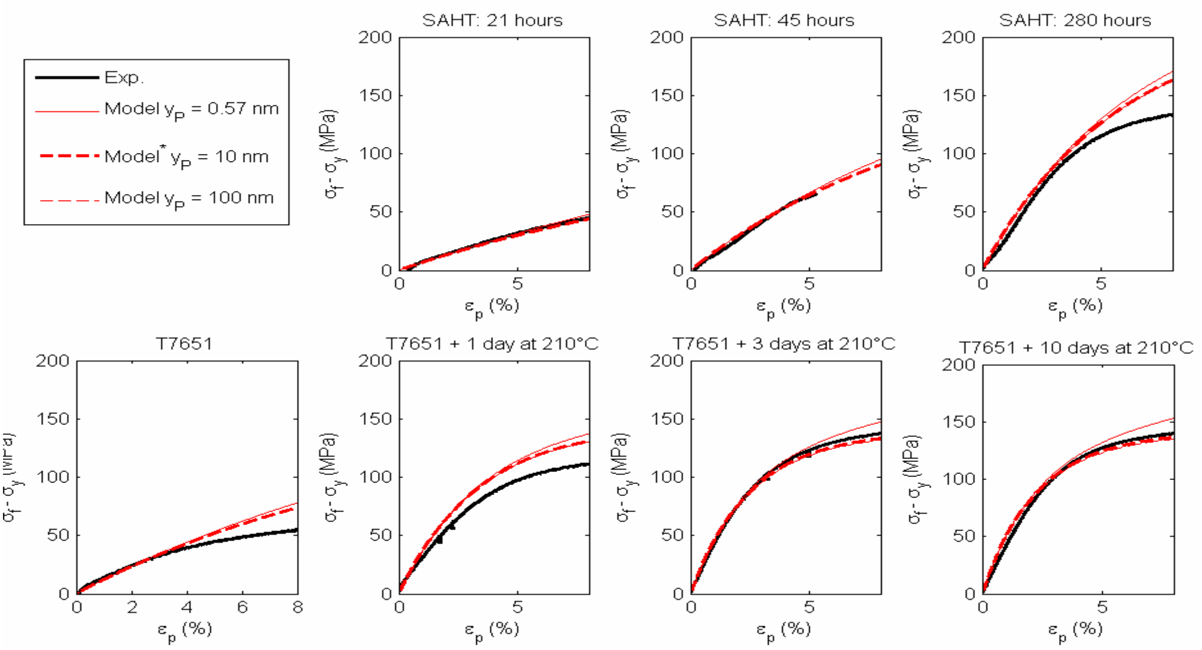

Fig. VI.7. Influence of y_p on work hardening

A.III.5. Evolution of total work hardening and fracture during aging

Elongation at ultimate tensile strength (or homogeneous elongation) and total hardening capability (defined as the difference between UTS and YS converted into true values) are respectively plot in Fig. VI.8 and Fig. VI.9.

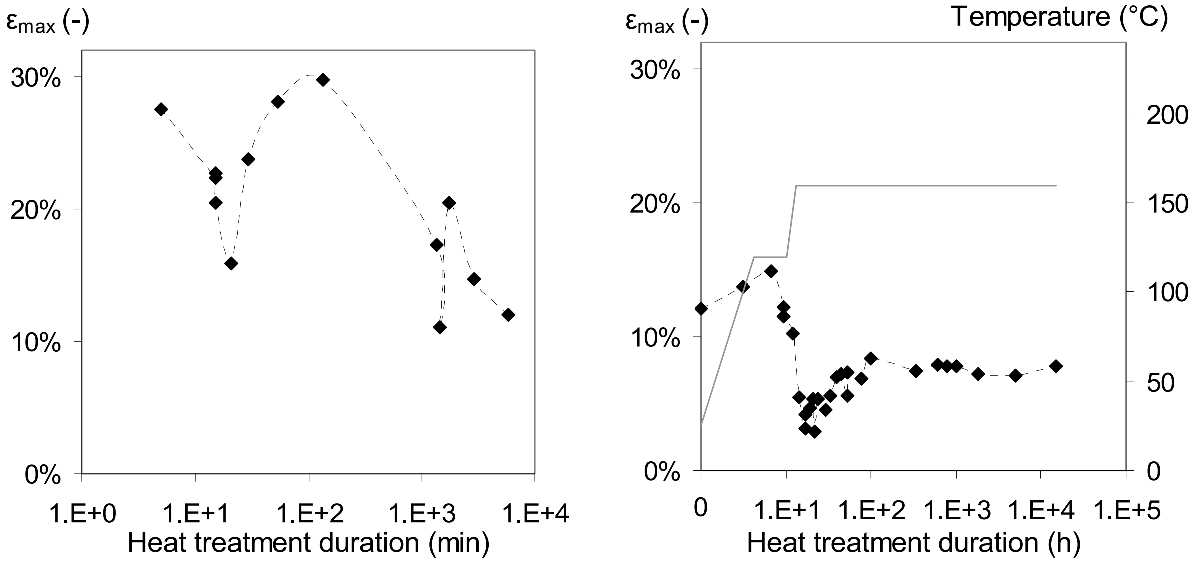

Fig. VI.8. Evolution of elongation as a function of ageing treatment

(a) Naturally aged tempers. (b) Artificially aged tempers. Note: True stress and strain values.

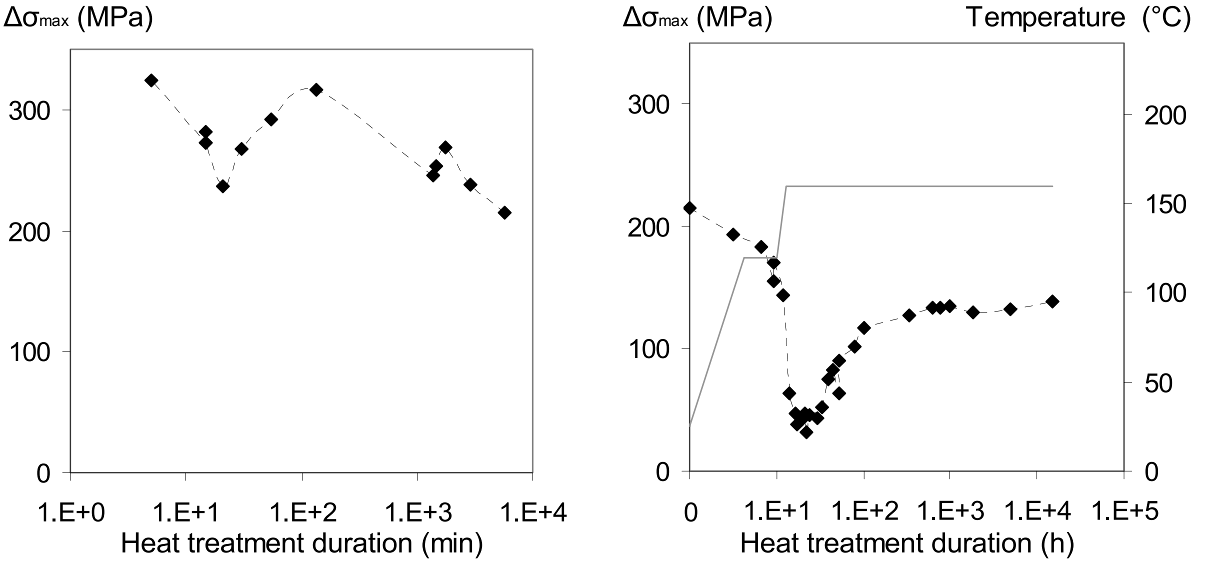

Fig. VI.9. Evolution of hardening capability as a function of ageing treatment

(a) Naturally aged tempers. (b) Artificially aged tempers. Note: True stress and strain values.

Those two parameters (maximum homogeneous elongation and total hardening) follow the same behaviour: they decrease up to peak strength and increase afterwards. A close look on those two figures shows the same discontinuity of the ductility as what have been observed in Fig. III.22 and Fig. III.23. at the very beginning of the natural aging treatment, only after a few minutes of aging.

Necking is a plastic instability which occurs when the material is not able to consolidate (to harden) in the smallest section: this leads to the localization of the deformation, and finally to collapse. In other words a material able to consolidate up to high values reaches high strain values. On the contrary at the peak strength, deformation localises more. A more intergranular fracture profile can be found at this stage (see Fig. VI.10.d), while it is more ductile for the under-aged and over-aged tempers.

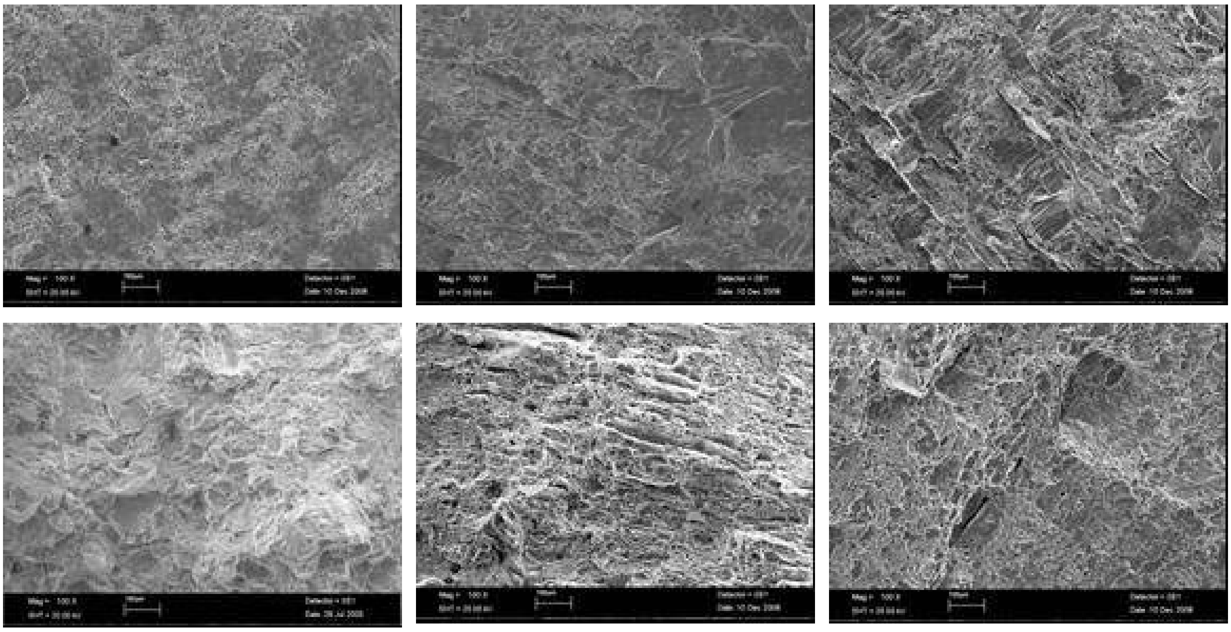

Fig. VI.10. Evolution of fracture profile during aging

TEM micrographs (a) After 2 hours days natural aging. (b) After 2 days natural aging. (c) After 5 hours artificial aging. (d) Peak temper. (e) After 20 hours of artificial aging. (f) After 700 hours of artificial aging.